

**Uncertainty quantification in a computationally
optimised volume conductor model for deep brain
stimulation**

Dissertation

zur

Erlangung des akademischen Grades

Doktor-Ingenieur (Dr.-Ing.)

der Fakultät für Informatik und Elektrotechnik

der Universität Rostock

vorgelegt von

Christian Schmidt, geboren am 06.08.1983 in Wismar
aus Rostock

Rostock, 21.06.2013

Tag der Einreichung: 21.06.2013
Tag der Verteidigung: 25.10.2013

Gutachter

Prof. Dr. Ursula van Rienen, Universität Rostock
Prof. Dr. Herbert de Gerssem, Katholische Universität Leuven
Prof. Dr. Ludger Klinkenbusch, Christian-Albrechts-Universität zu Kiel

Diese Arbeit ist meiner Mutter
Regina Schmidt (★21.5.1961; †6.11.2005)
gewidmet.

"There is a theory which states that if ever anybody discovers exactly what the Universe is for and why it is here, it will instantly disappear and be replaced by something even more bizarre and inexplicable. There is another theory which states that this has already happened."
Douglas Adams

Danksagungen

Diese Arbeit wurde von der Deutschen Forschungsgemeinschaft (DFG) im Rahmen des Graduiertenkollegs "welisa" 1505/1 unterstützt.

An erster Stelle möchte ich meiner Betreuerin Frau Prof. Ursula van Rienen für die Themenstellung, die erfahrene Förderung und die zahlreichen Gespräche danken. Dank gilt auch der AG "Theoretische Elektrotechnik" für das tolle Arbeitsklima und die fachliche Unterstützung. Besonderer Dank gilt dabei Thomas für ein immer offenes Ohr und eine Vielzahl an "Ohrwürmern" aus dem Bereich des deutschen Schlagers, Korinna und Gisela für seelische Unterstützung und die Geduld bei meinen mitunter ausufernden fachlichen Erläuterungen, Alex für seine motivierenden Sprüche, und nicht zuletzt Ulf für eine tolle Atmosphäre im Büro und viele heitere Momente.

Aus meiner Zeit am University College Dublin möchte ich vor allem Madeleine, Peadar, Moe, Brian und Clare für die freundliche Aufnahme in die AG, für zahlreiche fachliche Gespräche, die schöne Zeit, und die Einführung in das irische Brauchtum danken. Tapadh leat!

Großer Dank gilt meiner Familie und meinen Freunden, ohne deren Unterstützung diese Arbeit nicht entstanden wäre. Ich bedanke mich vor allem bei Julia und Konstantin für das ausdauernde Korrekturlesen meiner Arbeit, André und Maria für die seelische Unterstützung, Adrian, Herr Schmidt und Jens für glorreiche und frustrierende Momente im Ostseestadion, und Mike, dem weltbesten Schokobären.

Zu guter letzt möchte ich allen danken, die ich hier nicht explizit aufgezählt habe. Sie haben einen maßgeblichen Anteil an der Entstehung dieser Arbeit und ich danke ihnen dafür, dass sie meine Freunde und Teil meines Lebens sind.

Contents

1	Introduction	1
2	Fundamentals of deep brain stimulation and its modelling	3
2.1	Parkinson's disease	3
2.1.1	Basal ganglia anatomy	4
2.1.2	Functional organization	4
2.2	Application and mechanism of deep brain stimulation	6
2.2.1	Electrode lead and stimulation protocol	7
2.2.2	Surgery planning and performance	8
2.2.3	Target selection	9
2.2.4	Mechanisms of deep brain stimulation	10
2.3	Computational modelling	11
2.3.1	Network modelling of the basal ganglia	11
2.3.2	Volume conductor models of the human brain	14
2.4	Objectives and research goals	16
3	Aspects of volume conductor models of the human brain	19
3.1	Electro-quasistatic and quasistatic formulation	19
3.1.1	Maxwell's equations in bio-electrical applications	19
3.1.2	Electrical properties of brain tissue	24
3.2	Finite element method	26
3.2.1	Galerkin method	26
3.2.2	Discretisation with finite elements	28
3.2.3	Assembly of the global system of linear equations	30
3.2.4	Finite element software	30
3.2.5	Fourier finite element method	31
3.3	Fourier finite element method with equivalent circuits (FFEMEC)	32
3.3.1	Modelling and Fourier transform of the stimulation pulse	35
3.3.2	Equivalent circuit model	37
3.3.3	Current-controlled stimulation	38
3.3.4	Voltage-controlled stimulation	40
3.4	Anisotropy of brain tissue	42
3.4.1	Diffusion tensor imaging	43
3.4.2	Conductivity tensor computation	44
3.4.3	Limitations of diffusion tensor imaging	45

3.5	Generation of an anatomical brain model	45
3.5.1	The SRI24 multi-channel brain atlas	46
3.5.2	Geometry generation and physical boundary conditions	47
3.5.3	Incorporation of electrical tissue properties and tissue anisotropy	49
3.6	Computation of the volume of tissue activated	51
4	Uncertainty quantification by the polynomial chaos technique	55
4.1	Overview of available methods for uncertainty quantification	55
4.2	Polynomial chaos technique	57
4.2.1	Generation of the polynomial basis	58
4.2.2	Numerical evaluation of the expansion coefficients	62
4.2.3	Non-intrusive projection approach	63
4.3	Multi-dimensional cubature	69
4.3.1	One-dimensional Clenshaw-Curtis rule	69
4.3.2	Multi-dimensional tensor grids	71
4.3.3	Multi-dimensional sparse grids	73
4.4	Implementation aspects	76
5	Results and discussion	79
5.1	Discretisation and solver aspects of the volume conductor model . . .	79
5.1.1	Discretisation of the volume conductor model	80
5.1.2	Numerical solver considerations	83
5.2	Fast computation of the time-dependent voltage response	85
5.2.1	Validity of the electro-quasistatic equation	85
5.2.2	Validation of FFEMEC	87
5.2.3	Single frequency approximation of the dispersive brain model .	91
5.3	Uncertainty quantification by the polynomial chaos technique	97
5.3.1	Validation of the non-intrusive projection approach	98
5.3.2	Uncertainty in the parameters of the electrode-tissue-interface	102
5.3.3	Uncertainty in the electrical properties of brain tissue	107
5.4	Influence of the anisotropic conductivity and electrode position	118
5.4.1	Anisotropic time-dependent voltage response	119
5.4.2	Variation of the electrode position	123
5.5	Limitations of the volume conductor model and the applied methods	125
6	Conclusion and outlook	133
A	Appendix	137
A.1	Representation of heterogeneous media by lumped equivalent circuit components	137
	Bibliography	141

Acronyms

BEM	boundary element method
BiCGSTAB	Biconjugate gradient stabilized method
CDF	cumulative distribution function
CG	conjugate gradient method
COCG	conjugate orthogonal conjugate gradient method
CPE	constant phase element
CPu	caudate putamen
CSF	cerebrospinal fluid
CT	computed tomography
DBS	deep brain stimulation
DTI	diffusion tensor imaging
EEG	electroencephalography
EQS	electro-quasistatic
FA	fractional anisotropy
FDA	Food and Drug Administration
FEM	finite element method
FFEM	Fourier finite element method
FFEMEC	Fourier finite element method with equivalent circuits
FFT	fast Fourier transform
FIT	finite integration technique
GMRES	generalized minimal residual method
GPe	globus pallidus externus
GPi	globus pallidus internus
IPS	idiopathic Parkinson syndrome
LFP	local field potential
MCS	Monte Carlo simulation
MPI	message passing interface
MRI	magnetic resonance imaging
MUMPS	multifrontal massively parallel sparse direct solver
NRRD	nearly raw raster data
PC	polynomial chaos
PD	Parkinson's disease
PDF	probability density function
PPN	pedunclopontine nucleus
RMS	root mean square

ROI	region of interest
SLE	system of linear equations
STN	subthalamic nucleus
SNC	substantia nigra pars compacta
SNr	substantia nigra pars reticulata
Vim	thalamic ventral intermediate nucleus
QS	quasistatic
UQ	uncertainty quantification
VTA	volume of tissue activated

1 Introduction

Deep brain stimulation (DBS) is a neurosurgical method based on implanting electrodes in selected brain areas to treat symptoms of neurological and psychiatric disorders. The implanted electrodes are connected to a pulse generator, which induces an electric field in the proximity of the electrode contacts. These electrode contacts are located at the tip of the electrode and form the connection between the electrode and the tissue. The time-varying field changes the activation pattern of the neurons in the stimulated area. The method became most popular for the treatment of the symptoms of drug-resistant Parkinson's disease (PD), but it is now applied to a growing number of diseases. Several neuropsychiatric disorders, such as essential tremor, dystonia, Tourette syndrome, obsessive compulsive disorders, and depression, are clinically field-tested or have been approved by the Food and Drug Administration (FDA). Since 1995 to date, about 80,000 DBS electrodes from the market leader Medtronic were implanted into patients suffering from PD, essential tremor, or dystonia.

Although the method is successfully applied in several clinical situations and has become a common procedure in clinical practise, the understanding of its mechanisms of action and long-term effects is still scarce. *In vitro* and *in vivo* experiments in animal models and humans as well as *in silico* computational models are used to achieve a deeper understanding of these mechanisms. Starting in the last decade, numerous computational models for predicting the effects of DBS were developed. These models can be categorized into (1) neural network models examining the effects of the stimulation pulses on the neural network as well as the activation of neurons and (2) volume conductor models predicting the field distribution and waveform of the stimulation pulse in the proximity of the electrode contacts. Clinical software aiming at the support in the planning and performance of the complex procedure of implanting and adjusting the DBS electrode take benefit from these models. Areas of possible neural activation based on the electrode location and the stimulation parameters help the physician to optimize the procedure in the pre- and intra-operative stage. The performance and practical usage of this software depends on the complexity of the input parameters and their reliability. Information on the electrical properties of brain tissue varies considerably in the literature. Despite this uncertainty in the model parameters, recent models of DBS are based on one set of deterministic values of the model parameters and, therefore, do not regard their uncertainty and its propagation on the model solution.

This thesis examines the influence of uncertainty in the model parameters on the time-dependent voltage response of the stimulation pulse and its impact on the neural activation in the proximity of the stimulated target area. An anatomical head model incorporating heterogeneous and anisotropic tissue properties was generated based on a digital brain atlas and used to undertake *in silico* studies. Chapter 2 introduces basics of DBS and hypotheses regarding the mechanisms of PD as well as of interventional effects of DBS. Recent models of DBS aiming at predicting the neural activation and the time-dependent voltage response in the proximity of the electrode tip are reviewed referring to these hypotheses. Various model parameters, such as the geometry, the electrical properties of the tissue, the stimulated target, and stimulation parameters, are examined in detail. In Chapter 3, finite element method and Fourier analysis are introduced as the fundamental methods for solving the field distribution in the proximity of the electrode contact. The electro-quasistatic and quasistatic formulation of bio-electrical applications in the human brain requires certain conditions for the simplification of the full set of Maxwell's equations, which are discussed in detail. Based on these conditions, a computationally efficient method to compute the time-dependent voltage response in a volume conductor model with finite element method (FEM) coupled with equivalent circuits is proposed. The generation of the anatomical head model based on the data of a digital brain atlas and the incorporation of heterogeneous, frequency dependent, and anisotropic material properties is described. The concept of the computation of the volume of tissue activated (VTA) and its implementation for the prediction of neural activation is introduced. The uncertainty quantification (UQ) of the electrical properties of brain tissue on the field distribution by using a non-intrusive approach is introduced in Chapter 4. The non-intrusive approach allows to leave the deterministic code unchanged and to use it similar to a "black box". This approach is based on an approximation of the probability distribution of the model parameters and model solutions by expanding them on a multi-dimensional orthogonal basis. Different methods of multi-dimensional cubature using tensor grids as well as sparse grids necessary to solve the expansion coefficients are described. Chapter 5 comprises the results and the discussion of the realized studies to validate the implemented methods and the investigation of the influence of various model parameters on the time-dependent voltage response and neural activation in the proximity of the stimulated target. Suggestions on the sensitivity of these quantities on the investigated model parameters are determined and limitations in the generated volume conductor model and the proposed methods are discussed. Chapter 6 provides a concluding summary of the realized work and further objectives.

2 Fundamentals of deep brain stimulation and its modelling

Deep brain stimulation (DBS) is a highly effective neurosurgical therapy to treat symptoms of neurodegenerative disorders. In DBS, small electrodes attached to a stimulator are implanted into selected brain areas, which are stimulated via the electrode contacts with short pulses of low amplitude. DBS is approved by the regulatory authorities in Europe and the US for treatment of PD, essential tremor, dystonia, and obsessive-compulsive disorder. In addition, the treatment of Tourette syndrome, cluster headache, addiction, and other neuropsychiatric diseases is studied in clinical trials [38]. Although the therapy is highly effective, knowledge about the fundamental mechanisms of action of DBS and its long-term effects is still scarce. The currently favoured hypothesis assumes that neurodegenerative disorders such as PD cause oscillatory firing patterns in the deep brain nuclei called basal ganglia, which are responsible for motor function [19]. The stimulation pulses override the firing patterns of these abnormally behaving nuclei with a high frequency pattern and provide a rehabilitation of the motor function close to the healthy state. Besides the successful treatment of motor symptoms, a misplaced electrode or wrong stimulation parameters can cause several undesired side effects, such as cognitive impairments and mental disorders [38].

2.1 Parkinson's disease

PD is a neurodegenerative disorder and was first described in 1817 by James Parkinson. Almost one hundred years later, in 1940, first surgical methods for the treatment of PD were introduced [18]. Its symptoms comprise the poverty of voluntary movements (akinesia), slowness of voluntary movements (bradykinesia), rigidity, tremor, and postural instability [64]. PD is caused by the death of dopaminergic cells of the substantia nigra. Administration of L-3,4-dihydroxyphenylalanine (levodopa), a dopamin-replacement drug introduced 1961 by Birkmayer and Hornykiewicz, can result in an ease of the motor dysfunction in the early stage of the disease [15]. PD can be categorised into hereditary parkinsonism and idiopathic Parkinson syndrome (IPS), which is the main target for the application of DBS. It is assumed that the reason for the motor dysfunction in PD correlates with an abnormal firing rate and pattern in the basal-ganglia neurons, which results in a changing oscillatory activity and excessive synchronization [19, 48].

2.1.1 Basal ganglia anatomy

The passages about the basal ganglia anatomy and its functional organization are based on the description of Young and Penney [141]. The basal ganglia are located at the base of the forebrain beneath the cerebral cortex and are responsible for the modulation and facilitation of motor and cognitive functions. They consist of a group of gray matter nuclei and are strongly connected to the thalamus and hypothalamus as well as to the cerebral cortex. The group of basal ganglia nuclei, which are important for involuntary motor functions, comprises parts of the striatum composed of the caudate nucleus and the caudate putamen (CPu), the globus pallidus internus (GPi), the globus pallidus externus (GPe), the subthalamic nucleus (STN), the substantia nigra pars compacta (SNc), and the substantia nigra pars reticulata (SNr) (Fig. 2.1).

2.1.2 Functional organization

The basal ganglia are connected via pathways characterised by inhibition and excitation of neural activity within the nuclei. The dopamine pathway from the substantia nigra pars compacta to the striatum modulates the basal ganglia function by controlling its response to cortical inputs, thereby enabling the normal performance of complex sensomotoric functions such as postural stability and secure gait. The cortex is responsible for the excitation of the brain stem and is therefore connected to the control of the muscle fibres as well as the striatum. The basal ganglia are

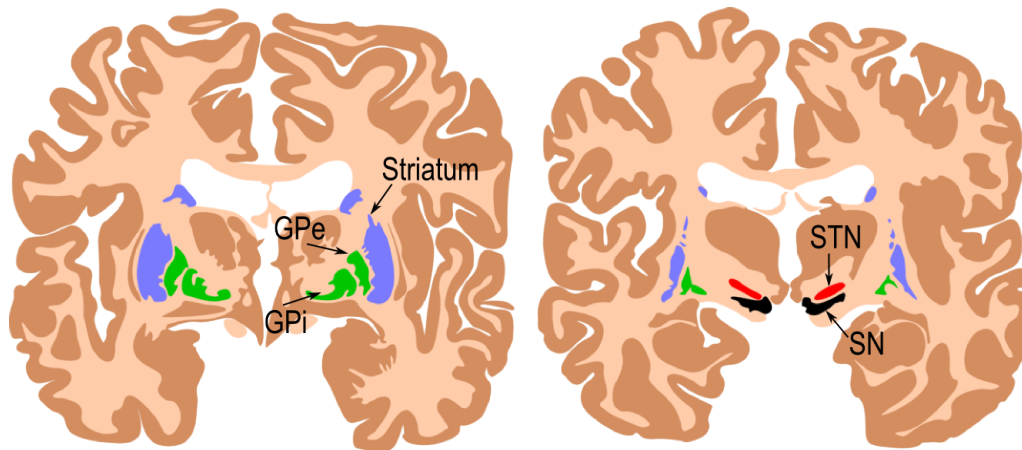


Figure 2.1: Coronal sections of the brain showing the basal ganglia. Globus pallidus internus (GPi), Globus pallidus externus (GPe), Subthalamic nucleus (STN), Substantia nigra (SN). Modified from the image Basal.ganglia.svg in Wikimedia Commons. By Andrew Gillies and Mikael Häggström. Licensed under the Creative Commons Attribution-Share Alike 3.0 Unported and the GNU Free Documentation License, Version 1.2.

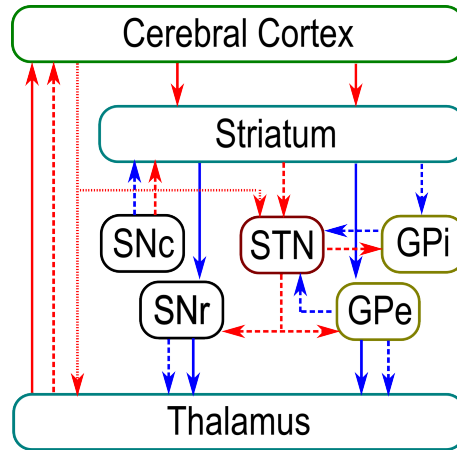


Figure 2.2: Direct, indirect, and hyperdirect pathways in the basal ganglia network. Red arrows refer to excitation, blue arrows to inhibition. Solid arrows indicate the direct pathway, dashed arrows the indirect pathway and dotted arrows the hyperdirect pathway. Image based on [141] with extension according to [48]. Abbreviations see Fig. 2.1.

closely connected to the cortex and over the striatum with the thalamus [48]. The striatum projects in two different directions, forming two distinct and reciprocally behaving pathways, the direct and the indirect pathway (Fig. 2.2). For the direct pathway, the striatum projects inhibitory neurons to the SNr and GPi, which send inhibitory signals to the thalamus. This inhibition by SNr and GPi on the thalamus results in a reduction of the thalamic activity, which inhibits the excitatory projection of thalamus to the cortex. For the indirect pathway, the striatum projects inhibitory neurons to the GPe, which tonically inhibits the STN. This reduction of inhibition results in an increased activity of the STN and subsequently in an increased excitation of the SNr and GPi. Both nuclei inhibit the thalamus, resulting in a decreased stimulation of the motor cortex by the thalamus and, therefore, reduced muscle activity. In PD, the indirect pathway becomes hyperactive and suppresses permanently normal involuntary motor functions [48]. Since the antagonistically acting direct and indirect pathways receive excitatory inputs from the motor cortex and influence its activity reversely via the thalamus, the hypothesis of feedback loops in the basal ganglia, resulting in oscillations and synchronous activity patterns has been developed [20, 48, 64].

However, the oscillations observed at different levels of the basal ganglia network in PD patients are not sufficiently explained by the simple argument of the direct and the indirect pathways. Gatev et al. [48] extended the governing model by describing oscillatory interactions between different nuclei of the basal ganglia. According to their model, the potential pacemaker is the oscillatory feedback circuit between the STN and GPi producing synchronised oscillatory activity (Fig. 2.2). This oscillatory activity is projected to other nuclei of the basal ganglia, e.g. to the GPi by the

STN, resulting in similar local spike patterns, which were confirmed in a local field potential (LFP) study in humans.

The currently favoured hypothesis of the PD pathogenesis claims that the death of dopaminergic cells in the SNc causes changes in the oscillatory firing pattern of the basal ganglia, resulting in excessive synchronization, which leads to the pathological motor symptoms of the disease [48]. LFP recordings in patients with parkinsonism showed synchronous neural activity in a 10 to 30 Hz band correlated with the frequency of muscle activity for tremor, which could be reduced by treatment with levodopa [19]. *In vivo* experiments with parkinsonian monkeys confirmed the pathological oscillation hypothesis by demonstrating oscillatory and synchronous burst patterns in the STN, GPe and GPi [64]. Another *in vivo* study with parkinsonian monkeys showed that a treatment with levodopa resulted in a reduction of this synchronous activity [48]. However, the exact mechanisms of how the death of dopaminergic cells generates synchronous oscillatory activity in the basal ganglia remain unclear.

2.2 Application and mechanism of deep brain stimulation

Until the 1990s, a surgical lesioning procedure of the thalamus and GPi was performed to treat the motor dysfunction of the basal ganglia network in PD. The method is controversial and raised concerns because of its irreversibility and adverse effects such as strokes and infections, which were in particular a consequence of misplaced lesions [18]. In the 1970s, DBS was first used to treat chronic central and peripheral pain [11, 38], and spasmodic torticollis [91]. Its application for the treatment of essential tremor and PD was introduced by the group of BENABID and POLLAK in the mid 1980s [13, 14]. Since the 1990s, the lesioning procedure was almost completely replaced by DBS in the industrial countries, which was approved by the FDA for essential tremor in 1997 and for PD in 2002 [18]. Meanwhile, more than 80,000 clinical DBS electrode implantations have been performed worldwide, mainly by using devices of the market leader Medtronic [86]. Unlike the irreversible lesioning procedure, DBS does not destroy nervous tissue when the electrodes are placed correctly and optimal stimulation parameters are applied. The best predictor for a beneficial effect of DBS in PD patients is the response to levodopa. In clinical practise, an initial improvement of 30 % of symptoms in the unified PD rating scale for motor symptoms should be reached by levodopa administration in order to recommend DBS therapy, when the efficiency of levodopa therapy vanishes and motor symptoms reexacerbate [61]. This is regularly the case after five to ten years of levodopa administration [64]. Referring to Bronstein et al. [18], best results of DBS in patients with advanced PD symptoms are reached when they meet the following

criteria: younger age (no clear age cut-off can be provided to date due to insufficient data), excellent initial levodopa response of PD symptoms, no other motor symptoms responsive to levodopa, no psychiatric diseases such as depression, and no cognitive disorders such as dementia. The fulfillment of these criteria is a prerequisite of adequate patient selection, since 30 % of complications of DBS surgery are ascribed to inappropriate indications [18].

2.2.1 Electrode lead and stimulation protocol

Clinical DBS is mainly performed using electrodes of the leader company Medtronic. Their specification is described by Farris and Giroux [38]. Currently, two FDA-approved electrodes, Medtronic DBS Models 3387 and 3389, are available. Both electrodes consist of a small-diameter lead wire with 4 electrode contacts at the top. The cylindrical electrode contacts are made of platinum-iridium and have a diameter of 1.27 mm and a length of 1.5 mm (Fig. 2.3). The lead is insulated by urethane. The spacing between the electrode contacts is 1.5 mm for model 3387 and 0.5 mm for model 3389. The lead is connected to a large-diameter extension, which is implanted under the skin and connected to the neurostimulator. The neurostimulator is typically implanted in the subclavicular region (beneath the collarbone) and consists of a battery and the electronic components necessary to provide the stimulation pulses to the electrode contacts [85]. The conventional neurostimulator can be continuously operated for about 2 to 5 years. Recently, a rechargeable neurostimulator has been introduced, which has a battery lifetime of up to 9 years.

The DBS system can be operated either in a bipolar mode with one active electrode contact and one electrode contact acting as ground or in a unipolar mode, where the neurostimulator case serves as ground plate. Currently, stimulation pulses used in DBS therapy are empirically determined and are delivered as voltage-controlled square-wave signals [19]. Typical stimulation parameters for chronic unipolar DBS are (1) a cathodic voltage amplitude of 2.5 to 3.5 V, (2) a pulse duration of 60 to

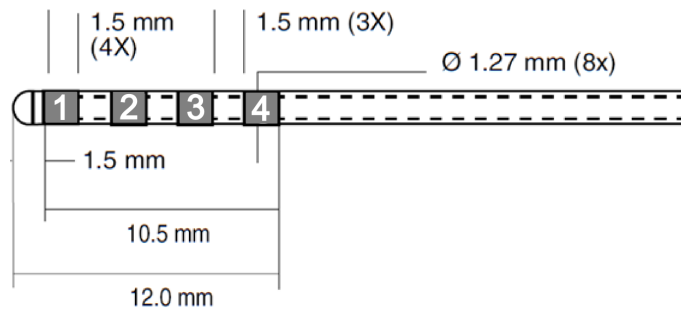


Figure 2.3: Schematic image of the Medtronic DBS Model 3387 electrode lead based on [85].

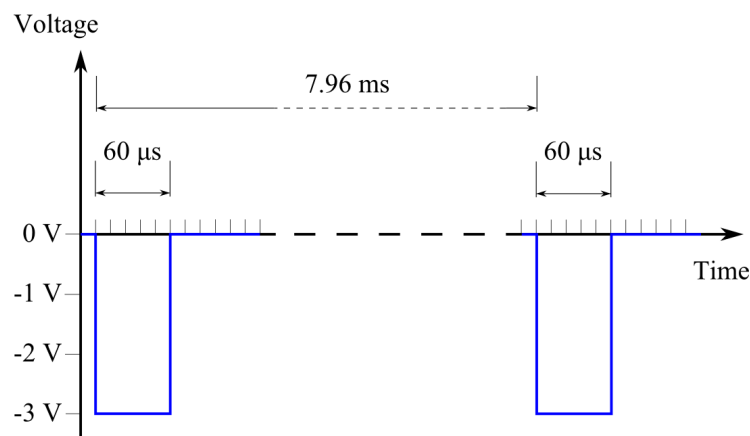


Figure 2.4: Example of a voltage-controlled mono-phasic stimulation pulse used in DBS therapy.

90 μ s, and (3) a frequency of 130 to 180 Hz (Fig. 2.4) [61]. In contrast to anodic stimulation, cathodic stimulation elicits a neural activation at smaller stimulation thresholds [146]. To avoid charge accumulation in the surrounding tissue of the driven electrode contact, bi-phasic pulses are applied, in which the cathodic stimulation pulse is followed by a "balancing" stimulation pulse with reversed polarity [88]. Despite the fact that voltage-controlled stimulation is the common stimulation type in human DBS, current-controlled stimulation is more and more regarded as an alternative. To date, current-controlled stimulation is mostly used in *in vivo* animal studies, but because of the increased stability of the delivered current as well as the reduction of unwanted side effects [78] and the promising results from first clinical trials [96], it attracts increasing interest for human DBS [112].

2.2.2 Surgery planning and performance

Before DBS can be started, a precise planning and a careful performance of stereotactic surgery is required. According to an expert consensus, the following recommendations should be considered [18]. Surgery should be performed by an interdisciplinary team of neurosurgeons, movement disorder neurologists, neuropsychologists, psychiatrists and neurophysiologists. Since the electrode position in the selected target area of the brain is crucial for the successful stimulation, detailed knowledge about the individual anatomical situation and the intended location of the electrode contacts is required in the pre-operative planning phase as well as in the phase of surgery. For this purpose, the patient's head is pre-operatively fixed in a stereotactic frame, which allows for the precise targeting of deep brain areas. If the STN is chosen as target region, the correct location of the electrode has to avoid both a position too much lateral, which can lead to tonic muscle contractions, and a position too

much medial, which can cause conjugate eye deviation [5]. The correct positioning is determined by the imaging techniques computed tomography (CT) and magnetic resonance imaging (MRI). The imaging data are converted to the stereotactic coordinate system. During the surgery, microelectrode recordings, microelectrode or macroelectrode stimulation, and tissue impedance monitoring provide information on the correct location of the electrode contacts. For the adjustment of the stimulation parameters pulse width, frequency, voltage, and electrode configuration, the patients remain usually awake to monitor the relief of symptoms and to exclude undesired side-effects. Further optimization of the stimulation parameters is carried out in the post-operative phase within 4 to 6 months by several programming sessions in out-patient units [38]. To approve the correct position of the implanted electrode, post-operative MRI and CT scans can only be performed under careful restrictions to avoid heating, movement, and induced currents in the electrode system. Data about the surgical complications of DBS vary in the literature and concern mainly bleeding (in 1 % to 12.5 % of cases), infections (in about 6 % of cases) as well as lead fracture and migration (in about 5 % of cases) [18, 38, 61].

2.2.3 Target selection

Several targets for DBS in PD patients have been tested in clinical practise. They include the STN, the GPi, the pedunculopontine nucleus (PPN), and the thalamic ventral intermediate nucleus (Vim) [61, 90]. While DBS of the Vim effectively treats tremor in PD, but has no effect on other symptoms such as akinesia and rigidity [14], and DBS of the PPN remains experimental, the GPi and STN are the preferred targets of DBS in this disease [61]. Despite the improvement of motor symptoms, DBS can lead to cognitive and emotional impairment such as depression and impulsivity [18]. For the STN and the GPi similar benefits of motor symptoms in PD have been reported. However, DBS of the GPi may lead to a slightly better improvement of the quality of life and less occurrence of depression compared to DBS of the STN [41, 145]. Nevertheless, methodological differences between published studies could explain the reported increase of cognitive side-effects of DBS of the STN compared to the GPi as pointed out by Moreines et al. [90]. Moreover, DBS of the GPi often allows no reduction of medication [61], requires higher stimulation amplitudes, resulting in a shorter battery lifetime [129], and could result in a weakened improvement over the years [70]. Therefore, the STN remains the favoured target for DBS in PD patients. Nevertheless, the target selection should also consider effects on non-motor symptoms of the individual patient besides the possible benefit of motor functions. With regard to the long-term improvements, stimulation parameters seem to remain stable in both nuclei and successful treatment of PD symptoms by DBS has been proven for up to 10 years [27].

2.2.4 Mechanisms of deep brain stimulation

The mechanisms of action of DBS are still a controversial issue in the literature [89]. Current hypotheses comprise depolarization blockade, synaptic inhibition, synaptic depression, stimulation-induced disruption of pathological network activity, and stimulation of afferent axons, e.g. of those projecting to the STN [61]. The currently favoured hypothesis assumes that DBS pulses override the pathologically oscillatory and synchronous spike patterns of the involved basal ganglia. Neuronal and LFP recordings in PD patients, who were withdrawn from therapy, showed an increased synchronous activity in the STN of a frequency between 10 and 30 Hz called the β -band [19]. In electroencephalography (EEG) measurements, oscillations in the β -band correlated with the severity of PD symptoms [48]. This oscillatory activity could be suppressed by levodopa as well as by DBS of the STN [19]. Studies reported an approximately linear relation between the suppression of bradykinesia and rigidity during DBS-induced β -band suppression at the cortical level. In addition, long-lasting *in vitro* experiments showed the replacement of spontaneous STN spikes by spikes driven by the stimulation pulses [64]. Currently, it is not clear whether DBS of the STN suppresses only the pathological activity of PD or maybe also certain functions of the physiological activity. Speech and cognitive impairments reported from patients who received DBS of the STN could be a hint on unwanted suppressions of physiological activity [19].

Several hypotheses of the mechanisms of DBS are based on an inhibitory effect of the DBS pulses on the stimulated target as recently summarised by Montgomery and Gale [89]. Historically, the hypothesis of inhibition was based on similar treatment results of DBS and lesioning procedures. Moreover, several initial studies confirmed a reduction of neuronal activity in the stimulated target, such as the thalamus and the STN. However, the situation might not be as simple, since a lesioning of the GPe can induce PD, while DBS of the GPe can suppress PD symptoms [128]. DBS of the STN can result in an increased activity in nuclei of the basal ganglia such as the GPi, which receive projections from the STN. Therefore, inhibition as well as excitation seem to occur in the nuclei of the basal ganglia network during DBS. Indeed, complex patterns of inhibition and excitation were reported in the literature [89].

In addition, the stimulation parameters play a crucial role for the successful treatment of PD by DBS. Only stimulation frequencies above 50 Hz were shown to suppress spontaneous activity in the basal ganglia network by imposing a new activity pattern of the stimulated target. Moreover, low frequencies in the range of 5 to 20 Hz seem to induce and exacerbate PD symptoms [64]. Besides the amplitude, pulse width and frequency of the DBS pulse, the waveform shape may influence the neuronal activity in the basal ganglia network. The rectangular waveform shape of DBS pulses originates from empirical clinical trials [19]. Information about the effect of different waveform shapes on the therapy success is still scarce. A computational

study by Yousif et al. [143] showed an effect of the electrical properties of brain tissue on the waveform shape of differently shaped DBS pulses, which may also change the neuronal activation in the target region. Investigating the mechanisms of DBS is of great practical interest and, therefore, it is in the focus of numerous experimental trials, but the mechanisms themselves and fundamental questions such as the therapeutical relevance of inhibition or excitation remain still unanswered [89].

2.3 Computational modelling

Currently, there is a discrepancy between the progress in clinical DBS and the understanding of basic mechanisms underlying its effects [64]. In this situation, computational models, which have been helpful in disclosing pathogenetic mechanisms of PD, could also contribute to the exploration of DBS effects on the disease. Moreover, they could lead to the discovery of new therapeutic strategies [88] and to the development of software tools supporting the physicians in the planning as well as during the performance of the surgery [29]. Starting in the last decade, several computational models have been developed, all of them aiming at modelling and simulating the mechanisms of DBS applied to PD. The scope of computational models of DBS can be divided into network models of the basal ganglia including neuronal models, and volume conductor models of the human brain. In this context, network modelling aims at exploring the neural and network effects, which are causing the symptoms of PD, as well as the mechanisms of the symptom improvement by DBS [88]. Volume conductor models reside on a macroscopic level, determining the local electric field distribution and the influences on the time-dependent voltage response caused by the application of the DBS pulses in the proximity of the stimulated target, whereby these field effects are based on the topology and the electrical properties of brain tissue.

2.3.1 Network modelling of the basal ganglia

The key task in network models of the basal ganglia is to reduce the model complexity by isolating relevant model parameters to which the model is restricted, while preventing the loss of the model dynamics [88]. Two approaches can be envisaged: (1) to combine the properties and behaviour of multiple neural populations on the basis of fundamental equations in a so-called population-based model, and (2) to model neuronal cells in each single nucleus and interrelating them by coupling equations in a so-called cellular-based model.

Modolo et al. [88] used a population-based model to explore oscillatory activity in a 2-population network. The two populations were coupled by exciting and inhibiting each other, similar to the STN-GPi feedback circuit in the PD state, resulting

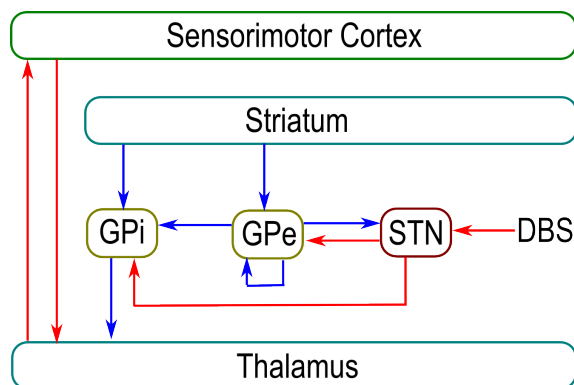


Figure 2.5: Connections within the basal ganglia network according to the modelling approach by Pirini et al. [99]. Red and blue arrows indicate excitatory and inhibitory connections, respectively. Abbreviations see Fig. 2.1.

in a synchronous firing pattern. The model consists of two non-linear and coupled differential equations, which are able to reproduce experimentally observed activation patterns. DBS was applied to the model by inducing DBS-like currents in one population of the network using a common square-wave stimulation pulse with a frequency of 130 Hz and an increased pulse width of 150 μ s. The authors reported a change in the synchronous activity of the model, with the firing rate of the neurons reaching a state of anti-phase dynamics. The advantage of this model lies in its limited number of parameters required to describe a large number of neurons within a neural population. However, this simplification also limits the model, since the population equations are derived from mean values, which do not take into account local variations.

To address the question how local variations affect the activity in the network, cellular-based models are better suited. Pirini et al. [99] used this approach to model the basal ganglia network in the PD state by including the STN, the GPi, the GPe and the thalamus. Each nucleus consisted of 16 neuronal cell models, which were representative for a distinct cell population and were described by a set of differential equations derived from the Hodgkin-Huxley model. The nuclei were connected by inhibitory and excitatory projections using coupling equations (Fig. 2.5). DBS pulses were applied as a train of square-wave stimulation pulses with frequencies between 30 and 180 Hz, and pulse widths between 0.15 and 1.2 ms. It was shown that the spontaneous spike patterns of the STN, the GPe and GPi have been overridden by the DBS pulses in DBS of the STN, resulting in a 1 : 1 response of the STN and GPi cells as well as burst patterns in the GPi with the same burst frequency as the 1 : 1 response (Fig. 2.6). These results confirm the hypothesis of the DBS induced change in the basal ganglia network activity through an override of their spike patterns by the DBS pulse. A stimulation at 120 Hz and 180 Hz resulted in lower membrane potentials and a total inhibition of the GPi activity. The thalamo-cortical activity

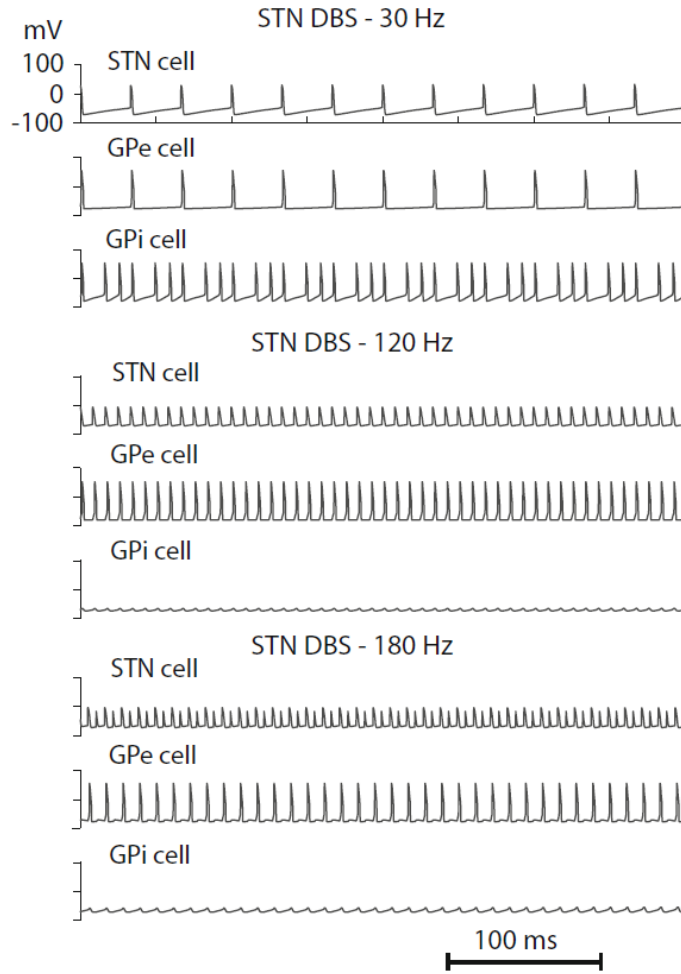


Figure 2.6: Membrane potentials of one STN, one GPe and one GPi cell during DBS of the STN at stimulation frequencies of 30, 120, and 180 Hz, respectively. Image courtesy of Pirini et al. [99].

could be restored by the application of DBS in the model. However, using the GPe and GPi as stimulation targets resulted in an over-activation and inhibition of this activity, respectively.

Volume of tissue activated

Although recent network models allow for the simulation of the dynamics between the nuclei of the basal ganglia and, therefore, a detailed investigation of the mechanisms of action of DBS as well as the pathogenesis of PD, they do not consider the time-dependent LFPs induced by the stimulation electrode in each nuclei. The consideration of these LFPs would require not only a realistic volume conductor model of the brain to compute the LFPs, but also a precise knowledge about the location and

extent of each nuclei, which makes the combination of network models and volume conductor models challenging. Therefore, a simplified approach allowing for a first prediction of the neural activation and its sensitivity to the model parameters is well established in the DBS modelling community [21, 22, 24, 25, 54, 57, 84, 120, 142] and allows for a prediction of neural activation in human DBS [23]. In this approach, a distribution of single neuron models in the proximity of the stimulated target is used to predict the neural activation extent, called the volume of tissue activated (VTA). For each neuron, the stimulus amplitude required for its activation, meaning to elicit an action potential, is determined based on the computed LFPs along the neuron body. The neuron model is based on a double cable model of generalised mammalian nerve fibres developed by McIntyre et al. [82]. It comprises 21 nodes of Ranvier separated by 20 internodal sections, the membrane dynamics of which were derived from experimental measurements. The action potential is characterised by a rapid change of the transmembrane potential [72], which is the difference between the inner potential of the axon and the extracellular potential (in this meaning LFP). Rattay [102] showed that for myelinated axons, the transmembrane voltage at an axon node is predominantly determined by the extracellular potential at this axon node and its neighbouring nodes, which corresponded to the second-order spatial difference quotient of the extracellular potential called activating function. For unmyelinated axons, the activating function is given by the second-order spatial derivative of the extracellular potential [102]. The transmembrane voltage in the axon model of McIntyre et al. [82] is computed by solving a system of differential equations based on the Hodgkin-Huxley-model, which describes the initiation and propagation of action potentials in axons [68]. To compute the VTA, a number of axons is aligned perpendicular in the proximity of the stimulated target. For each axon, the threshold necessary to elicit an action potential is computed based on a given stimulus amplitude. The resulting spatial information on activated and inactivated axons is then used to determine the activated volume.

2.3.2 Volume conductor models of the human brain

The time-dependent extracellular potential is influenced not only by the properties of the DBS pulse, but also by the topology and the electrical properties of the brain tissue. Especially capacitive effects in the tissue seem to modulate the time-dependent voltage response in the proximity of the stimulated target, rendering them a crucial parameter [87]. Volume conductor models can provide the electric field distribution as well as the time-dependent voltage response in the proximity of the electrode contact, which can be used as input for network models and the VTA. Therefore, the combination of these models can help to gain a deeper insight into the mechanisms of action of DBS. Volume conductor models are based on a discretised model of the brain, using numerical techniques to find an approximate solution of the governing equations determined by the underlying physics. Common numerical

techniques are the FEM, the finite integration technique (FIT), and the boundary element method (BEM).

The volume conductor models necessary to compute the time-dependent voltage response of the DBS pulse in the tissue depend on various parameters with the consequence of long computation times [29]. Therefore, a model reduction to achieve less complexity is rather challenging. In addition, validation of the simulation results is required to verify the influence of the various parameters experimentally. This demands careful consideration of ethical issues. Validation attempts are often carried out *in vitro* or, in order to get most reliable results, *in vivo*, using animal models. First promising results were obtained by the comparison of voltage distributions in an *in vivo* study of parkinsonian monkeys with data of volume conductor models, which led to the identification of crucial parameters for the theoretical models [87].

The model parameters influencing the time-dependent voltage response of the DBS pulse in the tissue can be categorised in active factors regarding the stimulation parameters such as amplitude, frequency, pulse width and waveform shape, and passive factors regarding the model parameters. The latter factors were explored in several simulation studies including the model geometry [56, 79, 132], the electrode geometry [53, 59], the dispersive properties of brain tissue [17, 57], the anisotropy of brain tissue [83, 120], the interactions at the electrode-tissue-interface [21, 26], and the inflammatory response of the tissue to the implanted electrode resulting in the growth of an encapsulation layer around the electrode [57, 142]. Studies regarding the geometry factors reported a strong influence of the model geometry on the resulting voltage distribution in the proximity of the stimulated target, suggesting the supremacy of an anatomically head model resembling the spatial dimensions of the human brain over simplified cubic models [56, 132]. These studies point out the need of the generation of anatomically realistic brain models to allow for a patient-specific investigation of the neural activation to support physicians in the pre-operative planning and during surgery.

The computation of the time-dependent voltage response in volume conductor models of DBS are commonly carried out using the well established Fourier finite element method (FFEM) [21], in which the DBS pulse is transformed into the frequency-domain using a fast Fourier transform (FFT), modified by the electrical properties of brain tissue, and transformed back into the time-domain by using an inverse FFT. For a square-wave DBS pulse, this method accounts for the dispersive electrical properties of brain tissue and requires the computation of the finite element volume conductor model for about 500 to 2,000 harmonic frequencies of the fundamental frequency of the DBS pulse [17, 57]. Results of the study of Bossetti et al. [17] suggest that dispersive effects of the electrical tissue properties could be neglected under current-controlled stimulation, but only solutions of a model with fixed conductivity values at a single frequency were compared with the dispersive solution using a non-anatomical homogeneous head model. Grant and Lowery [57] confirmed the essential results from this study and extended it by computing voltage-controlled

solutions as well as comparing them to those under current-controlled stimulation at several single frequencies with the dispersive solution in an anatomical, but also homogeneous head model regarding the brain tissue.

2.4 Objectives and research goals

Despite the high current interest in models of DBS and their progress in the field of simulating the action of DBS, several mechanisms of this method are still elusive and open questions remain unanswered. The time-dependent voltage response in the tissue around the stimulated target does not itself predict the neural activation in this area, but interacts with the neurons by varying their membrane potentials and could be used in several network models. Therefore, knowledge on how the voltage response in the tissue changes the parameters of the stimulation pulse is necessary to receive realistic predictions from the network models. To date, no study determined the influence of the interaction of various dispersive brain tissues on the voltage response of voltage and current-controlled DBS pulses over a wide frequency range in one model. The anisotropy of brain tissue was implemented in several models, but quantitative results about the influence of anisotropic tissue properties in the proximity of the stimulated target on the voltage response and VTA are still scarce. This applies especially to slight variations of the electrode location in the target area, which frequently occur during surgery. The majority of current models of DBS are deterministic and consider only one set of values for the model parameters. For example, for the electrical properties of the electrical properties of brain tissue, these values reported in the literature vary tremendously ranging from 38 % to 70 % of their mean values [42, 46, 49, 76].

Measuring these properties is challenging due to the number of influencing factors that have to be controlled and the ethical issues that have to be dealt with *in vivo* and *in vitro*. The dielectric properties of biological tissue depend on various factors: (1) their water content [43], (2) their temperature [10], (3) their frequency [113], and (4) their anisotropy [60]. These factors require a careful consideration during *in vitro* or *ex vivo* dielectrical measurements, including the preparation of the sample, its homogeneity and location in the brain, as well as the time lapse between the abstraction of the sample and the actual measurement. An *in vivo* study in pigs showed a substantial change of the electrical properties of excised brain tissue of about 15 % after 60 min [107]. This change can be transferred to human brain tissue, since the difference of the electrical properties between human and mammalian animal tissue is considered to be small according to Grimnes and Martinsen [60], who further state that irreversible changes to brain tissue may occur within 5 minutes. *In vitro* and *ex vivo* studies often use excised tissue with different time lapses after abstraction, which results in different electrical properties throughout the literature [45]. To date, *in vivo* dielectrical measurement data is

scarce due to the challenging invasive measurement process and the corresponding ethical considerations that have to be dealt with. A promising non-invasive technique is the magnetic resonance electrical impedance tomography, which was applied by Oh et al. [94] on biological tissue phantoms to determine their conductivity *in vivo*. However, in non-invasive methods, the low conductivity of the scalp will most likely cause uncertainty in the measured electrical properties of brain tissue [60]. In addition, electrode polarization effects interfere with the actual electrical properties of brain tissue in the low frequency range of Hz to several kHz, the consideration of which is challenging, because it results in uncertainty in the measured data [147] as well. The differences in the tissue data of the small number of available studies and the resulting uncertainty in the model parameters claim the necessity of including the investigation of the influence of these uncertainties on the voltage response and neural activation in models of DBS.

The resulting aim of this thesis is the investigation of the influence of the frequency-dependent and anisotropic tissue properties as well as the uncertainties arising from the electrical properties of brain tissue on the time-dependent voltage response and the VTA in the area of the stimulated STN during human DBS. Regarding the available volume conductor models, a consideration of the uncertainty in the model parameters is only possible with a large computational effort, requiring about 500 FEM computations for one parameter set with a computation time of about 4 min for each simulation on a four Intel® Xeon cores @ 2.4 GHz workstation. The consideration of uncertainties demands a probabilistic formalism, such as Monte Carlo simulation (MCS). This would require the evaluation of the volume conductor model for a large number of random samples of the model parameters. This number depends on the demanded accuracy of the probabilistic quantities, which converges relatively slow with $1/\sqrt{N}$ for N random samples [138]. Combining the required deterministic FEM computations for one parameter set with a large number of random samples to provide an adequate representation of the probabilistic quantities, about 500,000 to 1,000,000 model evaluations, including the FEM computation of the volume conductor model and the solution of the system of differential equations to obtain the neural activation, would be necessary. Therefore, the investigation of the influence of the uncertainty in the model parameters on the time-dependent voltage-response and neural activation in models of DBS requires the application of model order reduction techniques, such as equivalent circuit models and the generation of probabilistic surrogate models based on the Polynomial Chaos, to reduce the computational expense to a compatible level.

3 Aspects of volume conductor models of the human brain

This chapter describes the generation of an anatomical head model, which was used for the studies carried out in this thesis. The model geometry and the tissue distribution in the brain were derived from the digital SRI24 multi-channel brain atlas, which comprises MRI data from 24 healthy human volunteers [104]. The fundamental equations modelling the governing physics were derived from a simplification of Maxwell's equations under the assumption of negligible propagation and inductive effects, which lead to the electro-quasistatic (EQS) and quasistatic (QS) formulation. The numerical technique of finite elements used to compute the voltage distribution in the model is described briefly and the used software is introduced. A model order reduction approach of the Fourier finite element method (FFEM) based on the application of equivalent circuit models called the Fourier finite element method with equivalent circuits (FFEMEC) approach is described in detail. This approach allows for the computation of the time-dependent voltage response in the volume conductor model of the human brain by evaluating the finite element model only once for voltage-controlled stimulation and twice for current-controlled stimulation, instead of computing the voltage response for a large number of harmonics as it is required for the FFEM approach [17].

3.1 Electro-quasistatic and quasistatic formulation

The voltage response in the stimulated target area of the brain can be computed by a simplification of Maxwell's equations, called the EQS and QS formulations. These formulations constitute "slowly" time-dependent and harmonic electrical fields induced in the biological tissue, if the magnetic induction is negligible [66]. Regarding the application of DBS, the EQS and QS equation provide a reasonable approximation for low-frequency fields in the absence of eddy currents [127].

3.1.1 Maxwell's equations in bio-electrical applications

In 1865, James Clerk Maxwell proposed a theory describing the fundamentals of transient electric and magnetic fields by introducing a set of differential equations,

called Maxwell's equations [81]. This set of equations is used to describe and investigate electric and magnetic field effects in various situations and forms the basis of modern electromagnetic and communications technology. In this context, Maxwell's equations also form the governing equations of the physics described in this thesis. In modern electromagnetic applications, the following four differential equations are used to describe the interrelation of the electric field \mathbf{E} , the magnetic induction \mathbf{B} , the electric displacement field \mathbf{D} and the magnetic field \mathbf{H} , namely

$$\operatorname{div} \mathbf{D} = \varrho \quad (\text{Gauss' law}) \quad (3.1)$$

$$\operatorname{div} \mathbf{B} = 0 \quad (\text{Gauss' law for magnetism}) \quad (3.2)$$

$$\operatorname{curl} \mathbf{H} = \mathbf{J} + \frac{\partial \mathbf{D}}{\partial t} \quad (\text{Ampère's law with Maxwell's extension}) \quad (3.3)$$

$$\operatorname{curl} \mathbf{E} = -\frac{\partial \mathbf{B}}{\partial t} . \quad (\text{Faraday's law of induction}) \quad (3.4)$$

Gauss' law (3.1) and Gauss's law for magnetism (3.2) describe the sources of the electric displacement field and of the magnetic induction. Since magnetic fields are solenoidal, in addition, equation (3.2) describes the absence of magnetic monopoles. The origin of electromagnetic waves can be found in the coupling of Ampère's law (3.3) and Faraday's law (3.4), where time-dependent electric fields generate magnetic fields and vice versa [66]. To determine the electromagnetics in media, this set of equations is extended by additional material equations, which have the following form for linear, isotropic, not polarised or magnetised media [71]:

$$\mathbf{D} = \varepsilon \mathbf{E} \quad (3.5)$$

$$\mathbf{B} = \mu_H \mathbf{H} \quad (3.6)$$

$$\mathbf{J} = \kappa \mathbf{E} \quad (3.7)$$

However, in bioelectromagnetism the material properties of biological tissue can be anisotropic [137] and frequency dependent [46], which requires the introduction of tensors and frequency dependent material parameters, as described in section 3.4.2 and 3.1.2, respectively. The displacement field \mathbf{D} and the electric field \mathbf{E} are connected by the permittivity ε , whereas the magnetic induction \mathbf{B} and the magnetic field \mathbf{H} are connected by the permeability μ_H in the medium. Equation (3.7) constitutes Ohm's law, which connects the current density \mathbf{J} with the electric field \mathbf{E} by the medium conductivity κ .

Based on the description of van Rienen [127], a harmonic time-dependence of, e. g., the electric field can be expressed as

$$\mathbf{E}(\mathbf{r}, t) = \Re (\mathbf{E}(\mathbf{r}) e^{j\phi} e^{j\omega t}) = \Re (\underline{\mathbf{E}}(\mathbf{r}) e^{j\omega t}) \quad (3.8)$$

with the angular frequency ω , the phase angle ϕ and the phasor $\underline{\mathbf{E}}(\mathbf{r}) = \mathbf{E}(\mathbf{r})e^{j\phi}$. Therefore, Maxwell's equations (3.1)–(3.4) can be rewritten as

$$\operatorname{div} \underline{\mathbf{D}} = \underline{\rho} \quad (3.9)$$

$$\operatorname{div} \underline{\mathbf{B}} = 0 \quad (3.10)$$

$$\operatorname{curl} \underline{\mathbf{H}} = \underline{\mathbf{J}}_c + \underline{\mathbf{J}}_i + j\omega \underline{\mathbf{D}} \quad (3.11)$$

$$\operatorname{curl} \underline{\mathbf{E}} = -j\omega \underline{\mathbf{B}} \quad (3.12)$$

where the current density $\underline{\mathbf{J}}$ is split up into a conduction current density $\underline{\mathbf{J}}_c$ arising from conductive materials and an impressed current density $\underline{\mathbf{J}}_i$. Using $\operatorname{div} \operatorname{curl} \equiv 0$ on equation (3.11) and inserting equation (3.5) results in the expression

$$0 = \operatorname{div} ([\kappa + j\omega\varepsilon] \underline{\mathbf{E}}) + \operatorname{div} \underline{\mathbf{J}}_i. \quad (3.13)$$

The electric potential φ can be derived from equation (3.12) and the vector potential $\underline{\mathbf{B}} = \operatorname{curl} \underline{\mathbf{A}}$:

$$\underline{\mathbf{E}} = -\operatorname{grad} \varphi - j\omega \underline{\mathbf{A}} \quad (3.14)$$

Inserting equation (3.14) into equation (3.13) and using the Lorenz gauge

$$\operatorname{div} \underline{\mathbf{A}} + \frac{1}{c^2} \frac{\partial \varphi}{\partial t} = 0 \quad (3.15)$$

results in the inhomogeneous Helmholtz equation [17]

$$\Delta \varphi + \frac{\omega^2}{c^2} \varphi = \frac{\operatorname{div} \underline{\mathbf{J}}_i}{\kappa + j\omega\varepsilon} \quad (3.16)$$

where c is the velocity of light in the medium. The solution of the electric potential can be obtained analytically from [6]

$$\varphi(\mathbf{r}) = \frac{-1}{4\pi(\kappa + j\omega\varepsilon)} \iiint_V \frac{\operatorname{div} \underline{\mathbf{J}}_i(\mathbf{r}') e^{-j\frac{\omega r}{c}}}{r} d\mathbf{r}' \quad (3.17)$$

where $r = \|\mathbf{r} - \mathbf{r}'\|_2$ is the Euclidean distance to the source. Plonsey and Heppner [100] used this equation to introduce several simplifications, which are applicable to the bio-electrical modelling in the human body. These simplifications comprise the neglect of the propagation of electromagnetic waves and of the inductive as well as capacitive effects.

Propagation of electromagnetic waves

The propagation of electromagnetic waves, i.e. the time in which the wave propagates in space, is induced according to Helmholtz' equation (3.16) by the term $\frac{\omega^2}{c^2}\varphi$, which results in the phase shift $e^{-j\omega r/c}$ in the equation of the electric potential (3.17). The series expansion of the phase shift leads to

$$e^{-j\frac{\omega r}{c}} = 1 - j\frac{\omega r}{c} + \frac{(\omega r)^2}{2!c^2} - j\frac{(\omega r)^3}{3!c^3} + \dots \quad (3.18)$$

The effect of propagation can be neglected if the expression

$$\frac{\omega r}{c} \ll 1 \quad (3.19)$$

is fulfilled for the used angular frequency ω , the spatial dimension of the model r , and the velocity of light c in the medium. This simplification is consistent with the neglect of the time-varying magnetic induction $\frac{\partial \mathbf{B}}{\partial t}$ in the time-harmonic Maxwell's equations (3.9)–(3.10) as described by van Rienen [127], leading to the omission of the term $\frac{\omega^2}{c^2}\varphi$ in the Helmholtz equation (3.16).

Inductive effect

The consistency of the neglect of the propagation effect and the omission of the time-varying magnetic induction $\frac{\partial \mathbf{B}}{\partial t}$ yields the basis for determining the inductive effects in bio-electrical models of human tissue. Regarding the equation of the electric potential (3.14), the influence of the magnetic induction is given by $\underline{\mathbf{E}}_{\text{ind}} = -j\omega \underline{\mathbf{A}}$. Plonsey and Heppner [100] stated that the inductive effect can be neglected in bio-electrical applications, if the quotient of the absolute value of the influence of magnetic induction and the gradient of the scalar potential $\text{grad } \varphi$ is much smaller than 1 for a differential current source element $\underline{\mathbf{J}}_i dV$:

$$\frac{|\omega \underline{\mathbf{A}}|}{|\text{grad } \varphi|} = \left| \frac{\omega r}{c} \right|^2 \ll 1 \quad (3.20)$$

For linear media, the impressed current density $\underline{\mathbf{J}}_i$ can be obtained from a superposition of multiple differential current source elements [100]. Therefore, the resulting condition for the neglect of the inductive effect in bio-electrical applications is already fulfilled, if the propagation effect is negligible, thereby being consistent with the requirement of the absence of a time-varying magnetic induction [127].

Capacitive effect

The solution of the electric potential (3.17) depends on the electrical properties of the medium, which comprise the conductivity κ and relative permittivity ε_r of brain

tissue. These material properties are described in equation (3.17) by a complex conductivity $\underline{\kappa}_c$

$$\underline{\kappa}_c = \kappa + j\omega\varepsilon_0\varepsilon_r = \kappa \left(1 + \frac{j\omega\varepsilon_0\varepsilon_r}{\kappa} \right) \quad (3.21)$$

where $\varepsilon_0 \approx 8.854 \cdot 10^{-12} \frac{\text{F}}{\text{m}}$ is the electric field constant. The capacitive effect results from the influence of displacement currents in the medium on the electric potential φ . If the absolute value of the influence of the displacement currents $j\omega\varepsilon_0\varepsilon_r$ is small compared to the conductivity κ in the medium, then the capacitive effect is negligible:

$$\frac{\omega\varepsilon_0\varepsilon_r}{\kappa} \ll 1 \quad (3.22)$$

Therefore, the neglect of the capacitive effect would result in a real-valued electric potential φ .

Electro-quasistatic and quasistatic equation

In bio-electrical applications, where the propagation effect (3.19) and the inductive effect (3.20) are negligible, Helmholtz' equation (3.16) can be simplified to

$$\text{div} \left([\kappa + j\omega\varepsilon_0\varepsilon_r] \text{grad } \varphi \right) = \text{div } \underline{\mathbf{J}}_i . \quad (3.23)$$

These bio-electrical applications can involve heterogeneously distributed biological tissue types with different material parameters. Under the assumption that the resting potentials of neurons (≈ -70 mV) are small compared to the stimulation amplitude of DBS pulses (several Volt), impressed currents can be neglected and equation (3.23) results in the so-called EQS equation

$$\text{div} \left([\kappa + j\omega\varepsilon_0\varepsilon_r] \text{grad } \varphi \right) = 0 \quad (3.24)$$

applying for resistive and capacitive tissue properties [127, p.17ff]. If also the capacitive effect (3.22) is negligible, the term $j\omega\varepsilon_0\varepsilon_r$ in equation (3.24) can be omitted, resulting in the QS equation¹

$$\text{div} (\kappa \text{grad } \varphi) = 0 , \quad (3.25)$$

which applies for purely resistive tissue properties. The decision whether the propagation, inductive and capacitive effect are negligible or not depends on the spatial dimension of the model, the considered frequency range, and the electrical properties of its tissue types. These parameters vary for different biological applications, which require an evaluation of these conditions for each application.

¹Here, the quasistatic (QS) formulation actually refers to a stationary current field problem [127]. However, the terms quasistatic (QS) and electro-quasistatic (EQS) are not consistently used in bio-electrical literature and can refer to the time-dependence of the DBS pulse even if the problem is related to a stationary current field problem. It should be noted that both terms are used without desire of universal validity.

3.1.2 Electrical properties of brain tissue

The electrical properties of biological tissue are crucial parameters of volume conductor models of the brain. Besides the brain topology, the electrode geometry, and the stimulation parameters, the electrical properties of brain tissue substantially influence the voltage response in the stimulated target area of the brain generated by DBS. As early as in 1957, Schwan [113] described the dependence of the conductivity and relative permittivity of biological tissue on the frequency in three distinct regions and the occurrence of "enormous values" of the relative permittivity at low frequencies. These regions are called α -, β -, and γ -dispersion and emerge in different frequency ranges (Fig. 3.1). The dispersion of the electrical properties of biological tissue characterises its frequency dependence according to relaxation theory [60]. The different dispersion regions account for the non-symmetrical distribution of the relaxation times in biological tissue and result from dielectric effects at the membranes of the tissue, which has the following origins [113]:

- α -dispersion (mHz-Hz): Translation of charges on the cell surface.
- β -dispersion (kHz-MHz): Polarisation at the poorly conductive membranes, resulting in a membrane capacitance.
- γ -dispersion (GHz): Polarisation of tissue water.

Gabriel et al. [46] characterised experimentally the electrical properties of various biological tissues, including the major brain tissue types white matter, gray matter, and cerebrospinal fluid (CSF), in the frequency range 10 Hz to 100 GHz. Based on the experimental data a mathematical model characterising the dispersion regions was used to parameterise the conductivity and relative permittivity of the investigated

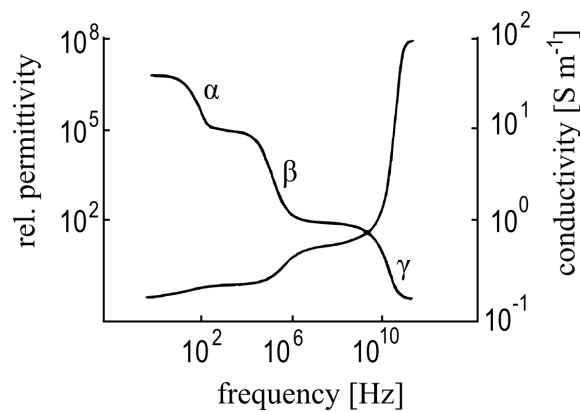


Figure 3.1: Example of relative permittivity (decreasing) and conductivity (increasing) of biological tissue within the three dispersion regions α , β , γ . Image based on [113]

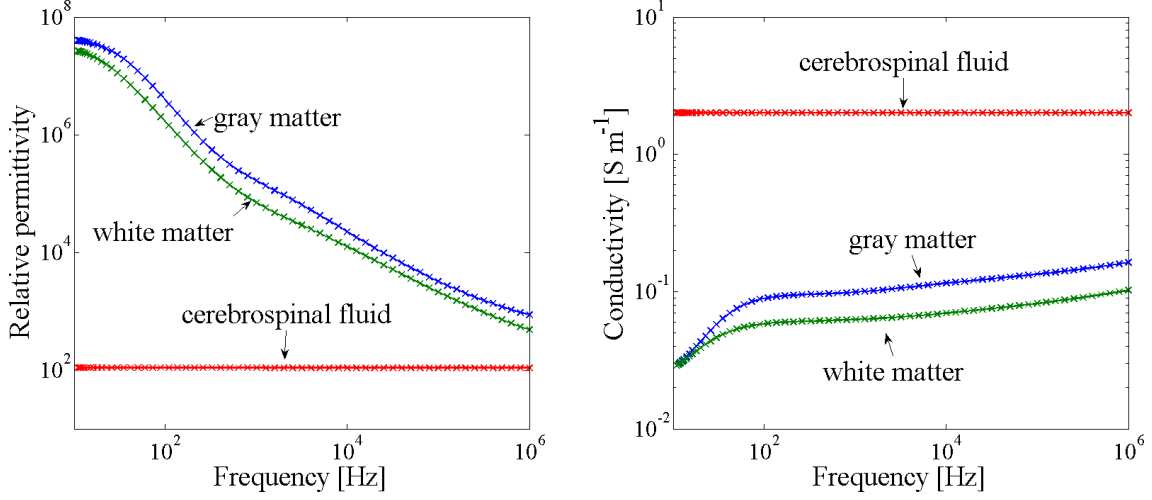


Figure 3.2: Relative permittivity and conductivity of gray matter, white matter and cerebrospinal fluid (CSF) in a frequency range from 10 Hz to 100 GHz. Image data based on the Cole-Cole dispersion parameters by Gabriel et al. [46] and Gabriel, S [47].

tissues. The mathematical model consists of the summation of four Cole-Cole dispersions to cover the spectrum of the electrical properties of the tissue by calculating the frequency-dependent complex relative permittivity $\varepsilon_c(\omega)$

$$\varepsilon_c(\omega) = \varepsilon_\infty + \sum_{n=1}^4 \frac{\Delta\varepsilon_n}{1 + (j\omega\tau_n)^{(1-\alpha_n)}} + \frac{\kappa_i}{j\omega\varepsilon_0} \quad (3.26)$$

where ε_∞ is the relative permittivity at high frequencies, $\Delta\varepsilon_n$ are the differences of the static relative permittivities ε_{sn} at low frequencies with $\omega\tau_n \ll 1$ and ε_∞ , α_n are the Cole-Cole-parameter found experimentally for every Cole-Cole equation, τ_n are the relaxation time constants, and κ_i is the static ionic conductivity [46]. Exploring the relative permittivity and conductivity of the different brain tissue types, white and gray matter show the "enormous" relative permittivity values for low frequencies mentioned by Schwan [113], which diminish with increasing frequency. This behaviour is characterised by the inertia of the electrical charges, which are not quick enough to follow the changes in the electric field [60]. The distinct dispersion regions mentioned by Schwan [113] are scarcely detectable for the gray and white matter data of Gabriel et al. [46], resulting from much broader dispersion regions in biological tissue, which overlap and emerge in an almost continuous decrease over a wide frequency range [60]. The conductivity of both tissue types is especially variable at frequencies below 100 Hz (Fig. 3.2). CSF is closely related to saline and includes only a small influence of cell membranes, resulting in almost constant electrical properties over frequency [10].

3.2 Finite element method

The following section is based on the work of Schwarz, 1991 [114, ch.2] and Bondeson et al., 2005 [16, ch.6]. In several applications including complex geometries, the solution of the partial differential equations used in the volume conductor model of the human brain in this thesis cannot any longer be computed analytically or their computation is rather challenging. In these cases numerical computations are necessary to obtain an approximated solution of the problem. The finite element method (FEM) is a numerical technique to solve boundary and initial value problems of partial differential equations on a discretised geometry. The discretisation of the geometry is carried out by dividing it into subdomains, called the finite elements. The boundary value problem is then solved by deriving a so-called weak formulation of the problem as well as by using an interpolated approximation of the solution, the so-called Galerkin method. For the EQS formulation in equation (3.24) and the QS formulation in equation (3.25), the application of the FEM results in a system of linear equations (SLE), the solution of which are the unknown quantities at the nodes (edges) of the nodal (edge) finite elements.

3.2.1 Galerkin method

In the following section, the Galerkin method is briefly described for a three-dimensional EQS example. A more detailed explanation of this method is described in [16]. The weak formulation of the partial differential equation is used to discretise the boundary value problem. Therefore, the solution on each finite element is interpolated by local basis functions and put into the derived (weak) formulation. For a three-dimensional problem, tetrahedral as well as hexahedral elements are commonly used to discretise a domain Ω . The generated model of the human brain consists of a geometrically complex domain, for which tetrahedral elements are more feasible as discretisation scheme. Therefore in the following, the description of the Galerkin method is carried out for these elements.

The EQS formulation in equation (3.24) is solved in a volume conductor model of the human brain, which forms the computational domain Ω , by applying conditions to the exterior boundaries $\partial\Omega_i$, $i = 1, \dots, N_b$ of the model, where N_b is the number of boundaries with different conditions. These conditions comprise the application of a potential

$$\underline{\varphi}|_{\partial\Omega_i} = V_i e^{j\phi_i} \quad (3.27)$$

with the constant amplitude V_i and phase ϕ_i to the surface of the electrode contacts and ground, corresponding to a Dirichlet boundary condition, and the application of a perfect insulator, where the gradient of the solution $\underline{\varphi}$ is orthogonal to the normal

component \mathbf{n} of each boundary element

$$\mathbf{n} \cdot \nabla \underline{\varphi} \big|_{\partial\Omega_i} = 0, \quad (3.28)$$

to the exterior boundary of the human brain as well as the electrode lead, i.e. homogeneous Neumann boundary condition. For the discretisation of the EQS formulation, the solution $\underline{\varphi}$ is approximated by an expansion

$$\underline{\varphi}(\mathbf{r}) = \sum_{j=1}^M \underline{u}_j \psi_j(\mathbf{r}), \quad (3.29)$$

using linearly independent basis functions $\psi_j(\mathbf{r})$. Substituting the solution $\underline{\varphi}$ in equation (3.24) by this expansion results in a residual, the integral of which multiplied by a set of test functions w_i should be zero. The Galerkin method consists of choosing the test functions w_i to be the global basis functions ψ_i for all nodes where the solution $\underline{\varphi}$ is unknown

$$\int_{\Omega} \psi_i [\nabla \cdot ((\kappa + j\omega\varepsilon_0\varepsilon_r)\nabla \underline{\varphi})] \, d\Omega = \int_{\Omega} \psi_i [\nabla \cdot (\underline{\kappa}\nabla \underline{\varphi})] \, d\Omega = 0 \quad (3.30)$$

where $\underline{\kappa} = \kappa + j\omega\varepsilon_0\varepsilon_r$ is a complex conductivity. This formulation is the so-called weak formulation and is equivalent to the so-called strong formulation (3.24) of the problem. The basis functions ψ_i are called global, since they are defined on the whole domain Ω . The weak form of the problem in equation (3.30) can be derived by integration by parts, resulting in

$$\int_{\Omega} \underline{\kappa} \nabla \psi_i \cdot \nabla \underline{\varphi} \, d\Omega = 0 \quad (3.31)$$

where the second derivatives disappear. It should be noted that the boundary integral vanishes at the parts of the Dirichlet boundary condition, where the solution is known, and at the homogeneous Neumann boundary condition [16]. Substituting $\underline{\varphi}$ in equation (3.31) with the expansion in equation (3.29) results in a system of linear equations (SLE) $\underline{\mathbf{S}}\underline{\mathbf{u}} = \mathbf{0}$ with the elements

$$\underline{S}_{ij} = \int_{\Omega} \underline{\kappa} \nabla \psi_i \cdot \nabla \psi_j \, d\Omega \quad (3.32)$$

where j is the index over all nodes and i only over those nodes, where $\underline{\varphi}$ is unknown. By reordering the components of $\underline{\mathbf{u}}$ in a vector $\underline{\mathbf{u}}_a$, where $\underline{\varphi}$ is known, and a vector $\underline{\mathbf{u}}_b$, where $\underline{\varphi}$ is unknown, results in partition of the matrix $\underline{\mathbf{S}}$

$$\begin{aligned} \underline{\mathbf{S}}_a \underline{\mathbf{u}}_a + \underline{\mathbf{S}}_b \underline{\mathbf{u}}_b &= \mathbf{0} \\ \Rightarrow \underline{\mathbf{S}}_b \underline{\mathbf{u}}_b &= -\underline{\mathbf{S}}_a \underline{\mathbf{u}}_a \end{aligned} \quad (3.33)$$

where the right-hand side is known and $\underline{\mathbf{S}}_b$ is a symmetric, complex-valued square matrix.

3.2.2 Discretisation with finite elements

In the following section, the discretisation of the domain Ω with finite elements and the affine transformation to map each finite element onto a unit tetrahedron is briefly described by following the descriptions of Schwarz [114] and Geus [50]. The domain Ω is partitioned into elements, which are formed in this example by tetrahedra E_k . In case of linear basis functions $\psi_i(\mathbf{r})$, the nodes of the tetrahedra correspond to entries in the solution vector $\underline{\mathbf{u}}$, which are the degrees of freedom. On each tetrahedron E_k local basis functions $\psi_j^{E_k}(\mathbf{r})$ are defined. To simplify the evaluation of the integrals in the components \underline{S}_{ij} in equation (3.33), the tetrahedra E_k are mapped onto a reference element, the unit tetrahedron E_r , using an affine transformation. The linear transformation \mathcal{T} , mapping the global coordinates $\mathbf{r} = (x, y, z)$ of a tetrahedron E_k with the corner points $P_i(x_i, y_i, z_i)$, $i = 1, \dots, 4$ onto the unit tetrahedron E_r with the local coordinates $\bar{\mathbf{r}} = (\bar{x}, \bar{y}, \bar{z})$, is given by

$$\begin{pmatrix} x \\ y \\ z \end{pmatrix} = \begin{pmatrix} x_1 \\ y_1 \\ z_1 \end{pmatrix} + \begin{pmatrix} x_2 - x_1 & x_3 - x_1 & x_4 - x_1 \\ y_2 - y_1 & y_3 - y_1 & y_4 - y_1 \\ z_2 - z_1 & z_3 - z_1 & z_4 - z_1 \end{pmatrix} \begin{pmatrix} \bar{x} \\ \bar{y} \\ \bar{z} \end{pmatrix}. \quad (3.34)$$

Considering the volume element $dx dy dz$ and using equation (3.34) results in the following expression:

$$dx dy dz = \begin{vmatrix} x_2 - x_1 & x_3 - x_1 & x_4 - x_1 \\ y_2 - y_1 & y_3 - y_1 & y_4 - y_1 \\ z_2 - z_1 & z_3 - z_1 & z_4 - z_1 \end{vmatrix} d\bar{x} d\bar{y} d\bar{z} = \det(\mathbf{J}) d\bar{x} d\bar{y} d\bar{z} \quad (3.35)$$

where $\det(\mathbf{J})$ is the determinant of the Jacobi matrix, containing all derivatives of x, y, z with respect to $\bar{x}, \bar{y}, \bar{z}$. The nodes of the tetrahedron E_k have a prescribed

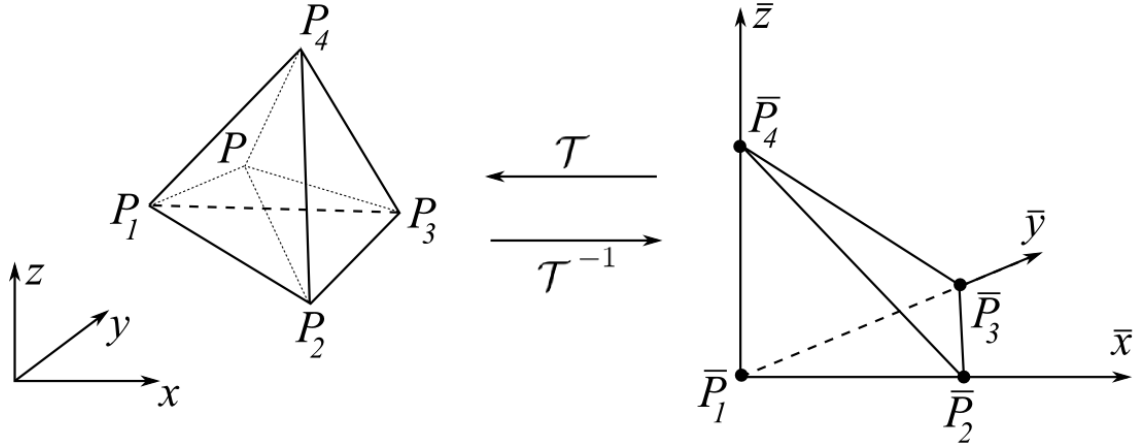


Figure 3.3: Affine transformation mapping the global coordinates of a tetrahedron $T^{(e)}$ onto the local coordinates of the unit tetrahedron $T^{(0)}$.

order so that the directions given by P_1P_2 , P_1P_3 , and P_1P_4 are forming a right-handed system (Fig. 3.3). In the case of tetrahedra with no vanishing volume, the transformation \mathcal{T} is regular and its inverse \mathcal{T}^{-1} exists. The transformation \mathcal{T}^{-1} can be defined by barycentric coordinates L_1, \dots, L_4 transforming a point $P(x, y, z)$ in the tetrahedron $T^{(e)}$ into the unit tetrahedron $T^{(0)}$. These barycentric coordinates have the following form

$$\begin{aligned} L_1 &= \frac{V_1}{V}, \quad L_2 = \frac{V_2}{V}, \quad L_3 = \frac{V_3}{V}, \quad L_4 = \frac{V_4}{V}, \\ V &= \sum_{i=1}^4 V_i \end{aligned} \quad (3.36)$$

where V_1, \dots, V_4 are the volumes of the subtetrahedra opposing the corner points P_1, \dots, P_4 and V is the volume of the entire tetrahedron. The local basis functions $\psi_i^{E_r}$, $i = 1, \dots, 4$ on the unit tetrahedron E_r are for a linear ansatz

$$\psi_i^{E_r} = c_{i,0} + c_{i,1}\bar{x} + c_{i,2}\bar{y} + c_{i,3}\bar{z}. \quad (3.37)$$

The condition of the local basis functions $\psi_i^{E_r}$ is to have the value 1 at the corner points $\bar{P}_i(\bar{x}_i, \bar{y}_i, \bar{z}_i)$ and the value 0 at the remaining corner points, which results in the following definition for the local basis functions:

$$\begin{aligned} \psi_1^{E_r} &= 1 - \bar{x} - \bar{y} - \bar{z} \\ \psi_2^{E_r} &= \bar{x} \\ \psi_3^{E_r} &= \bar{y} \\ \psi_4^{E_r} &= \bar{z} \end{aligned} \quad (3.38)$$

The local basis functions $\psi_j^{E_k}$ in the tetrahedron E_k can be expressed by the barycentric coordinates in equation (3.36):

$$\psi_1^{E_k} = L_1, \quad \psi_2^{E_k} = L_2, \quad \psi_3^{E_k} = L_3, \quad \psi_4^{E_k} = L_4 \quad (3.39)$$

The integral in equation (3.32) is defined over the entire domain Ω and is evaluated by the combined contribution of the integral evaluated for each tetrahedron $T^{(e)}$. Therefore, the integral in equation (3.32) has to be evaluated for each tetrahedron E_k . If the partition of the domain Ω into these elements fulfils the property that the complex conductivity $\underline{\kappa}$ is constant in each element, and using equation (3.35), the entries of the element matrices $\underline{\mathbf{S}}^{E_k}$ can be derived to be

$$\underline{S}_{ij}^{E_k} = \underline{\kappa}^{E_k} \int_{E_k} \nabla \psi_i^{E_k} \cdot \nabla \psi_j^{E_k} \det(\mathbf{J}) \, d\bar{x} \, d\bar{y} \, d\bar{z}. \quad (3.40)$$

Element	Nodes			
	1	2	3	4
1	1	2	3	4
2	2	5	3	4

Table 3.1: Elements' table

Node	x	y	z
1	x_1	y_1	z_1
2	x_2	y_2	z_2
3	x_3	y_3	z_3

Table 3.2: Coordinates' table

3.2.3 Assembly of the global system of linear equations

The global basis function $\psi_i(\mathbf{r})$ is composed of the local basis functions $\psi_j^{E_k}(\mathbf{r})$ assigned to the node i with $i = 1, \dots, M$, M being the number of global basis functions. Thus, only those elements, which have node i in common, contribute to the global basis function $\psi_i(\mathbf{r})$, which results in non-zero entries of \underline{S}_{ij} only for adjacent finite elements and, therefore, in a sparse system matrix $\underline{\mathbf{S}}$ in equation (3.33). The system matrix $\underline{\mathbf{S}}$ with the node variables \underline{u}_i numbered globally from $i = 1, \dots, M$ is constructed out of the element matrices $\underline{\mathbf{S}}^{E_k}$ with the local numbering $j = 1, \dots, 4$ by adding up the element matrices according to the affine transformations E_k . In general, the nodes corresponding to the tetrahedra E_k are stored in an elements' table 3.1 and the coordinates of the nodes are stored in a coordinates' table 3.2. The finite element solution is achieved by solving the matrix formulation in equation (3.33). The obtained solution is just an approximation of the analytical solution (if existing), the accuracy of which depends on the mesh density, the quality of the mesh, and the applied solver. In cases where a comparison of the numerical results with an analytical solution is not possible, error-controlled adaptive mesh refinement is carried out until a prescribed error in the derived solution quantities is reached. The obtained solution is then assumed to be close to the physical solution.

3.2.4 Finite element software

The basics of the method described in the previous section can be rewritten for two-dimensional and three-dimensional geometries by using, for example, triangular and tetrahedral finite elements of several orders or interpolation degrees (linear, quadratic, cubic, ...). However, the implementation of the method for different dimensions and element orders is rather challenging and time consuming. Nowadays, various open source and commercial toolboxes exist for finite element computations of different applications and physics, such as Elmer [33], GetDP [35], and Comsol Multiphysics™ [32]. The finite element computations of the human brain model used in this thesis were carried out using the commercial software Comsol Multiphysics™ version 4.2a, which is a finite element toolbox offering, among others, a

graphical user interface for geometry generation, several mesh algorithms and adaptive refinement techniques, consideration of anisotropic material parameters, various direct and indirect solvers for linear and non-linear problems, and an application programming interface to MATLAB®, allowing for the control of Comsol Multiphysics™ via script files and functions.

3.2.5 Fourier finite element method

The voltage response in the stimulated target area of the brain is obtained by solving the EQS equation (3.24) and QS equation (3.25), respectively, in a volume conductor model with FEM, which is based on a time-harmonic sine-wave stimulus applied to the electrode contacts of the DBS electrode. To compute the voltage distribution in the tissue as a function of time for, in this case, a square-wave stimulus, one single sine-wave computation of the model is not sufficient. Butson and McIntyre [21] suggested the use of a so-called Fourier finite element method (FFEM) to compute the time-dependent voltage response in a volume conductor model of the human brain. This method is carried out in four steps (Fig. 3.4):

1. The stimulation waveform is modelled in the time-domain as a square-wave signal using parameters similar to those used in clinical practise as described in section 2.2.1.
2. The stimulation waveform is transformed into the frequency-domain using Fourier transform.

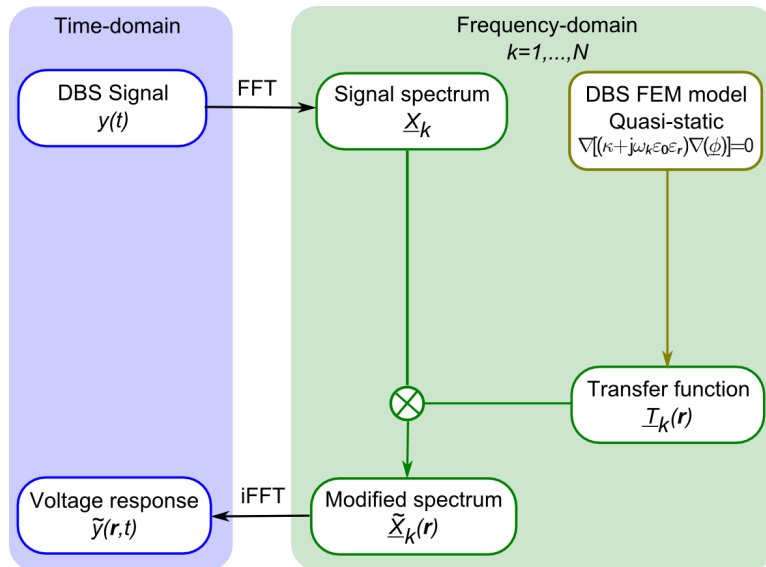


Figure 3.4: Schematic description of the Fourier finite element method (FFEM).

3. The partial differential equation is solved for each frequency component of the Fourier transform. The resulting voltage at a certain point in the model is then scaled and phase-shifted by the results of the Fourier transform of the stimulation waveform.
4. The modified signal in frequency-domain is transformed back into the time-domain by using an inverse Fourier transform.

Since the method uses Fourier transforms for the computation of the time-dependent voltage response, the material properties and the voltage distribution in the volume conductor model have to be linear. In addition, the propagation effect in equation (3.19) and inductive effect (3.20) have to be negligible. This method was used in several simulation studies [21, 57, 142] and is experimentally validated *in vitro* [87]. By considering the values of the frequency-dependent electrical tissue properties at each frequency, it is further possible to investigate dispersive effects on the voltage response in the tissue [57].

The disadvantage of FFEM constitutes the required computation of the transfer function within the finite element model, resulting in a large number of FEM computations. In addition, the costly FEM computations have to be redone, if the control type of the stimulus is changed from a voltage-controlled to a current-controlled one and vice versa. For this case, the third step of the method was modified in this thesis, based on the work of Yousif et al. [143] and Potratz [101]. Instead of computing each component of the transfer function with FEM, the transfer function is generated by an equivalent circuit, in which the resistance and capacitance of the tissue is computed with FEM at a certain single frequency. To obtain the voltage response at a certain point in the tissue, the results of the Fourier transform of the stimulation waveform are scaled by the potential at this point. This is possible, since firstly, the resistance and capacitance do not change with frequency, if assumed to be non-dispersive, and secondly, the solution obtained from the finite element model is linear. These parameters are used to generate an equivalent circuit describing the transfer function, which is then used to scale and phase-shift the results of the Fourier transform of the voltage waveform.

3.3 Fourier finite element method with equivalent circuits (FFEMEC)

The method to compute the time-dependent voltage response in the tissue is based on FEM computations of the volume conductor model of the human brain and a Fourier transform of the waveform of the DBS pulse (Fig. 2.4). This computation is carried out in four steps, which will be described in detail in the following paragraphs 3.3.1 to 3.3.4. The proposed method differs from common FFEM only in the third step,

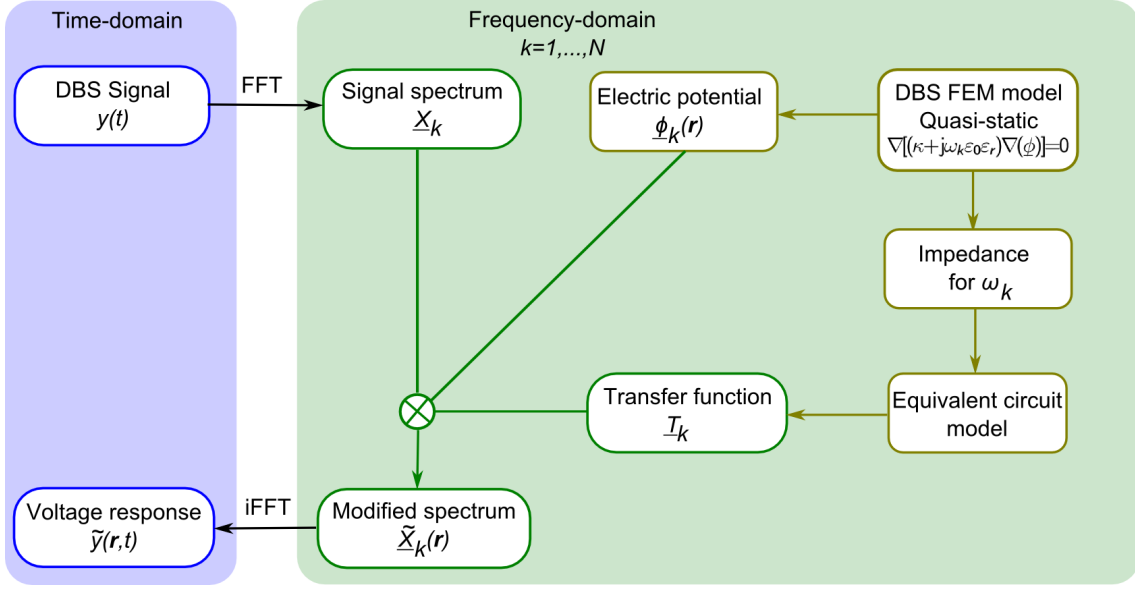


Figure 3.5: Schematic description of the Fourier finite element method with equivalent circuits (FFEMEC).

where the transfer function is not obtained directly from the voltage response in the volume conductor model, but is determined by a surrogate model, which comprises an equivalent circuit model (Fig. 3.5). This surrogate model requires the impedance of the volume conductor model to derive the equivalent circuit components. This impedance can be obtained by only one FEM computation for non-dispersive material properties.

1. Modelling of the DBS pulse.
The DBS pulse is modelled in the time-domain using the common stimulation pulse parameters used in clinical practise described in section 2.2.1.
2. Fourier transform of the DBS pulse.
The DBS pulse is transformed into the frequency-domain using a FFT, which results in the power spectrum of the DBS pulse with the Fourier components \underline{X}_k for $k = 1, \dots, N$ with N sampling points.
3. Equivalent circuit model of the tissue.
The electrical tissue properties are modelled at the frequency ω_k as a parallel RC circuit, which is derived from the impedance of the volume conductor model. This impedance is computed, using the applied voltage and total current between the stimulation electrode contact and ground. The transfer function \underline{T}_k obtained from the RC circuit and the electric potential at a certain spatial point \mathbf{r} in the model is used to modify the Fourier components \underline{X}_k of the DBS pulse, resulting in the power spectrum of the voltage response $\underline{\tilde{X}}_k(\mathbf{r})$.

4. Inverse Fourier transform of the voltage response in the tissue.

The Fourier components $\tilde{X}_k(\mathbf{r})$ of the scaled and phase-shifted voltage response in the frequency-domain at a certain spatial point in the tissue is transformed back into the time-domain using an inverse FFT, resulting in the time-dependent voltage response.

To be consistent with FFEM, the proposed method requires the computation of the model impedance for each angular frequency ω_k of the signal spectrum X_k with $k = 1, \dots, N$, which results in a larger computational expense due to the equivalent circuit computation compared to FFEM. The computational advantage of the model arises if the electrical properties of the biological tissue are assumed to be frequency-independent (non-dispersive). Under this assumption, the equivalent circuit can be derived from one FEM evaluation of the volume conductor model at the frequency ω_s (Fig. 3.6). Despite the assumption that the electrical properties of each biological tissue type are non-dispersive, the combined electrical properties of them in a volume conductor model can be dispersive, as described in appendix A.1, where conditions for the electrical properties of the biological tissue types are derived, for which the combined electrical properties in the volume conductor model can be assumed to be non-dispersive. These conditions are roughly the square of the condition for the neglect of the capacitive effect in section 3.1.1, but depend on the model geometry as well. Therefore, the validity of this method has to be examined for the generated volume conductor model of the human brain.

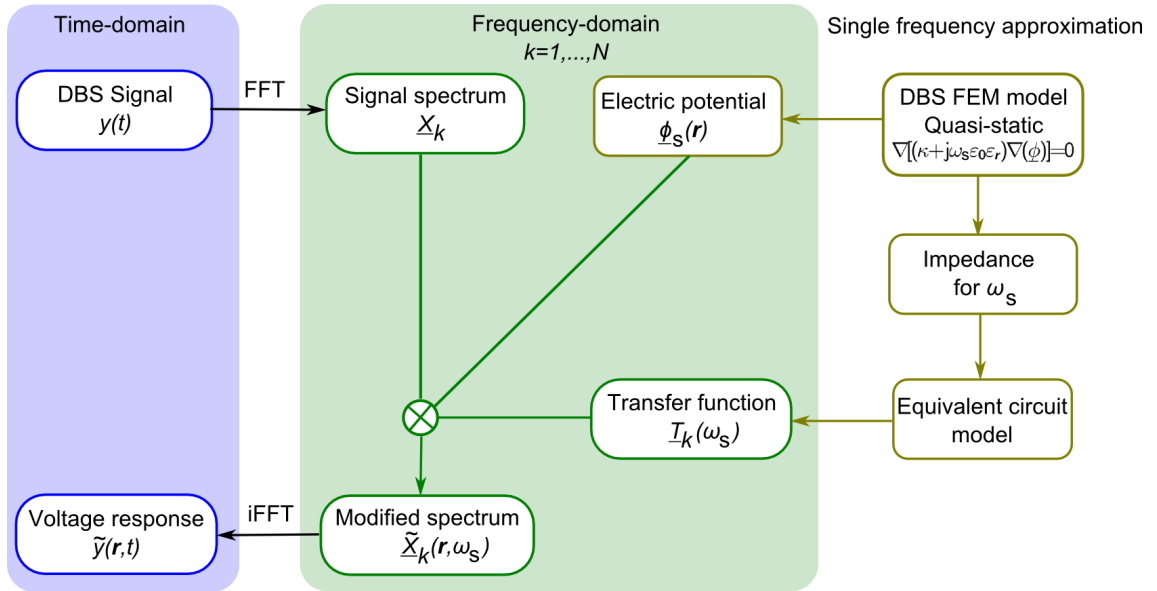


Figure 3.6: Schematic description of the Fourier finite element method with equivalent circuits (FFEMEC) with a single frequency approximation of the electrical properties of the biological tissue at the angular frequency ω_s .

3.3.1 Modelling and Fourier transform of the stimulation pulse

The DBS pulse is delivered to the electrode in two possible modes, keeping the voltage or the current at a constant amplitude. These modes are called voltage-controlled or current-controlled stimulation, respectively. The majority of applied DBS pulses in human patients are voltage-controlled [130]. Current-controlled DBS pulses are commonly applied in animal models [52], but recently gained more interest for the human DBS as well, since the current-controlled stimulation is less influenced by effects of the electrode-tissue-interface [78]. To avoid harmful side effects caused by a charge imbalance supplied by the DBS pulse, it is necessary to use a charge-balanced stimulation signal in clinical practise [85]. Such a signal can be obtained by providing an oppositely charged stimulation period after each active stimulation period. Since the charge supply in the tissue depends on the delivered current in time, the charge-balancing pulse can be set to a relatively low amplitude with a long time period compared to the active stimulation period.

The mono-phasic DBS pulse $y(t)$ commonly used in DBS of the STN is a square-wave signal with a repetition frequency of $f_p = 130$ Hz, a pulse duration of $d_p = 60$ μ s and cathodic amplitudes A_{vc} for voltage-controlled stimulation and A_{cc} for current-controlled stimulation as described in section 2.2.1. This signal can be modelled as a periodic discontinuous step function in time

$$y(t) = \begin{cases} A & 0 \leq t < d_p \\ 0 & d_p \leq t < \frac{1}{f_p} \end{cases} \quad (3.41)$$

where A is the amplitude of the signal. The points of discontinuity at $t = 0$ and $t = d_p$ can result in overshooting if the Fourier components of the signal are truncated. This

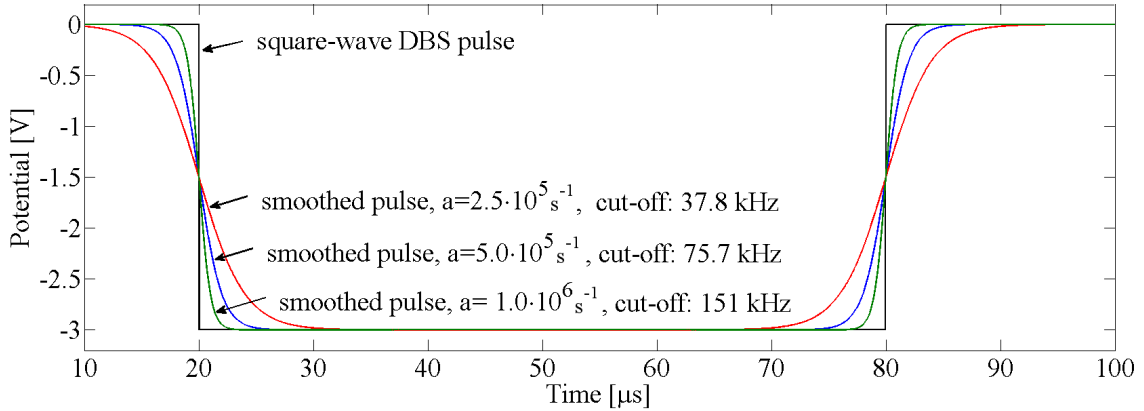


Figure 3.7: Theoretical square-wave DBS pulse and smoothed pulses in the time-domain for different slope coefficients a . The smoothing of the DBS pulse reduces the overshooting at the points of discontinuity after a Fourier transform of the signal.

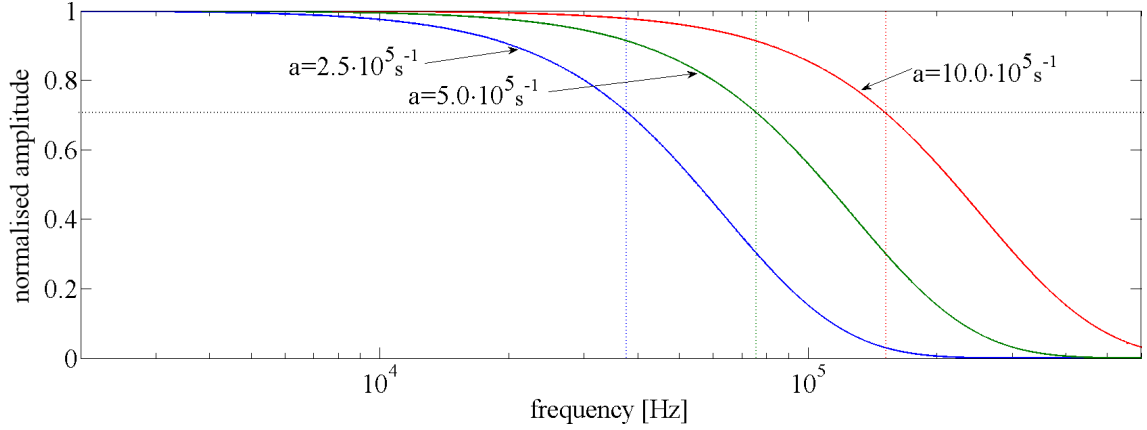


Figure 3.8: Voltage spectrum of the smoothed pulses normalised to the theoretical square-wave DBS pulse. Cut-off frequencies are determined at -3dB to be at 37.8 kHz ($a = 2.5 \cdot 10^5\text{ s}^{-1}$), 75.7 kHz ($a = 5 \cdot 10^5\text{ s}^{-1}$), and 151 kHz ($a = 10 \cdot 10^5\text{ s}^{-1}$), respectively.

overshooting is independent of the numbers of harmonics considered in the Fourier transform and is known as Gibbs' phenomenon, which is in the order of 9 % for a square-wave signal [65]. To investigate the influence of overshooting in the time-dependent voltage response, the theoretical square-wave DBS pulse in equation (3.41) was smoothed using the function

$$y(t) = \frac{A}{2} \left\{ 1 + \tanh \left[a \left(\frac{d_p}{2} - |t| \right) \right] \right\} \quad (3.42)$$

where the coefficient a determines the slope of the signal, which influences the truncation effect, i.e. the cut-off frequency, of the Fourier components (Fig. 3.7). The time-dependent pulse is transformed into the frequency-domain by a FFT, using the MATLAB® function `fft` with a sampling rate of 1 MHz. The smoothing of the pulse (3.42) acts as a high frequency filter on the theoretical DBS pulse, resulting in cut-off frequencies depending on the slope coefficient a (Fig. 3.8). For a slope coefficient of $a = 5 \cdot 10^5\text{ s}^{-1}$, the overshooting at the points of discontinuity of the DBS pulse is reduced to a value below 0.1 % [110]. To achieve the time-dependent voltage response in the tissue, the Fourier components of the DBS pulse are modified by the transfer function derived from the equivalent circuits, described in 3.3.2, as well as by the electric potential at the spatial point of interest in the volume conductor model. These scaled and phase-shifted Fourier components of the time-dependent voltage response are then transformed back into the time-domain by an inverse FFT using the MATLAB® function `ifft`. The modelled DBS pulses in the equations (3.41) and (3.42) are mono-phasic and, therefore, do not provide a charge-balanced stimulation over time. The charge-balancing is commonly carried out by using a bi-phasic DBS pulse with an additional charge-balancing period of substantially smaller

amplitude compared to the active stimulation period. As described in section 3.6, the neural activation is predicted in this thesis by computing the thresholds necessary to elicit an action potential in a myelinated axon model. Considering that the activation of a neuron is mainly influenced by the amplitude of the DBS pulse, a mono-phasic signal neglecting the charge-balancing stimulation pulse of low amplitude will most likely have no influence on the computation of the VTA [57].

3.3.2 Equivalent circuit model

The electrical properties and the heterogeneous distribution of biological tissue in a volume conductor model of DBS influence the waveform shape of the voltage response of the DBS pulse applied to the DBS electrode. The bulk properties of the tissue can be represented in volume conductor models by the parallel combination of its resistance and capacitance. The computation of these circuit elements in the model is carried out by determining the phasor \underline{I} , corresponding to equation (3.8), of the total current for a peak voltage U of an applied sinusoidal voltage at an angular frequency ω_k between the active stimulation electrode and ground. In the EQS formulation, the current \underline{I} is a complex quantity allowing to determine the resistance $R_{k,t}$ and capacitance $C_{k,t}$ of the tissue:

$$\underline{I} = \Re(\underline{I}) + j\Im(\underline{I}) = \left(\frac{1}{R_{k,t}} + j\omega_k C_{k,t} \right) U \quad (3.43)$$

$$R_{k,t} = \frac{U}{\Re(\underline{I})} \quad (3.44)$$

$$C_{k,t} = \frac{\Im(\underline{I})}{\omega_k U} \quad (3.45)$$

In the QS formulation, which only applies for purely resistive tissue properties, the current I is real-valued and, therefore, the electrical properties of the tissue can be fully described by the resistance $R_{k,t}$.

Electrode-tissue-interface

Beside the electrical properties of the biological tissue, processes at the electrode-tissue-interface resulting from charge transfers (Faradaic processes) and capacitive charging of the interface (non-Faradaic processes) influence the voltage response in the tissue [103]. These processes are responsible for the formation of an electric double-layer at the electrode-tissue-interface, which can be described by a constant phase element (CPE)

$$\underline{Z}_{\text{CPE}} = \frac{K}{A_e(j\omega)^\beta} \quad (3.46)$$

where K is the magnitude of the element, A_e is the electrode contact surface area, and $\beta \in [0, 1]$ is a factor determining the deviation from a pure capacitance ($\beta = 1$) and a pure resistance ($\beta = 0$) [103]. Therefore, the constant phase element can be used to characterise the non-ideal capacitive behaviour at the electrode-tissue-interface [60]. The values for platinum electrodes in a saline environment, such as the DBS electrodes used in this thesis, are as follows: $K = 1.57 \Omega \text{m}^2 \text{s}^{-\beta}$ and $\beta = 0.91$ [57]. The surface area of the electrode contact of a Medtronic DBS Mo. 3387 electrode is $A_e = 5.98 \cdot 10^{-6} \text{m}^2$. Due to non-linear effects at the electrode-tissue-interface, the CPE is only applicable for small stimulation amplitudes [103]. Wei and Grill [135] investigated the electrode-tissue-interface at DBS electrodes and confirmed the non-linear effects, but stated that these effects mainly occur in the low-frequency range ($< 100 \text{ kHz}$) and not for higher frequencies [135]. The investigated frequency range in this thesis is restricted to frequencies between 130 Hz and several kHz. The spectral energy density below 130 Hz is only about 1.5 % of the total spectral energy of the applied DBS pulse [110]. Therefore, it is assumed in this thesis that the behaviour of the electrode-tissue-interface can be described by a CPE.

3.3.3 Current-controlled stimulation

The frequency spectrum of the voltage response $\tilde{X}_{k,\text{cc}}(\mathbf{r})$ for $k = 1, \dots, N$ at a spatial point \mathbf{r} in the volume conductor model can be directly determined from the FEM solution at each frequency in the considered frequency spectrum. The aim is to use a surrogate model of the electrical properties of the volume conductor model based on an equivalent circuit to avoid the large number of required FEM computations using FFEM. In the proposed approach, the frequency spectrum of the voltage response at a spatial point \mathbf{r} can be computed with the help of the transfer function of the volume conductor model, which is derived from the equivalent circuit, and its spatial distribution of the electric potential.

The equivalent circuit comprises the parallel RC circuit in series with the CPE representing the electrical properties of the brain tissue and of the electrode-tissue-interface at the active electrode contact, respectively (Fig. 3.9). Since the current delivered to the tissue is kept constant for current-controlled stimulation, the voltage \underline{U}_k at an angular frequency ω_k in the equivalent circuit can be determined by

$$\underline{U}_k = \underline{T}_{k,\text{cc}} I_k = \left(\frac{1}{R_{k,\text{t}}} + j\omega_k C_{k,\text{t}} \right)^{-1} I_k \quad (3.47)$$

with the transfer function $\underline{T}_{k,\text{cc}}$. According to the constant current delivered, the transfer function is not influenced by the CPE, which is in agreement with results of simulation studies, suggesting that the electrical properties of the surrounding tissue dominate the waveform shape of the voltage response for current-controlled stimulation [21, 57]. The resistance $R_{k,\text{t}}$ and the capacitance $C_{k,\text{t}}$ can be determined

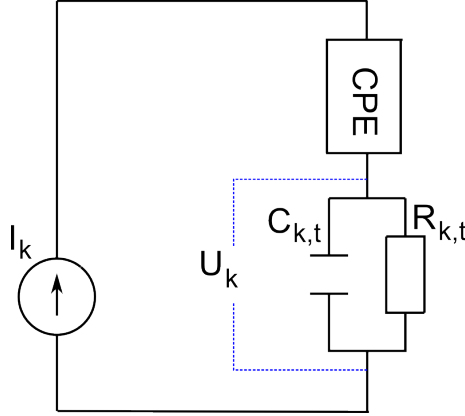


Figure 3.9: Equivalent circuit for the current-controlled stimulation with an ideal current source. The electrical properties of the volume conductor model are described by the CPE and the resistance $R_{k,t}$ as well as capacitance $C_{k,t}$ representing the electrical properties of the electrode-tissue-interface and of the brain tissue, respectively.

from the impedance of the volume conductor model described in the first paragraph of section 3.3.2. To obtain the frequency spectrum of the voltage response $\tilde{X}_{k,cc}(\mathbf{r})$ in the volume conductor model, the voltage response \underline{U}_k of the equivalent circuit is scaled by the electric potential $\underline{\varphi}_{k,cc}(\mathbf{r})$ at a spatial point \mathbf{r} in the volume conductor model computed for the angular frequency ω_k . This is possible if two conditions hold: Firstly, the field distribution has to be linear, and secondly, propagation effects have to be negligible. The first condition is met by the application of linear electrical properties of brain tissue. The second condition has to be checked by equation (3.19) for the spatial dimension of the area, in which the time-dependent voltage response is of interest as well as for the frequency-dependent electrical properties of brain tissue in the considered frequency range. The spatial distribution of the electric potential $\underline{\varphi}_{k,cc}(\mathbf{r})$ for current-controlled stimulation can then be computed using the EQS formulation with a constant normal current density applied to the active electrode contact and a constant electric potential of $V_0 = 0$ V applied to the ground electrode, resulting in the total current $A_{cc,FEM}$. The frequency spectrum of the voltage response $\tilde{X}_{k,cc}(\mathbf{r})$ can then be determined by

$$\tilde{X}_{k,cc}(\mathbf{r}) = \frac{\underline{T}_{k,cc}}{|\underline{T}_{k,cc}|} \frac{|\underline{\varphi}_{k,cc}(\mathbf{r})|}{|A_{cc,FEM}|} \underline{X}_k \quad (3.48)$$

which leads for a point \mathbf{r}_s at the electrode surface to the solution of the equivalent circuit equation in (3.47)

$$\begin{aligned} \tilde{X}_{k,cc}(\mathbf{r}_s) &= \frac{\underline{T}_{k,cc}}{|\underline{T}_{k,cc}|} \frac{|\underline{\varphi}_{k,cc}(\mathbf{r}_s)|}{|A_{cc,FEM}|} \underline{X}_k = \frac{\underline{T}_{k,cc}}{|\underline{T}_{k,cc}|} \frac{|A_{cc,FEM} \underline{T}_{k,cc}|}{|A_{cc,FEM}|} \underline{X}_k \\ &= \underline{T}_{k,cc} \underline{X}_k \end{aligned} \quad (3.49)$$

where \underline{X}_k is the applied current phasor \underline{I}_k of the frequency spectrum of the applied current-controlled DBS pulse at the angular frequency ω_k . Since the transfer function $\underline{T}_{k,cc}$ and the electric potential $\underline{\varphi}_{k,cc}(\mathbf{r})$ are computed at each frequency, this model is also applicable for the dispersive electrical properties of brain tissue. However, this formulation of Fourier finite element method with equivalent circuits (FFEMEC) would not have any computational advantage over the common FFEM under these conditions.

Thus, to use the advantage of the proposed method, non-dispersive electrical properties and small capacitive effects of the considered tissue types have to be assumed. For a volume conductor model with frequency-independent material properties and under the assumptions formulated in section 3.3, the transfer function

$$\underline{T}_{k,cc}(\omega_s) = \left(\frac{1}{R_{s,t}} + j\omega_k C_{s,t} \right)^{-1} \quad (3.50)$$

and the potential distribution $\underline{\varphi}_{s,cc}(\mathbf{r})$ can each be obtained by only one FEM computation at the angular frequency ω_s , which constitutes a substantially computational advantage compared to FFEM. The transfer function $\underline{T}_{k,cc}(\omega_s)$ and the electric potential $\underline{\varphi}_{s,cc}(\mathbf{r})$ lead to the frequency spectrum $\underline{\tilde{X}}_{k,cc}(\mathbf{r}, \omega_s)$

$$\underline{\tilde{X}}_{k,cc}(\mathbf{r}, \omega_s) = \frac{\underline{T}_{k,cc}}{|\underline{T}_{s,cc}|} \frac{|\underline{\varphi}_{s,cc}(\mathbf{r})|}{|A_{cc,FEM}|} \underline{X}_k. \quad (3.51)$$

3.3.4 Voltage-controlled stimulation

Constant voltage DBS pulses are applied to the DBS electrode for voltage-controlled stimulation, which results in the formation of an electric double layer at the electrode-tissue-interface. Regarding the equivalent circuit in Figure 3.9 for current-controlled stimulation, the ideal current source is replaced by an ideal voltage source and, therefore, the CPE has to be considered for voltage-controlled stimulation. Accordingly, the transfer function $\underline{T}_{k,vc}$ is determined by applying the frequency-dependent voltage divider rule and equation (3.46), resulting in the following expression:

$$\begin{aligned} \underline{T}_{k,vc} &= \frac{(R_{k,t}^{-1} + j\omega_k C_{k,t})^{-1}}{(R_{k,t}^{-1} + j\omega_k C_{k,t})^{-1} + \underline{Z}_{k,CPE}} = \frac{1}{1 + (R_{k,t}^{-1} + j\omega_k C_{k,t}) \underline{Z}_{k,CPE}} \\ &= \left(1 + \left(\frac{1}{R_{k,t}} + j\omega_k C_{k,t} \right) \frac{K}{A_e(j\omega_k)^\beta} \right)^{-1} \end{aligned} \quad (3.52)$$

where $A_{vc,FEM}$ is the voltage between the active stimulation electrode, which is set to the constant potential $V_1 = A_{vc,FEM}$, and the ground electrode set to the constant

potential $V_0 = 0$ V. With equation (3.48), it follows that the frequency spectrum of the voltage response $\tilde{X}_{k,\text{vc}}(\mathbf{r})$ at a spatial point \mathbf{r} in the volume conductor model is

$$\tilde{X}_{k,\text{vc}}(\mathbf{r}) = \frac{\underline{T}_{k,\text{vc}}}{|\underline{T}_{k,\text{vc}}|} \frac{|\varphi_{k,\text{vc}}(\mathbf{r})|}{|A_{\text{vc},\text{FEM}}|} \underline{X}_k \quad (3.53)$$

Instead of requiring $2N$ FEM computations for determining the impedance as well as the field distribution for current-controlled stimulation with dispersive material properties, the computation of the time-dependent voltage response with frequency-dependent electrical properties of brain tissue for voltage-controlled stimulation requires N FEM computations, which are as many as with FFEM. Again, the computational advantage of the proposed method is achieved, if the dispersive material properties in the considered frequency range are approximated at a certain angular frequency ω_s . The corresponding transfer function $\underline{T}_{k,\text{vc}}(\omega_s)$ and the frequency spectrum of the voltage response $\tilde{X}_{k,\text{vc}}(\mathbf{r}, \omega_s)$ are:

$$\underline{T}_{k,\text{vc}}(\omega_s) = \left(1 + \left(\frac{1}{R_{s,t}} + j\omega_k C_{s,t} \right) \frac{K}{A_e(j\omega_k)^\beta} \right)^{-1} \quad (3.54)$$

$$\tilde{X}_{k,\text{vc}}(\mathbf{r}, \omega_s) = \frac{\underline{T}_{k,\text{vc}}(\omega_s)}{|\underline{T}_{k,\text{vc}}(\omega_s)|} \frac{|\varphi_{k,\text{vc}}(\mathbf{r})|}{|A_{\text{vc},\text{FEM}}|} \underline{X}_k \quad (3.55)$$

With the proposed method, the computation of the time-dependent voltage response for voltage-controlled stimulation requires only one FEM computation, which is necessary to obtain the impedance of the volume conductor model and its field distribution with the EQS formulation for the frequency ω_s .

For both stimulation types, the modified frequency spectrum of the DBS signal in equation (3.51) and (3.55) is transformed back into the time-domain using an inverse FFT to obtain the time-dependent voltage response at any point \mathbf{r} in the proximity of the stimulated target. With the proposed method it is possible to compute the time-dependent voltage response in a volume conductor model of the human brain with a substantially lower computational effort compared to the common FFEM. This fast computation of the time-dependent voltage response allows for advanced simulations, such as parameter studies, sensitivity analysis, and uncertainty quantification, which otherwise would only be possible with a large computational effort using FFEM. However, the computational advantage of FFEMEC is limited to the assumption of non-dispersive material properties. Therefore, the validity of this assumption has to be verified in the used volume conductor of the human brain and for the considered brain tissue types.

3.4 Anisotropy of brain tissue

In contrast to isotropy, anisotropy refers to the directional dependence of a physical property, e.g. the diffusion of water molecules or the electrical properties of biological tissue. For example, a medium has an isotropic conductivity if the electric current in the medium has the same direction as the applied electric field with no change in its magnitude if the direction of the electric field is changed. In anisotropic medium, direction and magnitude of the electric current may change according to an applied electric field, which is not in the main direction of the anisotropy. Regarding the diffusion of water molecules, brain tissue such as gray and white matter exhibit an anisotropic behaviour [9]. Water molecules are in constant motion due to thermal effects, called Brownian motion. The motion of the water molecules in tissue is constrained by its microscopic structure, leading to a tendential diffusion along the cells, reflecting the structure of the tissue, which influences the permittivity and conductivity in different directions. Especially for fibre-like structures such as axons in brain tissue, the diffusion of water molecules can deliver information about their location and orientation, while in non-constrained fluids such as CSF the diffusion is more random and uniform [28]. The anisotropic conductivity of brain tissue results from the geometry of the neuronal fibres, comprising a small resistance longitudinal and a large resistance transversal to the fibre. In general, this property results in conductivity tensors with two similar eigenvalues denoting the transversal conductivity κ_{trans} and one larger eigenvalue denoting the longitudinal conductivity κ_{long} (Fig. 3.10). Since the capacitive membranes of axons are short-circuited at high frequencies, anisotropy of the electrical properties of brain tissue will most likely occur in the low frequency range of DBS [60]. In 2001, Tuch et al. investigated the relation between the diffusion of water molecules and the ionic movement in brain tissue. According to the authors, a linear relation between both properties can be found, which allows to compute the anisotropic conductivity of brain tissue directly from the anisotropic diffusion of the water molecules in the tissue. This anisotropic diffusion in the brain tissue can be measured by diffusion tensor imaging, which is based on the technique of MRI.

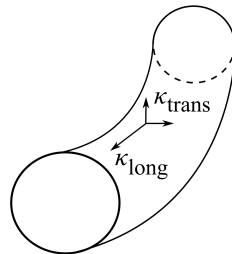


Figure 3.10: Schematic illustration of a neuronal fibre with the longitudinal conductivity κ_{long} and the transversal conductivity κ_{trans} .

3.4.1 Diffusion tensor imaging

The following section is based on the description of diffusion tensor imaging (DTI) of Chanraud et al. [28]. DTI is based on the technique of MRI, which generates maps of the relaxation of hydrogen protons, the spin-echo, resulting from the alignment of the protons in the applied homogeneous magnetic field of the MRI scanner. This mapping is dependent on the immediate environment of the water protons restricting their movement. The detection of this movement is carried out by using magnetic fields, where the field strength is varied linearly in one direction by the application of a magnetic field gradient. This inhomogeneous magnetic field results in a larger movement of freely diffusing water molecules than for those, which are restricted by physical boundaries. The characterisation of the orientation of the diffusion in the three-dimensional space is then obtained by applying multiple field gradients with different non-collinear orientations. The diffusion is quantified by subdividing the brain into small cubes (voxels) and computing the diffusion tensor \mathbf{D}

$$\mathbf{D} = \begin{pmatrix} D_{11} & D_{12} & D_{13} \\ D_{21} & D_{22} & D_{23} \\ D_{31} & D_{32} & D_{33} \end{pmatrix} \quad (3.56)$$

which represents the magnitude and orientation of the diffusion, in each voxel. The diffusion tensor can be mathematically described as a three-dimensional ellipsoid, the eigenvectors and eigenvalues (d_1, d_2, d_3) of which correspond to the orientation and length of the semi-axes of the ellipsoid, respectively (Fig. 3.11). The largest eigenvalue corresponds to the diffusion along an axon (longitudinal diffusivity), while the smallest eigenvalue reflects the diffusion perpendicular to the membrane of the axon (transversal diffusivity). The degree of anisotropy within a voxel can be

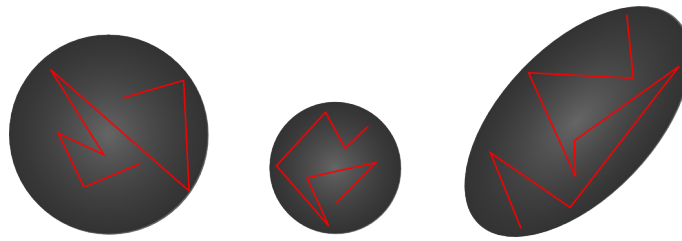


Figure 3.11: Examples of diffusion tensor ellipsoids estimated from the random movement of water molecules for a free diffusivity (left), such as in water or CSF, a constrained, but uniform diffusivity (centre), and a strongly non-uniform diffusivity (right), as in white matter fibres. Image based on <http://www.cabiatl.com/Resources/DTI/images/dti.jpg>, Access: 30.01.2013

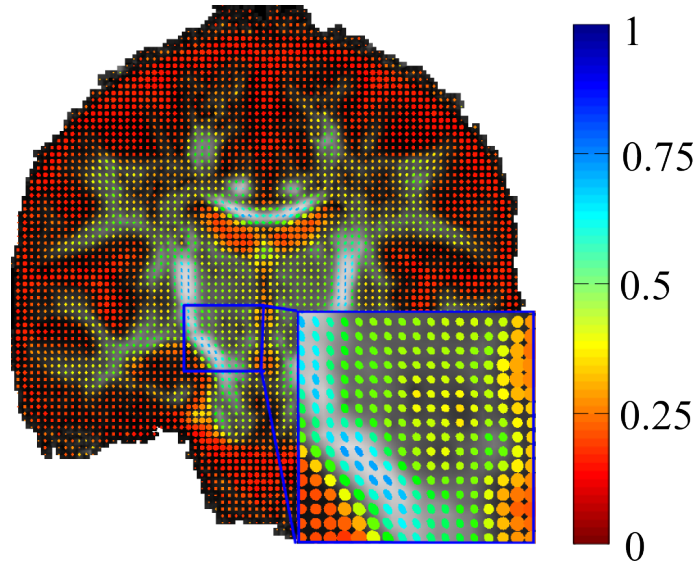


Figure 3.12: Diffusion tensor ellipsoids color-coded by their fractional anisotropy (FA) in a coronal section of a DTI MRI scan of the human brain from the SRI24 multi-channel brain atlas [104]. The ellipsoids are mainly non-uniform and of large FA in the white matter fibre tracts, whereas in ventricular CSF, the diffusivity is more uniform with small FA.

measured by the fractional anisotropy (FA) [9]

$$\text{FA} = \sqrt{\frac{1}{2} \frac{\sqrt{(d_1 - d_2)^2 + (d_2 - d_3)^2 + (d_3 - d_1)^2}}{\sqrt{d_1^2 + d_2^2 + d_3^2}}} \quad (3.57)$$

which is zero if $d_1 = d_2 = d_3$ in the case of free diffusion, such as in water. If one eigenvalue is substantially larger than the other two eigenvalues, the FA value approaches 1. Therefore, a voxel with a FA value close to 1 characterises a highly anisotropic area, while a voxel with a FA value close to 0 refers to an almost isotropic area (Fig. 3.12).

3.4.2 Conductivity tensor computation

Tuch et al. [126] described a linear relation between the diffusion of water molecules and the ionic motion in brain tissue. This relation was confirmed in an *in vitro* study, in which the conductivity and diffusivity of an anisotropic silk yarn model was measured [95]. Exploiting this linear relation, the anisotropic conductivity, described by the conductivity tensor κ , can be derived from the diffusion tensor \mathbf{D} by multiplying it with a scaling factor s

$$\kappa = s\mathbf{D} . \quad (3.58)$$

Different methods are proposed in literature to determine the scaling factor s , which include but are not limited to: (1) averaging the diffusion tensor data using least-squares method [106], (2) using an predefined anisotropy ratio of 1:10 for white matter [79, 69], (3) using an empirical value [126], and (4) mapping the volume of each isotropic conductivity tensor on the corresponding anisotropic conductivity tensor [63]. The latter approach can be used if the isotropic conductivity of the tissue in the voxel is known. The scaling factor s can then be computed by normalizing the volume of the diffusion tensor ellipsoid and scaling it with the isotropic conductivity in the voxel. The resulting conductivity tensor eigenvalues are then determined by

$$\kappa_i = \frac{\kappa_{\text{iso}}}{\sqrt[3]{d_1 d_2 d_3}} d_i \quad (3.59)$$

The average anisotropy ratio R_a in a voxel is computed by determining the quotient of the longitudinal conductivity and the geometrical mean value of the transversal conductivities. Assuming without loss of generality that κ_1 is the largest eigenvalue, the average anisotropy ratio R_a is determined by

$$R_a = \frac{\kappa_1}{\sqrt{\kappa_2 \kappa_3}}, \quad \kappa_1 \geq \kappa_2, \quad \kappa_1 \geq \kappa_3 \quad (3.60)$$

3.4.3 Limitations of diffusion tensor imaging

Although DTI can provide structural information of the brain by measuring the magnitude and orientation of the diffusion of water molecules, the method is limited by its resolution. According to Grimnes and Martinsen [60], heterogeneity of biological tissue exists at different levels ranging from the macroscopic structures such as white matter and gray matter regions, to microscopic structures such as axons and even smaller cell components. While the microscopic structure of axons and other brain tissue compartments is in the nm - μm range, the resolution of currently available DTI remains in the mm range, resulting in a common voxel size of 1 – 3 mm³. Therefore, DTI does not provide the structural information of single axons, but of the summation of the diffusion within one voxel, resulting in only an averaged anisotropy value within each voxel [60]. In addition, DTI is sensitive to fibre crossing in which no predominant orientation exists. This could result in a lower FA, which is not necessarily corresponding to a reduced anisotropy within the voxel.

3.5 Generation of an anatomical brain model

Based on the previous considerations on the bio-electrical conditions for the computation of the time-dependent voltage response in a volume conductor model using FFEMEC, an anatomical brain model was generated. The motivation of the generation of a full brain model incorporating the heterogeneity and anisotropy of brain

tissue instead of using a simplified, e.g. cuboid or spherical, volume conductor model is due to the influence of the geometry of the model on the voltage response and VTA as described in section 2.3.2 as well as allowing for the application of patient-specific data in further studies, since patient-specific modelling is a crucial component of predicting the neural activation in volume conductor models of DBS. To provide the time-dependent voltage response in the proximity of the stimulated target for an applied DBS pulse, an anatomical volume conductor model of the human brain incorporating tissue heterogeneity and anisotropy was generated using MRI and DTI data from the SRI24 multi-channel brain atlas. The generation of a volume conductor model of the human brain constitutes a modelling problem on a multi-scale. While the overall dimension of the human brain is in the range between 11 cm and 16 cm [104], the height of the electrode contacts and the surrounding encapsulation layer, which results from the tissue-implant reaction, are in a range between 0.2 mm and 1.5 mm.

3.5.1 The SRI24 multi-channel brain atlas

The SRI24 multi-channel brain atlas is a digital standard atlas of the human brain based on MRI data. It was developed by Rohlfing et al. [104]. The atlas comprises averaged MRI and DTI data as well as tissue segmentations of gray matter, white matter and CSF of 24 normal human subjects of an age between 19 and 83 years. This data allowed for the investigation of the neural activation and voltage response in this thesis on a "normal" brain, averaging possible patient-specific characteristics, which otherwise may have occurred if only the data of one patient had been used. According to Rohlfing et al. [104], the imaging was performed using a 3T MRI scanner. DTI data was obtained by measuring the diffusion in 30 non-collinear directions. The MRI and DTI data of each subject was registered non-rigidly and then registered to a reference coordinate by an affine and nonrigid transformation. Finally, the co-registered image data of all subjects as well as the tissue probability maps obtained for each subject were averaged. Based on the tissue probability maps, the MRI data was segmented into gray matter, white matter and CSF. The averaged MRI and DTI data have an isotropic voxel size of 1 mm³.

Location of the stimulated target and electrode orientation

One preferred target for DBS is the STN. Since the STN is a small brain nucleus and almost not visible on the standard T_1 -weighted MRI images, the determination of the location of the STN is rather challenging. Therefore, the location of the (left) STN in the SRI24 multi-channel brain atlas was determined by comparing the MRI data in 3D Slicer [39] with sections of the standard brain atlas by Kretschmann and Weinrich [74] by using the ventricles, the anterior commissure, and the optic tract as landmarks. To avoid complications during the surgery, the DBS electrode is implanted not

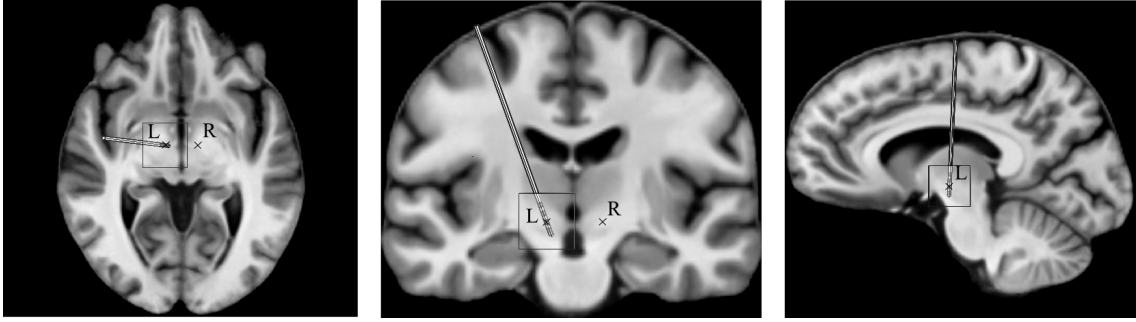


Figure 3.13: Location of the left (L) and right (R) STN in the MRIs of the SRI24 multi-channel brain atlas overlaid with a projection of the DBS electrode. Section views: axial (left), coronary (center), sagittal (right).

directly from top of the head, but under certain spherical angles. These angles were derived from CT data of a patient who underwent DBS surgery at the University Medicine Greifswald, Department of Neurosurgery (private communication with Dr. A. Müller). The resulting information was used to determine the location of the left and right STN as well as the trajectory of the DBS electrode in the MRIs (Fig. 3.13).

3.5.2 Geometry generation and physical boundary conditions

Since the time-dependent voltage response is especially of interest in the proximity of the stimulated target area, which is situated in the deep brain, an accurate representation of the time-dependent voltage response close to the skull was not required. Apart from that, it is necessary to obtain a realistic spatial dimension and representation of the biological tissue in the model to obtain an accurate model impedance [132]. Therefore, the exterior geometry of the brain model was idealised by an ellipsoid, overall dimension of which was derived from the MRI data of the SRI24 multi-channel brain atlas by visually fitting the ellipsoid's semi-axes on the brain geometry with 3D Slicer [39]. The semi-axes of the ellipsoid were determined to be 64 mm transversally, 81 mm longitudinally, and 55 mm sagittally. The added up volume of the idealised brain is about 1200 cm^3 , which is in the range of average brain volumes [105]. A realistic representation of the geometry of the Medtronic DBS electrode 3387 was generated and positioned at the stimulated target with the second electrode contact located in the target centre (Fig. 3.14). Since the STN constitutes a small target area, the Medtronic DBS electrode model 3389 with a smaller spacing between the electrode contacts would be more suitable in clinical practise. Nevertheless, both electrodes are used for STN DBS in clinical practise [34, 73]. The DBS electrode model 3387 is used in several *in silico* studies, which

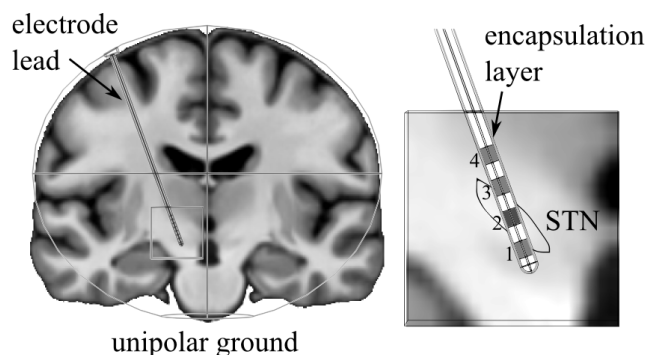


Figure 3.14: Coronal section of the magnetic resonance image and the idealised brain model with the implanted electrode lead. The four electrode contacts and the active second electrode contact are highlighted in gray and dark gray, respectively. The STN is illustrated according to the image data by Kretschmann and Weinrich [74]

conclude among others Butson and McIntyre [21], Grant and Lowery [57], and Yousif and Liu [142]. For comparison of the obtained results with other *in silico* studies, the DBS electrode model 3387 was used in this thesis. For the investigation of the voltage response and VTA, only unilateral stimulation with the left STN as target area was modelled. In clinical practise, also bilateral stimulation of both STNs is used [85].

To reduce the model complexity, the electrode geometry was subtracted from the brain model. Boundary conditions representing perfect conductors and insulators were applied to the surface of the active and grounded electrode contacts and of the insulation of the electrode, respectively. Since the electrode materials comprise platinum-iridium for the electrode contacts and urethane for the insulation, these idealised boundary conditions provide a reasonable approximation of their electrical properties [21]. Inactive electrode contacts, which are not connected to the neurostimulator and which are, therefore, devoid of a net current flow through their surface, were represented by a floating potential boundary condition. The exterior boundary of the idealised brain model was insulated. Bipolar and unipolar electrode configurations were modelled by setting the appropriate boundary conditions at the active electrode contacts and ground. In the bipolar mode, the first electrode contact was grounded, whereas in the unipolar mode, the ground was formed by a plane circle with a radius of 22 mm at the bottom of the model. To incorporate the tissue-implant reaction, an encapsulation layer with a thickness of 0.2 mm surrounds the electrode lead [142]. Since the focus of the studies was on the time-dependent voltage response and the VTA in the proximity of the stimulated target, a region of interest (ROI) in the form of a cuboid incorporating a refined mesh was implemented to increase the mesh density around the stimulated target (Fig. 3.15). The size of the

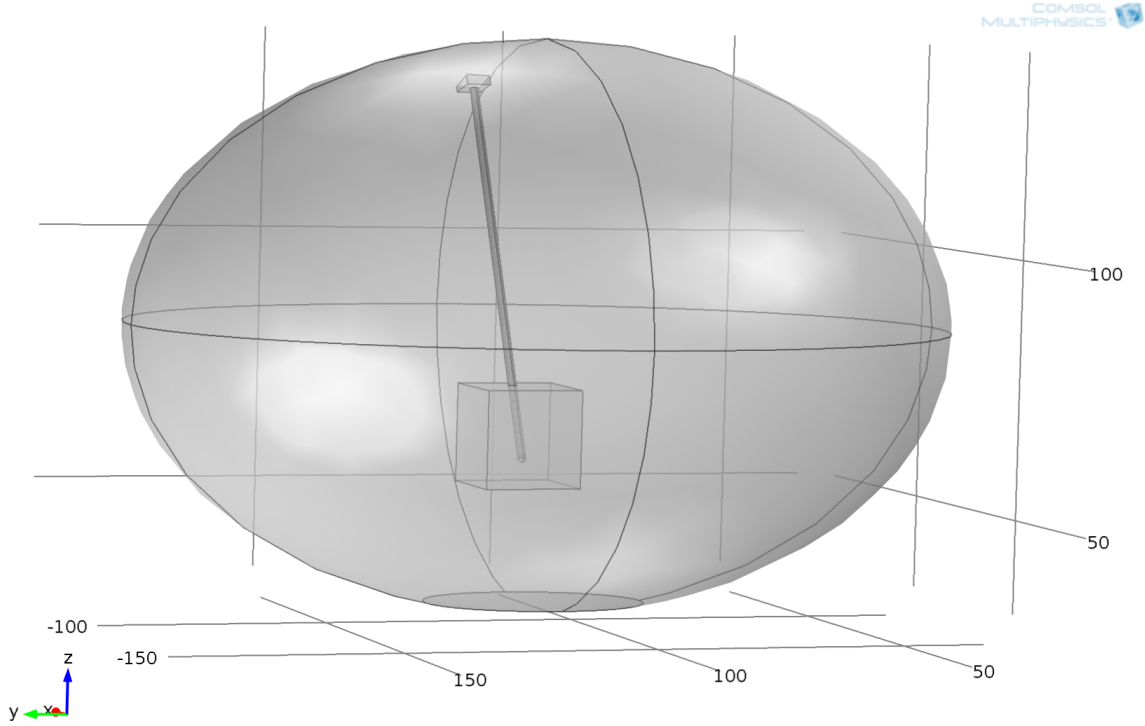


Figure 3.15: Domain geometries of the idealised brain model, the implemented electrode, and the region of interest (ROI) in Comsol Multiphysics™. The unit of the values is set to mm.

ROI is determined by computing the maximum relative error between the voltage distribution of a fully heterogeneous brain model without a ROI and a homogeneous brain model incorporating a heterogeneous ROI [109], as carried out in section 5.1.

3.5.3 Incorporation of electrical tissue properties and tissue anisotropy

The electrical tissue properties of gray matter, white matter and CSF were incorporated into the brain model by using the spatial information of the segmented MRI data of the SRI24 multi-channel brain atlas and the Cole-Cole equations derived from the data of Gabriel et al. [46]. The electrical properties of the encapsulation layer vary over time, from an acute phase immediately after the surgery to a chronic phase after some weeks, resulting from cell growth in this layer [58]. Therefore, the electrical properties of the encapsulation layer are adjusted using literature data [21, 142], depending on whether the acute or chronic phase should be modelled.

The anisotropic conductivity of gray matter and white matter were computed by using the spatial information of the segmented MRI data to identify the tissue type at each node of the brain model and scaling the accordingly normalised diffusion

```

NRRD00X
<field>: <desc>
# <comment>
...
<key>:=<value>
# <comment>

<data>

```

Table 3.3: General format of a NRRD file [124].

tensor derived from the DTI data with the electrical properties of the respective tissue type as described in section 3.4.2. The image data is available in the NRRD format, which allows to store the three-dimensional raster data of the MRI and DTI data sets including additional information. Data files in the NRRD format consist of the raw data and a header comprising the version number, fields, such as the data type, coordinate system, and the encoding of the data, and keys, including information about the dimension, size, spacing, and orientation of the data (Table 3.3). The NRRD file can be split in separate files for the header and the raw data using the open source software package 3D Slicer [39]. The MRI and DTI data from the SRI24 multi-channel brain atlas are oriented in a clinical right-anterior-posterior (RAS) coordinate system, which means that the data are aligned from left to right (x-axis), back to front (y-axis), and bottom to up (z-axis). In this coordinate system the anatomical x-axis and y-axis are numerically descending. To incorporate the brain atlas data into the volume conductor model generated with the FEM toolbox Comsol Multiphysics™, a right-handed coordinate system with ascending axes for the processing of the data is required. Therefore, the image data was preprocessed in MATLAB® by transforming the global coordinate system, which describes the alignment of the voxels, as well as the local coordinate system of each diffusion tensor to the appropriate coordinate system of Comsol Multiphysics™ (Fig. 3.16). Since only mirroring transformations are used, the NRRD data is required to be in a non-rotated coordinate system. A set of MATLAB® functions were created to cover the orientation transformation for further patient-specific data sets in future studies. The data aligned in a hexahedral grid was mapped onto the tetrahedral finite element mesh by using a nearest neighbour function. Due to the idealization of the spatial dimension of the human brain by an ellipsoid, certain regions close to the exterior boundary of the brain model are not covered by the MRI and DTI data and were set to the isotropic electrical properties of CSF.

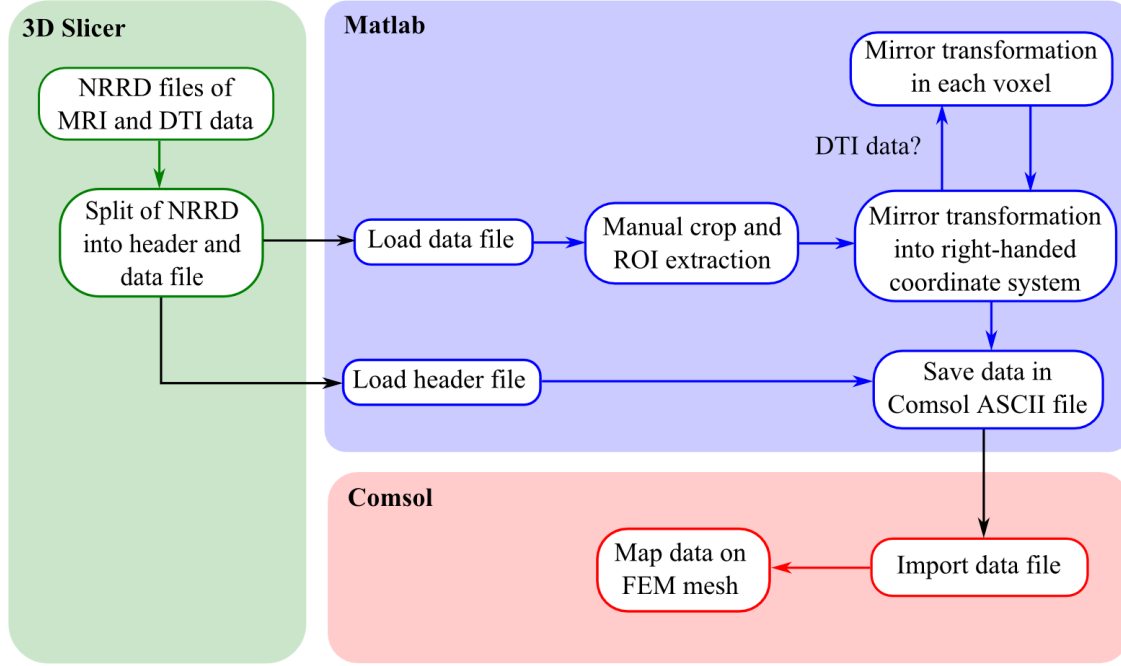


Figure 3.16: Flowchart of the pre-processing of the MRI and DTI data of the digital brain atlas for the incorporation in the volume conductor model by applying the software packages 3D Slicer (green), MATLAB® (blue), and Comsol Multiphysics™ (red).

3.6 Computation of the volume of tissue activated

The volume of tissue activated (VTA) was computed using the generalised mammalian axon model by McIntyre et al. [82] described in section 2.3.1. The STN axons are modelled with a fibre diameter of $5.7\text{ }\mu\text{m}$ similar to previous simulation studies [57, 83, 142]. The model comprises 21 nodes of Ranvier, at which the time-dependent extracellular potential of the volume conductor model is used as an input parameter for the computation of the membrane potential of the axon. To achieve a spatial map of the activation pattern, a set of these axon models are arranged perpendicular to an intersection of the volume conductor model including the electrode body, which was set to the coronary plane [21]. The axons are arranged in the rectangular grid with an equidistant spacing of 0.5 mm parallel and perpendicular to the electrode body (Fig. 3.17). On each node of Ranvier of each axon, the time-dependent extracellular potential is determined from the time-dependent voltage response of the volume conductor model for a stimulation amplitude of $A_{vc} = 1\text{ V}$ for voltage-controlled stimulation and $A_{cc} = 1\text{ mA}$ for current-controlled stimulation. For each axon the minimum stimulation amplitude necessary to elicit an action potential in the axon is determined by using Brent’s optimisation method for the time-dependent voltage response at each node multiplied with a scaling factor. It is mentioned again that

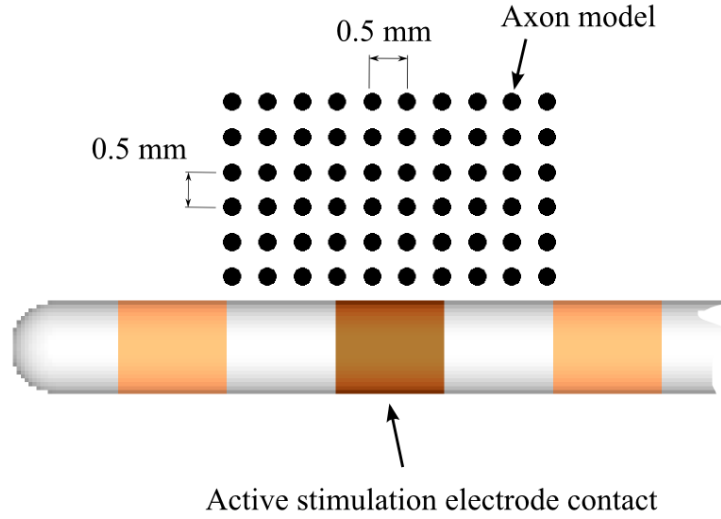


Figure 3.17: Arrangement of the axon model in an intersection of the volume conductor model including the electrode body of the Medtronic electrode Mo. 3387. The axon grid is centered to the second electrode contact.

the linear scaling of the time-dependent voltage response in the volume conductor model is applicable due to the linear properties of the FEM solution. For a certain stimulation amplitude A_v for voltage-controlled stimulation and A_c for current-controlled stimulation, in each row (perpendicular line to the electrode body) of the axon grid, the distance at which the axons are still activated is determined by a linear interpolation of the threshold-distance relation in this row. These interpolation points are used to determine a curve $f_{A,iso}(y)$, using the least-squares method, which corresponds to the isoline of activation for the set stimulation amplitude (Fig. 3.18). The VTA is computed by revolving the isoline $f_{A,iso}(y)$ around the electrode body with the disk integration method and subtracting the enclosed electrode body:

$$VTA = \pi \int_a^b f_{A,iso}^2(y) dy \quad (3.61)$$

with the limits of the integral determined by the roots a and b of the isoline with an offset of the electrode radius. The computation of the VTA is limited by two major assumptions: Firstly, it is assumed that all axons in the axon grid have the same properties, such as diameter, number of nodes of Ranvier, internodal spacing, and orientation. Secondly, by only computing the activation pattern in one intersection of the volume conductor model, it is assumed that the field distribution in the proximity of the stimulation electrode contact is similar to that in each intersection around the electrode body.

The computation of the membrane potential in each axon is carried out with

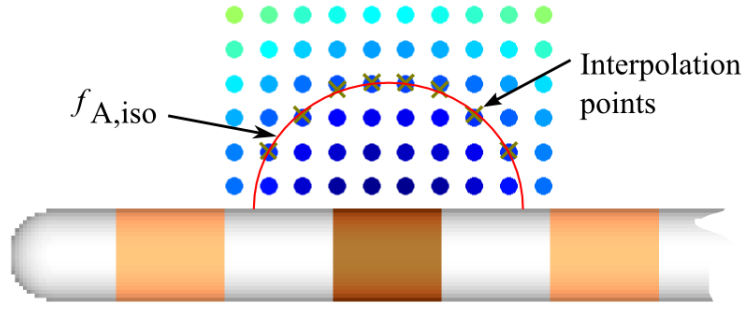


Figure 3.18: In each row (perpendicular line to the electrode body) of the axon grid, the distance of activation to the electrode is interpolated. These interpolation points are used to determine an isoline of activation using the least-squares method.

NEURON (ver. 7.2), which solves the governing differential system of equations with backward Euler implicit integration [67]. The computation of the VTA is automatised using a Python script developed in cooperation with Peadar Grant from the University College Dublin, Dublin, IE. This Python script includes the NEURON functionalities and computes the minimum stimulation amplitude necessary to elicit an action potential for each axon as well as the disk integration to obtain the VTA. To allow for a parallel computation of the stimulation amplitudes in the axon grid, the script is parallelized using the message passing interface (MPI) standard.

4 Uncertainty quantification by the polynomial chaos technique

Volume conductor models of the human brain, as described in section 2.3.2, are a crucial component for the realistic modelling of the mechanisms of action of DBS. Current models comprise heterogeneous and anisotropic tissue properties as well as bio-electrical effects at the electrode-tissue-interface and the inflammatory response of the body tissue to the implanted electrode [29]. Despite their complexity due to the incorporation of several input parameters such realistic brain models are based only on one deterministic set of parameters and, therefore, do not consider uncertainty in these parameters. This uncertainty leads to not only one deterministic solution, but to a probabilistic solution. One major goal of this thesis is to quantify the influence of the uncertainty in the electrical properties of brain tissue on the time-dependent voltage response as well as neural activation in the proximity of the stimulated target. The results could suggest sensitive parameters of volume conductor models of the human brain and their influence on the voltage response, neural activation and other desired quantities. In addition, the method could be used in software tools for planning and surgery of DBS to make the physician aware of the uncertainty in the actual neural activation in the target area. This chapter comprises a brief description of available methods for uncertainty quantification (UQ) in computational models and focuses on the non-intrusive projection approach based on the polynomial chaos technique to quantify the influence of uncertainty in the parameters of the brain model on the time-dependent voltage response as well as VTA.

4.1 Overview of available methods for uncertainty quantification

Uncertainty quantification (UQ) describes the investigation of the solution of a mathematical model in dependence of the uncertainty in its parameters. The solution of a mathematical model becomes probabilistic if the parameters are subject to uncertainty or the mathematical model itself has probabilistic properties. This thesis focuses on the investigation of the probabilistic time-dependent voltage-response and VTA of the generated volume conductor model of the human brain for uncertainty in its parameters. The corresponding stochastic methods have in common that they recast the original deterministic system as a stochastic system [138]. These

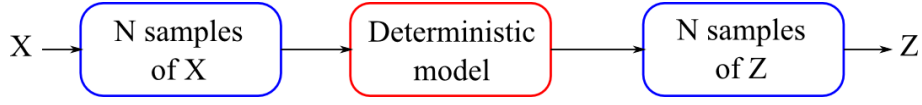


Figure 4.1: Scheme of the Monte Carlo simulation (MCS). The deterministic model is computed for a sequence of N samples obtained from the probabilistic model parameter \mathbf{X} , resulting in N samples of the probabilistic solution Z of the model.

stochastic methods for uncertainty quantification in engineering can be classified into non-probability and probability sampling methods. While non-probability sampling methods use deterministic samples, probability sampling methods are based on generating independent random samples of the probabilistic model parameters.

The most widely used non-probability sampling methods are perturbation methods, where the probabilistic quantities are expanded around their mean values via Taylor series and are incorporated into the system of equations of the mathematical model. This system of equations becomes extremely complicated for higher order expansions, resulting in a truncation of the Taylor series at first or second order terms [51]. This restriction limits the magnitude of uncertainties for the model parameters as well as the solution to a value of typically less than 10 % [138]. A famous probability sampling method is Monte Carlo simulation (MCS). For each generated sample of a probabilistic parameter X , the mathematical model is fixed and deterministic. The computation of the deterministic solution for each sample results in a set of solutions from which the probabilistic properties of the solution Z can be derived (Fig. 4.1) [138]. One probabilistic quantity of interest is the mean value $\mathbb{E}[Z]$ of the probabilistic solution Z , which can be estimated by

$$\tilde{\mathbb{E}}[Z] = \frac{1}{N} \sum_{i=1}^N Z(\mathbf{x}^{(i)}) \quad (4.1)$$

where $\mathbf{x}^{(i)}$ is the i -th sample of the probabilistic model parameters. The mean value $\mathbb{E}[Z]$ can be found most likely in the 95 % confidence interval

$$\left[\tilde{\mathbb{E}}[Z] - \frac{1.96\sigma_Z}{\sqrt{N}}, \tilde{\mathbb{E}}[Z] + \frac{1.96\sigma_Z}{\sqrt{N}} \right] \quad (4.2)$$

where σ_Z is the standard deviation of the probabilistic solution Z [31]. The relation in equation (4.2) implies that the absolute error of the mean value $\mathbb{E}[Z]$ converges with $1/\sqrt{N}$ for N generated samples, which can result in a large number of samples and, therefore, executions of the deterministic model to obtain a sufficiently accurate result [40]. In general, to increase the solution accuracy by one digit, about 100 times more executions of the deterministic model are required [138]. By its definition, the total computational cost of the method depends directly on the computational cost of one execution of the deterministic model. Therefore, MCS is not applicable for

computationally expensive deterministic models, such as volume conductor models of the human brain with up to several millions of unknowns. Apart from that, the convergence of MCS does not depend on the number of independent probabilistic parameters, which makes the method highly applicable for volume counting and integration in multi-dimensional spaces [40]. Beside the standard MCS, several techniques such as latin hypercube sampling and quasi Monte Carlo sampling exist to accelerate the convergence [138]. However, these techniques are limited in application and can only reduce the computational expense to a certain level. A similar approach is the worst-case scenario described by Babuška et al. [4], in which the uncertainty interval of the quantity of interest is determined for a prescribed uncertainty interval of the model parameters. However, this approach does not specify the probability distribution of the uncertain parameters and does not allow for an estimation of the mean value and higher order moments of the quantity of interest.

The polynomial chaos (PC) technique approximates the probabilistic properties of the model solution by a series expansion in a basis of orthogonal polynomials. The probability density function of the model solution and further statistical quantities are obtained by applying N independent samples to its polynomial expansion similar to MCS. Therefore, the PC technique can be assigned to the probability sampling methods. The difference to MCS is that the deterministic model is replaced by a surrogate model, which is represented by the multi-variate polynomial expansion of the model solution. The computation of the coefficients of this polynomial expansion requires numerical techniques such as the application of multi-dimensional cubature. Instead of solving the deterministic model for each sample, as it is the case for MCS, the model needs only to be executed at the nodes of the multi-dimensional cubature, the number of which depends on the number of independent parameters. For a sufficiently small number of parameters, the PC technique can provide a computationally efficient framework for the approximation of the probabilistic properties of the model solution. A detailed description of the PC technique, its implementation as well as insights into the multi-dimensional cubature will be given in the following sections 4.2, 4.2.3, and 4.3.

4.2 Polynomial chaos technique

The polynomial chaos (PC) technique was first introduced by Ghanem and Spanos [51] for solving several engineering related problems including FEM. The authors used Hermite polynomials to generate the multi-variate basis, which originates from the work of Wiener [136], who used these polynomials to decompose Gaussian stochastic processes. Contrary to the common physical meaning of chaos as the sensitive dependence of a dynamical system on small changes in its initial conditions [119], the term polynomial chaos refers to the dependence of the polynomial basis on random variables. The method was introduced with the basis generated out of Hermite

polynomials, but is not restricted to them. Xiu and Karniadakis [139] introduced a generalization of the classical PC technique, which uses different types of orthogonal polynomials to generate the basis for the polynomial expansion, allowing for a better convergence for non-Gaussian distributed parameters. For simplicity reasons, the term polynomial chaos (PC) in this thesis stands for the generalised PC technique and estimations of the mean and standard deviation of a probabilistic quantity are denoted by μ and σ .

4.2.1 Generation of the polynomial basis

By incorporating mutually independent probabilistic model parameters X_1, \dots, X_M with known probability density functions (PDFs) $f_{X,1}, \dots, f_{X,M}$ with finite variance in a deterministic mathematical model, the model is recast as a stochastic system resulting in a probabilistic solution Z . Results from Xiu [138] allow to expand the probabilistic quantity Z with finite moments in a series of multi-variate orthogonal polynomials $\psi(\boldsymbol{\xi})$

$$Z = \sum_{i=0}^{\infty} c_i \psi_i(\boldsymbol{\xi}) \quad (4.3)$$

where $\boldsymbol{\xi} = (\xi_1, \dots, \xi_M)$ is a multi-variate random variable with prescribed PDF $f_{\boldsymbol{\xi}}$ and mutually independent components with finite variance. The orthogonality of the multi-variate polynomials $\psi_i(\boldsymbol{\xi})$ is defined by the use of an inner product $\langle \cdot, \cdot \rangle$, which is in the uni-variate case for the uni-variate polynomial $h_i(\xi)$ with degree i given by

$$\langle h_i(\xi), h_j(\xi) \rangle = \int_I h_i(x) h_j(x) w(x) \mathrm{d}x = \gamma_i \delta_{ij} \quad (4.4)$$

where I is the support range of the uni-variate basis polynomial, $w(x)$ the corresponding weight function, γ_i a non-zero constant, and

$$\delta_{ij} = \begin{cases} 1 & i = j \\ 0 & i \neq j \end{cases} \quad (4.5)$$

the Kronecker delta. Regarding the random variable ξ , the expectation of a function $g(\xi)$ is defined by

$$E[g(\xi)] = \int_{-\infty}^{\infty} g(x) f_{\xi}(x) \mathrm{d}x \quad (4.6)$$

where $E[\cdot]$ denotes the mathematical expectation [122]. Observing the inner product equation (4.4) and the mathematical expectation equation (4.6), an optimal set of

Distribution	PDF $f_\xi(x)$	Polynomial	$w(x)$	I
Normal	$\frac{1}{\sqrt{2\pi}} e^{-\frac{x^2}{2}}$	Hermite	$e^{-\frac{x^2}{2}}$	$[-\infty, \infty]$
Uniform	$\frac{1}{2}$	Legendre	1	$[-1, 1]$
Beta	$\frac{(1-x)^\alpha(1+x)^\beta}{2^{\alpha+\beta+1}B(\alpha+1, \beta+1)}$	Jacobi	$(1-x)^\alpha(1+x)^\beta$	$[-1, 1]$
Exponential	e^{-x}	Laguerre	e^{-x}	$[0, \infty]$
Gamma	$\frac{x^\alpha e^{-x}}{\Gamma(\alpha+1)}$	Generalised Laguerre	$x^\alpha e^{-x}$	$[0, \infty]$

Table 4.1: Overview on different standard continuous PDFs $f_\xi(x)$ and the corresponding optimal uni-variate orthogonal basis polynomial including its weight function $w(x)$ and support range I . Since the integral of the PDF $f_\xi(x)$ over its support range is required to be one, the weight function $w(x)$ varies from the PDF by a constant factor. Table taken from Eldred et al. [36].

orthogonal basis functions can be obtained by considering a set of functions, for which the weight function $w(x)$ of the inner product and the support range correspond to the PDFs $f_\xi(x)$ of the random variable ξ (Table 4.1) [138]. In the multi-variate case, the inner product in equation (4.4) becomes a multi-dimensional integral. The requirement on the model parameters X_1, \dots, X_M to be independent allows for a decoupling of the multi-dimensional integrals into the product of one-dimensional integrals and, therefore, into the generation of the multi-variate basis polynomials $\psi(\boldsymbol{\xi})$ out of the product of the uni-variate basis polynomials $h_i(\xi_j)$ and $j = 1, \dots, M$ [36]. To address the one-dimensional degree of each basis polynomial, a multi-index α

$$\alpha = (\alpha_1, \dots, \alpha_M), \quad \alpha_j \in \mathbb{N}_0, \quad j = 1, \dots, M \quad (4.7)$$

is introduced. According to Xiu [138], the multi-variate basis polynomial $\psi_\alpha(\boldsymbol{\xi})$ is then determined by

$$\psi_\alpha(\boldsymbol{\xi}) = \prod_{j=1}^M h_{\alpha_j}(\xi_j) \quad (4.8)$$

with a total degree p

$$p \geq \|\alpha\|_1 = \sum_{j=1}^M |\alpha_j|. \quad (4.9)$$


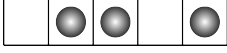
Box sample	α	multi-variate basis polynomial $\psi_\alpha(\boldsymbol{\xi})$
	$(0, 0, 2, 0)$	$h_2(\xi_3)$
	$(1, 0, 1, 0)$	$h_1(\xi_1) \cdot h_1(\xi_3)$

Figure 4.2: Example of generating the multi-index α for a PC with the systematic sequence suggested by Sudret and Der Kiureghian [121]. The number of empty boxes between two neighbouring balls and the exterior boundaries of the box determines the multi-index α and, therefore, the multi-variate basis polynomial $\psi_\alpha(\boldsymbol{\xi})$.

where $\|\alpha\|_1$ is the 1-norm of the multi-index α . The generation of the complete set of multi-variate basis functions of the PC denoted by \mathcal{P}_p^M with the maximal total degree p and dimension M for the random variables ξ_1, \dots, ξ_M can be obtained by generating a sequence of α which covers all possible combinations for the condition in equation (4.9). Based on this condition, the span of \mathcal{P}_p^M is the linear space of all polynomials of maximal degree p in M random variables [138]. Sudret and Der Kiureghian [121] suggested a systematic construction of the sequence of α by solving the problem of distributing $(M - 1)$ balls into $(M + q - 1)$ boxes for each degree $q = 1, \dots, p$. Their suggested algorithm will be described in the following passage.

The equivalence between the distribution of $(M - 1)$ balls into $(M + q - 1)$ boxes and the values of $\alpha = (\alpha_1, \dots, \alpha_M)$ is given by the definition that each value of α_j with $j = 1, \dots, M$ corresponds to the number of empty boxes between two neighbouring balls as well as the exterior boundaries of the box (Fig. 4.2). In addition, only one ball is allowed to be positioned in each box. For a certain degree q with $1 \leq q \leq p$, the sequence of α is generated as follows:

1. Start with $q = 1$.
2. In the initial state, all $(M - 1)$ balls are positioned in the leftmost spaces of the $(M + q - 1)$ boxes, which corresponds to $\alpha = (0, \dots, 0, q)$.
3. The next state is reached by shifting the rightmost ball one space to the right. If this shift is not possible, the next rightmost ball is chosen and shifted one space to the right with all remaining balls right to it positioned in its right neighbouring spaces.
4. If all balls are positioned in the rightmost spaces, q is increased by one. If q is not larger than p , the algorithm continues at step 2 and stops otherwise.

This algorithm prescribes a certain order of the sequence of α resulting in a single index i (Fig. 4.3). The single index i is obtained by introducing the notation $i := \alpha^{(i)}$, which assigns the i -th multi-index $\alpha^{(i)}$ to the single index i . The polynomial basis function $\psi_0(\boldsymbol{\xi})$ is the product of the uni-variate polynomials $h_0(\xi_j)$ of degree zero with

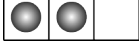
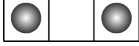
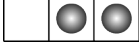
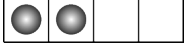

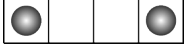
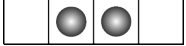


Index i	Box sample	α	multi-variate basis polynomial $\psi_\alpha(\boldsymbol{\xi})$
1		$(0, 0, 1)$	$h_1(\xi_3)$
2		$(0, 1, 0)$	$h_1(\xi_2)$
3		$(1, 0, 0)$	$h_1(\xi_1)$
4		$(0, 0, 2)$	$h_2(\xi_3)$
5		$(0, 1, 1)$	$h_1(\xi_2) \cdot h_1(\xi_3)$
6		$(0, 2, 0)$	$h_2(\xi_2)$
7		$(1, 0, 1)$	$h_1(\xi_1) \cdot h_1(\xi_3)$
8		$(1, 1, 0)$	$h_1(\xi_1) \cdot h_1(\xi_2)$
9		$(2, 0, 0)$	$h_2(\xi_1)$

Figure 4.3: Example of the generation of the sequence of the multi-index α for a dimension of $M = 3$ and a degree of $q = 1$ and $q = 2$. The first three multi-indices are generated for $q = 1$ and the remaining multi-indices for $q = 2$. The algorithm by Sudret and Der Kiureghian [121] results in a unique order of the sequence represented by the single index i .

$j = 1, \dots, M$. Therefore, $\psi_0(\boldsymbol{\xi})$ can be determined to be one. By using the single index i and including the first polynomial basis function $\psi_0(\boldsymbol{\xi}) = 1$, a unique order for the multi-variate basis polynomial $\psi_i(\boldsymbol{\xi})$ in equation (4.3) is defined. According to Xiu [138], for a certain degree p and dimension M , the basis polynomials $\psi_i(\boldsymbol{\xi})$ form a complete orthogonal set of functions denoted by the polynomial basis \mathcal{P}_p^M . The number of basis polynomials P can be determined by

$$P + 1 = \sum_{q=0}^p \binom{M+q-1}{q} = \binom{M+p}{p}. \quad (4.10)$$

In practice, the expansion of the model solution Z in equation (4.3) is truncated for a certain degree p , resulting in an approximation \tilde{Z} of the probabilistic properties of the model solution Z expanded into the polynomial basis \mathcal{P}_p^M :

$$Z \approx \tilde{Z} = \sum_{i=0}^P c_i \psi_i(\boldsymbol{\xi}) \quad (4.11)$$

Following the results of Xiu [138], the approximation of Z in equation (4.11) can be applied to classical approximation theory, resulting in the best approximation \tilde{Z} with the elements of the space \mathcal{P}_p^M . A detailed mathematical description of the application of the PC technique to classical approximation theory would be beyond

the scope of this thesis. A thorough investigation of this topic can be found in Xiu [138] as well as in Malliavin and Thalmaier [80] and Ghanem and Spanos [51].

4.2.2 Numerical evaluation of the expansion coefficients

Practical engineering problems generally result in complex mathematical models for which an analytic solution does not exist or is only available for certain problem cases. Since the computation of the coefficients c_i for $i = 0, 1, \dots, P$ in equation (4.11) is based on the solution of the mathematical model, numerical techniques are required to compute these coefficients. These techniques can be classified into intrusive methods, in which the PC is incorporated into the deterministic code resulting in a probabilistic mathematical formulation of it, as well as into non-intrusive methods, in which the deterministic code remains unchanged [122].

The stochastic Galerkin approach is a common intrusive method, which is based on the Galerkin method to minimize the error by Galerkin projection [138]. By introducing random parameters, the system matrix resulting from Galerkin projection as well as the solution vector become random quantities and are expanded onto a finite-order polynomial chaos expansion [122]. This expansion results in a set of coupled deterministic equations, which can take complicated forms and require additional effort to solve [138]. Therefore, using the stochastic Galerkin approach requires to rewrite an already established code.

Contrary to an intrusive method, a non-intrusive method does not require a change on the deterministic code, but uses it as some kind of a "black-box". The coefficients of the truncated expansion in equation (4.11) are computed either by utilizing interpolation in the stochastic collocation method or integration in the projection method. The collocation method was introduced by Webster et al. [134] and is based on a least square minimization of the discrepancy between the probabilistic parameters X_1, \dots, X_M and their truncated approximations $\tilde{X}_1, \dots, \tilde{X}_M$ on prescribed nodes defined by the probabilistic parameters [122]. These nodes are generally chosen as roots of the used orthogonal polynomial type. The least square minimization leads to a linear system, from which the expansion coefficients can be derived by repetitive execution of the deterministic code [138]. The projection approach, also known as non-intrusive Galerkin projection, projects the truncated model solution \tilde{Z} in equation (4.11) against each polynomial basis function $\psi_i(\boldsymbol{\xi})$ for $i = 0, 1, \dots, P$, using the multi-variate inner product and exploiting the orthogonality of the basis polynomials [36]. Each projection results in a multi-dimensional integral which is evaluated numerically, using multi-dimensional cubature. The deterministic model has to be executed repetitively on the nodes of the chosen multi-dimensional cubature rule, which can be generated using a simple tensor grid approach as well as sparse grid techniques based on the work by Smolyak [118]. Because of the non-intrusive property of the projection approach allowing for the usage of already available finite element tool boxes and the application of multi-dimensional cubature rules, the

non-intrusive projection approach was implemented in this thesis to investigate the influence of uncertainty in the model parameters of a volume conductor model of the human brain on the probabilistic voltage response as well as the VTA, as described in detail in the following section.

4.2.3 Non-intrusive projection approach

In the non-intrusive projection approach of the PC technique, the coefficients c_i of the expanded probabilistic model solution $\tilde{Z}(\boldsymbol{\xi})$ in equation (4.11), which is truncated at a number P of polynomial basis functions $\psi_i(\boldsymbol{\xi})$, are computed by projecting \tilde{Z} against each polynomial basis function $\psi_j(\boldsymbol{\xi})$ for $j = 0, 1, \dots, P$. Using the bilinear property of the inner product in equation (4.4), the projection of \tilde{Z} against each polynomial basis function $\psi_j(\boldsymbol{\xi})$ is given by

$$\begin{aligned} \langle \tilde{Z}(\boldsymbol{\xi}), \psi_j(\boldsymbol{\xi}) \rangle &= \left\langle \sum_{i=0}^P c_i \psi_i(\boldsymbol{\xi}), \psi_j(\boldsymbol{\xi}) \right\rangle \\ &= \langle c_0 \psi_0(\boldsymbol{\xi}), \psi_j(\boldsymbol{\xi}) \rangle + \langle c_1 \psi_1(\boldsymbol{\xi}), \psi_j(\boldsymbol{\xi}) \rangle + \dots + \langle c_P \psi_P(\boldsymbol{\xi}), \psi_j(\boldsymbol{\xi}) \rangle \\ &= c_0 \langle \psi_0(\boldsymbol{\xi}), \psi_j(\boldsymbol{\xi}) \rangle + c_1 \langle \psi_1(\boldsymbol{\xi}), \psi_j(\boldsymbol{\xi}) \rangle + \dots + c_P \langle \psi_P(\boldsymbol{\xi}), \psi_j(\boldsymbol{\xi}) \rangle \\ &= \sum_{i=0}^P c_i \langle \psi_i(\boldsymbol{\xi}), \psi_j(\boldsymbol{\xi}) \rangle . \end{aligned} \tag{4.12}$$

Since the multi-variate polynomial basis functions $\psi_i(\boldsymbol{\xi})$ with the multi-index $\alpha^{(i)} = (\alpha_1^{(i)}, \dots, \alpha_M^{(i)})$ are orthogonal, the application of equation (4.4) and equation (4.8) leads to the inner product of $\psi_i(\boldsymbol{\xi})$ with $\psi_j(\boldsymbol{\xi})$

$$\langle \psi_i(\boldsymbol{\xi}), \psi_j(\boldsymbol{\xi}) \rangle = \gamma_{\alpha_1^{(i)}} \cdots \gamma_{\alpha_P^{(i)}} \delta_{ij} \tag{4.13}$$

for the i -th and j -th multi-variate polynomial basis function. The orthogonal property of the multi-variate polynomial basis function applied to equation (4.12) results in

$$\langle \tilde{Z}(\boldsymbol{\xi}), \psi_j(\boldsymbol{\xi}) \rangle = c_j \langle \psi_j(\boldsymbol{\xi}), \psi_j(\boldsymbol{\xi}) \rangle \tag{4.14}$$

from which the coefficients c_j for $j = 0, 1, \dots, P$ can be determined by

$$c_j = \frac{\langle \tilde{Z}(\boldsymbol{\xi}), \psi_j(\boldsymbol{\xi}) \rangle}{\langle \psi_j(\boldsymbol{\xi}), \psi_j(\boldsymbol{\xi}) \rangle} . \tag{4.15}$$

While the denominator can be evaluated analytically by equation (4.13), the nominator requires further consideration. Since the probabilistic properties of the truncated model solution \tilde{Z} depend on the probabilistic model parameters X_1, \dots, X_M of the

deterministic model, a transformation \mathcal{T}_i has to be defined, which maps the random variables ξ_1, \dots, ξ_M onto the probabilistic parameters X_1, \dots, X_M [77]. This transformation \mathcal{T}_i is expressed by

$$X_i = \mathcal{T}_i(\xi_i) = G_{X_i}^{-1}(F_{\xi_i}(\xi_i)), \quad i = 1, \dots, M \quad (4.16)$$

where G_{X_i} is the cumulative distribution function (CDF) of the probabilistic parameter X_i and F_{ξ_i} is the CDF of the random variable ξ_i . The transformation $\mathcal{T}_i(\xi_i)$ exists if the CDF G_{X_i} of the random parameter X_i is continuous and strictly monotonically increasing. The application of the transformation on the probabilistic parameters X_1, \dots, X_M on the nominator of equation (4.15) results in the expression

$$\begin{aligned} \langle \tilde{Z}(\boldsymbol{\xi}), \psi_j(\boldsymbol{\xi}) \rangle &= \int_{I^M} \tilde{Z}(X_1(x_1), \dots, X_M(x_M)) \cdot \psi_j(x_1, \dots, x_M) \cdot \\ &\quad \cdot w_1(x_1) \cdots w_M(x_M) \, dx_1 \cdots dx_M \end{aligned} \quad (4.17)$$

where I^M is the multi-dimensional support range of the uni-variate basis polynomial functions in Table 4.1 [36]. The computation of the coefficients c_i in equation (4.15) of the truncated expansion of the probabilistic model solution Z requires a numerical evaluation of equation (4.17) by, for example, multi-dimensional cubature. Applying a multi-dimensional cubature, the deterministic mathematical model is required to be repetitively executed to compute the model solution $Z(X_1(t_{1,k}), \dots, X_M(t_{M,k}))$ at the nodes $\mathbf{t}_k = (t_{1,k}, \dots, t_{M,k})$ of the used cubature rule. The described non-intrusive projection approach can be summarised in the following scheme (Fig. 4.4):

1. Transform the probabilistic model parameters X_i on the chosen random variables ξ_i for $i = 1, \dots, M$.
2. Generate the nodes $\mathbf{t}_k = (t_{1,k}, \dots, t_{M,k})$ of the chosen multi-dimensional cubature rule and determine the model parameters $X_i(t_{i,k})$ at these nodes, which results in a list of non-probability samples of the model parameters X_i .
3. Repetitively solve the deterministic mathematical model for each non-probability sample of the model parameters X_i to determine $Z(X_1(t_{1,k}), \dots, X_M(t_{M,k}))$.
4. Compute the coefficients c_j for the generated PC basis up to a total degree p for $j = 0, 1, \dots, P$.
5. Use MCS to apply probability samples of ξ_1, \dots, ξ_M on the truncated expansion of the model solution Z to obtain the probabilistic properties of \tilde{Z} .

Comparing the scheme of the non-intrusive projection approach in Figure 4.4 with common MCS in Figure 4.1, it is evident that the truncated expansion of the model solution Z constitutes a surrogate model of the deterministic mathematical model.

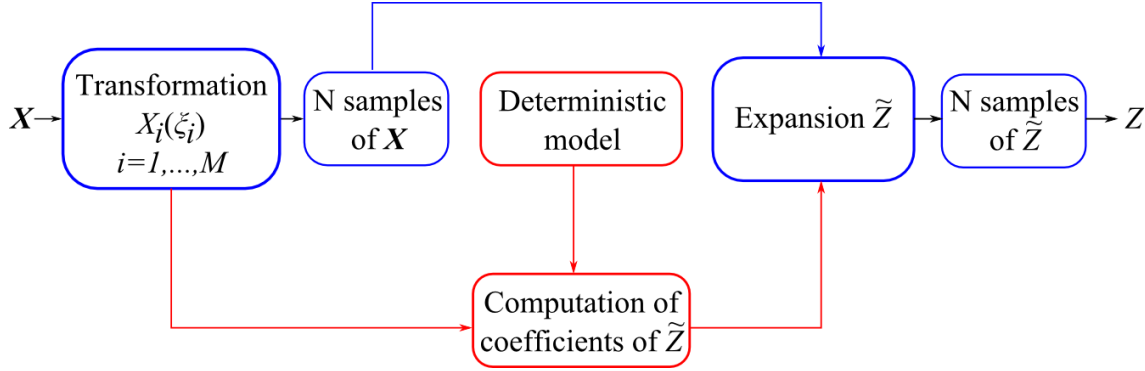


Figure 4.4: Scheme of the non-intrusive projection approach. The deterministic model is used to compute the coefficients of the polynomial approximation of Z on which the probability samples of \mathbf{X} are applied using MCS.

Therefore, the application of probability samples on this model using MCS can be carried out in post-processing, using the non-intrusive projection approach. Depending on the number of probabilistic parameters X_i and the chosen multi-dimensional cubature rule, the number of deterministic model evaluations and, therefore, the computational effort can be much smaller than for MCS [77]. The major advantage of the non-intrusive projection approach relies on using the deterministic model as some kind of a "black-box" by not requiring any adaption of the deterministic code. Furthermore, its mathematical formulation accounts for non-linearities as well [92]. These properties allow for a fast application to various deterministic models and, therefore, makes it an attractive technique for many problem-types in engineering. Although the approach accounts for non-linearities in the mathematical model, the convergence of the probabilistic properties of the expanded model solution Z depends on the smoothness in its functional dependencies on the model parameters X_1, \dots, X_M [138]. Therefore, non-linearities and discontinuities can limit the application of the non-intrusive projection approach.

As described in section 2.4, literature data on the parameters of volume conductor models of the human brain is scarce, which exacerbates the determination of the probabilistic properties of these parameters out of a review of the available literature. In this case, one approach is to determine the upper and lower boundaries of this model parameter and assuming a uniform probability distribution, which accounts for the lack of information on the probabilistic properties of the parameter. To account for the modelling of the probabilistic parameters with restricted intervals, the PC is generated on standard uniformly distributed random variables ξ_1, \dots, ξ_M in the support range $I = [-1, 1]$. An additional advantage of choosing uniformly distributed random variables with a support range in $I = [-1, 1]$ is the application of efficient cubature rules defined on this support range, which will be described in section 4.3. According to table 4.1, the optimal choice of polynomial basis functions

for uniformly distributed random variables are Legendre polynomials. The generation of the series expansion and the generation of the multi-variate polynomial basis functions using Legendre polynomials will be described in detail in the following section.

Series expansion by Legendre polynomials

The mutually independent and standard uniformly distributed random variables ξ_1, \dots, ξ_M for M probabilistic model parameters X_1, \dots, X_M all have the same prescribed PDF

$$f_\xi(x) = \begin{cases} \frac{1}{2} & -1 < x < 1 \\ 0 & \text{else} \end{cases} \quad (4.18)$$

and CDF

$$F_\xi(x) = \begin{cases} 0 & x \leq -1 \\ \frac{x+1}{2} & -1 < x \leq 1 \\ 1 & x > 1 \end{cases} \quad (4.19)$$

in the support range $I = [-1, 1]$. According to equation (4.4) and equation (4.6) as well as Table 4.1, Legendre polynomials are the optimal choice for the generation of the multi-variate polynomial basis \mathcal{P}_p^M , because their weight function $w(x) = 1$ corresponds to the PDF $f_\xi(x) = \frac{1}{2}$ in the same support range $I = [-1, 1]$ except a constant factor. According to Funaro [44], the Legendre polynomials $L_k(x)$ for $k \in \mathbb{N}_0$ are a subset of Jacobi polynomials with $\alpha = \beta = 0$ and can be derived from the differential equation

$$(1 - x^2) \frac{\partial^2 L_k(x)}{\partial x^2} - 2x \frac{\partial L_k(x)}{\partial x} + k(k+1)L_k(x) = 0 \quad (4.20)$$

with the conditions

$$L_k(1) = 1, \quad L_k(-1) = (-1)^k, \quad L_0(x) = 1, \quad L_1(x) = x. \quad (4.21)$$

The Legendre polynomials $L_k(x)$ with degree k can be generated using Bonnet's recursion formula

$$\begin{aligned} L_{k+1}(x) &= \frac{2k+1}{k+1} x L_k(x) - \frac{k}{k+1} L_{k-1}(x) \\ \Rightarrow L_k(x) &= \frac{2k-1}{k} x L_{k-1}(x) - \frac{k-1}{k} L_{k-2}(x), \quad k \geq 2. \end{aligned} \quad (4.22)$$

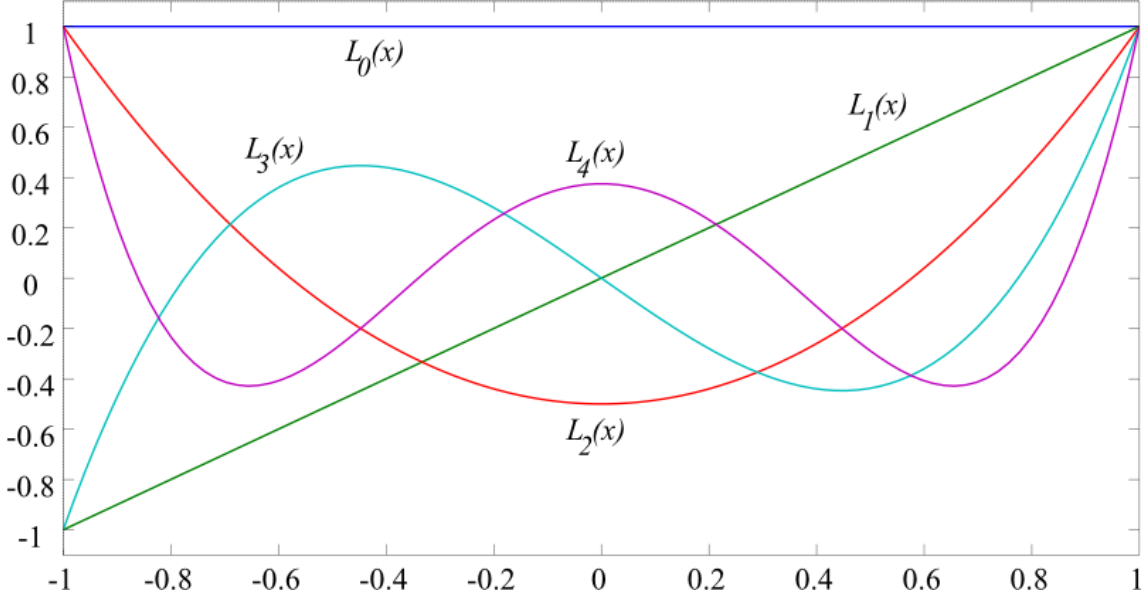


Figure 4.5: Illustration of the first five Legendre polynomials $L_0(x), L_1(x), \dots, L_4(x)$ in the support range $I = [-1, 1]$.

Regarding this formula, the first five Legendre polynomials $L_0(x), L_1(x), \dots, L_4(x)$ in the support range $[-1, 1]$ can be determined to be (Fig. 4.5):

$$\begin{aligned} L_0(x) &= 1, & L_1(x) &= x, & L_2(x) &= \frac{1}{2}(3x^2 - 1), \\ L_3(x) &= \frac{1}{2}(5x^3 - 3x), & L_4(x) &= \frac{1}{8}(35x^4 - 30x^2 + 3) \end{aligned} \quad (4.23)$$

Because of the mutually stochastic independence of the parameters X_1, \dots, X_M , the multi-variate basis polynomials $\psi_i(\boldsymbol{\xi})$ for $i = 0, 1, \dots, P$ for the polynomial basis \mathcal{P}_p^M in equation (4.11) can be generated by the product of the uni-variate Legendre polynomials $L_k(x)$ using equation (4.8). This polynomial basis \mathcal{P}_p^M includes the multi-variate basis polynomials up to a maximal total degree p . Using equation (4.4) and the orthogonality of the Legendre polynomials, the inner product of $L_i(x)$ and $L_j(x)$ is

$$\langle L_i(x), L_j(x) \rangle = \frac{1}{2i+1} \delta_{ij}. \quad (4.24)$$

Therefore, the denominator in the coefficients equation (4.15) can be determined by the multi-variate inner product (4.13) to be

$$\langle \psi_i(\boldsymbol{\xi}), \psi_j(\boldsymbol{\xi}) \rangle = \prod_{k=1}^M \frac{1}{2\alpha_k^{(i)} + 1} \delta_{ij} \quad (4.25)$$

where $\alpha_k^{(i)}$ is the k -th component of the multi-index $\alpha^{(i)}$ for the i -th polynomial basis function $\psi_i(\boldsymbol{\xi})$.

Uniformly and non-uniformly distributed model parameters

As described in section 4.2.3, the chosen random variables ξ_1, \dots, ξ_M with standard uniform distributions $F_{\xi_i}(x) \in \mathcal{U}[-1, 1]$ for $i = 1, \dots, M$ have to be mapped on the probabilistic model parameters X_1, \dots, X_M . If the prescribed CDFs of the model parameter X_i is as well a uniform distribution $G_i(x) \in \mathcal{U}[a_i, b_i]$ with lower and upper boundaries a_i and b_i , the CDF $G_{X_i}(x)$ is

$$G_{X_i}(x) = \begin{cases} 0 & x \leq a_i \\ (x - a_i)(b_i - a_i)^{-1} & a_i < x \leq b_i \\ 1 & x > b_i \end{cases} \quad (4.26)$$

Since the CDF G_{X_i} exists and is strictly monotonically increasing in the support range $I = [a_i, b_i]$, the inverse CDF $G_{X_i}^{-1}$ exists and is

$$G_{X_i}^{-1}(y) = y(b_i - a_i) + a_i \quad (4.27)$$

with $y \in [0, 1]$. Using the equation for the CDF F_{X_i} (4.19) and equation (4.16), the transformation T_i linearly scales the random variable ξ_i and determines the probabilistic model parameter X_i :

$$\begin{aligned} X_i &= G_{X_i}^{-1}(F_{\xi_i}(\xi_i)) = F_{\xi_i}(\xi_i)(b_i - a_i) + a_i = \frac{\xi_i + 1}{2}(b_i - a_i) + a_i \\ &= \frac{b_i - a_i}{2}\xi_i + \frac{b_i + a_i}{2} \end{aligned} \quad (4.28)$$

with $\xi_i \in \mathcal{U}[-1, 1]$ and $X_i \in \mathcal{U}[a_i, b_i]$.

For probabilistic model parameters X_i with a non-uniform distribution, a univariate polynomial expansion of the model parameter X_i on the Legendre polynomials $L_k(x)$ for $k = 0, 1, \dots, P_{in}$ can be used to obtain a truncated approximation \tilde{X}_i :

$$X_i \approx \tilde{X}_i = \sum_{k=0}^{P_{in}} c_k L_k(\xi_i) \quad (4.29)$$

Analogous to equation (4.15), the coefficients c_k can be determined by the projection of equation (4.29) against each basis polynomial $L_k(x)$ for $k = 0, 1, \dots, P_{in}$. Using the transformation (4.16), the equation for the coefficients c_k results in

$$c_k = \frac{1}{\langle L_k, L_k \rangle} \int_{-1}^1 G_{X_i}^{-1}(F_{\xi_i}(x)) L_k(x) \, dx. \quad (4.30)$$

While the denominator of equation (4.30) can be determined by equation (4.24), the computation of the nominator generally requires the application of numerical quadrature [122].

4.3 Multi-dimensional cubature

The computation of the coefficients in equation (4.30) and (4.15) requires the evaluation of one-dimensional and multi-dimensional integrals, respectively. In general, the solution of these integrals cannot be obtained analytically, as mentioned in section 4.2.2. Therefore, the integrals in equation (4.30) and (4.15) require a numerical evaluation by a one-dimensional quadrature or multi-dimensional cubature, which is based on a one-dimensional quadrature rule, respectively. Therefore, the domain $\Omega \subseteq [-1, 1]^M$ comprising the support range $I = [-1, 1]$ of each independent random variable ξ_1, \dots, ξ_M is discretised into a number of nodes $\mathbf{t}_k = (t_{1,k}, \dots, t_{M,k})$ with corresponding weights $w_{1,k}, \dots, w_{M,k}$ derived from the chosen one-dimensional quadrature rule. According to equation (4.17), the model solution Z is computed by executing the deterministic model with the model parameters $X_1(t_{1,k}), \dots, X_M(t_{M,k})$ fixed at the values of the cubature node \mathbf{t}_k . Since the support range of the random variables ξ_1, \dots, ξ_M as well as the Legendre polynomials L_k is $I = [-1, 1]$, all quadrature rules applicable to a restricted support range could be used. Because of the property to generate "nested" quadrature nodes, the Clenshaw-Curtis rule is used as the basic one-dimensional quadrature rule in this thesis.

4.3.1 One-dimensional Clenshaw-Curtis rule

A one-dimensional quadrature rule constitutes a numerical integration method to compute an approximated numerical solution to a definite integral

$$\int_a^b f(x) \, dx \quad (4.31)$$

where the approximated numerical solution is obtained by the one-dimensional quadrature rule $Q_n^{(1)}$:

$$Q_n^{(1)} f = \sum_{k=1}^n f(t_k) w_k \quad (4.32)$$

where n is the number of quadrature nodes t_k and weights w_k [115]. To allow for a reuse of already computed function values $f(t_k)$ at the n quadrature nodes t_k for applying finer grid resolutions (larger number of quadrature nodes) as well as allowing for a fast convergence analysis (smaller number of quadrature nodes) the quadrature nodes of the one-dimensional quadrature rule should be "nested". This property means that for a number of nodes n_{new} with $n_{\text{new}} > n$ or $n_{\text{new}} < n$, the already computed function values $f(t_k)$ at the n quadrature nodes t_k with recomputed weights $w_1, \dots, w_{\text{new}}$ can be reused.

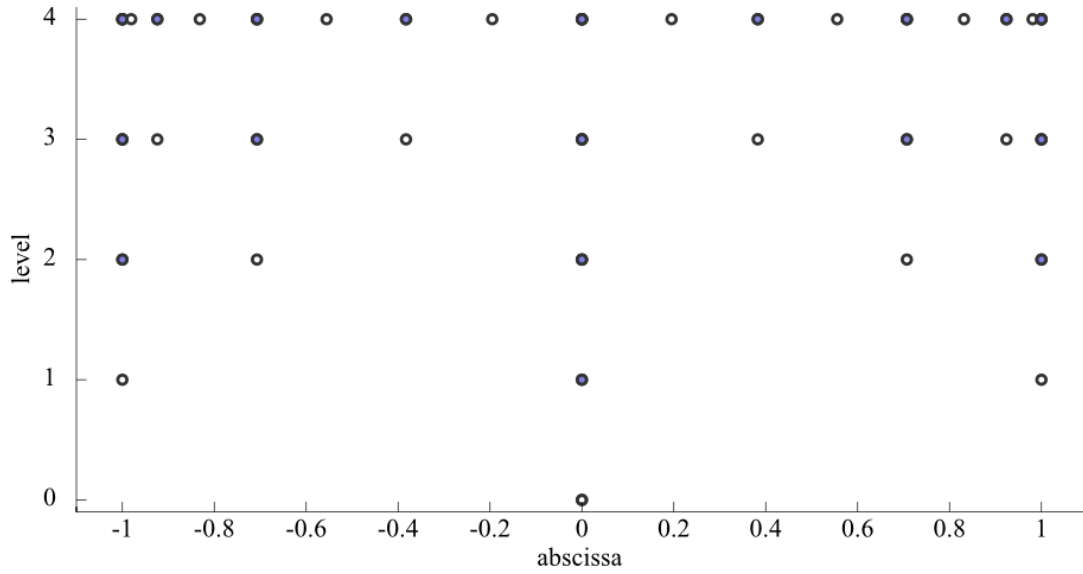


Figure 4.6: Illustration of the nested nodes, i. e. Chebyshev points, of the Clenshaw-Curtis rule for the levels 1 to 4. The reused points of the previous level are shown as solid circles.

This property is fulfilled by the Clenshaw-Curtis rule, if the number of quadrature nodes n corresponds to

$$n := n(l) = \begin{cases} 2^l + 1, & l \in \mathbb{N} \\ 1, & l = 0 \end{cases} \quad (4.33)$$

where l is denoted as the grid level (Fig. 4.6). The nodes of the Clenshaw-Curtis rule are determined by the extrema of the n -th Chebyshev polynomial $C_n(t)$

$$C_n(t) = \cos(n \arccos(t)), \quad t \in [-1, 1] \quad (4.34)$$

at n equidistant points in $[-1, 1]$. According to Trefethen [125], the nodes t_k of the Clenshaw-Curtis rule, with k being the index of the n equidistant points, can be expressed by

$$t_k = \cos\left(\frac{k-1}{n-1}\pi\right), \quad k = 1, \dots, n. \quad (4.35)$$

For a number n of quadrature nodes, as described in equation (4.33), the nodes t_k of the Clenshaw-Curtis rule are nested (Table 4.2). For the implementation of the Clenshaw-Curtis rule, the nodes and weights of the rule were determined by a FFT based on the results of [133]. The Clenshaw-Curtis rule with $n + 1$ nodes exactly integrates polynomials up to a degree n . This is below the optimal degree of $2n + 1$

Level l	Number of nodes n	Clenshaw-Curtis nodes t_k
0	1	0
1	3	$-1, 0, 1$
2	5	$-1, -0.707, 0, 0.707, 1$

Table 4.2: Nodes of the Clenshaw-Curtis rule for different grid levels l . The value of the nodes was rounded to 3-digit accuracy.

as reached with Gaussian quadrature using the roots of the Legendre polynomial $L_{n+1}(x)$. However, following the results of Trefethen [125], the Clenshaw-Curtis rule and Gaussian quadrature can have in practice a similar accuracy for the same number of nodes. In addition, the nodes of the Gaussian quadrature are not nested. The similar convergence behaviour of both methods and the property to generate nested quadrature points makes the Clenshaw-Curtis rule an important technique for efficient multi-dimensional cubature and will be used as basic quadrature rule for the generation of the multi-dimensional cubature rules described in the sections 4.3.2 and 4.3.3.

4.3.2 Multi-dimensional tensor grids

The general procedure of expanding the one-dimensional Clenshaw-Curtis rule onto a multi-dimensional domain is to generate a grid including every possible combination of the one-dimensional nodes for the multi-dimensional cubature, which is also known as a tensor grid. A multi-dimensional cubature $Q_N^{(M)}$ on a tensor grid based on the one-dimensional quadrature $Q_n^{(1)}$ in equation (4.32) can be obtained by forming the tensor product

$$Q_N^{(M)} = Q_n^{(1)} \otimes \cdots \otimes Q_n^{(1)} \quad (4.36)$$

with the number of tensor grid nodes N . The cubature $Q_N^{(M)}$ of a multi-dimensional definite integral of a function $f(\mathbf{x})$ with $\mathbf{X} = (X_1, \dots, X_M)$ is

$$Q_N^{(M)} f = \sum_{k_1}^{n_1} \cdots \sum_{k_M}^{n_M} f(t_{1,k}, \dots, t_{M,k}) w_{1,k} \cdots w_{M,k} \quad (4.37)$$

with the multi-dimensional cubature nodes $\mathbf{t}_k = (t_{1,k}, \dots, t_{M,k})$ and the weights $W_k = w_{1,k} \cdots w_{M,k}$ [36]. The product of the sums in equation (4.37) can be rewritten as

$$Q_N^{(M)} f = \sum_{k_1}^N f(t_{1,k}, \dots, t_{M,k}) w_{1,k} \cdots w_{M,k} . \quad (4.38)$$

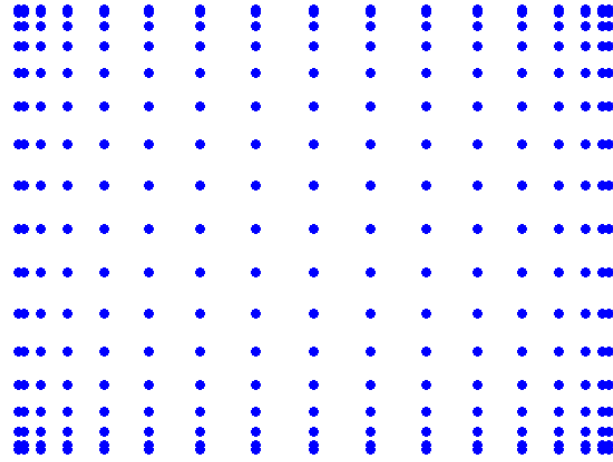


Figure 4.7: Example of a two-dimensional tensor grid with 289 nodes based on the one-dimensional Clenshaw-Curtis rule with $l = 4$ ($n = 17$).

M	1	2	3	4	5	6
$l = 1$	3	9	27	81	243	729
$l = 2$	5	25	125	625	3,125	15,625
$l = 3$	9	81	729	6,561	59,049	531,441
$l = 4$	17	289	4,913	83,521	$\approx 1.4 \cdot 10^6$	$\approx 24 \cdot 10^6$

Table 4.3: Nodes of multi-dimensional tensor grids depending on the level l of the one-dimensional Clenshaw-Curtis rule.

If each one-dimensional quadrature rule has the same number n of quadrature nodes, the number of cubature nodes is $N = n^M$ (Fig. 4.7). Using equation (4.38), the numerical evaluation of the nominator equation (4.17) of the coefficients c_k of the polynomial expansion of the model solution Z can be obtained by

$$\langle Z(\boldsymbol{\xi}), \psi_j(\boldsymbol{\xi}) \rangle \approx \sum_k^{n^M} Z(X_1(t_{1,k}), \dots, X_M(t_{M,k})) \cdot \psi_j(\mathbf{t}_k) \cdot W_k. \quad (4.39)$$

According to Table 4.1, the weight function of Legendre polynomials $L_k(x)$ is one and, therefore, has not to be considered in equation (4.39). Despite the easy implementation of the tensor grid cubature for the computation of the coefficients c_k in equation (4.15), it has one major disadvantage. Since the number of cubature nodes N and, therefore, the number of required executions of the mathematical deterministic model grows exponentially with the number M of multi-variate parameters, it is only efficiently applicable for a small number M of multi-variate parameters X_1, \dots, X_M . (Table 4.3). This phenomenon is also known as the "curse of dimensionality" and

was introduced by Bellman [12].

4.3.3 Multi-dimensional sparse grids

The efficient computation of the coefficients of the polynomial approximation of the quantity Z using tensor grids is limited by the "curse of dimensionality". As described in section 4.2.1, the model parameters X_1, \dots, X_M are mutually independent. Therefore, assuming that each model parameter X_i can be represented by polynomials of a maximal degree p , only multi-variate polynomial basis functions with a maximal total degree p are required to represent the model parameters X_1, \dots, X_M . However, the cubature nodes of a tensor grid cover all basis polynomials with a maximal degree p in each variable, resulting in a maximal total degree p^M of the multi-variate polynomial basis, which includes a large amount of "unneeded" cubature nodes. Here it is the idea to use only these cubature nodes that are required for an exact integration of the polynomial basis functions.

Sparse grids were introduced by Smolyak [118] and are based on a sparse combination of tensor products which only consider a subset of the tensor grid nodes. The description of the sparse grid generation in this section follows the results of Nobile et al. [93], which are adapted to the previously used notations for multi-indices and quadrature rules.

The sparse combination of the tensor products for a level L and a number M of mutually independent probabilistic parameters X_i is determined from the Smolyak equation $S(L, M)$

$$S(L, M) = \sum_{j=1}^{N_S} (\Delta_{\beta_1^{(j)}} \otimes \dots \otimes \Delta_{\beta_M^{(j)}}) \quad (4.40)$$

where N_S is the number of combined tensor products comprising the difference operator $\Delta_{l,i}$ for $i = 1, \dots, M$. This difference operator subtracts the one-dimensional quadrature rule $Q_{n(l)}^{(1)}$ of level $l - 1$ from that of level l :

$$\Delta_l := Q_{n(l)}^{(1)} - Q_{n(l-1)}^{(1)} \quad (4.41)$$

Similar to the multi-index α in equation (4.7), which represented the degree α_i of the multi-variate polynomial basis function $\psi(\boldsymbol{\xi})$ in each random variable $\boldsymbol{\xi} = (\xi_1, \dots, \xi_M)$ with $\|\alpha\|_1 \leq p$, the multi-index β

$$\beta = (\beta_1, \dots, \beta_M), \quad \beta_i \in \mathbb{N}_0, \quad i = 1, \dots, M \quad (4.42)$$

with

$$\|\beta\|_1 = \sum_{i=1}^M |\beta_i| \leq L \quad (4.43)$$

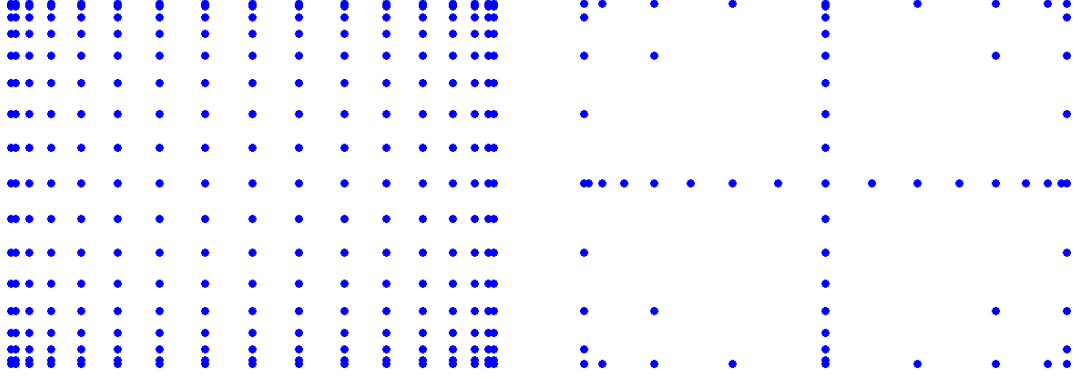


Figure 4.8: Comparison of a two-dimensional level 4 tensor grid with 289 nodes (left) and a two-dimensional level 4 sparse grid $S(4,2)$ with 65 nodes (right) based on the one-dimensional Clenshaw-Curtis rule with $l = 4$ ($n = 17$).

M	1	2	3	4	5	6
$L = 1$	3	5	7	9	11	13
$L = 2$	5	13	25	41	61	85
$L = 3$	9	29	69	137	241	389
$L = 4$	17	65	177	401	801	1,457

Table 4.4: Nodes of multi-dimensional sparse grids depending on the level L and the dimension M for using a nested quadrature rule.

represents the corresponding grid level $\beta_i^{(j)}$ of the j -th tensor grid in equation (4.40) in each random variable ξ_1, \dots, ξ_M . From the similarity of the multi-index α with the multi-index β it is evident that the Smolyak sparse grids constitute an optimal choice for the numerical cubature on polynomial expansions in the polynomial basis \mathcal{P}_p^M . To avoid the computation of the difference operator, Nobile et al. [93] specified a rewritten but mathematically identical version of the Smolyak equation (4.40):

$$S(L, M) = \sum_{j=1}^{\tilde{N}_S} (-1)^{H(L, M, \tilde{\beta}^{(j)})} \binom{M-1}{H(L, M, \tilde{\beta}^{(j)})} \left(Q_{n(\tilde{\beta}_1^{(j)})}^{(1)} \otimes \dots \otimes Q_{n(\tilde{\beta}_M^{(j)})}^{(1)} \right) \quad (4.44)$$

where the function H is given by

$$H(L, M, \tilde{\beta}^{(j)}) = L + M - \|\tilde{\beta}^{(j)}\|_1 \quad (4.45)$$

and the modified multi-index $\tilde{\beta}$ is determined by the condition

$$L - M + 1 \leq \|\tilde{\beta}\|_1 \leq L. \quad (4.46)$$

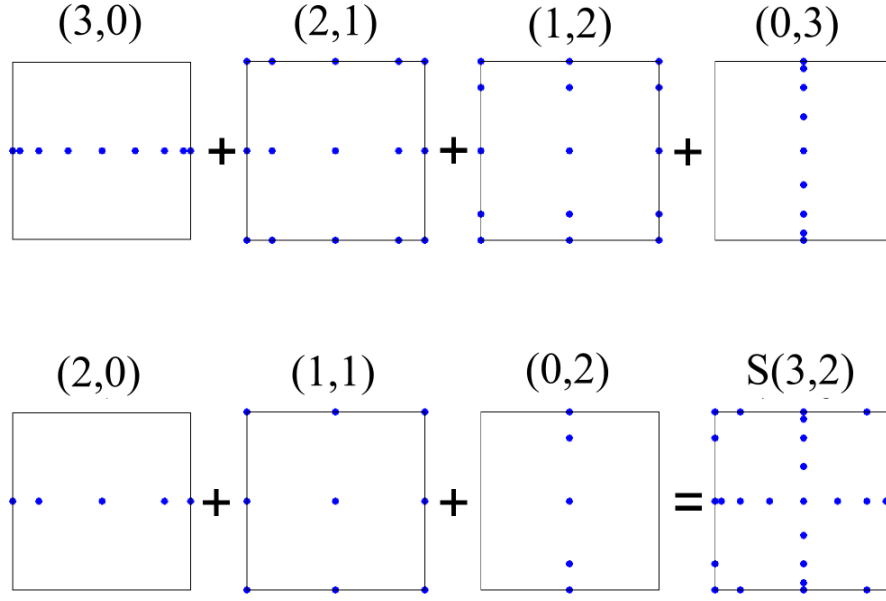


Figure 4.9: Example of the generation of the nodes of a level $L = 3$ and dimension $M = 2$ Smolyak sparse grid $S(3, 2)$ by combination of the sparse tensor products denoted by $(\beta_1^{(j)}, \beta_2^{(j)})$ for $j = 1, \dots, N_{\tilde{S}}$.

Due to different conditions of the multi-index β and the modified multi-index $\tilde{\beta}$, the number of tensor products N_S and \tilde{N}_S of the corresponding Smolyak equations (4.40) and (4.44) are not equal. Besides using only a combination of tensor products, which corresponds to the chosen polynomial basis \mathcal{P}_p^M , the major advantage of the sparse Smolyak grids originates from using a one-dimensional quadrature rule with nested quadrature points, such as the Clenshaw-Curtis-rule described in 4.3.1. In this case, certain nodes occur multiple times when applying the rule to the Smolyak equation (4.44), which requires only to recompute the corresponding weights, but no additional nodes have to be added to the sparse grid. These two properties of the sparse Smolyak grid substantially reduce the number of cubature nodes compared to a corresponding tensor grid (Fig. 4.8). The fraction of "saved" nodes to the total number of nodes in the tensor grid increases with growing level L and dimension M of the sparse Smolyak grid $S(L, M)$, which reduces the "curse of dimensionality" occurring for tensor grids (Table 4.4). The algorithm for the generation of these sparse grids can be described by the following steps (Fig. 4.9):

1. Generate the multi-index sequence $\tilde{\beta}^{(i)}$ with the condition (4.46) based on the algorithm for the generation of the multi-index sequence $\alpha^{(i)}$ of the multi-

dimensional orthogonal basis functions $\psi_i(\boldsymbol{\xi})$ described in section 4.2.1.

2. Compute the nodes \mathbf{t}_k and the weights W_k of the tensor products of the one-dimensional quadrature rule based on the indices $\tilde{\beta}_j^{(i)}$ for $j = 1, \dots, M$.
3. Assemble the nodes \mathbf{t}_k and weights W_k of the tensor products by using the Smolyak equation (4.44).
4. Solve the nominator equation (4.39) for the $N_{\tilde{\mathbf{g}}}$ cubature nodes of the sparse Smolyak grid $S(L, M)$.

The application of sparse grids is based on a quadrature rule with nested nodes and allows for a computationally inexpensive investigation of the convergence in post-processing, because the sparse grid $S(L, M)$ contains the nodes of the sparse grids $S(1, M)$ to $S(L - 1, M)$. Every sparse grid including the nodes for M parameters X_1, \dots, X_M contains the nodes for each uni-variate parameter X_i as well. This property allows for the investigation of the influence of uncertainty on the model solution for a subset of these parameters, using the already computed solutions. Therefore, a sensitivity analysis for each parameter and the combination of them requires only the model solutions at the nodes of the $S(L, M)$ sparse grid.

4.4 Implementation aspects

The PC technique as well as the multi-dimensional cubature based on tensor and sparse Smolyak grids was implemented using MATLAB®, which allowed for the application of certain already implemented code fragments. Since the advantage of the non-intrusive projection approach is its application to various mathematical deterministic models describing different engineering problems by using these models as some kind of a "black-box", the aim was to allow for an easy and fast change of the deterministic code. Therefore, several functions for the different parts of the non-intrusive projection approach, which are, among others, the basis generation, the polynomial evaluation, and the cubature grid generation, were implemented and summarised in a MATLAB® library called QUNIPALM (Quantifying Uncertainties using a Non-Intrusive Projection Approach Library for Matlab). The generation of the Clenshaw-Curtis rule by using FFT was adapted from the results of Waldvogel [133] and the Matlab implementation of von Winckel [131]. The implementation of the algorithm for generating the multi-index sequence in equation (4.7) was adapted from the results of Sudret et al. [122] and the implemented algorithm of Sudret, B and Der Kiureghian, A [123].

The implementation of the non-intrusive projection approach can be categorised in a pre-processing, a deterministic model computation, and a post-processing stage (Fig. 4.10). The pre-processing is carried out in MATLAB® and comprises the

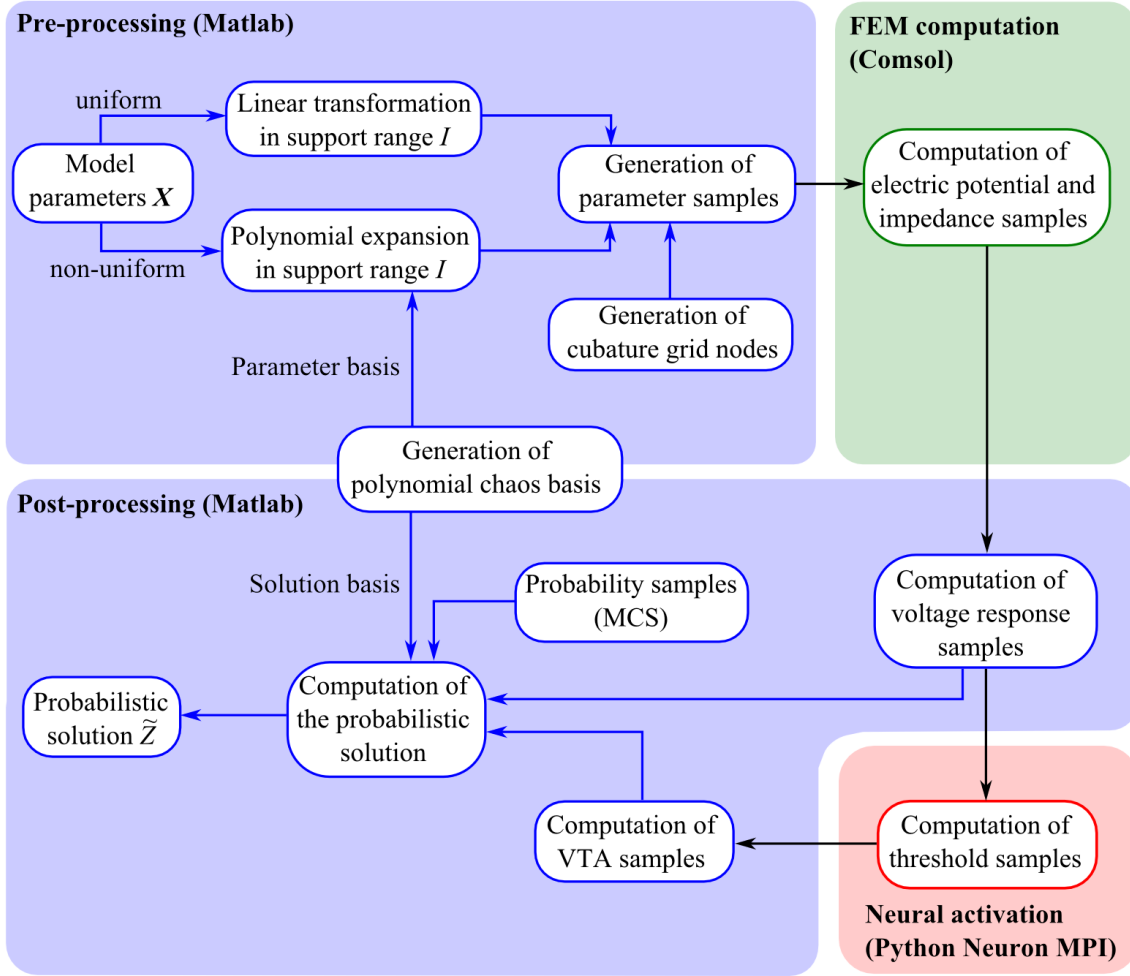


Figure 4.10: Flowchart of the implementation of the non-intrusive projection approach. The scheme is divided into pre-processing and post-processing stage with MATLAB® (blue) as well as the computation of the deterministic model with Cmsol Multiphysics™ (green) and the NEURON library for Python with MPI (red).

transformation of the model parameters \mathbf{X} in the support range I of the chosen polynomial basis, which is in case of Legendre polynomials the support range $I = [-1, 1]$. This transformation is obtained by applying a linear transformation for uniformly distributed model parameters and a polynomial expansion for non-uniformly distributed model parameters. Based on the chosen cubature grid, which can consist of a multi-dimensional tensor grid or a multi-dimensional sparse grid of a certain level L , the parameter samples for the deterministic model are computed. The time-dependent voltage response is computed for the model parameter samples, including the solution of the volume conductor model with Cmsol Multiphysics™ and the post-processing with MATLAB®. For the computation of the VTA samples,

these time-dependent voltage response samples are used as parameters for the computation of the neural activation with the NEURON library for Python with MPI. The post-processing in MATLAB® comprises the generation of the probability samples using MCS and the polynomial expansion of the probabilistic time-dependent voltage response and VTA, based on the computed samples.

5 Results and discussion

This chapter comprises the results from own publications and additional studies carried out in this thesis. Since an accurate computation of the distribution of the electric potential and of the impedance of the volume conductor model of the human brain described in section 3.5 is essential for the further studies, the mesh properties of the volume conductor model as well as the solver accuracy are investigated. The EQS formulation derived from Maxwell’s equations in section 3.1.1 is justified for the generated human brain model and the proposed method for the fast computation of the time-dependent voltage response is validated. To benefit from the computational advantage of FFEMEC over FFEM, a best single frequency approximation of the dispersive human brain model is determined. This approximated brain model is further used to carry out advanced computational studies, which comprise the investigation of the influence of anisotropic conductivity, the electrode position, and uncertainty in several model parameters on the time-dependent voltage response in the proximity of the stimulated target and the resulting VTA. Based on the obtained results, recommendations on the complexity and uncertainty in the parameters of volume conductor models of the human brain for the simulation of DBS are derived.

5.1 Discretisation and solver aspects of the volume conductor model

The computation of the time-dependent voltage response in the generated volume conductor model of the human brain described in section 3.5 is carried out by solving the discretised EQS formulation in equation (3.24) by FFEMEC described in section 3.3. The generation of the finite element mesh plays a crucial role in the accurate approximation of the EQS solution in the volume conductor model by FEM. Especially in areas with large field gradients, a finer mesh is necessary to ensure an accurate solution. Therefore, the required size of the ROI (Fig. 3.15), which ensures a fine mesh in the proximity of the stimulated target, as well as the element size in this region and at the electrode contacts were determined by computing the sensitivity of the computed voltage distribution and total current in the volume conductor model on a set of values of these parameters.

5.1.1 Discretisation of the volume conductor model

Each of these parameter studies to obtain a robust and sufficiently refined mesh were performed using the EQS formulation in equation (3.24) at a frequency of 1 kHz. The electrode was operated in bipolar electrode configuration by setting a potential of 1 V at the second electrode contact and using the first electrode contact as ground (Fig. 2.3). The resulting FEM formulation with quadratically shaped basis functions was generated and solved with the finite element toolbox Comsol Multiphysics™, using the generalized minimal residual method (GMRES) with a geometric multigrid preconditioner with a relative tolerance of $1 \cdot 10^{-6}$ if not mentioned otherwise.

The accuracy of the computation of the total current \underline{I} in the volume conductor model is an important factor of FFEMEC, since the equivalent circuit components necessary for the computation of the time-dependent voltage response with this method are derived from the total current \underline{I} as described in section 3.3.2. The total current \underline{I} of the volume conductor model is computed with the finite element toolbox Comsol Multiphysics™, using the reaction force operator `reacf()`. According to the documentation of Comsol Multiphysics™, this operator allows for an accurate computation of the current flow with FEM. To investigate the influence of the mesh resolution at the electrode contacts of the incorporated Medtronic Mo. 3387 electrode in the volume conductor model of the human brain on the computed total current \underline{I} , the mesh density at the electrode contacts is manually refined by controlling the maximum element size of the triangular mesh at these surfaces. Since each electrode contact has a height of 1.5 mm, the initial maximum element size was set to 0.8 mm and was divided into halves in five parametric steps, resulting in a final value of 0.05 mm. A further refinement of the maximum element size at these surfaces was limited by the automatic meshing algorithm of Comsol Multiphysics™. To ensure a robust mesh, the maximum element size at the insulation of the electrode was set at most to the double value of the maximum element size at the electrode contacts. The maximum element size of the ROI with an edge length of 19 mm and the remaining computational domain was set to 0.5 mm and 5 mm, respectively. The deviation in the resulting total current \underline{I} was determined by computing the relative error of its absolute value and phase angle between the (k) -th and $(k - 1)$ -th refinement step (*a posteriori*). The results showed a decrease of this deviation with decreasing maximum element size (Fig. 5.1), resulting in an asymptotic convergence with an order of $q \approx 2$ in dependence of the degrees of freedom, which is approximately the order of the quadratic basis functions. Theoretical considerations on the error analysis of the potential energy functional for adaptive mesh refinement suggests a convergence order close to the maximum order of the chosen basis functions [3]. However, this is only an evidence for the observed convergence order, because the convergence order of the total current \underline{I} was investigated instead. The final maximum element size at the electrode contacts was set to 0.1 mm, resulting in a relative error of the absolute value and phase of the total current \underline{I} of approximately 0.02 % and

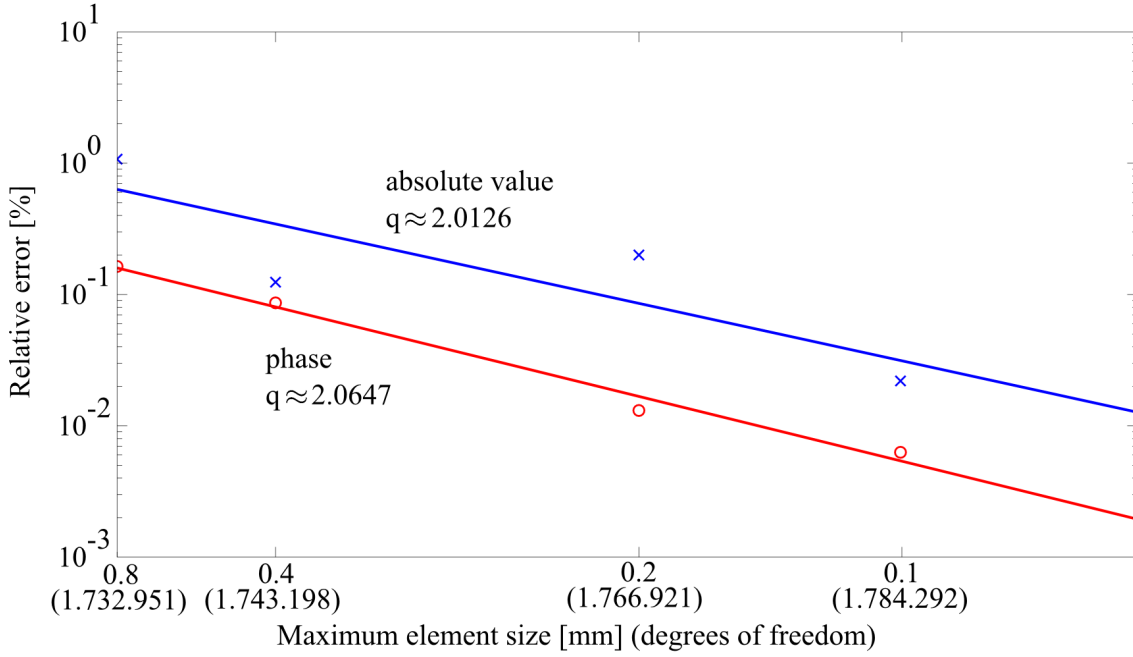


Figure 5.1: Relative error of the absolute value (blue) and phase (red) of the total current \underline{I} in the volume conductor model of the human brain, depending on the degrees of freedom (ndof) at the chosen maximum element size at the surface of the electrode contacts. The relative error is successively determined between the (k) -th and $(k - 1)$ -th refinement step up to a maximum element size of 0.05 mm.

0.01 % with respect to the values obtained for a maximum element size of 0.05 mm.

The voltage distribution in the proximity of the stimulated target is a crucial factor for the computation of the time-dependent voltage response and VTA. The accuracy of the voltage distribution is mainly influenced by the size of the ROI, which has a refined mesh resolution compared to the rest of the human brain model. Therefore, the influence of the size of the ROI on the accuracy of the computed voltage distribution was investigated in a parameter study. The influence was quantified by computing the maximum deviation of the voltage distribution in the ROI between the human brain model and a partially heterogeneous brain model, where the segmented tissue data of the digital brain atlas were only incorporated into the ROI, while the rest of the tissue was assumed to consist of white matter. The deviation between the resulting voltage distributions in both cases was computed for an edge length of the ROI between 10 mm and 40 mm with a step size of 1 mm. According to the results illustrated in Fig. 5.1, the maximum element size at the surface of the electrode contacts and at the surface of the electrode insulation inside and outside the ROI was set to 0.1 mm, 0.2 mm, and 0.3 mm, respectively. A maximum deviation of the voltage distributions was found to be below 1 % for an edge length of the ROI

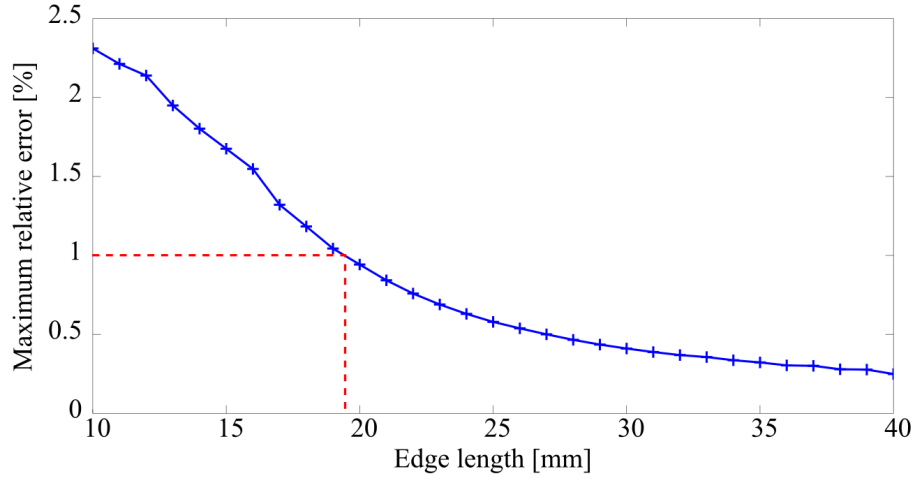


Figure 5.2: Maximum relative error between the voltage distribution of the partially and fully heterogeneous brain model, depending on the edge length of the ROI.

above 19 mm (Fig. 5.2). Therefore, this result allows for a computation of the time-dependent voltage response for a bipolar electrode setup, using a reduced segmented tissue data set, which covers the heterogeneous tissue properties in the proximity of the stimulated target area. However, for a unipolar electrode setup the deviation of the electric potential and the impedance between the reduced heterogeneous volume conductor model and the completely heterogeneous volume conductor model was determined to be about 4.7 % and up to 9.2 %, respectively, which suggests that for a unipolar electrode setup a full incorporation of the segmented MRI data into the volume conductor model is necessary to obtain a precise time-dependent voltage response.

The major motivation for the incorporation of a ROI around the stimulated target area with a refined mesh resolution was to reduce discontinuities at tissue boundaries occurring by the mapping of the hexahedral data mesh with a resolution of 1 mm in each spatial dimension on the tetrahedral finite element mesh of the volume conductor model. Therefore, the maximal element length inside the ROI was reduced to 0.5 mm, which is half the length of the isotropic data voxels. The investigation of the mesh conformity for the values of the FA, which is a marker for the anisotropy as described in section 3.4, at each node of the tetrahedral mesh of the volume conductor model showed a good agreement with the hexahedral mesh of the digital brain atlas data (Fig. 5.3). The final mesh was generated according to the results of the realised parametric studies and resulted in a number of mesh elements of approximately $1.3 \cdot 10^6$ with approximately $1.7 \cdot 10^6$ degrees of freedom for the application of quadratically shaped basis functions.

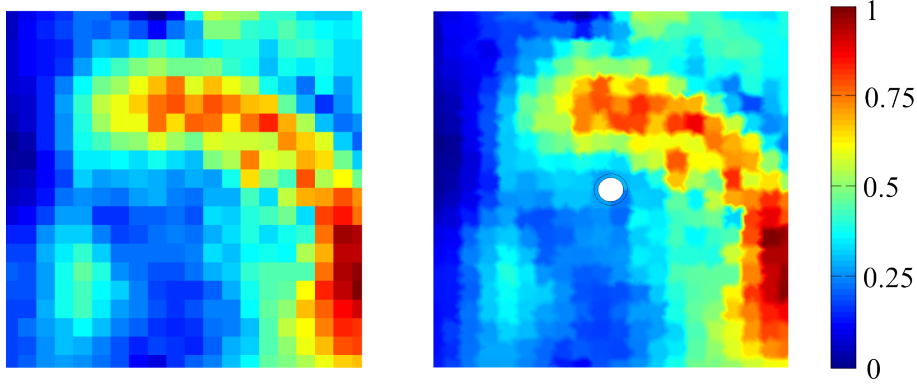


Figure 5.3: Fractional anisotropy (FA) computed for an axial section of the DTI hexahedral data from the SRI24 multi-channel brain atlas (left) and for an axial section of the tetrahedral mesh of the brain model with the DBS electrode (right).

5.1.2 Numerical solver considerations

Instead of computing a direct solution for the obtained degrees of freedom using a memory-intensive direct solver, iterative solvers such as conjugate gradient method (CG) and GMRES compute a sequence of approximate solutions for a given relative tolerance. Using GMRES, which is implemented in Comsol MultiphysicsTM, with a relative tolerance of $1 \cdot 10^{-6}$ and a geometric multigrid preconditioner, a solution of the system matrices was obtained in about 3 minutes on a workstation with 4×3.6 GHz processors with a memory consumption of approximately 7 GB for approximately 1.7 million degrees of freedom. Since the EQS formulation results in a symmetric and complex-valued system matrix, as described in section 3.2.1, CG is not applicable and other methods such as conjugate orthogonal conjugate gradient method (COCG) and Biconjugate gradient stabilized method (BiCGSTAB) should be applied [30, 127]. From these methods, BiCGSTAB is implemented in Comsol MultiphysicsTM. In comparison with GMRES, the solution with the same relative tolerance was obtained with BiCGSTAB in approximately 3 minutes and 30 seconds. In general, both methods are appropriate for the solution of the system matrix, but the convergence of BiCGSTAB may stagnate [127], which was noticed in parametric sweeps of the electrical properties of brain tissue. In the numerical studies carried out in this thesis, GMRES showed a more stable convergence. Despite the larger memory consumption of GMRES compared to BiCGSTAB [127], GMRES was favoured, since a stable convergence was required for the sensitivity analyses carried out. Solving the system matrices using a direct solver in Comsol MultiphysicsTM, e.g. multifrontal massively parallel sparse direct solver (MUMPS), as for the two-dimensional and circular-symmetric saline cylinder model described in section 5.2.2 resulted in a memory consumption of approximately 69 GB and a solution time of 1 hour and 30 minutes on the same workstation. Comparing the computation

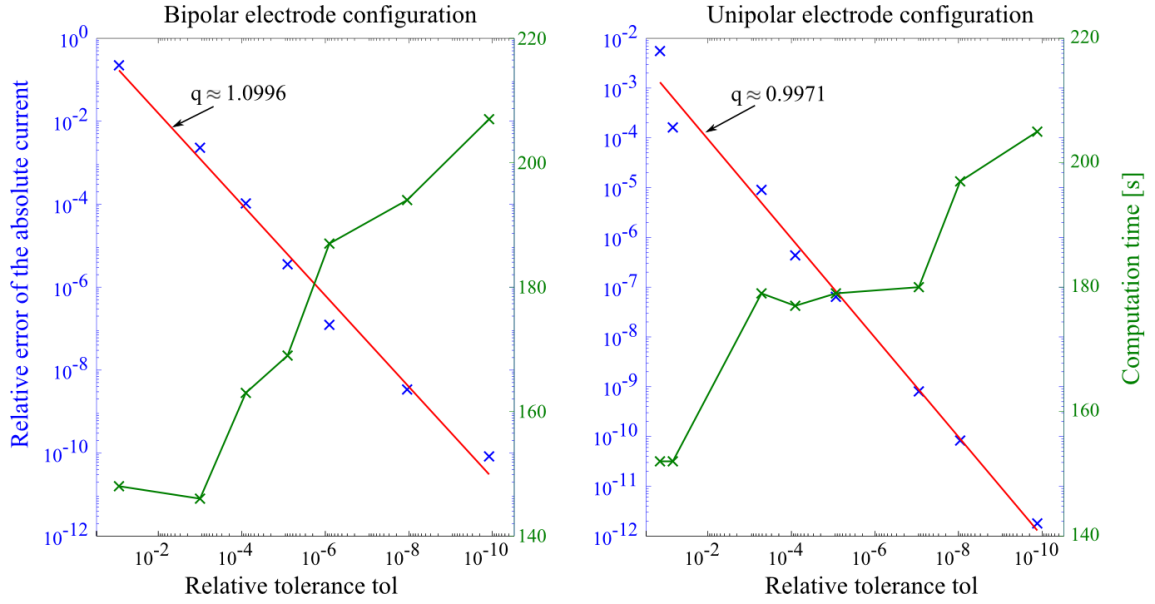


Figure 5.4: Relative error of the absolute value of the total current \underline{I} of the volume conductor model (blue) in dependence of the relative tolerance `tol` of the iterative solver GMRES as well as the corresponding computation time (green) on a workstation with 4×3.6 GHz processors. The relative error was computed *a posteriori*, i.e. between the actual and the following refinement step. The red curve shows the linear fit of the relative error with a convergence tol^q with $q \approx 1.0997$ for bipolar electrode configuration and $q \approx 0.9971$ for unipolar electrode configuration.

time and memory consumption of the direct solver with GMRES, it is evident that a direct solver is no longer efficiently applicable for such problem sizes. However, it has to be ensured that the chosen iterative solver converges for a given initial approximation. Therefore, the influence of the relative tolerance of the iterative solver on the computed total current \underline{I} of the volume conductor model for bipolar as well as unipolar electrode configuration was investigated by computing its *a posteriori* relative error. Applying a linear fit to the relative error of the absolute value of the total current $|\underline{I}|$ in dependence of the relative tolerance `tol` of the GMRES shows a convergence behaviour of tol^q of the relative error with $q \approx 1.0997$ for bipolar electrode configuration and $q \approx 0.9971$ for unipolar electrode configuration, which, in both cases, corresponds to an asymptotic convergence of approximately $\mathcal{O}(\text{tol})$. The results suggest that a relative tolerance of the GMRES solver of $1 \cdot 10^{-6}$ is sufficient to ensure a relative error in the computed total current \underline{I} of approximately $1 \cdot 10^{-5} \%$ (Fig. 5.4).

5.2 Fast computation of the time-dependent voltage response

The fast computation of the time-dependent voltage response with FFEMEC as proposed in section 3.3 is based on several assumptions, such as the EQS formulation of Maxwell's equations and the validity of the representation of the volume conductor model by equivalent circuits, which have to be verified. In this section, the results from several studies aiming for the validation of the EQS formulation in human brain models and the proposed method for the fast computation of the time-dependent voltage response are presented. Since FFEMEC is only computationally superior to FFEM for frequency-independent material properties, a best single frequency approximation of the dispersive human brain model is determined for voltage-controlled and current-controlled stimulation by comparing the time-dependent voltage response and neural activation for a single frequency approximation of the human brain model with those for a dispersive human brain model over a wide range of frequencies. The computation of the volume conductor model is carried out using quadratically shaped finite elements and the mesh parameters obtained in section 5.1.

5.2.1 Validity of the electro-quasistatic equation

In section 3.1.1 the simplifications of Maxwell's equations for bio-electrical applications were determined to be the propagation effect (3.19), the inductive effect (3.20), and the capacitive effect (3.22), which are based on the work of Plonsey and Heppner [100]. These simplifications further lead to the EQS and QS formulation in the equations (3.24) and (3.25), respectively, which depend on the conductivity κ and the relative permittivity ε_r of biological tissue at a certain angular frequency ω , and the spatial dimension r of the model. Since these parameters change for every specific volume conductor model, the validity of neglecting of these effects has to be verified. As described in section 3.1.2, the electrical properties of biological tissue are frequency-dependent. In addition, DBS pulses used in clinical practise are square-wave shaped (Fig. 2.4) and consist of harmonic frequencies in the range of Hz to several kHz [17]. Therefore, the conditions for the use of the EQS and QS formulation have to be investigated not only for a single frequency, but also a range of frequencies. In general, the brain tissue, especially in deep brain areas which constitute the targets for DBS, consists of gray and white matter. In addition, several parts, such as the ventricles, are filled with cerebrospinal fluid. Since the electrical properties of cerebrospinal fluid show a comparatively small frequency-dependence (Fig. 3.2), the investigation of a possible neglecting of the effects characterised by the equations (3.19), (3.20), and (3.22) is carried out for gray and white matter only.

The diameter of the stimulated target STN varies within the mm range and is determined to be approximately 10 – 13 mm [75]. To ensure a precise computation of

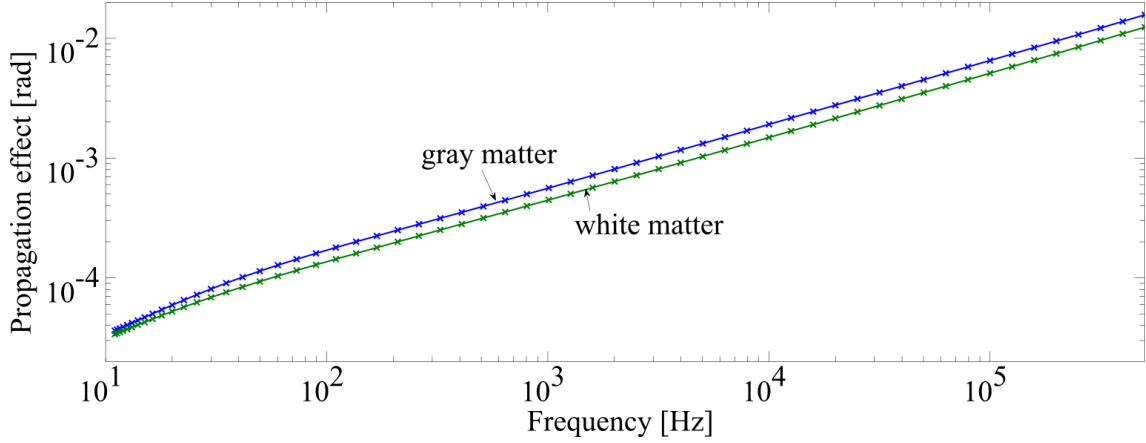


Figure 5.5: Propagation effect $\frac{\omega r}{c}$ for a spatial dimension of $r = 0.04$ m and a frequency range of 10 Hz to 500 kHz considering the electrical properties of gray and white matter.

the voltage distribution in the proximity of the stimulated target by using the EQS and QS formulation, the limit of the spatial dimension r , in which the neglect of the effects is investigated, is set to 4 cm, which is substantially larger than the STN diameter. The power spectrum X_k of the DBS pulses in the kHz range is small compared to that in the low frequency range (Fig. 3.8). However, to get an estimate of the worst case, frequencies from 10 Hz up to 500 kHz were used to investigate the influence of the effects. Considering this frequency range, the maximal propagation effect in the proximity of the stimulated target composed of gray and white matter is approximately $2 \cdot 10^{-4}$ rad at the frequency component of 130 Hz and approximately $2 \cdot 10^{-2}$ rad for the frequency component of 500 kHz of the DBS pulse, and therefore regarded to be negligible (Fig. 5.5). Since the inductive effect (3.20) is the square of the propagation effect (3.19), it is also negligible considering the used parameters.

The capacitive effect in equation (3.22) plays a crucial role in the modelling of bio-electrical applications, because the neglect of this condition determines whether a real-valued QS formulation or a complex-valued EQS formulation is applicable. Considering the same frequency range from 10 Hz to 500 kHz and the electrical properties of gray and white matter, the capacitive effect (3.22) suggests that an EQS formulation would be appropriate, especially for low frequency components between 10 Hz and approximately 110 Hz. The capacitive effect had a maximal value of approximately 0.87 for 14 Hz (Fig. 5.6). Common DBS pulses used in clinical practise have a stimulation frequency of 130 – 180 Hz, which could in certain cases allow for a neglect of the capacitive effect and, therefore, the use of the QS formulation by only considering purely resistive tissue properties. Nevertheless, the capacitive effect is shown to be the "weakest" condition of the mentioned simplifications of Maxwell's equations for bio-electrical models of the brain. Therefore, the application of the EQS formulation was preferred in the studies carried out in this thesis.

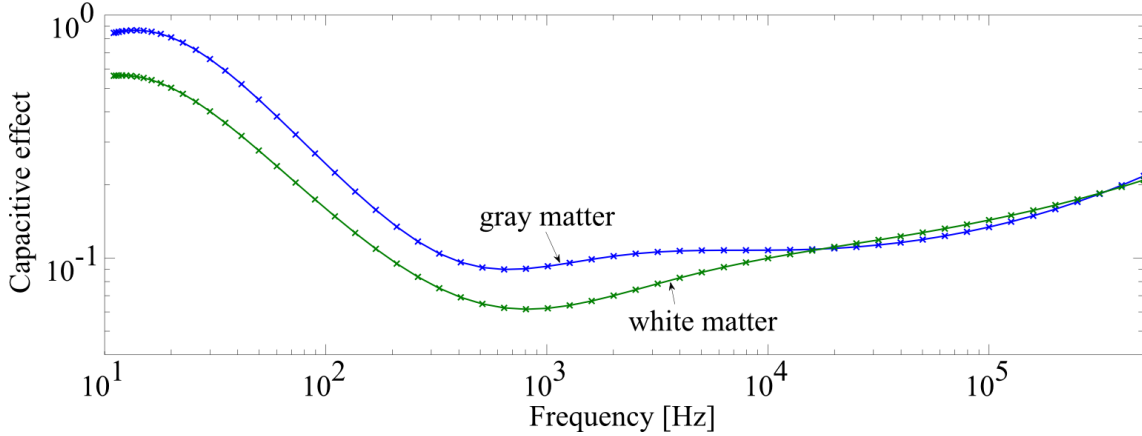


Figure 5.6: Capacitive effect $\frac{\omega \epsilon_0 \epsilon_r}{\kappa}$ in a frequency range of 10 Hz to 500 kHz for the electrical properties of gray and white matter.

5.2.2 Validation of FFEMEC

The studies and results presented in the following section are based on the publication "Single Frequency Approximation of Volume Conductor Models of Deep Brain Stimulation Using Equivalent Circuits" [110] and have been extended to include the validation for bipolar electrode configuration as well as the time-dependent voltage response in a saline cylinder model for voltage-controlled stimulation.

To validate the proposed Fourier finite element method with equivalent circuits (FFEMEC) described in section 3.3, the time-dependent voltage response in the proximity of the stimulated target within the volume conductor model computed with FFEMEC was compared with that computed with Fourier finite element method (FFEM). The electrical properties of the brain tissue were taken from Gabriel et al. [46] at a frequency of 1 kHz. As described in section 3.5.3, the electrical properties of the encapsulation layer vary over time. To model the longterm effects of DBS, the electrical properties of the encapsulation layer were modelled to resemble the chronic phase by using the halved conductivity value of gray matter [21] and the relative permittivity of brain tissue [142]. The DBS electrode was operated for unipolar and bipolar electrode configuration mode [85]. The second electrode contact is used for active stimulation and the ground electrode is allocated at the bottom of the volume conductor model for unipolar mode and at the first electrode contact for bipolar mode with a constant potential of $V_0 = 0$ V (Fig. 3.15). The applied DBS pulse was modelled in the time-domain according to equation (3.41) with a pulse duration of $d_p = 60 \mu\text{s}$, a frequency of $f = 130$ Hz and a current-controlled cathodic amplitude of $A_{cc} = 1.5$ mA. As described in section 3.3.1, a Fourier transform of this pulse can result in overshooting if the Fourier components are truncated. To investigate the influence of overshooting in the time-dependent voltage response as well, a smoothed DBS pulse according to equation (3.42) with a slope coefficient of

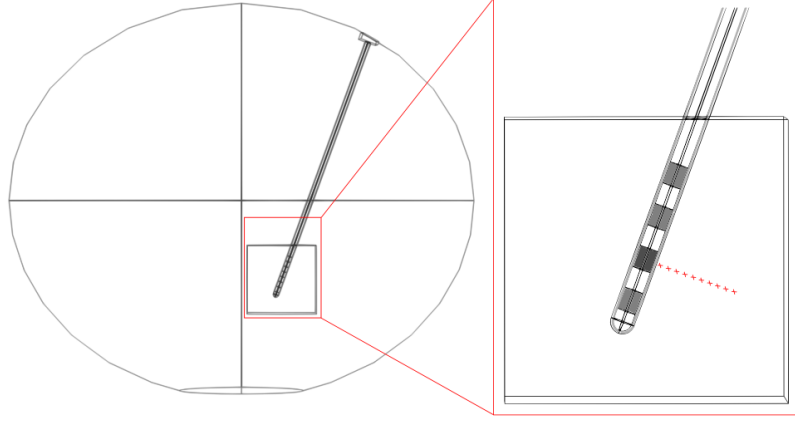


Figure 5.7: Schematic illustration of a coronary section of the volume conductor model and the investigated points of interest (red) positioned caudal from the active electrode contact.

$a = 1 \cdot 10^6$ was used, which corresponds to a cut-off frequency of 151 kHz (Fig. 3.7). The time-dependent DBS pulses $y(t)$ are transformed into the frequency-domain using a FFT with a sampling rate of 1 MHz, resulting in the Fourier components \underline{X}_k with $k = 1, \dots, N$. According to the Nyquist-Shannon sampling theorem, a sampling rate of 1 MHz results in frequency components \underline{X}_k of up to 500 kHz. To obtain the current-controlled transfer function $\underline{T}_{k,\text{FFEM}}$, a normal current density boundary condition corresponding to a current amplitude $A_{\text{cc}} = 1.5 \text{ mA}$ was applied at the second electrode contact. The values of the electric potential $\varphi_k(\mathbf{r})$ at the investigated spatial points \mathbf{r} of the volume conductor model were determined for the frequencies f_k , with a number of 50 logarithmically distributed frequencies in each decade, and interpolated linearly on $k = 1, \dots, N$. For the computation of the time-dependent voltage response with FFEMEC, the resistance $R_{1 \text{ kHz}, t}$ in (3.44) and the capacitance $C_{1 \text{ kHz}, t}$ in (3.45) were determined from the volume conductor model using a constant potential at the second electrode contact of $V_1 = 1 \text{ V}$.

To verify the assumption of using only one transfer function in combination with the electric potential at a spatial point \mathbf{r} in the proximity of the stimulated target to obtain the modified frequency spectrum $\tilde{X}_k(\mathbf{r}, \omega_s)$ in equation (3.51) using FFEMEC, the deviation of the normalised transfer functions was computed using FFEM for spatial points \mathbf{r} in a distance of 0.5 mm to 5 mm caudal from the active electrode contact in a coronary section of the volume conductor model (Fig 5.7)¹.

¹Figure 5.7 is mirrored compared to Figure 3.13 because the x-axis is descending in the anatomical coordinate system as described in section 3.5.3

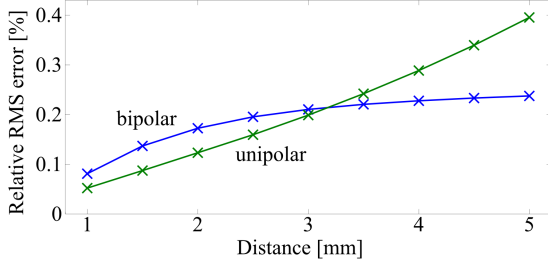


Figure 5.8: Deviation of the RMS value of the normalised transfer function with respect to the values at a distance of 0.5 mm from the active electrode contact computed with FFEM.

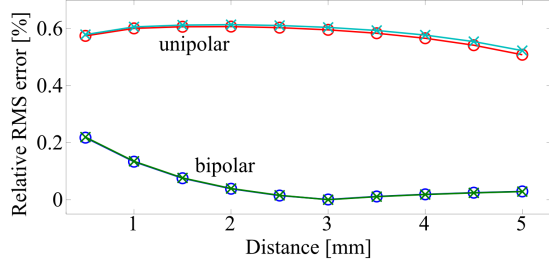


Figure 5.9: Deviation of the RMS value of the time-dependent voltage response for a square-wave DBS pulse (circle data points) and a smoothed DBS pulse (cross data points) computed with FFEMEC and FFEM.

The computation of the deviation between the root mean square (RMS) value of the normalised transfer function at each investigated point \mathbf{r} and its value at a distance of 0.5 mm from the active electrode contact resulted in a value below 0.4 % for unipolar electrode configuration and below 0.25 % for bipolar electrode configuration (Fig 5.8). Therefore, the transfer function in the proximity of the stimulated target can be considered to be constant for bipolar as well as unipolar electrode configuration, which allows for a computation of the time-dependent voltage response in this area by using only one transfer function. This result allowed for comparing the time-dependent voltage responses obtained with FFEMEC and with FFEM. The deviation of the RMS values of the time-dependent voltage response for a square-wave DBS pulse computed with both methods remained between 0.52 % and 0.61 % for unipolar electrode configuration and was below 0.25 % for bipolar electrode configuration (Fig. 5.9). A similar behaviour could be observed using smoothed DBS pulses as stimulation signal. The larger deviation between FFEMEC and FFEM for bipolar electrode configuration could be a result from cumulative numerical errors of the total current \underline{I} , which has to pass a larger area including a less homogeneous material distribution of brain tissue to the ground electrode. Nevertheless, regarding these maximal deviations in the time-dependent voltage response, its computation with FFEMEC for bipolar as well as unipolar electrode configuration is in good agreement with the time-dependent voltage response computed with the computationally expensive FFEM. The waveform shapes of the time-dependent voltage response for unipolar electrode configuration resemble the time-dependent voltage response for bipolar electrode configuration and only differ in their amplitude (Fig 5.10). A computational study, comparing the distribution of the electric potential in the proximity of the stimulated target area, showed similar results for bipolar and unipolar electrode configuration [85]. These results are an evidence that results in further investigations of the time-dependent voltage response and neural activation

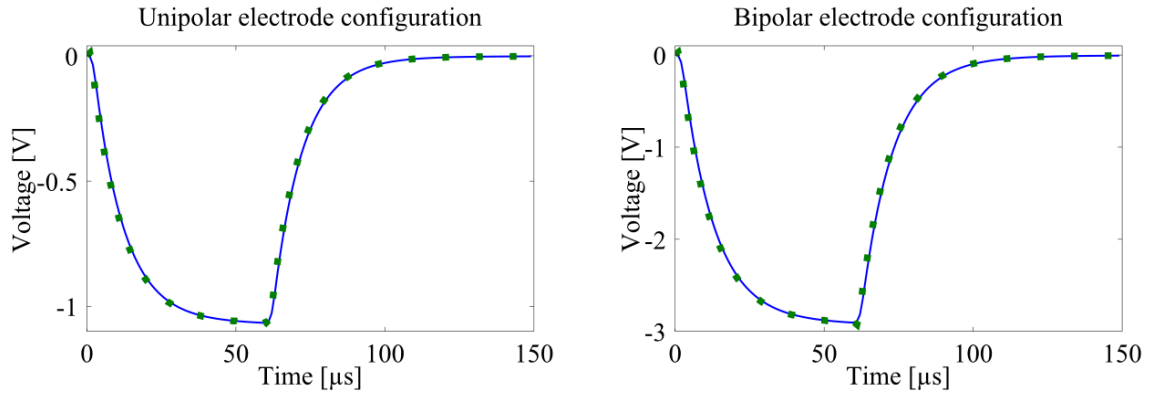


Figure 5.10: Time-dependent voltage response in 1 mm distance from the active electrode contact computed with FFEM (blue) and the proposed method FFEMEC (green) for unipolar as well as bipolar electrode configuration for a square-wave DBS pulse.

for both electrode configurations may be similar. Because of these results and since unipolar electrode configuration is the typical configuration type in human DBS [85], the studies in this thesis are solely carried out for unipolar electrode configuration.

Time-dependent voltage response in a saline cylinder model

Based on the study of Miocinovic et al. [87] the computation of the time-dependent voltage response in a volume conductor model using FFEMEC for voltage-controlled stimulation was carried out in a circular-symmetric model of a DBS electrode located in a cylinder filled with saline (Fig. 5.11). Parameters for the electrical properties of the medium and the electrical double layer were set according to the volume conductor model of Grant [55], which was computed using FFEM. The circular-symmetric model consists of 169,654 mesh elements. Similar to the validation for current-controlled stimulation, the FEM computations were carried out at a frequency

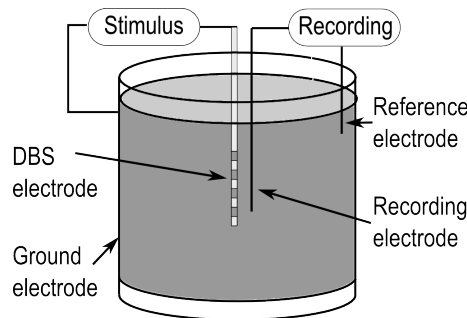


Figure 5.11: Experimental setup to measure the voltage response of a DBS pulse applied to a DBS electrode in a cylinder filled with saline based on [87].

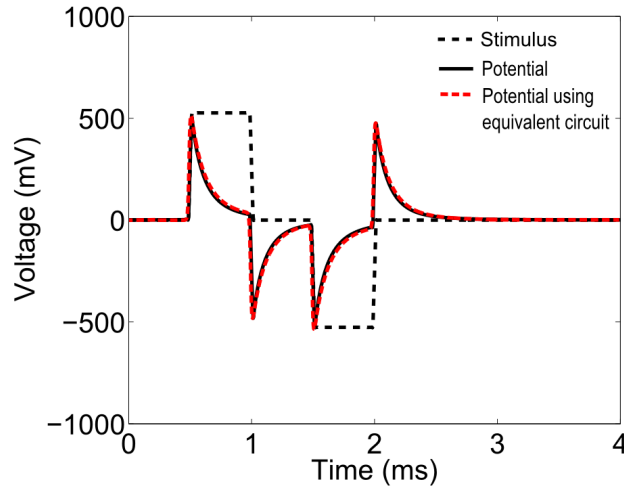


Figure 5.12: Voltage response of a voltage-controlled pulse in saline in 1 mm distance from the stimulating electrode obtained by FFEM (solid line). The black dotted line shows the DBS pulse normalised to the maximum of the voltage waveform. Image courtesy by Grant [55]. The image is overlaid by the time-dependent voltage response (scaled) computed with FFEMEC shown as red dotted line.

of 1 kHz. The resulting system of linear equations (SLE) was solved using the direct solver MUMPS. The time-dependent voltage response in a distance of 1 mm from the active electrode contact computed with the proposed method was compared to that computed by Grant [55] with FFEM and was found to be in good agreement (Fig. 5.12).

The presented results for current-controlled as well as voltage-controlled stimulation allow for a fast computation of the time-dependent voltage response for frequency-independent electrical properties of brain tissue in the presented volume conductor model of the human brain by executing at maximum two FEM computations. In contrast, FFEM requires a large number of FEM computations [57]. Therefore, the proposed method allows for more advanced computational studies, such as parameter studies, to be carried out within a reasonable time frame.

5.2.3 Single frequency approximation of the dispersive brain model

The studies and results presented in the following section are based on the publication "Single Frequency Approximation of Volume Conductor Models of Deep Brain Stimulation Using Equivalent Circuits" [110].

As described in section 3.1.2, the electrical properties of brain tissue are frequency-dependent over a wide range of frequencies, including the investigated frequency spectrum of the DBS pulse from 130 Hz to 500 kHz. The proposed method for the

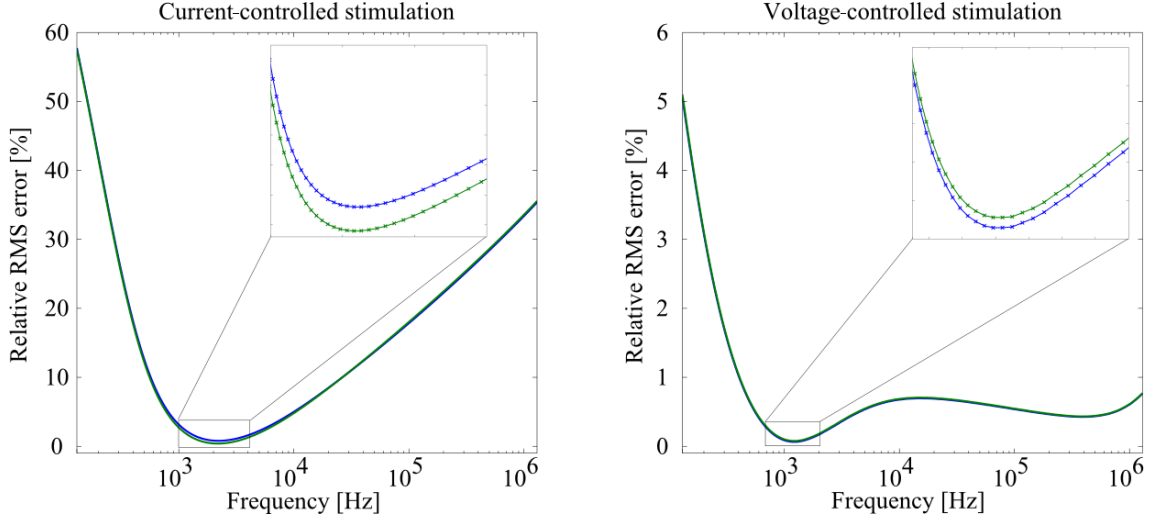


Figure 5.13: Relative RMS error of the time-dependent voltage response for single frequency approximations of the brain model between 130 Hz and 1.3 MHz with respect to that for the dispersive brain model for a square-wave DBS pulse (blue) and a smoothed DBS pulse (green).

DBS pulse	Current-controlled stimulation		Voltage-controlled stimulation	
	f_{best} [kHz]	ϵ_{RMS} [%]	f_{best} [kHz]	ϵ_{RMS} [%]
square-wave	2.259	0.799	1.186	0.064
smoothed	2.157	0.399	1.241	0.078

Table 5.1: Best single frequency approximation and the corresponding RMS error with respect to the dispersive brain model.

fast computation of the time-dependent voltage response is limited to the application of frequency-independent material properties. However, using the proposed FFEMEC, the time-dependent voltage response in the proximity of the stimulated target can be obtained by executing a maximum of two FEM computations to determine the transfer function as well as the spatial distribution of the electric potential in the volume conductor model, which facilitates the comparison of the single-frequency approximation with the dispersive solution of the volume conductor model across a wide range of frequencies within a reasonable time frame. The deviation between a single-frequency approximation and the dispersive solution of the volume conductor model is investigated by computing the time-dependent voltage response as described in section 5.2.2 for the electrical properties of brain tissue for each frequency f_k based on the data of Gabriel et al. [46]. In addition to

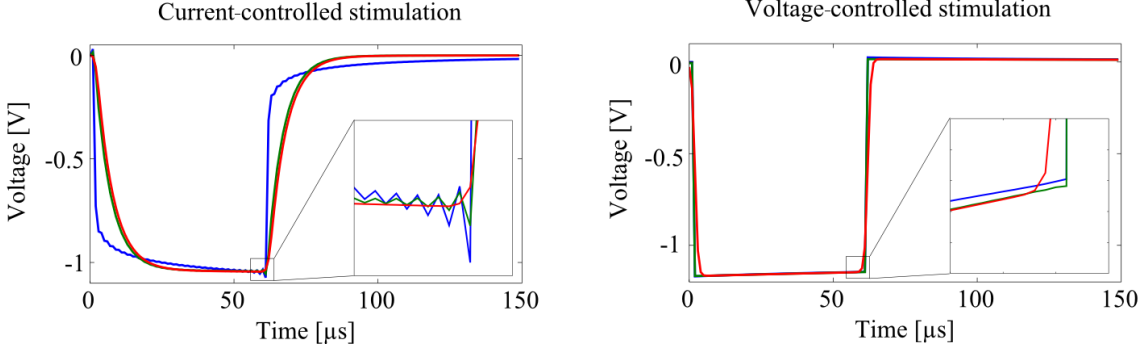


Figure 5.14: Time-dependent voltage response of the dispersive brain model (blue) and best single frequency approximation (green) for a square-wave DBS pulse as well as the best single frequency approximation for a smoothed DBS pulse (red).

the dispersive solution, the results provide the required parameters for determining the time-dependent voltage response for each single-frequency approximation of the volume conductor models at the frequencies f_k . Computations of the best single frequency approximation of the human brain model with FFEMEC were carried out for voltage-controlled and current-controlled stimulation. Since the transfer function was found to be almost constant at different spatial points \mathbf{r} in the proximity of the stimulated target (Fig. 5.8), the time-dependent voltage response for the single frequency approximation and the dispersive solution of the brain model is investigated at only one representative point in 1 mm distance from the active electrode contact.

For voltage-controlled stimulation the best single frequency approximation was found at a frequency of approximately 1.2 kHz with a RMS error of approximately 0.06 % for a square-wave DBS pulse and approximately 0.08 % for a smoothed DBS pulse (Table 5.1). For current-controlled stimulation, the best single frequency approximation was found at a slightly higher frequency of approximately 2.2 kHz with a RMS error of approximately 0.8 % for a square-wave DBS pulse and 0.4 % for a smoothed DBS pulse. Compared to the RMS errors for the voltage-controlled stimulation, those for current-controlled stimulation are about one magnitude larger and substantially increase in the lower and higher frequency range to approximately 58 % and 36 % for 130 Hz and 1.3 MHz, while the maximal RMS error for voltage-controlled stimulation in this frequency range was approximately 5.1 % at 130 Hz (Fig. 5.13). Despite the smaller slope of the time-dependent voltage response for a smoothed DBS compared to a square-wave DBS pulse, no apparent difference exists between both time-dependent voltage responses for voltage-controlled stimulation at the best single frequency approximation (Fig. 5.14). Overshooting in the time-dependent voltage response was only noticeable for current-controlled stimulation with a magnitude of approximately 3 % for the square-wave DBS pulse, which results

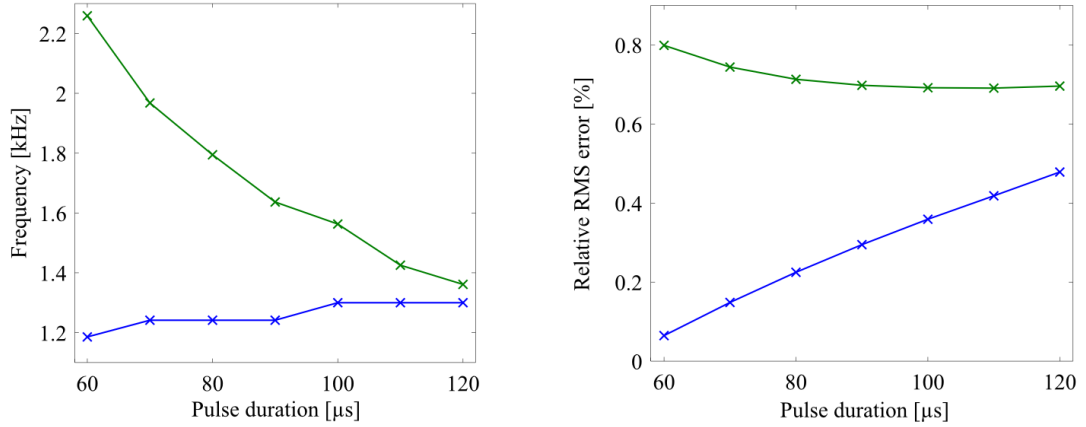


Figure 5.15: Best approximating frequency and corresponding relative RMS error of the dispersive brain model for different pulse durations of a square-wave DBS pulse for current-controlled (green) and voltage-controlled stimulation (blue).

from the truncation in the high frequency spectrum of the DBS pulse by the capacitive filtering of the electrical properties of brain tissue. Since the frequency spectrum of the smoothed DBS pulse is reduced (Fig 3.7), the truncation effect and, therefore, the overshooting for the smoothed DBS pulse is smaller. The smaller RMS errors and overshooting for voltage-controlled stimulation can be ascribed to the influence of the constant phase element impedance, which reduces the capacitive filtering effect of the electrical properties of brain tissue by the voltage divider rule used in equation (3.52).

The best single frequency approximation of the brain model was computed for a common DBS pulse with a pulse duration of $d_p = 60 \mu s$. However, in clinical practise different pulse durations are used as well. Medtronic, Inc [85] mentions a range of pulse durations from $60 \mu s$ to $120 \mu s$, at which the suppression of symptoms should occur. Since the pulse duration changes the frequency spectrum \underline{X}_k of the DBS pulse, it may change the frequency of the best single frequency approximation of the brain model as well. To investigate the sensitivity of this frequency on the pulse duration d_p , square-wave DBS pulses in the mentioned pulse duration range have been investigated with a step size of $10 \mu s$. The frequency of the best single frequency approximation of the human brain model monotonically decreased from approximately 2.2 kHz to 1.4 kHz for current-controlled stimulation and slightly increased from approximately 1.2 kHz to 1.3 kHz for voltage-controlled stimulation, while the RMS error for both stimulation types remained below 0.8 % (Fig. 5.15). Similar best approximating frequencies were obtained in a preliminary study of an anatomical volume conductor model of the brain consisting of white matter [57].

Influence on the volume of tissue activated

The best single frequency approximation of the human brain model resulted in a change of the waveform shape of the time-dependent voltage response especially for current-controlled stimulation (Fig. 5.14). To investigate the influence of this change on the neural activation, the volume of tissue activated (VTA) was computed for the best single frequency approximation and the dispersive human brain model for square-wave and smoothed DBS pulses with a pulse duration of $d_p = 60 \mu\text{s}$ based on the results in Table 5.1. The VTA was computed as described in section 3.6 using 100 axon models aligned in a 10×10 grid in a coronal plane of the brain model caudal to the DBS electrode. The spacing between the axon models was 0.5 mm parallel and perpendicular to the DBS electrode (Fig. 3.17). The threshold computations were carried out in parallel using MPI with a speedup of approximately 0.81 determined on a workstation with six physical Intel® Xeon cores @ 2.4 GHz (Fig. 5.16). A linear fit with fourth order polynomials was applied to compute the activation isoline in equation (3.61) from the threshold pattern obtained for a stimulus amplitude of 1 V for voltage-controlled stimulation and 0.5 mA for current-controlled stimulation (Fig. 5.17). The obtained threshold patterns were similar to the threshold patterns computed for a volume conductor model of the human brain by Butson and McIntyre [21]. The resulting VTA remained between 58.1 mm^3 and 60.6 mm^3 for voltage-controlled stimulation and 43.4 mm^3 and 46.5 mm^3 for current-controlled stimulation (Table 5.2). The relative error of the VTA between the best single frequency approximation and the dispersive solution of the human brain model was below 0.3 % for voltage-controlled stimulation and 5.5 % for current-controlled stimulation. Similar small deviations of the computed VTA between a single frequency approximation and a dispersive solution of a point source model were reported by Bossetti et al. [17]. Compared to the relative RMS errors of the time-dependent voltage responses in Table 5.1, the deviation between the VTA of the best single frequency approximation and dispersive brain model slightly increased for

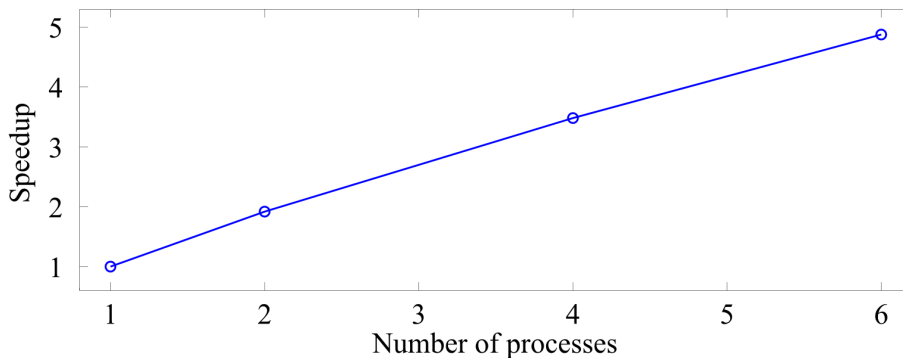


Figure 5.16: Speedup of the parallel Python script using NEURON MPI functionality.

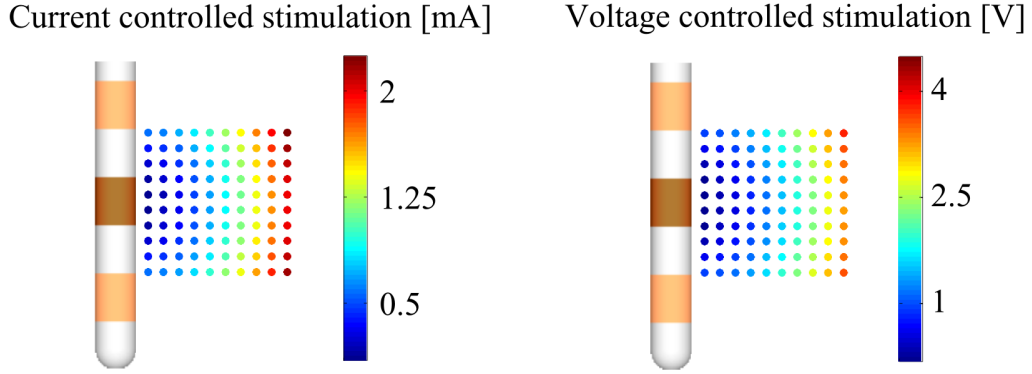


Figure 5.17: Computed thresholds necessary to elicit an action potential in the axon models of the dispersive human brain model.

voltage-controlled stimulation and substantially for current-controlled stimulation. In the latter case, the VTA of the best single frequency approximation was smaller than the VTA of the dispersive brain model. Taking into account the different waveform shape of the time-dependent voltage response for both models (Fig. 5.14), the larger deviation of the VTA for current-controlled stimulation results most likely from the smaller slope in the best single frequency approximation of the human brain model. This assumption is assured when comparing the VTA for voltage-controlled stimulation for the square-wave DBS pulse and the smoothed DBS pulse, which has a slightly smaller slope, resulting in a deviation of the computed VTA of 4.2 %. Since no overshooting was noticeable in the time-dependent voltage response for voltage-controlled stimulation, this deviation is presumably caused by the smaller slope of the smoothed DBS pulse as it was noticeable in the VTA deviation for current-controlled stimulation. These results suggest that the slope of the time-dependent voltage response is a more important factor for the computation of the VTA than a possible slight overshooting in the time-dependent voltage response. Therefore, a smoothing of the DBS pulse to reduce overshooting should be relinquished. As mentioned above, the volume of the STN is about 160 mm^3 and differs patient-individually as well. A VTA deviation of about 5 %, as determined for current-controlled stimulation, would most likely be of no or only small clinical relevance. Therefore, the computation of the VTA for the best single frequency approximation of the human brain model with FFEMEC allows for a first prediction of the activated area in DBS and can be obtained in a reasonable time compared to utilizing FFEM, which was used in previous computational studies [21, 57, 142].

Summarizing the results, a frequency of 2 kHz for a DBS pulse with a pulse duration of $d_p = 60 \mu\text{s}$ applied to the STN seems to be suitable for a single frequency approximation of the dispersive volume conductor model of the brain, leading to relative RMS errors of the time-dependent voltage response of approximately 0.2 % for voltage-controlled stimulation and 0.8 % for current-controlled stimulation. However,

DBS pulse	Solution type	Volume of tissue activated [mm ³]	
		Voltage-controlled	Current-controlled
square-wave	dispersive	60.53	46.48
	single-frequency	60.60	43.93
smoothed	dispersive	57.96	45.76
	single-frequency	58.10	43.38

Table 5.2: Computed VTA for the frequency-dependent and best approximated single-frequency voltage responses for square-wave and smoothed DBS pulses as well as voltage-controlled and current-controlled stimulation.

it should be kept in mind that this best approximating frequency may change patient-individually for different volume conductor models of the human brain, different target areas and different electrical properties of brain tissue.

5.3 Uncertainty quantification by the polynomial chaos technique

The time-dependent voltage response and the resulting VTA in the proximity of the stimulated target in the generated volume conductor model of the human brain depends on various factors as described in section 3.5. Several of these factors, such as the distribution of brain tissue, its electrical properties and anisotropy, and the parameters of the electrode-tissue-interface are subject to uncertainty in literature [112]. While the uncertainty in the distribution of the brain tissue can be controlled by using averaged MRI data of different patients such as in the SRI24 multi-channel brain atlas, which is based on the MRI data of 24 patients, the uncertainty quantification for the electrical properties of brain tissue and in the electrode-tissue-interface requires a more profound investigation. The quantification of the resulting uncertainty in the time-dependent voltage response and VTA in the human brain model for DBS is carried out by using the non-intrusive projection approach based on the PC technique as described in section 4.2.3. To allow for a computation of the uncertainties in a reasonable time, a time-efficient computation of the time-dependent voltage response is crucial. Therefore, the single frequency approximation of the human brain model determined in section 5.2.3 is used. Since the modelling of the anisotropic conductivity of brain tissue is dependent on its isotropic conductivity as described in section 3.4.2, its influence on the time-dependent voltage response

is investigated separately in section 5.4. To ensure a precise computation of the probabilistic time-dependent voltage response and VTA, the method is validated in a simplified brain model with MCS. Since the time-dependent voltage response for voltage-controlled stimulation depends on the parameters of the electrode-tissue-interface, the sensitivity of the time-dependent voltage response and VTA on these parameters is investigated in a preceding study to the investigations carried out in section 5.3.3.

5.3.1 Validation of the non-intrusive projection approach

The performance and accuracy of the implemented non-intrusive projection approach for quantifying the uncertainty in the model parameters of the human brain model was compared with the MCS. Since MCS requires the execution of the deterministic model for a large set of probability samples N as described in section 4.1, a simplified human brain model was generated, which requires substantially less computation time compared to the anatomical human brain model described in section 3.5. The simplified human brain model consists of a white matter area with a height of 15 mm and a width of 30 mm, an ellipsoidal gray matter nuclei with a width of 8 mm and a height of 2 mm, and a model of the DBS electrode Mo. 3387 described in section 2.2.1 (Fig. 5.18). The two-dimensional and circular-symmetric finite element model was generated in Comsol Multiphysics™. The mesh was generated with the Delaunay algorithm using a maximum element length of 0.5 mm, resulting in a number of 4,612 mesh elements. An execution of the deterministic model was obtained using the direct solver MUMPS in approximately 4 s. The EQS formulation was applied to the model to compute the probabilistic time-dependent voltage response. The model was solved for a single frequency approximation of the electrical properties of brain tissue at 2 kHz and a square-wave current-controlled DBS pulse as used in section 5.2.3. The electrical conductivity of gray and white matter were modelled as uniformly distributed probabilistic parameters based on the values of Gabriel et al.

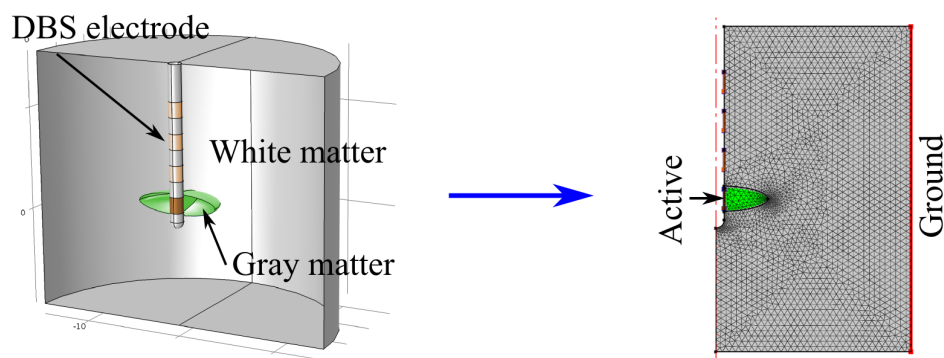


Figure 5.18: Geometry and mesh of the simplified human brain model.

Brain tissue	Conductivity [S m^{-1}]	Relative permittivity
White matter	$\mathcal{U}[0.053, 0.075]$	40,234
Gray matter	$\mathcal{U}[0.085, 0.121]$	93,983

Table 5.3: Electrical properties of white and gray matter in the simplified human brain model.

[46], with a mean value of $\kappa_{\text{gm}} = 0.103 \text{ S m}^{-1}$ and $\kappa_{\text{wm}} = 0.064 \text{ S m}^{-1}$, respectively, and a relative standard deviation of $\sigma_r = 10\%$, while the relative permittivity of both brain tissues were kept constant (Table 5.3). A number of $N = 10,000$ probability samples were used to determine the probabilistic time-dependent voltage response 1 mm from the active electrode contact. Based on the description in section 4.3, tensor and sparse grids based on the Clenshaw-Curtis rule with a grid level of $L = 4$ and a polynomial expansion of degree $p = 3$ was used to compute the probabilistic time-dependent voltage response with the non-intrusive projection approach. The probability density of the probabilistic time-dependent voltage response was estimated using the MATLAB® function `ksdensity` with 1,000 sample points.

Probabilistic time-dependent voltage response

The probabilistic time-dependent voltage response was computed for $N = 10,000$ probability samples of the probabilistic conductivity of gray and white matter with

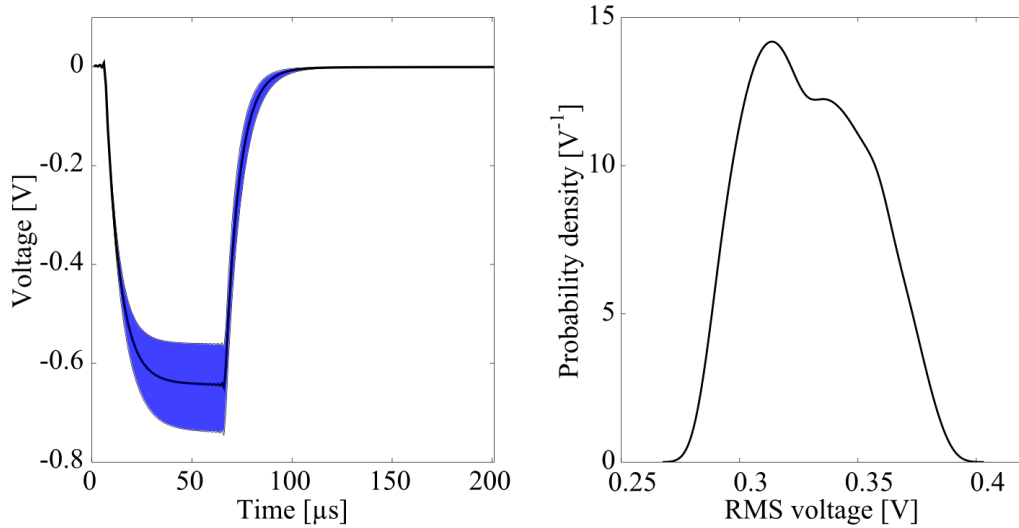


Figure 5.19: Mean value and 0.025 as well as 0.975 quantiles of the probabilistic voltage response (left) and probability density of its RMS value (right) computed with MCS.

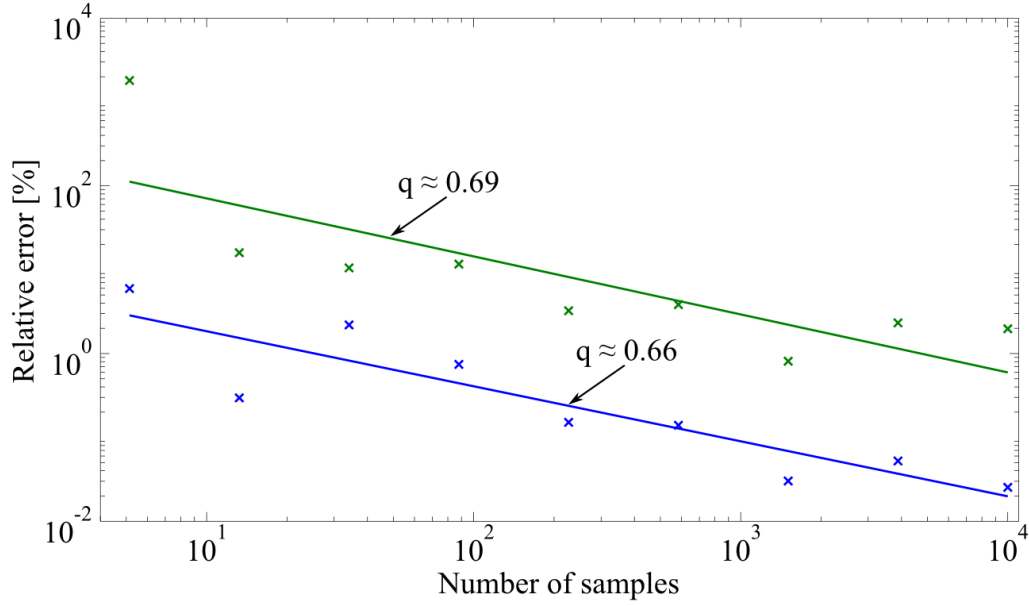


Figure 5.20: Relative *a posteriori* error of the mean (blue) and variance (green) of the RMS voltage response computed with MCS. A convergence order of approximately $q = 0.66$ for the mean and $q = 0.69$ for the variance was determined using a linear fit polynomial.

MCS (Fig. 5.19). The convergence of the mean and the variance of the RMS value shows a slow convergence of MCS as described in section 4.1 (Fig. 5.20). This result emphasises the requirement of a larger number of probability samples for MCS and its inapplicability for problems with a computationally expensive deterministic model.

The number of required executions of the deterministic model, using the non-intrusive projection approach, was 289 for a tensor grid of level $L = 4$ and 65 for a sparse grid of corresponding level, which is in both cases substantially smaller than the number of probability samples used for MCS. The results computed with the PC technique were in good agreement with those computed with MCS, using tensor grids as well as sparse grids (Fig. 5.21). For both grids, the convergence of the variance of the probabilistic RMS voltage response was similar, which can be explained by the algorithm for the generation of the sparse grids. As described in section 4.3.3, sparse grids are composed by the hierarchical combination of tensor grids with a maximal level sum L . These combinations are generated with the same algorithm which is used to build the multi-variate polynomial basis of the PC technique and, therefore, form an efficient choice of integration nodes. However, the convergence rate depends on the smoothness and continuity of the functional dependencies of the deterministic model and, therefore, has to be investigated for each model solution of the used deterministic model. The application of nested integration grids allows for

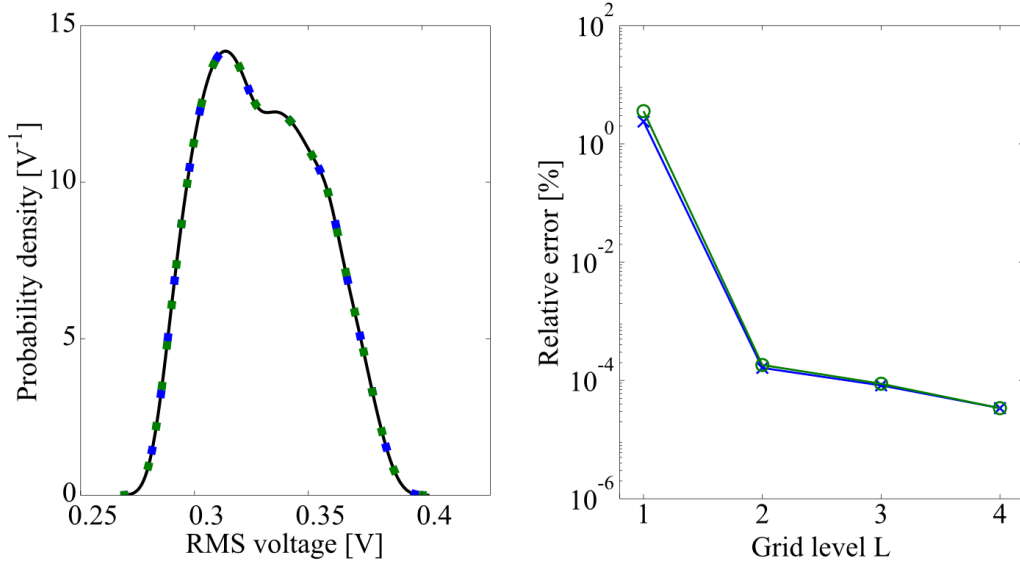


Figure 5.21: Probability density (left) and convergence of the variance (right) of the probabilistic time-dependent voltage response computed with PC technique with tensor grids (blue) and sparse grids (green) in dependence of the variance computed with MCS (black).

Integration method	Relative error to MCS [%] (Time: ≈ 11 h)		
Tensor grid ($L = 4$)	$5.7 \cdot 10^{-5}$	$3.4 \cdot 10^{-3}$	≈ 20 min
Sparse grid ($L = 4$)	$5.5 \cdot 10^{-5}$	$3.9 \cdot 10^{-3}$	≈ 5 min
Sparse grid ($L = 2$)	$7.5 \cdot 10^{-4}$	$2.8 \cdot 10^{-2}$	≈ 1 min

Table 5.4: Relative error of the mean and variance of the investigated quantity between the non-intrusive projection method and MCS. Computation time of MCS is based on the utilisation of $N = 10,000$ probability samples.

a fast investigation of the convergence and accuracy of the computed probabilistic model solution, because each solution for a grid level L contains the solutions for the grid levels $\tilde{L} = 1, \dots, L - 1$. While the results using MCS and PC technique were in good agreement, the computation time of the probabilistic voltage response in the simplified brain model could be substantially reduced using the non-intrusive projection approach (Table 5.4). The relative error of the mean and variance decreased by the order of one magnitude, using a sparse grid of level $L = 2$ compared to a sparse grid of level $L = 4$, but was still smaller than that of MCS while decreasing the computation time by a factor of about 750. However, the computation time of the non-intrusive projection approach would increase for a larger grid level and amount

of probabilistic model parameters as described in sections 4.3.2 and 4.3.3.

Based on the good agreement of the obtained results using MCS and the implemented PC technique, it is assumed that the non-intrusive projection approach allows for a precise computation of the probabilistic time-dependent voltage response and VTA in a volume conductor model of the human brain as long as the convergence of these quantities to a sufficient value is ensured.

5.3.2 Uncertainty in the parameters of the electrode-tissue-interface

The studies and results presented in the following section are based on the publication "Modelling the Probabilistic Neural Activation in Deep Brain Stimulation: Influence of Uncertainty in the Parameters of the Electrode-Tissue-Interface" [111]. As described in section 3.3, the electrical properties of the electrode-tissue-interface, which are modelled by a constant phase element, influence the time-dependent voltage response for voltage-controlled stimulation, but have a negligible influence for current-controlled stimulation. Therefore, the investigation of the influence of uncertainty in the parameters of the constant phase element on the probabilistic voltage response and VTA are only carried out for voltage-controlled stimulation, which is to date the common stimulation type for human DBS. The model parameters of the constant phase element in equation (3.46), which comprise the coefficient K and the exponent $\beta \in [0, 1]$, are based on an experimental study by Richardot and McAdams [103] as described in section 3.3.2. Since the parameters obtained from the experiment are subject to uncertainty, the aim was to investigate the sensitivity of the probabilistic voltage response and VTA on these parameters. Therefore, the parameters were modelled as uniformly distributed parameters to present a "worst-case" scenario, in which each value of the model parameters has the same probability within their prescribed boundaries. To ensure an assessment of a large set of possible parameter values, a relative standard deviation of 50 % on K and 10 % on β around the corresponding experimental mean values were used for the modelling of the uniformly distributed parameters (Table 5.5). To investigate the sensitivity of the probabilistic voltage response and VTA on each probabilistic parameter, different study cases were defined, in which (1) the exponent β , (2) the coefficient K , (3) and

Parameter	Mean	$\mathcal{U}[a, b]$	Uncertainty σ_r
Coefficient K	1.57	$\mathcal{U}[0.21, 2.93]$	50 %
Exponent β	0.85	$\mathcal{U}[0.7, 1.0]$	10 %

Table 5.5: Probabilistic model parameters $\mathcal{U}[a, b]$ of the constant phase element.

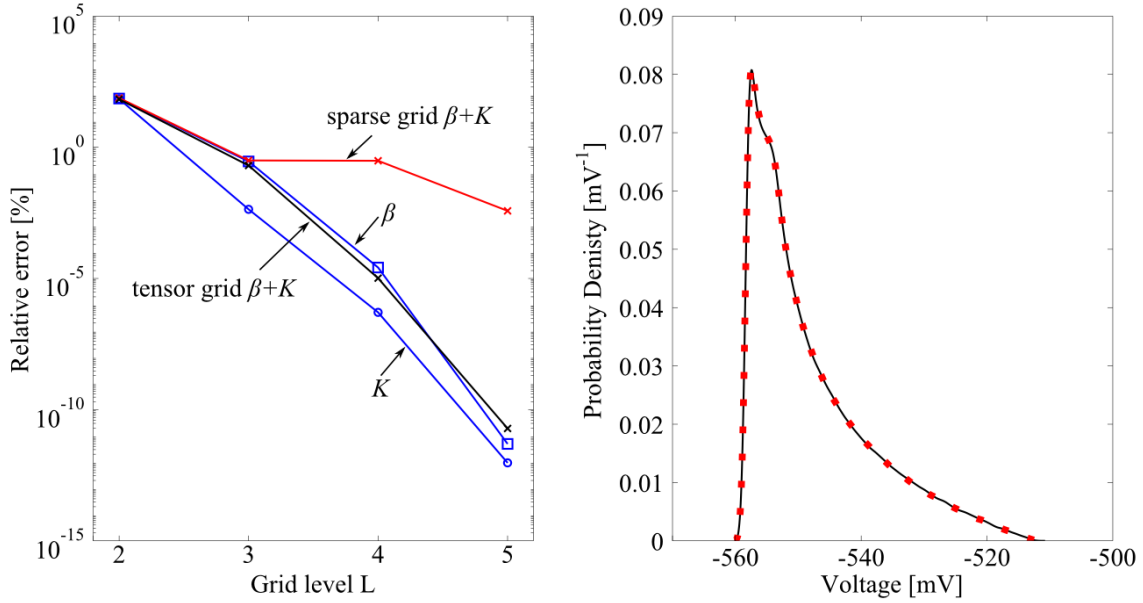


Figure 5.22: Convergence of the variance of the probabilistic voltage response 1 mm from the active electrode contact at a time step $t = 64 \mu\text{s}$ (left) and the corresponding probability density determined using a tensor grid (black) as well as a sparse grid (red).

β as well as K were modelled as probabilistic parameters. In the first two cases the non-probabilistic parameter was set to its mean value. The computation of the time-dependent voltage response was carried out using FFEMEC, which allows for its fast computation for different samples of the probabilistic parameters of the constant phase element in post-processing. The VTA was determined for a stimulation amplitude of $A_{\text{vc}} = -1 \text{ V}$ using a 7×18 grid of axon models as described in section 3.6. The probabilistic voltage response was computed using the non-intrusive projection approach for a degree $p = 3$ of the multi-variate polynomial basis and $N = 1 \cdot 10^6$ probability samples of each probabilistic parameter. It was ensured that the application of higher order polynomial approximations resulted in a deviation of the variance of the probabilistic voltage response below 1 %. For the third study case, the coefficients of the polynomial expansion were computed with tensor grids and sparse grids of a grid level $L = 5$, resulting in 1,089 and 145 executions of the deterministic model, respectively, whereas for the first and second study case, only a uni-dimensional polynomial expansion was required. The convergence in each case was ensured by determining the deviation of the variance of the probabilistic voltage response 1 mm from the active electrode contact at a time step $t = 64 \mu\text{s}$ (Fig. 5.22). The results showed a decreased convergence rate for the application of the sparse grid for grid levels $L > 3$ compared to the application of the tensor grid, which resembles the convergence of the uni-variate cases. The slow convergence can be explained by the strong asymmetry of the probability density function of the result-

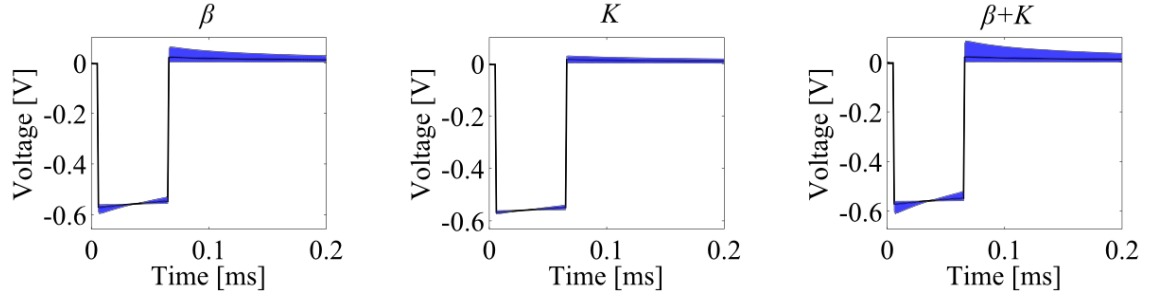


Figure 5.23: Mean value and 0.025 quantile as well as 0.975 quantile of the probabilistic voltage response 1 mm from the active electrode contact for the probabilistic parameters β (left), K (middle), and $\beta + K$ (right).

ing probabilistic voltage response, which corresponds to large changes in a small area of the integration area. These changes are better approximated by the nodes of the tensor grid compared to the sparse grid [93]. Nevertheless, the estimated probability density functions using the sparse grid and the tensor grid are in a good agreement, while the sparse grid solution required only 145 executions of the deterministic model instead of 1,089 using the tensor grid. The uncertainty in the probabilistic voltage response is substantially smaller than the prescribed uncertainty in the parameters of the constant phase element, which were 10 % for the exponent β and 50 % for the coefficient K (Fig 5.23). Both parameters influenced mostly the waveform shape in the stimulation period, but less its amplitude. Considering the prescribed magnitude of uncertainty in the parameters, the uncertainty in the coefficient K had a negligible influence on the uncertainty in the time-dependent voltage response, but increased its magnitude when combined with the probabilistic parameter β . An explanation for the minor influence on the time-dependent voltage response can be ascribed to the computation of the time-dependent voltage response, which determines the transfer function for voltage-controlled stimulation by application of the voltage divider rule as described in section 3.3.4. This decreased influence of the electrode-tissue-interface on the voltage response for voltage-controlled stimulation is in agreement with results from another computational study in a volume conductor model of the human brain [21].

Because of the good agreement of the sparse grid and tensor grid solution for the probabilistic voltage response, the computationally expensive determination of the probabilistic VTA was only carried out for sparse grids in the third study case. The convergence of the variance of the probabilistic VTA decreased compared to that of the probabilistic voltage response (Fig. 5.24). To ensure a relative error of the variance of the VTA of below 1 %, a sparse grid of level $L = 7$ was required, resulting in 705 executions of the deterministic model. The slow convergence is ascribed to the higher order functional dependencies in the used axon model described in section 3.6, which especially affect the convergence using sparse grids [93]. A polynomial degree

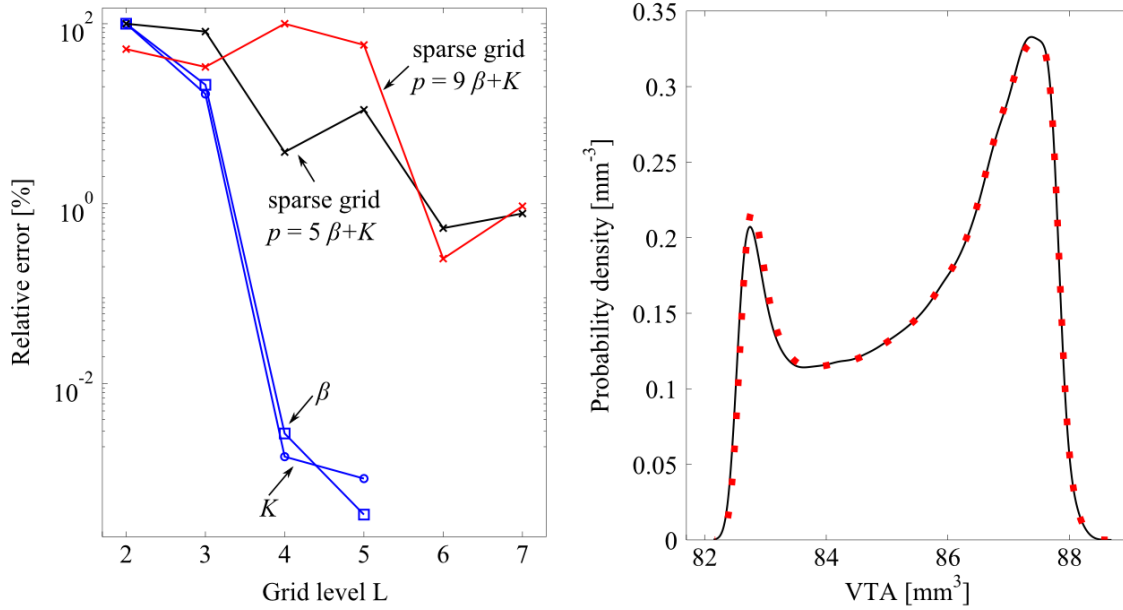


Figure 5.24: Convergence of the variance of the probabilistic VTA with a polynomial degrees $p = 5$ for a stimulation amplitude $A_{vc} = -1$ V (left) and the corresponding probability density determined using a sparse grid with a polynomial degree $p = 5$ (black) and $p = 9$ (red) using a sparse grid of level $L = 7$ (right).

of $p = 5$ for the multi-variate expansion of the probabilistic VTA was used to obtain an accurate representation of its PDF. An increase of the polynomial degree to $p = 9$ resulted in a relative error of the magnitude of uncertainty σ_r of below 0.3 % for the application of sparse grids with a grid level of $L = 7$. The PDF of the probabilistic voltage response for an uncertain β and K shows a bimodal distribution with the major mode located above the mean value of approximately 85.66 mm^3 , which results in a most likely larger VTA than presented by its mean value, when assuming a uniform distribution of the parameters β and K . The bimodal distribution of the probabilistic VTA results mostly from the influence of the exponent β of the CPE in equation (3.46), which resembles for $\beta \approx 1$ the properties of an ideal capacitor, as described in section 3.3.2. This capacitive CPE has only a small influence on the shape of the time-dependent voltage response. This influence on the waveform of the voltage response increases with decreasing values of β , because of an increased resistive component of the CPE, which is at maximum at $\beta = 0.7$ for $\beta \in \mathcal{U}[0.7, 1]$. The resulting voltage response for different β shows a larger variation of its waveform for smaller values of β , which intersect that for values of $\beta \approx 1$ (Fig. 5.23). This effect results in an inversion of the PDF regarding its mean value in the duration of the DBS pulse. Since the amplitude and the shape of the stimulation pulse of the voltage-response mostly influence the VTA, this effect of the exponent β on the

	Parameter	Uncertainty [%]	
		RMS voltage response	VTA
Coefficient K	50	0.01	1.47
Exponent β	10	0.47	1.57
K & β	50 & 10	0.66	1.91

Table 5.6: Uncertainty in the probabilistic RMS value of the voltage response within 2.5 mm from the active electrode contact and VTA in dependence of the uncertainty in the model parameters.

voltage response causes the bimodal distribution of the probabilistic VTA.

To compare the magnitude of uncertainty in the probabilistic VTA with the time-dependent voltage response in the proximity of the stimulated target, its average RMS value within a distance of 2.5 mm from the active electrode contact was determined by considering the probabilistic voltage response at the nodes of a 4×4 grid in the coronary plane, which is a part of the already used grid for the computation of the probabilistic VTA. The computation of the average RMS value by considering the nodes in the coronary plane is valid as long as the distribution of the electric potential is homogeneous in the proximity of the stimulated target. Since the stimulated target area consists of mostly white matter in the used MRI data set and only voltage responses in the proximity of the stimulated target area are considered, this assumption is considered to be verified. The magnitude of uncertainty in the average RMS value of the time-dependent voltage response was between approximately 0.01 % for the probabilistic parameter K and 0.66 % for the probabilistic parameters β and K (Table 5.6). These magnitudes of uncertainty for the different cases correspond to the determined quantiles of the probabilistic voltage responses 1 mm from the active electrode contact (Fig. 5.23). The magnitude of uncertainty of the probabilistic VTA remained between approximately 1.47 % for the probabilistic parameter K and 1.9 % for the probabilistic parameters β and K , which qualitatively resembled the influence of uncertainty in the probabilistic voltage response for the different cases. Although the magnitude of uncertainty of the probabilistic VTA was slightly larger than that of the probabilistic voltage response within a distance of 2.5 mm from the active electrode contact, the uncertainty in the VTA can be considered to be negligible compared to the prescribed magnitude of uncertainty in the parameters of the constant phase element. Despite the fact that no optimal convergence was obtained using the sparse grid, the number of 705 required executions of the deterministic model was substantially lower than the applied number of $N = 1 \cdot 10^6$ probability samples. The number of probability samples was set to this value to ensure that the probability density of the time-dependent voltage response and VTA was accurately

represented. Since the evaluation of the polynomial expansion of these quantities is carried out in post-processing and, therefore, is not computationally expensive, the used number of probability samples is not critical regarding the computation time, but a smaller number of samples would also likely be sufficient for the application of classical MCS. However, the difference in potentially required executions of the deterministic model using classical MCS suggests that the non-intrusive projection approach with sparse grids constitutes a computationally efficient alternative, despite the given non-linearities in the computation of the probabilistic VTA.

The magnitude of uncertainty in the parameters of the constant phase element were set to cover a large set of possible values. In practice, this magnitude of uncertainty would be most likely substantially smaller. Considering this fact, the results of this section suggest that the influence of uncertainty in the parameters of the constant phase element on the probabilistic voltage response and VTA can be considered to be negligible in the generated volume conductor model of the human brain.

5.3.3 Uncertainty in the electrical properties of brain tissue

The studies and results presented in the following section are based on the publication "Influence of Uncertainties in the Material Properties of Brain Tissue on the Probabilistic Volume of Tissue Activated" [112] and have been extended by the prediction of limits in the uncertainty of the model parameters to obtain a prescribed magnitude of uncertainty in the VTA.

Recent deterministic volume conductor models of the human brain consider only one parameter set out of the possible range of literature values and do not consider the uncertainty in these parameters [21, 57, 142]. Therefore, the aim was to quantify the influence of uncertainty in the electrical properties of brain tissue on the probabilistic time-dependent voltage response and VTA in the generated volume conductor model of the human brain. The magnitude of uncertainty in the electrical properties of brain tissue was modelled according to the variation of their values in experimental studies. To investigate the sensitivity of the probabilistic voltage response and VTA on the electrical properties of brain tissue, for which no information on the distribution of its values is presently available, a uniform distribution of these parameters was assumed with lower and upper boundaries according to the literature values to cover a "worst-case" scenario, in which every value within these boundaries has the same probability. The probabilistic voltage response and VTA were computed with PC technique with sparse grids as carried out in section 5.3.

Modelling of the probabilistic parameters

In bio-electrical applications, such as the computation of the time-dependent voltage response and VTA in a volume conductor model of the human brain, uncertainty in the model parameters may have a large influence on the desired model solution. A

White matter [S m^{-1}]	Gray matter [S m^{-1}]
0.064 ¹	0.103 ¹
0.138 ²	0.237 ²
0.211 ³	0.229 ³
0.375 ⁴	0.538 ⁴

Table 5.7: Range of conductivity values for white and gray matter at a frequency of 2 kHz obtained from the following literature: ¹ Gabriel et al. [46], ² Geddes and Baker [49] scaled, ³ Latikka et al. [76] scaled, ⁴ Foster and Schwan [42] scaled.

review of the available experimental data for the electrical properties of brain tissue shows substantial differences in the data. An explanation for these differences can be attributed to the measurement process, which is made challenging not only by the occurrence of interfering effects, such as electrode polarization at low frequencies, but also with the appearance of difficulties associated in *in vivo* as well as *in vitro*. Therefore, literature values on the electrical properties of brain tissue are scarce, especially for frequencies below 1 MHz, and are based either on experiments carried out on live tissue or on excised tissue, which is known to be subject to uncertainty compared to live tissue [45]. According to the substantial variation in the scarce literature data, a precise deterministic value for the electrical properties of the human brain model cannot be determined. For the modelling of the magnitude of uncertainty in the probabilistic electrical properties of brain tissue, conductivity values from a series of studies reported in literature were considered [42, 46, 49, 76]. Depending on the available measurement devices and the different experimental methods carried out *in vivo*, *ex vivo*, and *in vitro*, the values reported in literature are measured at different frequencies. For the fast computation of the time-dependent voltage response described in section 5.2.3, the electrical properties of brain tissue are required at a frequency of 2 kHz. To date, the only available literature source for the electrical properties of brain tissue over a wide range of frequencies is available from Gabriel et al. [46]. Therefore, the conductivity values in the other experimental studies were approximated at 2 kHz by scaling the data from Gabriel et al. [46] by the quotient of the conductivity values reported in literature and the value from Gabriel et al. [46] at the corresponding frequency (Table 5.7). As an example, the average conductivity value in the *in vivo* study from Latikka et al. [76] for white matter was 0.256 S m^{-1} at a frequency of 50 kHz. This value was divided by the conductivity value for white matter at 50 kHz (0.078 S m^{-1}) and multiplied by the conductivity value for white matter at 2 kHz (0.064 S m^{-1}) from the data of Gabriel et al. [46], resulting in a scaled conductivity value of 0.211 S m^{-1} at 2 kHz. Using these pre-processed values of the conductivity as boundaries for a uniform distribution, where the lower

boundary was set to the values of Gabriel et al. [46], resulted in relative standard deviations from approximately 21.1 % to 40.9 % for the conductivity of white matter and from approximately 22.8 % to 39.2 % for the conductivity of gray matter. To cover the range of uncertainty in the available literature and to allow for a prediction of uncertainty limits in the electrical properties of brain tissue in dependence of a prescribed uncertainty limit in the probabilistic VTA, different magnitudes of uncertainty in these parameters between 10 % and 40 % were used. As described in section 3.5.3, the electrical properties of the encapsulation layer vary in dependence of the time after the surgery. Since the focus was on the investigation of the influence of uncertainty in the conductivity and relative permittivity of brain tissue, the material properties of the encapsulation layer were not investigated separately, but were modelled as a function of the uncertainty in the material properties of brain tissue to cover the chronic phase of the implant as described in section 5.2.2.

Probabilistic time-dependent voltage response

Similar to the investigation of the sensitivity of the probabilistic voltage response and VTA on the uncertainty in the parameters of the electrode-tissue-interface in section 5.3.2, the sensitivity of these quantities on the uncertainty in the conductivity as well as relative permittivity of gray and white matter was investigated in three study cases, in which (1) uncertainty in the conductivity, (2) uncertainty in the relative permittivity, (3) and uncertainty in the conductivity as well as relative permittivity of brain tissue was investigated. In the first and second case, the remaining parameters were set to their mean values. The magnitude of uncertainty in the probabilistic parameters was set to 20 % based on the variation reported in literature (Table 5.8). The convergence of the truncated polynomial expansion of the probabilistic voltage response was investigated for the representative voltage response 1 mm from the active electrode contact at a time step of $t = 64 \mu\text{s}$ with a stimulation amplitude of $A_{\text{vc}} = -1.0 \text{ V}$ and $A_{\text{cc}} = -1.5 \text{ mA}$ for voltage-controlled and current-controlled stimulation, respectively. To ensure a relative error below 1 % in its variance, sparse grids with a grid level $L = 4$ were required (Fig. 5.25). The

Brain tissue	Conductivity [S m^{-1}]		Relative permittivity	
	Mean	$\mathcal{U}[a, b]$	Mean	$\mathcal{U}[a, b]$
White matter	0.098	$\mathcal{U}[0.064, 0.132]$	40,234	$\mathcal{U}[26, 297, 54, 171]$
Gray matter	0,158	$\mathcal{U}[0.103, 0.212]$	93,983	$\mathcal{U}[61, 426, 126, 540]$

Table 5.8: Probabilistic model parameters $\mathcal{U}[a, b]$ of the electrical properties of white and gray matter for a relative standard deviation of $\sigma_r = 20 \%$.

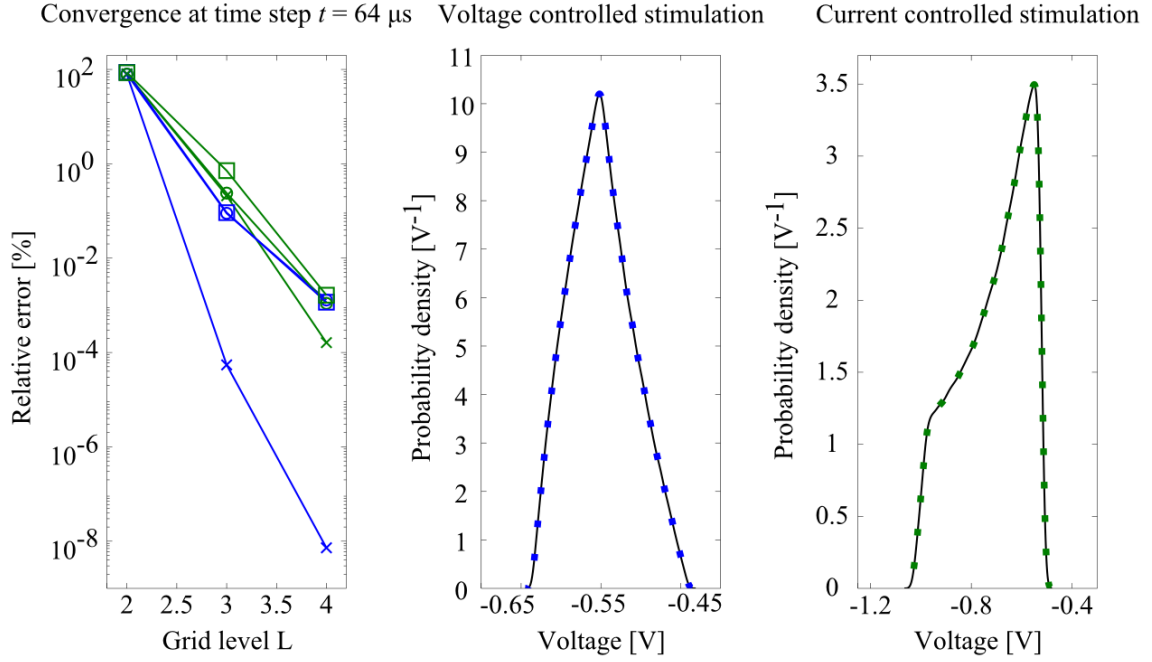


Figure 5.25: Convergence of the variance of the probabilistic voltage response 1 mm from the active electrode contact at a time step $t = 64 \mu\text{s}$ (left) and the corresponding probability density determined using a sparse grid with grid level $L = 3$ (black) as well as with grid level $L = 4$ for voltage-controlled (middle) and current-controlled stimulation (right) for a probabilistic relative permittivity as well as conductivity. Convergence is shown for probabilistic relative permittivity (crosses), probabilistic conductivity (circles), and probabilistic relative permittivity and conductivity (squares) for voltage-controlled (blue) and current-controlled stimulation (green).

required grid level resulted in the application of a $S(4, 2)$ and $S(4, 4)$ sparse grid corresponding to 65 and 401 executions of the deterministic model for the first two cases and the third case, respectively. The convergence of the applied $S(4, 2)$ and $S(4, 4)$ sparse grids in the corresponding study cases was similar for voltage-controlled and current-controlled stimulation with a minimum in the relative error in the case of a probabilistic relative permittivity for voltage-controlled stimulation compared to the other cases. Investigating the magnitude of uncertainty of the probabilistic voltage response revealed a value of below 0.01 % in this case, which is negligible compared to the other cases and may be one explanation for the faster convergence (Table 5.9). While the probability density for voltage-controlled stimulation is almost symmetric, that for current-controlled stimulation revealed an asymmetric probability density, which results from the inversely proportional dependence of the impedance of the volume conductor model described in section 3.3.2 and, therefore, of the transfer function on the applied stimulation current as stated in Ohm's law. For voltage-controlled stimulation, this influence is decreased by the impedance of the constant

Parameters	Uncertainty in RMS voltage response [%]	
	Voltage-controlled	Current-controlled
κ	7.23	18.34
ε_r	0.01	0.70
κ & ε_r	7.23	18.36

Table 5.9: Uncertainty in the probabilistic RMS value of the voltage response within 2.5 mm from the active electrode contact for voltage-controlled and current-controlled stimulation for a magnitude of uncertainty in the model parameters of $\sigma_r = 20\%$.

phase element acting as a frequency dependent voltage divider as described in equation (3.54) [57]. The different influence of uncertainty on the probabilistic voltage response for voltage-controlled and current-controlled stimulation is apparent from the investigation of its 0.025 and 0.975 quantiles for both stimulation types as well (Fig. 5.26). Similar results were determined for the magnitude of uncertainty of the probabilistic voltage response within 2.5 mm of the active electrode contact, which was determined as described in section 5.3.2.

The uncertainty in the probabilistic voltage response for current-controlled stimulation was of the same magnitude as the uncertainty in the probabilistic conductivity of brain tissue (Table 5.9), while the relative permittivity of brain tissue had a negligible influence on the uncertainty in the probabilistic voltage response for voltage-controlled as well as for current-controlled stimulation. A similar result was reported in a computational DBS study for current-controlled stimulation [17]. However, the mentioned parameter study was limited to the investigation of a halved and doubled relative permittivity value in a homogeneous analytical model and did not consider uncertainty in the material properties of brain tissue to quantify the integrated influence for the conductivity as well as relative permittivity for gray matter and white matter. The major influence of uncertainty in the probabilistic conductivity suggests that uncertainty in the probabilistic relative permittivity is negligible in the generated volume conductor model for DBS, which arises from the domination of the real part of the complex conductivity compared to the imaginary part, which represents the capacitive properties of the brain tissue, and is in agreement with the investigation of the capacitive effect for the frequency spectrum of the DBS pulse (Fig. 5.6) [100]. Therefore, this result confirms the statement that for the computation of the time-dependent voltage response in the volume conductor model of the human brain, the application of the QS formalism could be a good approximation of the EQS formalism for combinations of the relative permittivity and conductivity of brain tissue, for which the capacitive effect is negligible. For the application of the QS formalism, the system matrix would be symmetric positive definite and real

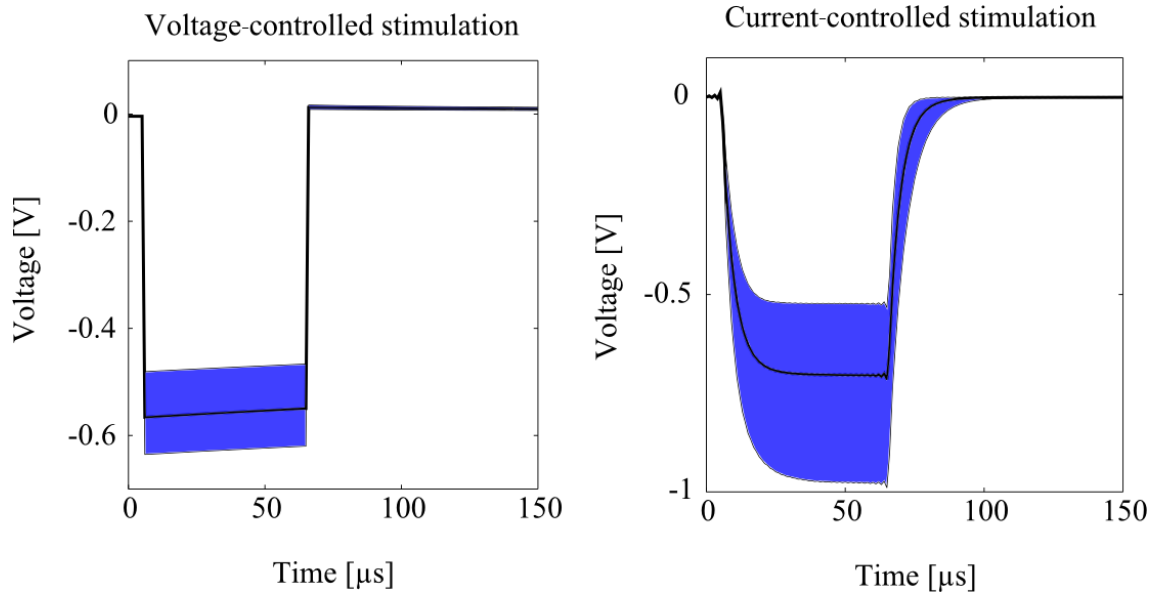


Figure 5.26: Mean value and 0.025 quantile as well as 0.975 quantile of the probabilistic voltage response 1 mm from the active electrode contact for a probabilistic conductivity and relative permittivity with $\sigma_r = 20\%$.

valued, which would allow for the application of the CG method. In addition, CG method uses short recurrences, while GMRES uses long recurrences, which makes CG method computationally less expensive than GMRES for these applications [127]. Nevertheless, it should be noted that the QS formalism would result in square-wave shaped voltage response for current-controlled stimulation. Nevertheless, the deviation of the QS solution from the EQS solution would presumably cause a substantial deviation in the computed VTA, which strongly depends on the slope of the voltage response in the proximity of the stimulated target, as described in section 5.2.2.

Probabilistic volume of tissue activated

The sensitivity analysis carried out on the probabilistic conductivity, the probabilistic relative permittivity, and their combination revealed that the uncertainty in the probabilistic voltage response in the proximity of the stimulated target can be modelled accurately by only considering the uncertainty in the probabilistic conductivity. Therefore, the computationally expensive investigation of the uncertainty in the probabilistic VTA is only carried out for this case. To allow for a prediction of the maximal magnitude of uncertainty in the probabilistic conductivity to obtain a prescribed magnitude of uncertainty in the probabilistic VTA, the probabilistic conductivity was modelled for different relative standard deviations σ_r of 10 %, 20 %, and 40 %, corresponding to its variations reported in literature. Depending on the

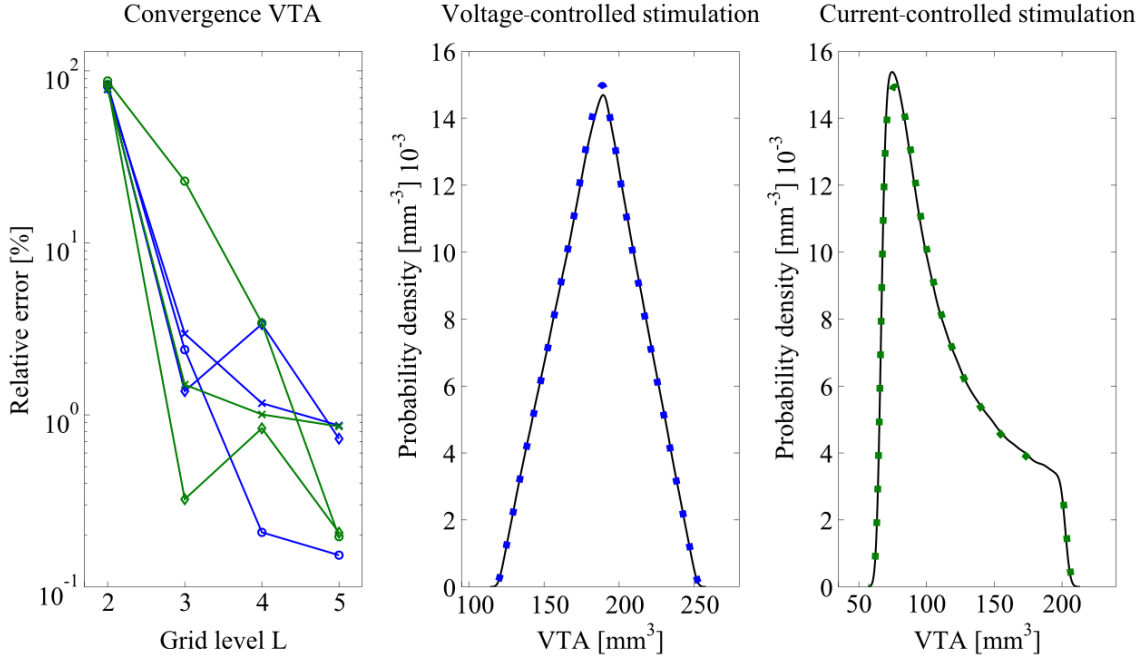


Figure 5.27: Convergence of the variance of the probabilistic VTA for a stimulation amplitude of $A_{vc} = -1.5$ V and $A_{cc} = -1.5$ mA (left) and the corresponding probability density determined using a sparse grid with level $L = 5$ for voltage-controlled (middle) and current-controlled stimulation (right) compared to a sparse grid with level $L = 4$ (black), respectively for a probabilistic conductivity with $\sigma_r = 20$ %. Convergence is shown for $\sigma_r = 10$ % (crosses), $\sigma_r = 20$ % (diamonds), and $\sigma_r = 40$ % (circles) for voltage-controlled (blue) and current-controlled stimulation (green).

application of the computed probabilistic voltage response and VTA in the volume conductor model of the human brain, such as the deployment as a supportive software for a clinician in the pre-operative planning stage of a DBS surgery, or for computational studies in neural networks to investigate the mechanisms of DBS, different magnitudes of uncertainty in these quantities are required. The computation of a large amount of different magnitudes of uncertainty in these quantities is computationally expensive, because it requires the computation of the model solutions at the nodes of the used integration technique for a large amount of different magnitudes of uncertainty in the model parameters. Therefore, a polynomial fit is applied to the magnitudes of uncertainty in the probabilistic VTA for the different relative standard deviations of the probabilistic conductivity using least-squares method.

It was ensured that the relative error of the variance of the probabilistic VTA for each case converged to a value below 1%, which required sparse grids up to a grid level $L = 5$, resulting in 145 executions of the deterministic model (Fig. 5.27). To allow for a better comparison of the absolute uncertainty in the VTA, a stimulation amplitude of $A_{vc} = -1.5$ V and $A_{cc} = -1.5$ mA for voltage-controlled and current-

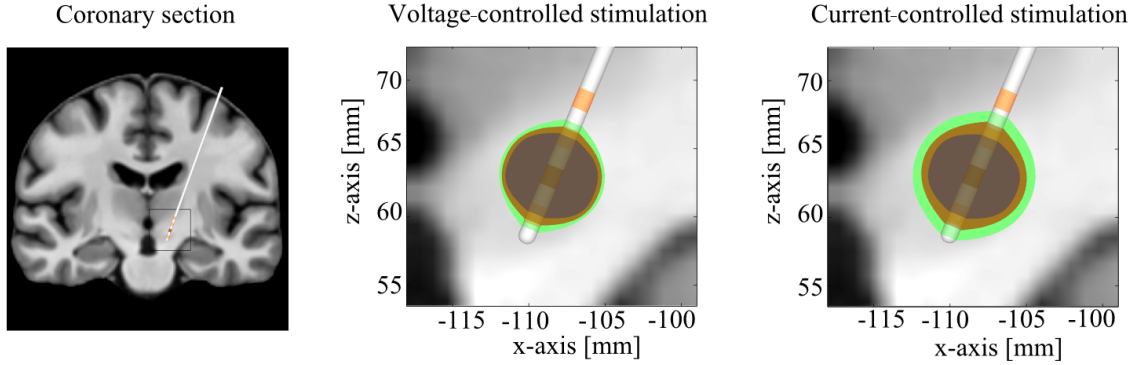


Figure 5.28: Coronary section of the MRI data set with the DBS electrode overlaid with the probabilistic VTA for voltage-controlled and current-controlled stimulation with $A_{vc} = -1.5$ V and $A_{cc} = -1.5$ mA, respectively. The mean value (orange), 0.025 quantile (dark blue), and 0.975 quantile (green) for a probabilistic conductivity with $\sigma_r = 20$ % are shown.

controlled stimulation were applied, respectively. Other stimulation amplitudes were used as well and a relative error in the variance of the VTA below 1 % was ensured in each case. Similar to the results of the uncertainty quantification for the parameters of the electrode-tissue-interface, the convergence of the variance of the probabilistic VTA decreased compared to the convergence of the variance of the probabilistic voltage response, which could be caused by the non-linear axon model required for the computation of the VTA and the application of backward Euler implicit integration to obtain the solution in time-domain as described in section 3.6. Despite the decreased convergence, an additional fluctuation is noticeable for an uncertain conductivity with $\sigma_r = 20$ % for voltage-controlled as well as for current-controlled stimulation, resulting in a local increase of the relative *a posteriori* error. These fluctuations are caused by the definition of the relative *a posteriori* error, which considers the relative local change from a certain grid level k to grid level $k + 1$. Nevertheless, it was ensured that the estimated PDFs for these cases at a sparse grid level $L = 5$ are in a good agreement compared to those obtained from their previous sparse grid level $L = 4$, which suggests that a further refinement of the integration grid is not necessary. The symmetry and asymmetry in the probability density of the probabilistic voltage response for voltage-controlled and current-controlled stimulation (Fig. 5.25), respectively, exists in the probability density of the corresponding probabilistic VTA as well ². In addition, the different influence of uncertainty in the electrical properties on the time-dependent voltage response for both stimulation

²For current-controlled stimulation, the PDF of the probabilistic VTA is mirrored compared to the PDF of the probabilistic voltage response, because cathodic stimulation amplitudes are used, which means that larger stimulation amplitudes resulting in larger VTAs are located at the left side of the plot.

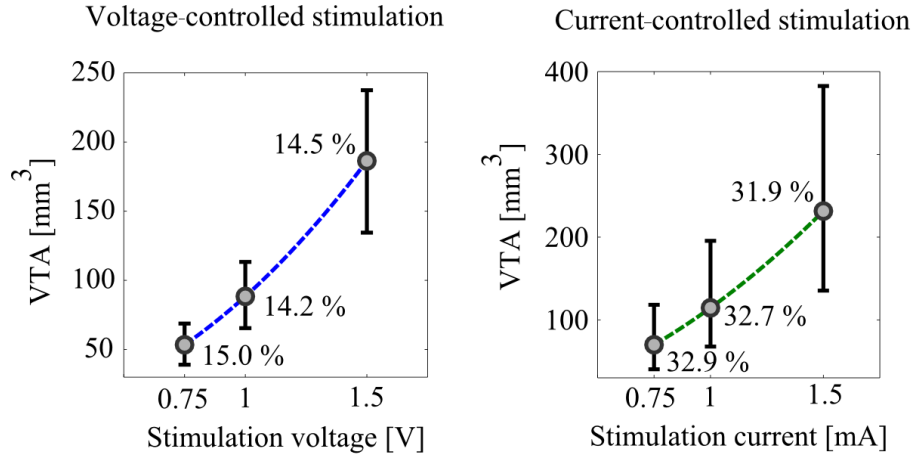


Figure 5.29: Mean value, 0.025 quantile, 0.975 quantile, and relative standard deviation of the probabilistic VTA for voltage-controlled and current-controlled stimulation with different stimulation amplitudes.

types is also noticeable in the corresponding VTAs, resulting in different extents of activated areas around the DBS electrode with a 0.025, mean value, and 0.975 quantile of approximately (139 mm^3 , 231 mm^3 , 370 mm^3) for a current-controlled stimulation with $A_{cc} = -1.5 \text{ mA}$ and (141 mm^3 , 186 mm^3 , 231 mm^3) for voltage-controlled stimulation with $A_{vc} = -1.5 \text{ mV}$ (Fig 5.28). Considering the computed probabilistic VTA in the generated volume conductor model of the human brain and the resulting range of values of the VTA for both stimulation types, the volume of the STN, which is about 160 mm^3 [140], would presumably be activated by these stimulation amplitudes.

The application of different stimulation amplitudes for voltage-controlled and current-controlled stimulation results in different extents of uncertainty in the VTA (Figure 5.29). The different PDFs for voltage-controlled and current-controlled stimulation types result in a symmetric and asymmetric uncertainty around the mean value, respectively. Although the absolute uncertainty of the VTA increases for larger stimulation amplitudes in both stimulation types, the relative standard deviation remains almost constant. Nevertheless, a larger absolute uncertainty in the probabilistic VTA results in a larger uncertainty of over- and underestimation of the predicted area of neural activation, in which no neural stimulation is desired. For current-controlled stimulation, the asymmetric PDF suggests that a larger range of probable VTAs exist above the mean predicted VTA, which results in larger areas of overestimated neural activation. The relative standard deviation of the VTA increased from approximately 7 % to 31 % for voltage-controlled stimulation and from approximately 14 % to 84 % for current-controlled stimulation in dependence of the magnitude of uncertainty in the probabilistic conductivity from 10 % to 40 % (Table 5.10). The uncertainty in the average RMS voltage response within 2.5 mm

Conductivity [%]	Voltage-controlled [%]		Current-controlled [%]	
	RMS voltage response	VTA	RMS voltage response	VTA
10	3.6	7.1	8.8	14.0
20	7.2	14.5	18.3	31.9
40	15.7	30.7	43.8	84.0

Table 5.10: Relative standard deviations σ_r in [%] of the average probabilistic RMS voltage response within 2.5 mm distance of the active electrode contact as well as of the probabilistic VTA for a stimulation amplitude of $A_{vc} = -1.5$ V and $A_{cc} = -1.5$ mA for voltage-controlled and current-controlled stimulation, respectively.

distance from the active electrode contact was computed similar to the investigation of uncertainty in the parameters of the electrode-tissue-interface described in section 5.3.2. The results reveal a larger magnitude of uncertainty for current-controlled stimulation in the probabilistic voltage response as well as the probabilistic VTA, for which evidence was noticeable in the probabilistic voltage response (Fig. 5.26) and the extent of the probabilistic VTA (Fig. 5.28). The uncertainty in the probabilistic voltage response is almost of the same magnitude as that in the probabilistic conductivity for different prescribed magnitudes of uncertainty as discussed already for a $\sigma_r = 20$ %. For a $\sigma_r = 40$ % of the probabilistic conductivity, the relative standard deviation of the probabilistic voltage response for current-controlled stimulation was approximately 44 % and, therefore, slightly larger than the parameter uncertainty. To exclude approximation errors, the relative standard deviation of the probabilistic voltage response was also computed for an increased polynomial degree of up to 7, which resulted in a change of below 0.1 % of its variance and almost no change in its PDF. Therefore, it is assumed that this effect results from the inversely proportional dependency of the voltage response on the applied stimulation current, as discussed earlier in this section. The magnitude of uncertainty in the probabilistic VTAs almost doubled compared to that in the average probabilistic RMS voltage response for both stimulation cases. It is assumed that this is an effect of the non-linear membrane dynamics of the mammalian nerve fibres used in the applied axon model of McIntyre et al. [82]. A larger fluctuation of the VTA compared to the change in the conductivity of brain tissue was also reported for voltage-controlled stimulation in an *in silico* study in which the same axon model was used for the computation of the VTA [24]. Although the magnitude of uncertainty in the probabilistic VTA for voltage-controlled stimulation was smaller than for current-controlled stimulation, impedance changes in voltage-controlled stimulation, caused, for example, by the post-operative impedance changes in the encapsulation layer described in section 3.5.3, could result in a substantial change of the VTA over time. Measurements

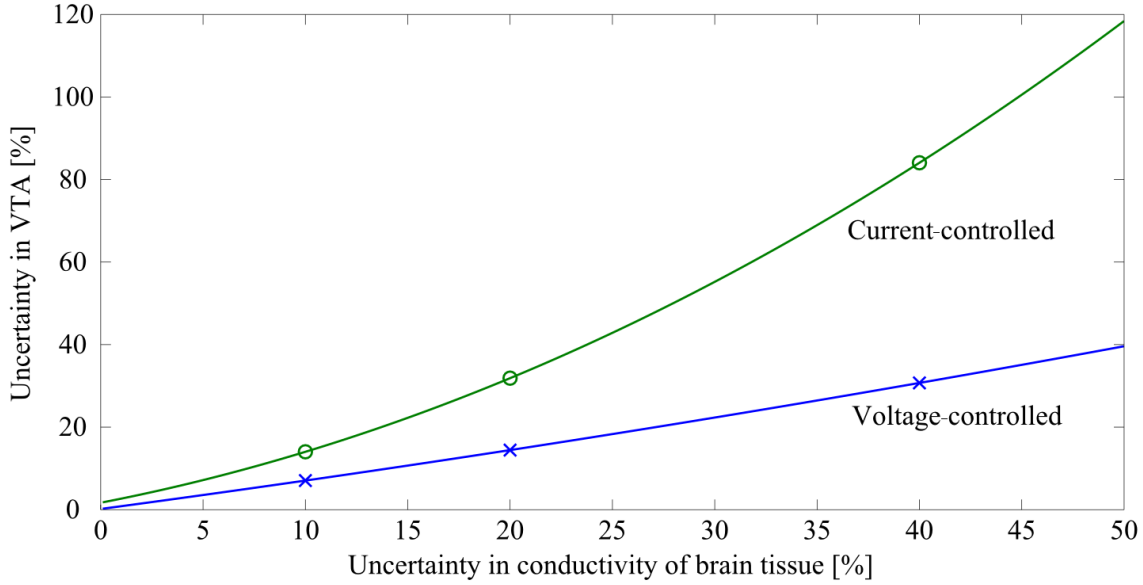


Figure 5.30: Magnitude of uncertainty in the VTA for voltage-controlled and current-controlled stimulation in dependence of the magnitude of uncertainty in the uniformly distributed conductivity of brain tissue overlayed with a polynomial fit of degree $p = 2$.

of the electrode impedance in an *in vivo* study performed in non-human primates showed a substantial change of the impedance and voltage distribution of approximately 50 % for voltage-controlled and only approximately 7 % for current-controlled stimulation after 60 minutes of stimulation [78]. This result suggests that the VTA for current-controlled stimulation would remain more constant over time, while the VTA for voltage-controlled stimulation could change substantially. Comparing the determined magnitude of uncertainty in the probabilistic voltage response and probabilistic VTA for uncertain parameters of the electrode-tissue-interface discussed in section 5.3.2, the determined influence of uncertainty in the electrical properties of brain tissue on these quantities is substantially larger, emphasising the insensitivity of the probabilistic voltage response and VTA on uncertainty in the electrode-tissue-interface in the generated volume conductor model of the human brain. As described at the beginning of this section, the aim was to predict boundaries for the magnitude of uncertainty in the probabilistic conductivity of brain tissue to obtain a prescribed magnitude of uncertainty in the probabilistic VTA. A polynomial fit of second degree was applied to their magnitudes of uncertainty in dependence of the prescribed values for the probabilistic conductivity (Fig. 5.30). Regarding the minor extent of the predicted neural activation for a magnitude of uncertainty in the probabilistic VTA of approximately 14 % voltage-controlled stimulation (Fig. 5.28), a value of 5 % was considered to be a proper first estimation boundary for the magnitude of uncertainty in the probabilistic VTA. Because of the similar magni-

tudes of uncertainty for different stimulation amplitudes, the determination of the uncertainty boundaries in the electrical properties of brain tissue was carried out for a representative stimulation amplitude of $A_{vc} = -1.5$ V and $A_{cc} = -1.5$ mA, which among the investigated stimulation amplitudes would most likely activate the area of the STN [97]. The results suggest that for a magnitude of uncertainty in the probabilistic VTA of below 5 %, the magnitude of uncertainty in the conductivity of brain tissue should remain below approximately 7.0 % for voltage-controlled and 3.1 % for current-controlled stimulation. These estimated boundaries of uncertainty in the conductivity of brain tissue are substantially lower than the variation of these values found in literature, as described in section 5.3.3. While this boundary of uncertainty for voltage-controlled stimulation increases almost linear with the uncertainty in the VTA, a quadratic dependence can be noted for current-controlled stimulation, resulting in the requirement of more precise knowledge about the electrical properties of brain tissue compared to voltage-controlled stimulation.

The results suggest that uncertainty in these parameters can have a substantial effect on the probabilistic time-dependent voltage response in the proximity of the stimulated target as well as on the predicted probabilistic VTA in the generated volume conductor model of the human brain. For example, the extent of the VTA varied by up to 2 mm for a current-controlled stimulation amplitude of $A_{cc} = -1.5$ mA and a magnitude of uncertainty of 20 % in the probabilistic conductivity (Fig. 5.28), which is still located in the lower value set of uncertainty in this parameter found in literature (Table 5.7). The stimulated target area, the STN, has a supposable diameter of about 10 mm [97] and can be classified in a limbic, associative and motoric domain [62], which have different effects on the motor symptoms of PD when stimulated [41]. Therefore, the results of this study suggest that even small changes of the electrical conductivity in volume conductor models of DBS can have a relevant influence on the computed therapeutical effect, especially for current-controlled stimulation. The boundaries for the magnitude of uncertainty in the electrical properties of brain tissue are determined for a "worst-case" scenario, assuming uniform distributions. These boundaries could vary for different probability distributions, such as Gaussian distributions, the application of which could result in sharper boundaries of uncertainty in the electrical properties of brain tissue.

5.4 Influence of the anisotropic conductivity and electrode position

The studies and results presented in the following section are based on the publication "Modeling the Field Distribution in Deep Brain Stimulation: The Influence of Anisotropy of Brain Tissue" [109] and have been extended by investigating the influence of the anisotropic conductivity and the electrode position on the time-dependent

voltage response computed for the single frequency approximation of the EQS volume conductor model of the human brain at a frequency of 2 kHz, as described in section 5.2.3.

Current volume conductor models of DBS include several parameters to allow for a realistic computation of the time-dependent voltage response and prediction of the neural activation [21, 57, 142]. Among others, these parameters include the electrode location as well as the electrical properties of brain tissue. Following the results and discussions in section 5.3.3, the electrical properties of brain tissue are subject to uncertainty, resulting in non-negligible uncertainties in the probabilistic voltage response and VTA in the human brain model. As described in section 3.4, the electrical properties of brain tissue are anisotropic with different extents, depending on their location in the brain. The anisotropic conductivity of brain tissue in the generated volume conductor model is determined out of the DTI data of the digital brain atlas and the isotropic conductivity of brain tissue at the corresponding location as described in equation (3.59). Regarding this dependency, the deviation in the probabilistic voltage response resulting from influence of anisotropic conductivity is considered to accumulate with the uncertainties in the probabilistic voltage response determined in section 5.3.3. Therefore, the influence of anisotropic conductivity on the time-dependent voltage response was investigated separately to the quantification of its uncertainties. Both parameters, the anisotropic conductivity and the variation of the electrode position, increase the model complexity which may lead to a larger computational expense. Consequently, a small influence of these parameters could result in volume conductor models with reduced complexity, because no acquisition and processing of DTI data would be necessary. This would increase the potential applicability of such a model as a supportive tool in clinical practise. Since the magnitude of anisotropy varies for the different brain tissue types and their locations in the brain, an accurate localisation of the electrode in the stimulated target area is crucial. Therefore, the aim was to investigate the influence of the anisotropic conductivity of brain tissue on the time-dependent voltage response for different locations of the DBS electrode in the proximity of the stimulated target area.

5.4.1 Anisotropic time-dependent voltage response

The anisotropic version of the volume conductor model was obtained by incorporating the anisotropic conductivity of gray and white matter into the ROI according to the description in section 3.5.3, using the DTI data of the digital brain atlas by Rohlfing et al. [104]. According to the description in section 3.4, gray matter and white matter are anisotropic, whereas CSF can be considered to be isotropic. The anisotropic conductivity at each node of the volume conductor model is denoted by the conductivity tensor in equation (3.58) with its eigenvalues representing the conductivity value along its corresponding eigenvector. The range of anisotropic conductivity values for gray and white matter based on their isotropic conductivity

Brain tissue	Conductivity values [Sm^{-1}]		
	κ_{iso}	$\min(\kappa_{\text{aniso}})$	$\max(\kappa_{\text{aniso}})$
White matter	0.06	0.03	0.21
Gray matter	0.10	0.07	0.16

Table 5.11: Range of anisotropic conductivity eigenvalues κ_{aniso} of gray and white matter within the ROI. Isotropic conductivity values κ_{iso} are taken from Gabriel et al. [46] at 2 kHz.

values from Gabriel et al. [46] at 2 kHz was computed within the ROI to determine their maximal and minimal boundaries (Table 5.11). According to Wolters et al. [137], white matter is known to be more anisotropic than gray matter, which is in agreement with the determined maximal and minimal conductivity values for both tissue types in the ROI. The influence of the anisotropic conductivity on the time-dependent voltage response was investigated in the proximity of the stimulated target with the electrode positioned at the location of the STN as described in section 3.5. Voltage-controlled and current-controlled stimulation of the previously used square-wave DBS signal in section 5.2.3 was applied with stimulation amplitudes of $A_{\text{vc}} = -1.5 \text{ V}$ and $A_{\text{cc}} = -1.5 \text{ mA}$, respectively. Investigating the resulting time-dependent voltage response 1 mm from the active electrode contact for voltage-controlled and current-controlled stimulation showed a minor influence of the anisotropic conductivity on the amplitude of the time-dependent voltage response and a negligible influence on its waveform shape (Fig. 5.31). The waveform shape of the time-dependent voltage response depends mostly on the computed transfer function of the volume conductor model, which is derived from its impedance. Since the anisotropic conductivity tensors are determined to resemble the volume of the isotropic conductivity tensors, the impedance of the anisotropic volume conductor model and, therefore, the transfer function resemble those of the isotropic volume conductor model, resulting in a similar waveform shape in both models. In addition to the time-dependent voltage response 1 mm from the active electrode contact, the distribution of the electric potential of the anisotropic and isotropic volume conductor model was investigated. The influence of the anisotropic conductivity deforms the shape and the spatial extent of the electric potential in the proximity of the DBS electrode (Fig. 5.32), which was also reported in other computational studies [23, 83]. Similar to the deviation in the time-dependent voltage response, only a minor deviation between the isolines of the anisotropic and isotropic electric potential could be noted. Evidently, the potential isolines of the anisotropic volume conductor model are influenced by the magnitude of the anisotropic conductivity ratio determined in each voxel by using equation (3.60). Since the anisotropic conductivity varies in the proximity

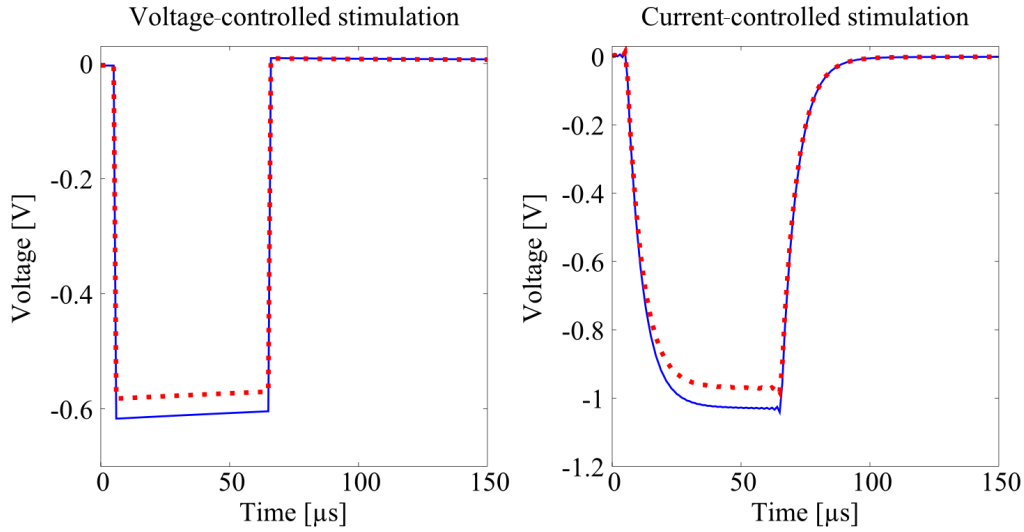


Figure 5.31: Time-dependent voltage response in 1 mm distance caudal from the active electrode contact for isotropic (blue) and anisotropic (red) electrical properties of gray and white matter.

of the stimulated target and around the electrode body, an investigation of the deviation between the anisotropic and isotropic time-dependent voltage response in this area is required for its quantification. Therefore, the relative error of the RMS of the time-dependent voltage response and the electric potential was computed at the nodes of a 4×4 grid revolved around the active electrode contact with a stepping of 10° , resulting in 576 nodes. The spacing of the nodes was 0.5 mm parallel and perpendicular to the electrode body. The average deviations for the time-dependent voltage response and electric potential at the nodes were similar for voltage-controlled as well as for current-controlled stimulation (Table 5.12). This is in agreement with previous results on the similarity between the influence of anisotropic conductivity on the time-dependent voltage response and electric potential in the proximity of the stimulated target in Figure 5.31 and Figure 5.32. Following these results, the anisotropic conductivity mostly influences the amplitude of the time-dependent voltage response in the proximity of the stimulated target, but not its waveform shape. Therefore, the VTA will most likely resemble these deviations, similar to the results in section 5.2.3. The magnitude of the deviation between the time-dependent voltage response in the proximity of the stimulated target was approximately 4 % for voltage-controlled and current-controlled stimulation (Table 5.12). This minor deviation results from the small anisotropy ratios in this area. Taking into account the DTI data voxels in the investigated area, which resembles a cube with the length $(x, y, z) = (6 \text{ mm}, 6 \text{ mm}, 4 \text{ mm})$, an average anisotropy ratio of approximately 1 : 1.7 was determined in this area (Fig. 5.33). About 92 % of the voxels have an anisotropy ratio smaller than 1 : 2. These anisotropy ratios in

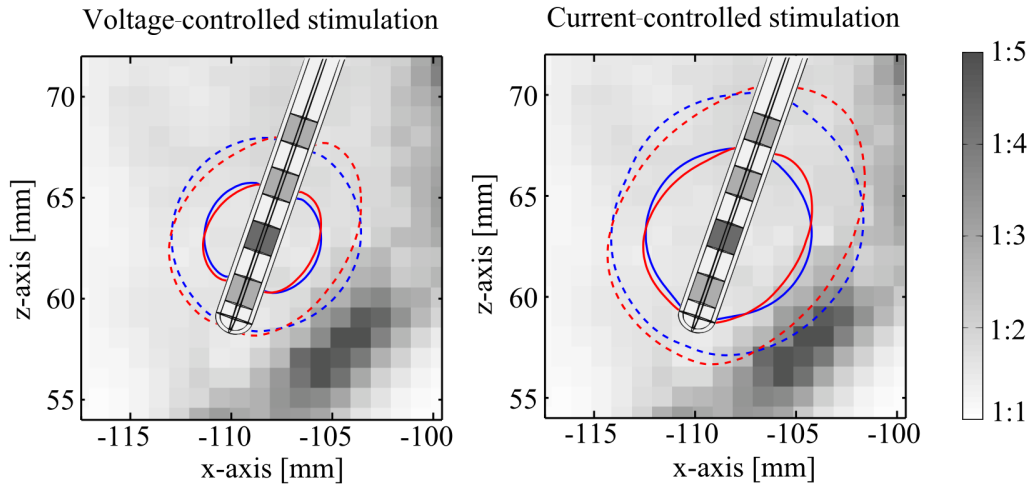


Figure 5.32: Distribution of the electric potential in a coronary section of the human brain model for isotropic (blue) and anisotropic (red) electrical properties of gray and white matter. Isolines for electric potential values of 0.3 V (solid) and 0.15 V (dashed) are shown. Anisotropy ratio of the anisotropic conductivity is illustrated in the background with dark gray voxels representing areas of a high anisotropy ratio.

Stimulation type	Quantity	Mean relative error [%]
Voltage-controlled	RMS voltage response	4.06
	Electric potential	4.06
Current-controlled	RMS voltage response	4.36
	Electric potential	4.35

Table 5.12: Average relative errors of the RMS values of the time-dependent voltage response and of the electric potential.

the proximity of the STN are much smaller than those used in other computational studies of an anisotropic volume conductor model of the human brain, where the anisotropy ratio was set to 1 : 10 [7, 137]. The STN is a nucleus consisting out of gray matter with axons oriented almost randomly. According to Shimony et al. [116] this histological property results in a minor average anisotropy ratio. Moreover, the fibre pathways around the STN are not parallel, thus yielding small anisotropy ratios in the proximity of the STN [2], which is in agreement with the minor deviation in the time-dependent voltage response and anisotropy ratio in the proximity of the stimulated target determined in the volume conductor model.

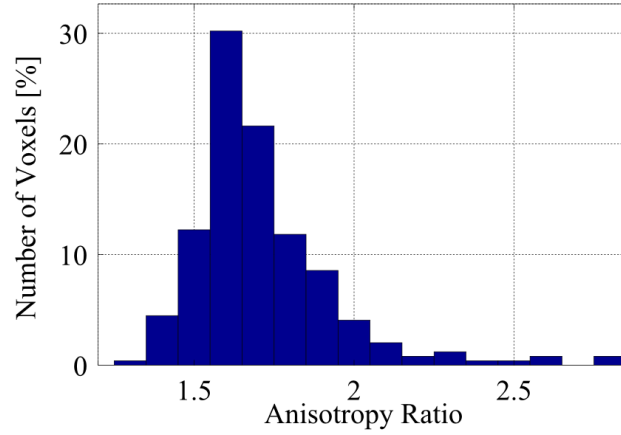


Figure 5.33: Histogram of the anisotropy ratio in the proximity of the stimulated target.

5.4.2 Variation of the electrode position

Despite the application of accurate methods, such as MRI, CT, and stereotactic surgery, the positioning of the DBS electrode in the deep brain target area may vary from the planned location in clinical practise [98]. To investigate the influence of a slightly misplaced DBS electrode, the electrode position in the volume conductor model was varied by ± 2 mm around the stimulated target location used in section

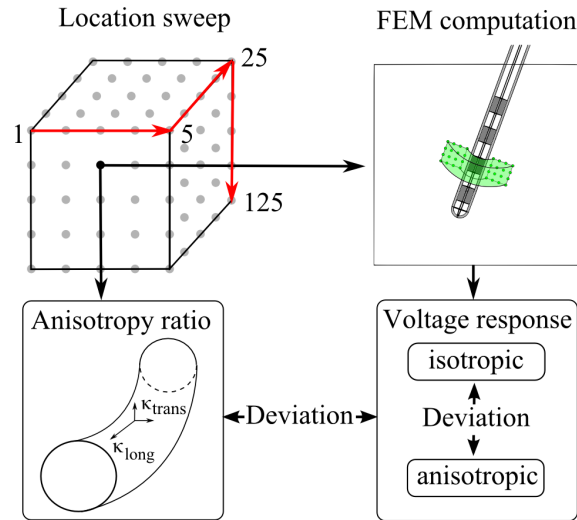


Figure 5.34: Schematic illustration of the variation of the electrode position. For each of the 125 nodes, the stimulation center, including the DBS electrode and ROI, is repositioned and the deviation of the RMS of the isotropic and anisotropic time-dependent voltage response is compared with the anisotropy ratio in the corresponding area.

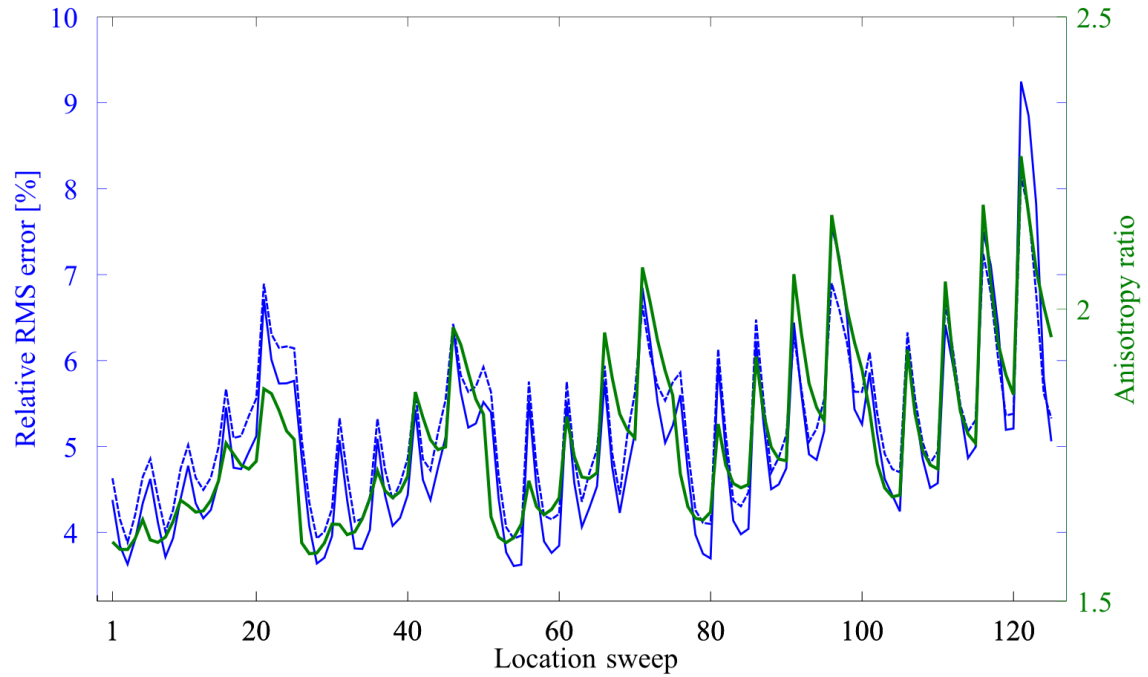


Figure 5.35: Relative RMS error (blue) for voltage-controlled (solid) and current-controlled (dashed) stimulation compared to the average anisotropy ratio (green) at each investigated electrode location.

5.4.1 with a stepping of 1 mm in each spatial direction resulting in a cuboid grid with 125 nodes (Fig. 5.34). At each node the deviation of the RMS value of the anisotropic and isotropic voltage response as well as the average anisotropy ratio in the proximity of the repositioned DBS electrode was computed as carried out for the position of the STN in section 5.4.1.

The deviation of the RMS value of the anisotropic and isotropic voltage response for voltage-controlled and current-controlled stimulation resembled the average anisotropy ratio at each investigated electrode position (Fig. 5.35). Computing the quotient of the average RMS deviation and the average anisotropy ratio resulted in a scaling factor of approximately 2.8 for voltage-controlled stimulation and 2.9 for current-controlled stimulation (Table 5.13). Since the computation of the average anisotropy ratio in the DBS target area can be carried out with a small computational expense in pre-processing, these scaling factors allow for a first prediction of the possible influence of the anisotropic conductivity on the time-dependent voltage response in the stimulated target area for different electrode locations. The variation of the electrode position resulted in a deviation of the time-dependent voltage response between approximately 3.6 % and 9.2 % with a mean value of approximately 5 % for both voltage-controlled and current-controlled stimulation. Under the assumption of a similar progression of the deviation in the time-dependent voltage response on

Stimulation type	Average RMS error [%]	Average scaling factor
Voltage-controlled	5.02 ± 1.06	2.80 ± 0.38
Current-controlled	5.24 ± 0.86	2.93 ± 0.29

Table 5.13: Average relative errors of the RMS values of the time-dependent voltage response and scaling factor for their prediction by the average anisotropy ratio.

the deviation in the corresponding VTA as obtained in section 5.3.3, the deviation between the anisotropic and isotropic VTA can be predicted to be in the order of approximately 8 % to 10 %. Considering the extent of the VTA for voltage-controlled stimulation with a magnitude of uncertainty σ_r of approximately 14 % in Figure 5.28, the predicted influence of anisotropic conductivity on the estimation of the VTA would most likely be of no interest in clinical practise, unless the deviation occurs more locally, as it would be the case in the proximity of white matter fibre bundles with the same orientation and a large anisotropy ratio. Nevertheless, as described in section 3.4, the anisotropic conductivity at each spatial position in the volume conductor model is dependent on the corresponding isotropic conductivity at this position, which suggests that the influence of uncertainty in the conductivity of brain tissue and the influence of anisotropy on the time-dependent voltage response and VTA would cumulate.

These results suggest that an isotropic volume conductor model of the human brain could be sufficient for several applications in the modelling of DBS as long as the electrical properties of brain tissue are known to a certain precision as discussed in section 5.3.3. The electrode positions at the peaks of the relative RMS error in Figure 5.35 resemble locations close to areas of a high average anisotropy ratio such as the internal capsule and corticospinal tract. These brain regions consist of white matter, have evenly oriented fibre bundles and, therefore, a high anisotropy ratio, resulting in larger deviations of the time-dependent voltage response [8]. Therefore, applications of DBS stimulation in which the DBS electrode is positioned in areas with a high anisotropy ratio may not be properly modelled by an isotropic volume conductor model of the human brain.

5.5 Limitations of the volume conductor model and the applied methods

The applied methods for the computation of the time-dependent voltage response and the VTA in the proximity of the stimulated target as well as the uncertainty quantification and sensitivity analysis for these quantities in the generated volume conductor model for human DBS are based on various assumptions and, therefore,

exhibit several limitations.

The application of a model geometry in the volume conductor model, which resembles the anatomy of the human brain, is based on computational studies, which determined the model geometry to be a crucial factor for an accurate computation of the time-dependent voltage response in the human brain [79, 132]. To represent the real anatomical dimensions of the human brain as well as a realistic distribution and representation of the electrical properties of different brain tissue types, MRI and DTI data from a digital brain atlas have been incorporated into the volume conductor model. These voxel data are available as a hexahedral mesh with an isotropic resolution of 1 mm in each spatial dimension. Contrary, the fibre diameters of the deviating oriented neurons in the STN are in the order of μm , resulting in an averaging to mean values in the fibre orientation and anisotropy ratio on a macroscopic level. In the case of crossing fibre bundles with a presumably large anisotropy ratio this averaging could result in a prediction of a locally small anisotropy ratio and, therefore, in a small anisotropic conductivity, which would not accurately represent accurately the real anisotropy at the corresponding location. An investigation of the effects of a higher resolution of the anisotropic conductivity within a macroscopic volume conductor model of the human brain could be obtained for DTI data with a voxel size below 1 mm^3 . However, smaller voxel sizes would not only require MRI scanners, which allow for such high resolutions, but would increase the computational complexity and intensity of the volume conductor model, for which at least in the proximity of the stimulated target a finer mesh resolution would be necessary. The volume conductor model is meshed using the Delaunay algorithm within Comsol MultiphysicsTM to discretise the computational domain into tetrahedral elements. To incorporate the electrical properties of brain tissue into the volume conductor model, the MRI and DTI data available as hexahedral mesh are mapped on the tetrahedral mesh of the human brain model using a nearest neighbour function, as described in 3.5.3. The resulting disconformities at the boundaries between the data voxels were sufficiently reduced by using a maximal element size in the tetrahedral mesh of 5 mm (Fig. 5.3). The application of a refined ROI around the stimulated target instead of using this maximal element size in the complete volume conductor model was necessary to keep the required amount of memory and computation time to obtain the model solution at a reasonable level. Compared to the approximately 1.4 million mesh elements in the optimised volume conductor model of the human brain, a mesh with a maximal element size of 0.5 mm in the complete volume conductor model would result in approximately 168 million mesh elements with approximately 224 million degrees of freedom for quadratically shaped finite element basis functions. This increase in the model complexity would result in a substantial increase of the computational expense for the acquisition of a better conformity of the finite element mesh with the tissue boundaries, which would most likely result in a comparatively small increase in the accuracy of the model solution in the proximity of the stimulated target area.

A possible approach to avoid these disconformities would be to explicitly model the nuclei of the basal ganglia motor network and their separate incorporation into the volume conductor model. To date however, no stable and precise automatic segmentation algorithm exists which is able to accurately segment the corresponding deep brain areas from MRI data of patients, who should undergo DBS surgery. Therefore, the explicit modelling of these nuclei would still require a manual segmentation of the MRI data as well as the subsequent volume mesh generation by a team of experts comprising computational engineers and physicians in the clinical field of neurology, which does not allow for a reasonably automated patient specific modelling. MRI data with a more refined segmentation in deep brain areas could improve the rendering of the heterogeneous tissue properties by automatic segmentation. The segmented MRI data from the SRI 24 multi-channel brain atlas agrees well with the overall anatomy of the brain, but does not fully render the comparatively small basal ganglia nuclei [104]. In the generated volume conductor model, the application of this already segmented MRI data resulted in areas of white matter which are anatomically consistent with gray matter and further in a prevalence of homogeneous white matter and, therefore, a small local effect of heterogeneous tissue properties in the proximity of the STN. Evidence for this almost homogeneous distribution of the electrical properties of brain tissue in the proximity of the stimulated target within the generated volume conductor model can be found by investigating the isolines of the electric potential of the isotropic human brain model (Fig. 5.32) and the thresholds of the axon models required for the computation of the VTA (Fig. 5.17), which both resembled a distribution of these quantities as they would be expected for a homogeneous distribution. These results suggest that a computation of the VTA by using a disk integration on the computed activation isoline in the coronary plane, as described in section 3.6, is a reasonable approximation for using the actual activation isolines around the electrode body at discretely distributed rotation angles for the prediction of the VTA. As described in section 5.3.2, this assumption was applied on the quantification of uncertainty in the average RMS value of the probabilistic voltage response in the isotropic volume conductor model as well, as described in section 5.3.2.

The method used for the computation of the VTA is a well-established procedure to predict the neural activation in volume conductor models for DBS and is applied in several computational studies [21, 57, 142]. Nevertheless, the method simplifies reality by prescribing a mutual parallel alignment of the neurons in the proximity of the stimulated target perpendicular to the electrode body. Contrary, the neurons of the STN exhibit a deviating orientation [2] and differ in fibre diameter, internodal spacing, and nodes of Ranvier, which results in different lengths of the neurons [120]. Considering the values of the axon model of McIntyre et al. [82] in the mentioned computational studies, the fibre diameter is set to a value of $5.7\text{ }\mu\text{m}$ [83]. However, the fibre diameters of neurons in the STN could be substantially smaller with values between $1\text{ }\mu\text{m}$ to $2\text{ }\mu\text{m}$ [1], which would reduce the excitability of the axons and,

therefore, increase the required stimulation amplitudes [120]. In the method for the computation of the VTA, predefined values for the parameters of the axon model are used and kept constant across each axon model at different spatial positions in the proximity of the stimulated target to compute the threshold voltages necessary to elicit an action potential in each of these axon models. The method only investigates whether an axon with the predefined parameters will be activated by the extracellular time-dependent electric potential of the volume conductor model and, therefore, does not investigate changes in the firing rate in the neurons of the STN. Computational studies showed that a change in the firing rate could already result in a beneficial effect on the pathological firing patterns in the basal ganglia network and is achieved for smaller thresholds compared to those for the computation of the VTA [144]. Moreover, since the method only considers neuron models in the proximity of the stimulated target, which are mutually independent in their activation, no insights about the effects of DBS on the complex network of the basal ganglia can be gained, as described in the computational network models of Modolo et al. [88] and Pirini et al. [99] in section 2.3.1.

The generated volume conductor model of the human brain, which is used to compute the time-dependent voltage response in the proximity of the stimulated target, depends on several parameters. Among these parameters, the sensitivity of the time-dependent voltage response on the electrode location, the parameters of the electrode-tissue-interface, and the electrical properties of brain tissue, including its frequency dependence and anisotropy, were investigated. The latter are subject to uncertainty because of the scarce measurement data of the dispersive electrical properties of brain tissue in literature [37]. This lack of data can be attributed to the taxing requirements and ethical questions that have to be dealt with during the realization of experimental studies [110]. Considering the anisotropy in the electrical properties of brain tissue, only data on the anisotropic conductivity was available, because DTI data only allows for its direct estimation [126]. To the author's knowledge, no applicable data on the anisotropy of the relative permittivity of brain tissue for volume conductor models of the human brain exists to date. A reasonable assumption would be to model the anisotropic relative permittivity to be perpendicularly oriented to the anisotropic conductivity along cell membranes [117]. However, considering the results for the influence of uncertainty in the relative permittivity of brain tissue on the probabilistic voltage response and VTA as discussed in section 5.3.3, an anisotropic conductivity would most likely have no influence on the computation of the time-dependent voltage response in the generated volume conductor model of the human brain. The electrical properties of the encapsulation layer, which is formed after surgery around the electrode body, were modelled to represent a stable post-operative state several weeks after surgery, as described in section 3.5.3. The variation of the electrical properties of the encapsulation layer for other post-operative phases would most likely result in a change of the time-dependent voltage response and VTA as reported for voltage-controlled stimulation [78].

The fast computation of the time-dependent voltage response in the generated volume conductor model of the human brain was carried out using the proposed Fourier finite element method with equivalent circuits (FFEMEC), which allows for its computation with a maximum of two executions of the volume conductor model. Yet, this method only considers frequency-independent material properties, which resulted in a maximal deviation of the VTA of about 5 % at the best approximating single frequency volume conductor model compared to that computed with the dispersive volume conductor model, using the frequency-dependent electrical properties data set from Gabriel et al. [46] as discussed in section 5.2.3. This maximal deviation only occurred for current-controlled stimulation and was substantially smaller for voltage-controlled stimulation. In addition, considering the results in section 5.3.3, a deviation of about 5 % would most likely have no substantial influence on the neuronal activation in clinical practise. However, the application of this method on other stimulated target areas in the human brain could result in different best approximating frequencies and orders of deviation in the computed VTA based on the distribution and characteristics of the dispersive material properties in the proximity of these areas as well as on the applied DBS pulse. Despite the assumption that the electrical properties of each biological tissue type are non-dispersive, the combined electrical properties of them in a volume conductor model can be dispersive, as described in section 3.3. The square of the capacitive effects allows for a first estimation whether the combined electrical properties in the volume conductor model are non-dispersive. It was shown in section 5.2.3 that the proposed method is valid for the computation of the time-dependent voltage response in the generated volume conductor model of the human brain. Nevertheless, the application of this method to different volume conductor models including biological tissue types has to be validated. For example, the condition (A.7), representing the combination of different tissue types, suggests that the method is only valid for biological tissue types, the electrical properties of which are in the same order of magnitude. Therefore, the proposed method may not be appropriate to model the acute phase of DBS, as described in section 3.5.3, in which the electrical properties of the encapsulation layer vary substantially from those of gray and white matter [143].

The quantification of uncertainty in the probabilistic voltage response and VTA was carried out by computing a polynomial approximation of these quantities, using the PC technique. This method requires the model parameters to be stochastically independent. To date, uncertainty quantification for stochastically dependent model parameters is still challenging. According to Cl  net [31], a possible approach would be to express the stochastically dependent model parameters as a function of probabilistic parameters depending on stochastically independent random variables, which is known as isoprobabilistic transformation. In general, for the computation of the polynomial approximations, a multi-variate basis of order $p = 3$ was used. It was ensured that an increase of the polynomial order does not substantially change the obtained PDFs of the investigated probabilistic quantity as well as its first two

moments, which were required to compute its relative standard deviation. This result is in agreement with empirical evidence obtained in other applications of the PC technique in different problems of engineering, where a polynomial expansion of third order was found to be the best compromise between accuracy and efficiency [122]. However, for non-uniformly distributed model parameters and non-linear functional dependencies in the deterministic model, a higher polynomial order might be necessary to obtain an accurate approximation of the probabilistic quantity. A higher polynomial order would most likely require an increase in the grid level of the multi-dimensional cubature rule as well, which would result in a larger computational intensity. Besides the order of the polynomial approximation and the number of cubature nodes, the convergence of the polynomial approximation depends on the functional characteristics of the investigated quantity of the deterministic model, such as continuity and smoothness, on the model parameters [122]. The EQS and QS formulations described in section 3.1 describe partial linear differential equations with mixed Neumann and Dirichlet boundary conditions, the solutions of which are smooth and continuous, resulting in an exponential convergence of the variance of the probabilistic voltage response (Fig. 5.25). The convergence of the variance of the probabilistic VTA decreased compared to that of the probabilistic voltage response, which is assumed to be an effect of the non-linear membrane dynamics of the multi-compartment axon model as described in section 5.3.3. Comparing sparse grid and tensor grid integration, the convergence for the application of sparse grids substantially decreased in certain cases (Fig. 5.24). These results show the limitation of the sparse grid integration technique, which theoretically reaches the same convergence order as tensor grids, but may decrease in applications with non-optimal functional characteristics [93].

In section 5.3.3 the influence of uncertainty in the electrical properties of gray and white matter on the probabilistic voltage response and VTA was investigated. Both brain tissue types form the proximity of the STN. CSF, which is mostly located in the ventricles, is a biological liquid, the electrical properties of which are comparatively well known. Therefore, possible uncertainty in the electrical properties of CSF was not investigated. However, for applications where the stimulated target is closer to areas of CSF, such as the ventricles, the influence of these uncertainties could be of interest [112]. Because of the scarce experimental literature for the electrical properties of gray and white matter, a uniform distribution of these parameters was assumed to represent some kind of a "worst case" scenario. For a more realistic representation of the parameter uncertainty, more experimental data would be required. In the case of the availability of a large data set of measurements with the same experimental setup, a Gaussian distribution of the data would be most likely. First tests carried out with Gaussian distributed model parameters showed a decreased convergence rate compared with that for uniformly distributed model parameters, which suggests that Legendre polynomials are not an optimal choice for non-uniformly distributed model parameters, which is in agreement with theory

as described in section 4.2.3. Especially for the simultaneous application of sparse grids, a too coarse integration grid can result in multi-modal PDFs, which would not properly reflect the "true" solution obtained with MCS. In the case of Gaussian distributed model parameters, a retrieval of the optimality could be obtained by using Hermite polynomials [108]. Since Hermite polynomials have a different support range compared to the Clenshaw-Curtis rule, a modification of the multi-dimensional cubature rule would be necessary to retain the benefits of using sparse Smolyak grids. Further studies are necessary to investigate the convergence and influence of model parameters with non-uniform distributions and the application of different sets of orthogonal basis functions as well as cubature rules on the probabilistic voltage response and VTA.

Despite the discussed simplifications, the proposed methods to quantify the uncertainty of the model parameters in an optimised anatomical volume conductor model of the human brain on the time-dependent voltage response and VTA allow for a first prediction of the uncertainty boundaries of the extent of neural activation with an optimised computational efficiency.

6 Conclusion and outlook

This thesis examines the influence of uncertainty in the electrical properties of brain tissue and the parameters of the electrode-tissue-interface on the time-dependent voltage response and VTA for DBS in a generated and optimised volume conductor model of the human brain. The generated volume conductor model was optimised in its complexity by investigating the influence of the anisotropic conductivity of brain tissue and the electrode position as well as by developing a method for the fast computation of the time-dependent voltage response in the proximity of the stimulated target by using the common Fourier finite element method (FFEM) in combination with equivalent circuits. The quantification of uncertainty in the time-dependent voltage response and VTA in the human brain model was obtained by using a computationally efficient polynomial expansion for the approximation of the probabilistic properties of these quantities. The results point out sensitive parameters of volume conductor models of the human brain and allow for a prediction of requirements in the precision of these model parameters, which could be used in software tools for planning surgery of DBS and to make physicians as well as engineers aware of the uncertainty in the predicted neural activation in the target area. Supportive software tools could be used in the pre-operative planning phase and during performance of the surgery, which claims the requirement of patient-specific human brain models.

The optimization of the computational expense and the reduction of the model order is carried out on two separate aspects, comprising the deterministic model and the uncertainty quantification based on probability sampling methods. The EQS formalism, which simplifies the full set of Maxwell's equations for bio-electrical applications, was verified for the human brain and its fast computation was carried out by the proposed Fourier finite element method with equivalent circuits (FFEMEC), which for frequency-independent material properties only requires a maximum of two executions of the finite element computation of the volume conductor model. The neural activation was predicted by using the well-established concept of the VTA. The uncertainty quantification of the time-dependent voltage response and the VTA was carried out using the non-intrusive PC technique, which requires the execution of the deterministic model only for the computation of the expansion coefficients instead of for a large number of probability samples in MCS. The required number of executions of the deterministic model was further reduced by the application of sparse grids with nested nodes. Besides the substantial reduction of the number of required model executions, nested sparse grids provide a convenient way of ensuring

convergence of the computed probabilistic quantity as well. Uncertainty quantification allows for several investigations of the probabilistic properties of the model solution from determining the moments of the probabilistic solution, such as its mean value and its variance as well as its confidence interval, to deriving functional characteristics from its PDF and prediction of uncertainty boundaries for the model parameters in dependence of a prescribed magnitude of uncertainty in the model solution. In addition, the non-intrusive variant of the PC technique does not require a modification of the deterministic model by utilizing it as some kind of a "black-box" and, therefore, allows for a simple application to other deterministic models subject to uncertainty in their model parameters. It could be shown that the non-intrusive PC technique in the present model of DBS is computationally advantageous compared to the classical MCS. This advantage is limited by the number of stochastically independent model parameters, which was at maximum four in this thesis. For a larger number of probabilistic model parameters, the classical MCS may be more appropriate. However, the computational expense of performing a classical MCS on the present model of DBS would be challenging to handle and a computation of the influence of their uncertainty on the model solution in a reasonable time would be questionable.

The validation of FFEMEC was carried out for the generated volume conductor model by comparing the time-dependent voltage response in the proximity of the stimulated target with that computed with common FFEM. The results showed a good agreement of both methods, suggesting that the proposed method is applicable in the generated volume conductor model of the human brain. The non-intrusive PC technique was compared with the classical MCS for 10,000 probability samples in the conductivity of brain tissue in a simplified volume conductor model of the human brain. A good agreement between the probabilistic time-dependent voltage response obtained with the PC technique and with MCS could be reached for the application of tensor grids as well as for sparse grids.

The computational advantage of the proposed FFEMEC is limited to the application of frequency-independent material properties. Since the electrical properties of brain tissue are frequency-dependent in the frequency spectrum of the applied DBS pulse, a best single frequency approximation of the dispersive volume conductor model was carried out, resulting in a best approximation of the frequency-dependent electrical properties of brain tissue at a frequency of approximately 2 kHz for a common DBS pulse. However, it should be kept in mind that this best approximating frequency may change patient-individually for different volume conductor models of the human brain, different target areas and electrical properties of brain tissue. Comparing the capacitive effect, which distinguishes the EQS and QS formulation in the frequency spectrum of the DBS pulse, the minimum of this effect may be a good predictor for the best single frequency approximation of the volume conductor model. Beside the application of common square-wave DBS pulses, smoothed DBS pulses were applied as well to reduce the number of required frequency components

in their spectrum using FFT. The discussion of the resulting VTAs for both DBS pulse types revealed that the slope of the pulse mostly influences the results, while the overshooting in the square-wave DBS pulse was of minor influence. Therefore, the results suggest that the computation of the time-dependent voltage response and VTA should be carried out for the application of the actual waveform of the DBS pulse despite a possible overshooting in the time-dependent voltage response. The investigation of the influence of uncertainty in the electrical properties of brain tissue and the parameters of the electrode-tissue-interface revealed a minor influence in the parameters of the electrode-tissue-interface. In addition, the results suggested that the uncertainty in the relative permittivity of brain tissue is negligible, and that consequently the uncertainty in the conductivity of brain tissue mostly influences the uncertainty in the time-dependent voltage response and VTA in the generated volume conductor model of the human brain. These results and those for the best single frequency approximation of the human brain model as well as the investigation of the capacitive effect, suggest that a QS formulation could be appropriate for modelling the time-dependent voltage response and VTA in the human brain model for DBS. The application of the QS formulation would result in a real valued system matrix, which is efficiently solvable using CG instead of GMRES.

The quantification of uncertainty in the probabilistic VTA revealed that for an uncertainty in the VTA of below 5%, the uncertainty in the conductivity of brain tissue has to be below 7% for voltage-controlled and 3% for current-controlled stimulation. To date, the variation in values of the conductivity of brain tissue in experimental literature is substantially larger than these predicted uncertainty boundaries, which demands a more precise determination of the electrical properties of brain tissue. Comparing the determined uncertainty in the time-dependent voltage response with the predicted influence of anisotropic conductivity in the proximity of the stimulated target, an isotropic volume conductor model of the human brain may be an appropriate simplification of the anisotropic human brain model. However, if more precise electrical properties of brain tissue are available and if the target areas are close to areas with a large anisotropy ratio, a consideration of anisotropic conductivity may be required. The quantification of uncertainty for the electrical properties of brain tissue and the parameters of the electrode-tissue-interface are important parameters for the computation of the time-dependent voltage response and VTA, but the uncertainty in the volume conductor model of the human brain is not limited to them. Further investigations of uncertainty in the parameters of the axon model, such as its fibre diameter, internodal spacing, and number of nodes of Ranvier, could result in a more thorough insight in the actual neural activation in the stimulated target area. In addition, to gain insight into the mechanisms of DBS, the computed probabilistic time-dependent voltage response should be used as a parameter for complex neural network models of the basal ganglia. Such an investigation would allow for a possible comparison of the simulation results and their determined uncertainty with experimental results from a closed loop DBS system,

which records LFPs in the motor cortex. Due to the lack of literature data, the uncertainty in the model parameters was assumed to be uniformly distributed to represent a "worst-case" scenario. The data of the model parameters obtained from experimental measurements with a large number samples would most likely resemble a Gaussian distribution. To allow for an optimal computation of the polynomial expansions with the PC technique for different distributions in the model parameters, corresponding basis functions and cubature methods have to be added to the already implemented non-intrusive projection method.

A Appendix

A.1 Representation of heterogeneous media by lumped equivalent circuit components

The following section describes the derivation of conditions for the representation of heterogeneous media in a volume conductor model by lumped equivalent circuit components. The proposed Fourier finite element method with equivalent circuits (FFEMEC), which is described in section 3.3, derives the transfer function for voltage-controlled and current-controlled stimulation in the proximity of the stimulated target in the generated volume conductor model of the human brain by using lumped equivalent circuit components, which are computed at a single frequency ω_k . This approach is only applicable, if the combinations of the electrical properties of the brain tissue types in the heterogeneous volume conductor model of the human brain are non-dispersive, which requires the fulfilment of certain conditions. In this section, these conditions are derived from a simplified volume conductor model comprising a plate capacitor with two media in series.

The admittance of both media can be described by their conductance G and capacitance C :

$$Y_1 = G_1 + j\omega C_1 \quad (\text{A.1})$$

$$Y_2 = G_2 + j\omega C_2 \quad (\text{A.2})$$

The total admittance of the volume conductor model is

$$Y = \left(\frac{1}{Y_1} + \frac{1}{Y_2} \right)^{-1} = \frac{Y_1 Y_2}{Y_1 + Y_2} = \frac{(G_1 + j\omega C_1)(G_2 + j\omega C_2)}{G_1 + G_2 + j\omega(C_1 + C_2)}. \quad (\text{A.3})$$

The application of a multiplication by one with the complex conjugate of the denominator as well as rearrangement of the terms results in the following expression for

the total admittance

$$\begin{aligned}
 Y = & \frac{G_1}{(G_1^2 + \omega^2 C_1^2) \left[\left(\frac{G_1}{G_1^2 + \omega^2 C_1^2} + \frac{G_2}{G_2^2 + \omega^2 C_2^2} \right)^2 + \left(\frac{\omega C_1}{G_1^2 + \omega^2 C_1^2} + \frac{\omega C_2}{G_2^2 + \omega^2 C_2^2} \right)^2 \right]} + \\
 & \frac{G_2}{(G_2^2 + \omega^2 C_2^2) \left[\left(\frac{G_1}{G_1^2 + \omega^2 C_1^2} + \frac{G_2}{G_2^2 + \omega^2 C_2^2} \right)^2 + \left(\frac{\omega C_1}{G_1^2 + \omega^2 C_1^2} + \frac{\omega C_2}{G_2^2 + \omega^2 C_2^2} \right)^2 \right]} + \\
 & j\omega \left\{ \frac{C_1}{(G_1^2 + \omega^2 C_1^2) \left[\left(\frac{G_1}{G_1^2 + \omega^2 C_1^2} + \frac{G_2}{G_2^2 + \omega^2 C_2^2} \right)^2 + \left(\frac{\omega C_1}{G_1^2 + \omega^2 C_1^2} + \frac{\omega C_2}{G_2^2 + \omega^2 C_2^2} \right)^2 \right]} + \right. \\
 & \left. \frac{C_2}{(G_2^2 + \omega^2 C_2^2) \left[\left(\frac{G_1}{G_1^2 + \omega^2 C_1^2} + \frac{G_2}{G_2^2 + \omega^2 C_2^2} \right)^2 + \left(\frac{\omega C_1}{G_1^2 + \omega^2 C_1^2} + \frac{\omega C_2}{G_2^2 + \omega^2 C_2^2} \right)^2 \right]} \right\} \\
 = & G_{\text{tot}} + j\omega C_{\text{tot}} .
 \end{aligned} \tag{A.4}$$

The lumped conductance G_{tot} and capacitance C_{tot} depend on the angular frequency ω , which means that they are dispersive. Assuming that the electrical properties of the media hold the conditions

$$\left(\frac{\omega C_1}{G_1} \right)^2 \ll 1 \text{ and } \left(\frac{\omega C_2}{G_2} \right)^2 \ll 1 , \tag{A.5}$$

the total admittance in equation A.4 can be approximated by

$$Y \approx \frac{G_1 G_2 (G_1 + G_2)}{(G_1 + G_2)^2 + 2\omega^2 C_1 C_2} + j\omega \frac{C_1 G_2^2 + C_2 G_1^2}{(G_1 + G_2)^2 + 2\omega^2 C_1 C_2} . \tag{A.6}$$

Under the condition that the following term, representing the combination of the electrical properties of both media, fulfils

$$\frac{2\omega^2 C_1 C_2}{(G_1 + G_2)^2} \ll 1 , \tag{A.7}$$

the total admittance can be approximated by

$$Y \approx \underbrace{\frac{G_1 G_2}{G_1 + G_2}}_{=G_{\text{tot}}} + j\omega \underbrace{\frac{C_1 G_2^2 + C_2 G_1^2}{(G_1 + G_2)^2}}_{=C_{\text{tot}}} , \tag{A.8}$$

which results in non-dispersive formulations for the lumped conductance G_{tot} and capacitance C_{tot} . For a straight plate capacitor with constant cross section A_s and

A.1 Representation of heterogeneous media by lumped equivalent circuit components

length l of each medium, the conductance G_i and capacitance C_i of the media are

$$G_i = \frac{\kappa_i A_s}{l} \text{ and } C_i = \frac{\varepsilon_0 \varepsilon_{r,i} A_s}{l} \quad (\text{A.9})$$

where κ_i is the conductivity and $\varepsilon_{r,i}$ is the relative permittivity of the medium i . Substituting the conductance and capacitance in the conditions (A.5) by these expressions result in the conditions

$$\left(\frac{\omega \varepsilon_0 \varepsilon_{r,1}}{\kappa_1} \right)^2 \ll 1 \text{ and } \left(\frac{\omega \varepsilon_0 \varepsilon_{r,2}}{\kappa_2} \right)^2 \ll 1, \quad (\text{A.10})$$

which is the square of the condition for the neglect of the capacitive effect in section 3.1.1. However, it has to be kept in mind that for an arbitrary geometry, the conditions in equation (A.10) depend on the geometry as well.

Bibliography

- [1] P Ashby, Y J Kim, R Kumar, A E Lang, and A M Lozano. Neurophysiological effects of stimulation through electrodes in the human subthalamic nucleus. *Brain*, 122:1919–1931, 1999.
- [2] M Axer, K Amunts, D Grässel, J Dammer, H Axer, U Petrzyk, and K Zilles. A novel approach to the human connectome: Ultra-high resolution mapping of fiber tracts in the brain. *NeuroImage*, 54:1091–1101, 2011.
- [3] I Babuška and B Szabo. On the rates of convergence of the finite element method. *Int J Numer Meth Eng*, 18:323–341, 1982.
- [4] I Babuška, F Nobile, and R Tempone. Worst case scenario analysis for elliptic problems with uncertainty. *Numer Math*, 101:185–219, 2005.
- [5] R A Bakay. *Movement Disorder Surgery: The Essentials*. Thieme, New York, 2008.
- [6] C A Balanis. *Advanced engineering electromagnetics*. Wiley, New York, 1989.
- [7] N B Bangera, D L Schomer, N Dehghani, Ulbert I, S Cash, S Papavasiliou, S R Eisenberg, A M Dale, and E Halgren. Experimental validation of the influence of white matter anisotropy on the intracranial EEG forward solution. *J Comput Neurosci*, 29:371–387, 2010.
- [8] G Barkhoudarian, T Klochkov, M Sedrak, A Frew, A Gorgulho, E Behnke, and A DeSalles. A role of diffusion tensor imaging in movement disorder surgery. *Acta Neurochir*, 152:2089–2095, 2010.
- [9] P J Basser and C Pierpaoli. Microstructural and Physiological Features of Tissues Elucidated by Quantitative-Diffusion-Tensor MRI. *J Magn Reson*, 111: 209–219, 1996.
- [10] S Baumann, D Wozny, S Kelly, and F C Meno. The electrical conductivity of human cerebrospinal fluid at body temperature. *IEEE Trans Biomed Eng*, 44: 220–223, 1997.
- [11] N P Bekhtereva, A N Bondarchuk, V M Smirnov, and L A Meliucheva. Therapeutic electric stimulation of deep brain structures, russ. *Vopr Neirokhir*, 36: 7–12, 1972.

- [12] R E Bellman. *Adaptive Control Processes: A Guided Tour*. Princeton University Press, Princeton, 1961.
- [13] A L Benabid, P Pollak, A Louveau, S Henry, and J de Rougemont. Combined (thalamotomy and stimulation) stereotactic surgery of the VIM thalamic nucleus for bilateral Parkinson disease. *Appl Neurophysiol*, 50:344–346, 1987.
- [14] A L Benabid, P Pollak, D Gao, D Hoffmann, P Limousin, E Gay, I Paven, and A Benazzouz. Chronic electrical stimulation of the ventral intermedius nucleus of the thalamus as a treatment of movement disorders. *J Neurosurg*, 84:203–214, 1996.
- [15] W Birkmayer and O Hornykiewicz. The effect of L-3,4-dihydroxyphenylalanine (=DOPA) on akinesia in parkinsonism. *Wien Klin Wochenschr*, 73:787–788, 1961.
- [16] A Bondeson, T Rylander, and P Ingeström. *Computational Electromagnetics*. Springer, Berlin, 2005.
- [17] C A Bossetti, M J Birdno, and W M Grill. Analysis of the quasi-static approximation for calculating potentials generated by neural stimulation. *J Neural Eng*, 5:44–53, 2008.
- [18] J M Bronstein, M Tagliati, R Alterman, A M Lozano, J Volkman, A Stefani, F Horak, M S Okun, K D Foote, P Krack, R Pahwa, J M Henderson, M I Hari, R A Bakay, F M Weaver, R E Gross, and M R DeLong. Deep Brain Stimulation for Parkinson Disease: An Expert Consensus and Review of Key Issues. *Arch Neurol*, 68:165–171, 2011.
- [19] P Brown and A Eusebio. Paradoxes of functional neurosurgery: clues from basal ganglia recordings. *Mov Disord*, 23:12–20, 2008.
- [20] C Brücke, J Huebl, T Schönecker, W J Neumann, K Yarrow, A Kupsch, C Blahak, G Lütjens, P Brown, J K Krauss, G H Schneider, and A Kühn. Scaling of movement is related to pallidal γ oscillations in patients with dystonia. *J Neurosci*, 32:1008–1019, 2012.
- [21] C R Butson and C C McIntyre. Tissue and electrode capacitance reduce neural activation volumes during deep brain stimulation. *Clin Neurophysiol*, 116:2490–2500, 2005.
- [22] C R Butson and C C McIntyre. Role of electrode design on the volume of tissue activated during deep brain stimulation. *J Neural Eng*, 3:1–8, 2006.

- [23] C R Butson, S E Cooper, J M Henderson, and C C McIntyre. Predicting the Effects of Deep Brain Stimulation with Diffusion Tensor Based Electric Field Models. *MICCAI*, pages 429–437, 2006.
- [24] C R Butson, C B Maks, and C C McIntyre. Sources and effects of electrode impedance during deep brain stimulation. *Clin Neurphysiol*, 117:447–454, 2006.
- [25] C R Butson, S E Cooper, J M Henderson, B Wolgamuth, and C C McIntyre. Probabilistic Analysis of Activation Volumes During Deep Brain Stimulation. *Neuroimage*, 54:2096–2104, 2011.
- [26] D R Cantrell, S Inayat, A Taflove, R S Ruoff, and J B Troy. Incorporation of the electrode–electrolyte interface into finite-element models of metal microelectrodes. *J Neural Eng*, 5:54–67, 2008.
- [27] A Castrioto, A M Lozano, Y Y Poon, A E Lang, M Fallis, and E Moro. Ten-year outcome of subthalamic stimulation in Parkinson disease: a blinded evaluation. *Arch Neurol*, 68:1550–1556, 2011.
- [28] S Chanraud, N Zahr, E V Sullivan, and A Pfefferbaum. MR Diffusion Tensor Imaging: A Window into White Matter Integrity of the Working Brain. *Neuropsychol Rev*, 20:209–225, 2010.
- [29] A Chaturvedi, C R Butson, S F Lempka, S E Cooper, and C C McIntyre. Patient-specific models of deep brain stimulation: Influence of field model complexity on neural activation predictions. *Brain Stimul*, 3:65–77, 2010.
- [30] M Clemens, T Weiland, and U van Rienen. Comparison of Krylov-Type Methods for Complex Linear Systems Applied to High-Voltage Problems. *IEEE T Magn*, 34:3335–3338, 1998.
- [31] S Clénet. Uncertainty Quantification in Computational Electromagnetics: The stochastic approach. *Int Compumag Soc Newsl*, 20:3–13, 2013.
- [32] COMSOL. Multiphysics Modeling and Simulation, 2013. URL <http://www.comsol.com/>. last checked: 03. June. 2013.
- [33] CSC. Elmer - Open Source Finite Element Software for Multiphysical Problems, 2012. URL <http://www.csc.fi/english/pages/elmer>. last checked: 03. June. 2013.
- [34] G Deuschl, C Schade-Brittinger, P Krack, J Volkmann, H Schäfer, K Bötzel, C Daniels, A Deutschländer, U Dillmann, W Eisner, D Gruber, W Hamel, J Herzog, R Hilker, S Klebe, M Klo, J Koy, M Krause, A Kupsch, D Lorenz,

- S Lorenzl, H M Mehdorn, J R Moringlane, W Oertel, M O Pinsker, H Reichmann, A Reu, G H Schneider, A Schnitzler, U Steude, V Sturm, L Timmermann, V Tronnier, T Trottenberg, L Wojtecki, E Wolf, W Poewe, and J Voges. A Randomized Trial of Deep-Brain Stimulation for Parkinson's Disease. *New Engl J Med*, 355:896–908, 2006.
- [35] Dular, P and Geuzaine, C. GetDP: a General Environment for the Treatment of Discrete Problems, 2013. URL <http://geuz.org/getdp/>. last checked: 03. June. 2013.
- [36] M S Eldred, C G Webster, and P G Constantine. Evaluation of Non-Intrusive Approaches for Wiener-Askey Generalized Polynomial Chaos. *Proceedings of the 10th AIAA nondeterministic approaches conference*, AIAA-2008-1892, 2008.
- [37] T J C Faes, H A van der Meij, J C de Munck, and R M Heethaar. The electric resistivity of human tissues (100 Hz–10 MHz): A meta-analysis of review. *Physiol Meas*, 20:R1–R10, 1999.
- [38] S Farris and M Giroux. Deep brain stimulation: A review of the procedure and the complications. *JAAPA*, 24:39–45, 2011.
- [39] A Fedorov, R Beichel, J Kalpathy-Cramer, J Finet, J-C Fillion-Robin, S Pujol, C Bauer, D Jennings, F Fennessy, M Sonka, J Buatti, S R Aylward, J V Miller, S Pieper, and R Kikinis. 3D Slicer as an Image Computing Platform for the Quantitative Imaging Network. *Magn Reson Imaging*, 30:1323–1341, 2012.
- [40] G S Fishman. *Monte Carlo: Concepts, Algorithms, and Applications*. Springer Series in Operations Research. Springer, New York, third edition, 1999.
- [41] K A Follett, F M Weaver, M Stern, K Hur, C L Harris, P Luo, W J Jr Marks, J Rothlind, O Sagher, C Moy, R Pahwa, K Burchiel, P Hogarth, E C Lai, J E Duda, K Holloway, A Samii, S Horn, J M Bronstein, G Stoner, P A Starr, R Simpson, G Baltuch, A De Salles, G D Huang, and D J Reda. Pallidal versus Subthalamic Deep-Brain Stimulation for Parkinson's Disease. *New Engl J Med*, 362:2077–2091, 2010.
- [42] K R Foster and H P Schwan. Dielectric properties of tissues and biological materials: A critical review. *Crit Rev Biomed Eng*, 17:25–104, 1989.
- [43] K R Foster, J L Schepps, R D Stoy, and H P Schwan. Dielectric Properties of Brain Tissue between 0.01 and 10 GHz. *Phys Med Biol*, 24:1177–1187, 1979.
- [44] D Funaro. *Polynomial Approximation of Differential Equations*. Lecture Notes in Physics Monographs. Springer-Verlag, Berlin, 1992.

- [45] C Gabriel, A Peyman, and E H Grant. Electrical conductivity of tissue at frequencies below 1 MHz. *Phys Med Biol*, 54:4863–4878, 2009.
- [46] S Gabriel, R W Lau, and C Gabriel. The dielectric properties of biological tissues: III Parametric models for the dielectric spectrum of tissues. *Phys Med Biol*, 41:2271–2293, 1996.
- [47] Gabriel, S. APPENDIX C: Modelling the frequency dependence of the dielectric properties to a 4 dispersions spectrum, 2012. URL <http://niremf.ifac.cnr.it/docs/DIELECTRIC/AppendixC.html>. last checked: 26. June. 2012.
- [48] P Gatev, O Darbin, and T Wichmann. Oscillations in the basal ganglia under normal conditions and in movement disorders. *Mov Disord*, 21:1566–1577, 2006.
- [49] L Geddes and L. Baker. The specific resistance of biological material. A compendium of data for the biomedical engineer and physiologist. *Med Biol Eng*, 5:271–293, 1967.
- [50] R Geus. *The Jacobi-Davidson algorithm for solving large sparse symmetric eigenvalue problems with application to the design of accelerator cavities*. PhD thesis, Swiss Federal Institute of Technology Zurich, 2002.
- [51] R G Ghanem and P D Spanos. *Stochastic Finite Elements: A Spectral Approach*. Springer-Verlag, New York, 1991.
- [52] J Gimsa, B Habel, U Schreiber, U van Rienen, U Strauss, and U Gimsa. Choosing electrodes for deep brain stimulation experiments: Electrochemical considerations. *J Neurosci Meth*, 142:251–265, 2005.
- [53] U Gimsa, U Schreiber, B Habel, J Flehr, U van Rienen, and J Gimsa. Matching geometry and stimulation parameters of electrodes for deep brain stimulation experiments: Numerical considerations. *J Neurosci Meth*, 150:212–227, 2006.
- [54] L Golestanirad, A P Izquierdo, S J Graham, J R Mosig, and C Pollo. Effect of realistic modeling of deep brain stimulation on the prediction of volume of activated tissue. *Pr Electromagn Res*, 126:1–16, 2012.
- [55] P F Grant. *Computational Modelling of Volume Conductor and Network Effects of Deep Brain Stimulation*. PhD thesis, School of Electrical, Electronic and Mechanical Engineering, University College Dublin, 2011.
- [56] P F Grant and M M Lowery. Electric field distribution in a finite-volume head model of deep brain stimulation. *Med Eng Physics*, 31:1095–1103, 2009.

- [57] P F Grant and M M Lowery. Effect of Dispersive Conductivity and Permittivity in Volume Conductor Models of Deep Brain Stimulation. *IEEE T Bio-med Eng*, 57:2386–2393, 2010.
- [58] W M Grill and J T Mortimer. Electrical Properties of Implant Encapsulation Tissue. *Ann Biomed Eng*, 22:23–33, 1994.
- [59] W M Grill and X F Wei. High Efficiency Electrode for Deep Brain Stimulation. *Conf Proc IEEE Eng Med Biol Soc*, 22:3298–3301, 2009.
- [60] S Grimnes and O G Martinsen. *Bioimpedance and Bioelectricity Basics*. Academic Press, Oxford, second edition, 2008.
- [61] S J Groiss, L Wojtecki, M Südmeyer, and A Schnitzler. Deep brain stimulation in Parkinson’s disease. *Ther Adv Neurol Disord*, 2:379–391, 2009.
- [62] C Guigoni, Q Li, I Aubert, S Dovero, B H Bioulac, B Bloch, A R Crossman, C E Gross, and E Bezard. Involvement of Sensorimotor, Limbic, and Associative Basal Ganglia Domains in L-3,4-Dihydroxyphenylalanine-Induced Dyskinesia. *J Neurosci*, 25:2912–2107, 2005.
- [63] D Güllmar, J Haueisen, and J R Reichenbach. Influence of anisotropic electrical conductivity in white matter tissue on the EEG/MEG forward and inverse solution: A high-resolution whole head simulation study. *NeuroImage*, 51: 145–163, 2010.
- [64] C Hammond, H Bergman, and P Brown. Pathological synchronizaion in Parkinson’s disease: Networks, models and treatments. *Trends in Neurosciences*, 30:357–364, 2007.
- [65] M Hanke-Bourgeois. *Grundlagen der Numerischen Mathematik und des Wissenschaftlichen Rechnens*. Vieweg+Teubner, Wiesbaden, third edition, 2009.
- [66] H A Haus and J R Melcher. *Electromagnetic Fields and Energy*. Prentice Hall, New Jersey, 1989.
- [67] M Hines. NEURON—a program for simulation of nerve equations. In J Skrzypek, editor, *Neural Network Simulation Environments*, pages 147–163. Kluwer, Norwell, MA, 1994.
- [68] A L Hodgkin and A F Huxley. A quantitative description of membrane current and its application to conduction and excitation in nerve. *J Physiol*, 117:500–544, 1952.

- [69] R N Holdefer, R Sadleir, and M J Russel. Predicted current densities in the brain during transcranial electrical stimulation. *Clin Neurophysiol*, 117:1388–1397, 2006.
- [70] J L Houeto, P B Bejjani, P Damier, C Staedler, A M Bonnet, B Pidoux, D Dormont, P Cornu, and Y Agid. Failure of long-term pallidal stimulation corrected by subthalamic stimulation in PD. *Neurology*, 55:728–730, 2000.
- [71] J D Jackson. *Klassische Elektrodynamik (4. Aufl.)*. de Gruyter, Berlin, 1999.
- [72] C Koch. *Biophysics of Computation: Information Processing in Single Neurons*. Oxford University Press, New York, 1999.
- [73] P Krack, A Batir, N Van Blercom, S Chabardes, V Fraix, C Ardouin, A Koudsie, P D Limousin, A Benazzouz, J F LeBas, A L Benabid, and P Pollak. Five-Year Follow-up of Bilateral Stimulation of the Subthalamic Nucleus in Advanced Parkinson’s Disease. *New Engl J Med*, 349:1925–1934, 2003.
- [74] H J Kretschmann and W Weinrich. *Klinische Neuroanatomie und kranielle Bilddiagnostik*. Georg Thieme Verlag, Stuttgart, 1991.
- [75] T Lanz and W Wachsmuth. *Praktische Anatomie: Kopf und übergeordnete Systeme (5. Aufl.)*. Springer, Berlin Heidelberg, 2003.
- [76] J Latikka, T Kuurne, and H Eskola. Conductivity of living intracranial tissues. *Phys Med Biol*, 46:1611–1616, 2001.
- [77] S H Lee and W Chen. A comparative study of uncertainty propagation methods for black-box-type problems. *Struct Multidisc Optim*, 37:239–253, 2009.
- [78] S F Lempka, M D Johnson, S Miocinovic, J L Vitek, and C C McIntyre. Current-controlled deep brain stimulation reduces in vivo voltage fluctuations observed during voltage-controlled stimulation. *Clin Neurophysiol*, 121:2128–2133, 2010.
- [79] M Liberti, F Apollonio, A Paffi, M Parazzini, F Maggio, T Novellino, P Ravazzani, and G D’Inzeo. Fundamental Electrical Quantities in Deep Brain Stimulation: Influence of Domain Dimensions and Boundary Conditions. *P Ann Int IEEE EMBS*, pages 6668–6671, 2007.
- [80] P Malliavin and A Thalmaier. *Stochastic Calculus of Variations in Mathematical Finance*. Springer Finance. Springer, New York, 2006.

- [81] J C Maxwell. A Dynamical Theory of the Electromagnetic Field. *Phil Trans R Soc Lond*, 155:459–512, 1865.
- [82] C C McIntyre, A G Richardson, and W M Grill. Modeling the excitability of mammalian nerve fibers: influence of afterpotentials on the recovery cycle. *J Neurophysiol*, 87:995–1006, 2002.
- [83] C C McIntyre, S Mori, D L Sherman, N V Thakor, and J L Vitek. Electric field and stimulating influence generated by deep brain stimulation of the subthalamic nucleus. *Clin Neurophysiol*, 115:589–595, 2004.
- [84] C C McIntyre, C R Butson, C B Maks, and A M Noecker. Optimizing Deep Brain Stimulation Parameter Selection with Detailed Models of the Electrode-Tissue Interface. *P Ann Int IEEE EMBS*, pages 893–895, 2006.
- [85] Medtronic, Inc. Medtronic DBS: Lead Kit for Deep Brain Stimulation, 2003.
- [86] Medtronic, Inc. Products and Procedures for Medtronic Deep Brain Stimulation, 2012. URL <http://professional.medtronic.com/pt/neuro/dbs-md/prod/index.htm>. last checked: 13. June. 2012.
- [87] S Miocinovic, S F Lempka, G S Russo, C B Maks, C R Butson, K E Sakaie, J L Vitek, and C C McIntyre. Experimental and theoretical characterization of the voltage distribution generated by deep brain stimulation. *Exp Neurol*, 216:166–176, 2009.
- [88] J Modolo, E Mosekilde, and A Beuter. New insights offered by a computational model of deep brain stimulation. *J Physiology-Paris*, 101:56–63, 2007.
- [89] E B Jr Montgomery and J T Gale. Mechanisms of action of deep brain stimulation. *Neurosci Behav Rev*, 32:388–407, 2008.
- [90] J L Moreines, S M McClintock, and P E Holtzheimer. Neuropsychological Effects of Neuromodulation Techniques for Treatment-Resistant Depression: A review. *Brain Stimul*, 4:17–27, 2011.
- [91] F Mundinger. New stereotactic treatment of spasmodic torticollis with a brain stimulation system, dt. *Med Klin*, 72:1982–1986, 1977.
- [92] L Nechak, S Berger, and E Aubry. Non-intrusive generalized polynomial chaos approach to the stability analysis of uncertain nonlinear dynamic systems. *8th International Multi-Conference on Systems, Signals and Devices (SSD)*, pages 1–6, 2011.

- [93] F Nobile, R Tempone, and C G Webster. A sparse grid stochastic collocation method for partial differential equations with random input data. *SIAM J Numer Anal*, 46:2309–2345, 2008.
- [94] S H Oh, B I Lee, E J Woo, S Y Lee, T S Kim, O Kwon, and J K Seo. Electrical conductivity images of biological tissue phantoms in MREIT. *Physiol Meas*, 16:S279–S288, 2005.
- [95] S H Oh, S Y Lee, M H Cho, T S Kim, and I H Kim. Electrical conductivity estimation from diffusion tensor and T2: A silk yarn phantom study. *Proc Intl Soc Mag Reson Med*, 14:3034, 2006.
- [96] M S Okun, B V Gallo, G Mandybur, J Jagid, K D Foote, F J Revilla, R Alterman, J Jankovic, R Simpson, F Junn, Leo Verhagen, J E Arle, B Ford, R R Goodman, R M Stewart, S Horn, G H Baltuch, B H Kopell, F Marshall, D Peichel, R Pahwa, K E Lyons, A I Trster, J L Vitek, and M Tagliati. Subthalamic deep brain stimulation with a constant-current device in Parkinson’s disease: an open-label randomised controlled trial. *Lancet Neurol*, 11: 140–149, 2012.
- [97] M S Okun et al. Cognition and Mood in Parkinson’s Disease in Subthalamic Nucleus versus Globus Pallidus Interna Deep Brain Stimulation: The COMPARE Trial. *Ann Neurol*, 65:586–595, 2009.
- [98] M ParvareshRizi, B Alijani, S Fereshtehnejad, and S Bakhti. Anatomical situation of the subthalamic nucleus (STN) from midcommissural point (MCP) in Parkinson’s disease patients who underwent deep brain stimulation (DBS): An MRI targeting study. *Med J Islam Repub Iran*, 24:35–42, 2010.
- [99] M Pirini, L Rocchi, M Sensi, and L Chiari. A computational modelling approach to investigate different targets in deep brain stimulation for Parkinson’s disease. *J Comput Neurosci*, 26:91–107, 2009.
- [100] R Plonsey and D B Heppner. Considerations of quasi-stationarity in electrophysiological systems. *B Math Biophys*, 29:657–664, 1967.
- [101] C Potratz. *Zur Optimierung elektrostimulativer Hüftgelenksimplanate mit externer magnetischer Anregung*. PhD thesis, Insitute of General Electrical Engineering, University of Rostock, 2010.
- [102] F Rattay. Analysis of models for external stimulation of axons. *IEEE Trans Biomed Eng*, 33:974–977, 1986.
- [103] A Richardot and E T McAdams. Harmonic Analysis of Low-Frequency Bioelectrode Behavior. *IEEE Trans Med Imag*, 21:604–612, 2002.

- [104] T Rohlfing, N M Zahr, E V Sullivan, and A Pfefferbaum. The SRI24 Multi-Channel Brain Atlas. *Proc Soc Photo Opt Instrum Eng*, 6914:691409, 2008.
- [105] J P Ruhston and C D Ankney. Brain size and cognitive ability: Correlations with age, sex, social class, and race. *Psychon B Rev*, 3:21–36, 1996.
- [106] M Rullmann, A Anwander, M Dannhauer, S K Warfield, F H Duffy, and C H Wolters. EEG source analysis of epileptiform activity using a 1 mm anisotropic hexahedra finite element head model. *NeuroImage*, 44:399–410, 2009.
- [107] G Schmid, G Neubauer, U M Illievich, and F Alesch. Dielectric Properties of Porcine Brain Tissue in the Transition From Life to Death at Frequencies From 800 to 1900 MHz. *Bioelectromagnetics*, 24:413–422, 2003.
- [108] C Schmidt and U van Rienen. Quantification of uncertainties in brain tissue conductivity in a heterogeneous model of deep brain stimulation using a non-intrusive projection approach. *Engineering in Medicine and Biology Society (EMBC), 2012 Annual International Conference of the IEEE*, pages 4136–4139, 2012.
- [109] C Schmidt and U van Rienen. Modeling the Field Distribution in Deep Brain Stimulation: The Influence of Anisotropy of Brain Tissue. *IEEE Trans Bio Eng*, 59:1583–1592, 2012.
- [110] C Schmidt and U van Rienen. Single Frequency Approximation of Volume Conductor Models for Deep Brain Stimulation Using Equivalent Circuits. *Proceedings of the International Conference on Bio-inspired Systems and Signal Processing*, pages 38–47, 2013.
- [111] C Schmidt and U van Rienen. Modelling the Probabilistic Neural Activation in Deep Brain Stimulation: Influence of Uncertainty in the Parameters of the Electrode-Tissue-Interface. *International Symposium on Electromagnetic Theory (EMTS 2013)*, (in press), 2013.
- [112] C Schmidt, P Grant, M Lowery, and U van Rienen. Influence of Uncertainties in the Material Properties of Brain Tissue on the Probabilistic Volume of Tissue Activated. *IEEE Trans Bio Eng*, 60:1378–1387, 2013.
- [113] H P Schwan. Electrical properties of tissues and cell suspensions: Mechanisms and models. *Adv Biol Med Phys*, 5:147–209, 1957.
- [114] H R Schwarz. *Methode der finiten Elemente*. Teuber, Stuttgart, third edition, 1991.
- [115] H R Schwarz and N Köckler. *Numerische Mathematik*. Lehrbuch Mathematik. Teubner B.G. GmbH, Wiesbaden, seventh edition, 2009.

- [116] J S Shimony, R C McKinstry, E Akbudak, J A Aronovitz, A Z Snyder, N F Lori, T S Cull, and T E Conturo. Quantitative Diffusion-Tensor Anisotropy Brain MR Imaging: Normative Human Data and Anatomic Analysis. *Radiology*, 212:770–784, 1999.
- [117] M Simeonova and J Gimsa. Dielectric anisotropy, volume potential anomalies and the persistent Maxwellian equivalent body. *J Phys Condens Matter*, 17: 7817–7831, 2005.
- [118] S A Smolyak. Quadrature and interpolation formulas for tensor products of certain classes of functions. *Dokl Akad Nauk SSSR*, 4:240–243, 1963.
- [119] C Soanes and A Stevenson. *Concise Oxford English dictionary*. Oxford University Press, 2006.
- [120] S N Sotiropoulos and P N Steinmetz. Assessing the direct effects of deep brain stimulation using embedded axon models. *J Neural Eng*, 4:107–119, 2007.
- [121] B Sudret and A Der Kiureghian. Stochastic finite element methods and reliability: a state-of-the-art report. *UCB/SEMM-2000/08*, pages 1–179, 2000.
- [122] B Sudret, M Berveiller, and M Lemaire. A stochastic finite element procedure for moment and reliability analysis. *Eur J Comp Mech*, 15:825–866, 2006.
- [123] Sudret, B and Der Kiureghian, A. Spectral Stochastic Finite Elements in Matlab (SSFEM), 2000. URL <http://www.ce.berkeley.edu/projects/FERUM/Download/ferumssfem.ZIP>. last checked: 26.Feb.2013.
- [124] Teem. Definition of NRRD File Format, 2008. URL <http://teem.sourceforge.net/nrrd/format.html>. last checked: 14.March.2013.
- [125] L N Trefethen. Is Gauss Quadrature Better than Clenshaw-Curtis? *SIAM Rev*, 50:67–87, 2008.
- [126] D Tuch, V J Weeden, A M Dale, J S George, and J W Belliveau. Conductivity tensor mapping of the human brain using diffusion tensor MRI. *Proc Natl Acad Sci USA*, 98:11697–11701, 2001.
- [127] U van Rienen. *Numerical Methods in Computational Electrodynamics*. Springer, Berlin Heidelberg, 2001.
- [128] J L Vitek, T Hashimoto, J Peoples, M R DeLong, and A E Bakay. Acute stimulation in the external segment of the globus pallidus improves Parkinsonian motor signs. *Mov Disord*, 19:907–915, 2004.

- [129] J Volkmann, N Allert, J Voges, and P H Weiss. Safety and efficacy of pallidal or subthalamic nucleus stimulation in advanced PD. *Neurology*, 56:548–551, 2001.
- [130] J Volkmann, J Herzog, F Kopper, and G Deuschl. Introduction to the Programming of Deep Brain Stimulators. *Mov Disord*, 17:S181–S187, 2002.
- [131] von Winckel. Fast Clenshaw-Curtis Quadrature, 2005. URL <http://www.mathworks.com/matlabcentral/fileexchange/6911-fast-clenshaw-curtis-quadrature/content/fclencurt.m>. last checked: 26.Feb.2013.
- [132] G Walckiers, B Fuchs, J P Thiran, J R Mosig, and C Pollo. Influence of the implanted pulse generator as reference electrode in finite element model of monopolar deep brain stimulation. *J Neurosci Meth*, 186:90–96, 2010.
- [133] J Waldvogel. Fast Construction of the Fejér and Clenshaw-Curtis Quadrature Rules. *BIT Numerical Mathematics*, 46:195–202, 2006.
- [134] M D Webster, M A Tatang, and G J McRae. *Application of the Probabilistic Collocation Method for an Uncertainty Analysis of a Simple Ocean Model*. Report (MIT Joint Program on the Science and Policy of Global Change). MIT Joint Program on the Science and Policy of Global Change, 1996.
- [135] X F Wei and W M Grill. Impedance characteristics of deep brain stimulation electrodes in vitro and in vivo. *J Neural Eng*, 6:046008, 2009.
- [136] N Wiener. The Homogeneous Chaos. *Am J Math*, 60:897–936, 1938.
- [137] C H Wolters, A Anwander, X Tricoche, D Weinstein, M A Koch, and R S Macleod. Influence of tissue conductivity anisotropy on EEG/MEG field and return current computation in a realistic head model: A simulation and visualization study using high-resolution finite element modeling. *NeuroImage*, 30:813–826, 2006.
- [138] D Xiu. *Numerical Methods for Stochastic Computations: A Spectral Method Approach*. Princeton University Press, 2010.
- [139] D Xiu and G E Karniadakis. The Wiener–Askey Polynomial Chaos for Stochastic Differential Equations. *SIAM J Sci Comput*, 24:619–644, 2002.
- [140] J Yelnik. Functional anatomy of the basal ganglia. *Mov Disord*, 17:S15–S21, 2002.

- [141] A B Young and J B Jr Penney. Biochemical and functional organization of the basal ganglia. In J J Jankovic and E Tolosa, editors, *Parkinson's Disease & Movement Disorders*, chapter 1, pages 1–10. Lippincott Williams & Wilkins, Philadelphia, 2002.
- [142] N Yousif and X Liu. Investigating the depth electrode-brain interface in deep brain stimulation using finite element models with graded complexity in structure and solution. *J Neurosci Meth*, 184:142–151, 2009.
- [143] N Yousif, B Richard, and X Liu. The influence of reactivity of the electrode-brain interface on the crossing electric current in therapeutic deep brain stimulation. *Neuroscience*, 156:597–606, 2009.
- [144] N Yousif, N Purswani, R Bayford, D Nandi, P Bain, and X Liu. Evaluating the impact of the deep brain stimulation induced electric field on subthalamic neurons: A computational modelling study. *J Neurosci Meth*, 188:105–112, 2010.
- [145] L B Zahodne, M S Okun, K D Foote, H H Fernandez, R L Rodriguez, S S Wu, L Kirsch-Darrow, C E Jacobson, C Rosado, and D Bowers. Greater improvement in quality of life following unilateral deep brain stimulation surgery in the globus pallidus as compared to the subthalamic nucleus. *J Neurol Neurosurg Ps*, 8:1321–1329, 2009.
- [146] T C Zhang and W M Grill. Modeling deep brain stimulation: Point source approximation versus realistic representation of the electrode. *J Neural Eng*, 7:066009, 2010.
- [147] J Zhuang, W Ren, Y Jing, and J F Kolb. Dielectric evolution of mammalian cell membranes after exposure to pulsed electric fields. *IEEE T Dielect El In*, 19:609–622, 2012.

Selbstständigkeitserklärung

Hiermit erkläre ich, dass ich die vorliegende Dissertation mit dem Titel "Uncertainty quantification in a computationally optimised volume conductor model for deep brain stimulation" selbstständig und ohne fremde Hilfe und nur unter Verwendung der von mir angegebenen Quellen und Hilfsmittel verfasst habe.

Rostock,

Christian Schmidt

Thesen

zur Dissertation

Uncertainty quantification in a computationally optimised volume conductor model for deep brain stimulation

von Christian Schmidt

These 1

Deep brain stimulation (DBS) is a neurosurgical method, in which an implanted DBS electrode causes a time-dependent voltage response in the stimulated target area by the application of voltage-controlled and current-controlled stimulation pulses.

These 2

An anatomical brain model incorporating the heterogeneous electrical properties of brain tissue is required for a realistic modelling of the time-dependent voltage response and neural activation in the stimulated target area.

These 3

For the frequency spectrum of the DBS pulse, propagation and inductive effects in the electromagnetic fields in the brain can be assumed to be negligible in the proximity of the stimulated target, which allows for the application of the electro-quasistatic formalism for the computation of the time-dependent voltage response in this area.

These 4

The Fourier finite element method with equivalent circuits (FFEMEC) allows for a fast computation of the time-dependent voltage response in agreement with the common Fourier finite element method (FFEM) for non-dispersive electrical properties of biological tissue, which exhibits a small capacitive effect.

These 5

The electrical properties of brain tissue are frequency-dependent in the frequency spectrum of the DBS pulse. A single frequency approximation of these properties in the brain model resulted in a sufficiently accurate approximation of the time-dependent voltage response.

These 6

The prediction of the neural activation in the stimulated target area is obtained by the concept of the volume of tissue activated (VTA). The amplitude and slope of the time-dependent voltage response influences the extent of the VTA.

These 7

The parameters of the electrode tissue interface and the electrical properties of brain tissue are subject to uncertainty in literature. The polynomial chaos technique (PCT) allows for an uncertainty quantification in the brain model for these model parameters by approximating the probabilistic model solutions by a polynomial expansion in random variables.

These 8

In the non-intrusive implementation of the PCT, the deterministic model remains unchanged. The coefficients of the polynomial expansions are computed with multi-dimensional numerical cubature. The application of sparse grids allows for a substantial reduction of the required integration nodes.

These 9

Compared to the influence of uncertainty in the electrical properties of brain tissue, the influence of uncertainty in the parameters of the electrode-tissue-interface is negligible.

These 10

The influence of uncertainty in the electrical properties of brain tissue on the voltage response and VTA was larger for current-controlled stimulation than for voltage-controlled stimulation. For both stimulation types the uncertainty in these quantities was mostly influenced by the conductivity of brain tissue.

These 11

Prescribing an uncertainty limit of 5 % in the probabilistic VTA, the electrical properties are required to be determined more precisely than actually available in literature.

These 12

The anisotropic conductivity in the stimulated target area has a minor influence on the time-dependent voltage response, resulting from a comparatively small anisotropy ratio in this area than in areas with evenly oriented white matter fibres.

These 13

A comparison of the determined uncertainty in the time-dependent voltage response with the influence of anisotropic conductivity suggests that an isotropic brain model provides a reasonable approximation of an anisotropic brain model for the modelling of DBS in this stimulated target area.

Abstract

Deep brain stimulation (DBS) is a neurosurgical method based on implanting electrodes in selected brain areas to treat symptoms of neurological and psychiatric disorders. Although the method has become a common procedure in clinical practice, the understanding of its mechanisms is still scarce. Starting in the last decade, numerous computational models for predicting the mechanisms of DBS and the volume of tissue activated (VTA) around the DBS electrode were developed, which are based on several parameters subject to uncertainty. To date, human brain models for DBS only consider one set of possible parameters and, therefore, do not regard their uncertainty and probabilistic nature. This thesis examines the influence of uncertainty in the model parameters on the time-dependent voltage response and neural activation in the proximity of the stimulated target. An anatomical head model incorporating heterogeneous and anisotropic tissue properties was generated, based on a digital brain atlas. The computation of the time-dependent voltage response in the proximity of the DBS electrode, based on the electro-quasistatic formulation of Maxwell's equations, was optimised by combining the common Fourier finite element method with equivalent circuits derived from the brain model. A best single frequency approximation of the dispersive volume conductor model could be determined for the frequency-dependent electrical properties of brain tissue and the application of a common DBS pulse. The quantification of uncertainty in the human brain model was obtained by approximating the probabilistic voltage response and VTA by a polynomial expansion, using the polynomial chaos technique. The reduction of the required number of executions of the deterministic model was further reduced by the application of sparse grids with nested nodes. The investigation of the influence of uncertainty in the electrical properties of brain tissue and the parameters of the electrode-tissue-interface revealed a minor influence in the parameters of the electrode-tissue-interface and suggested that the uncertainty in the relative permittivity of brain tissue is negligible, and that consequently the uncertainty in the conductivity of brain tissue mostly influences the uncertainty in the time-dependent voltage response and VTA in the generated volume conductor model of the human brain. The determined uncertainty boundaries for the conductivity of brain tissue demand for a more precise determination of the electrical properties of brain tissue. Comparing the determined uncertainty in the time-dependent voltage response with the predicted influence of anisotropic conductivity in the proximity of the stimulated target, an isotropic volume conductor model of the human brain was determined to be an appropriate simplification of the anisotropic human brain model.

Zusammenfassung

Die Tiefe Hirnstimulation (THS) ist eine neurochirurgische Methode, bei der Elektroden in tief gelegene Hirnareale implantiert werden, um Symptome von neurodegenerativen Krankheiten zu behandeln. Obwohl die THS eine gängige Methode in der klinischen Praxis darstellt, sind die Mechanismen der THS noch weitgehend unverstanden. In den letzten Jahren wurden zahlreiche computergestützte Modelle zur Erforschung dieser Mechanismen und zur Prognose des aktivierten Volumens (engl.: volume of tissue activated - VTA) der THS entwickelt, welche jedoch auf unsicheren Modellparametern beruhen. Bisherige Modelle betrachten lediglich deterministische Parameter und berücksichtigen nicht deren Unsicherheiten und stochastische Eigenschaften. Diese Arbeit untersucht den Einfluss dieser Unsicherheiten auf die zeitabhängige Spannungsantwort und das VTA in der Umgebung der THS Elektrode. Ein anatomisches Kopfmodell, welches die heterogenen und anisotropen elektrischen Eigenschaften von Hirngewebe wiedergibt, wurde auf Grundlage eines digitalen Hirnatlas erstellt. Die Berechnung der zeitabhängigen Spannungsantwort, basierend auf der elektroquasistatischen Formulierung der Maxwell'schen Gleichungen, wurde durch die Kombination der bekannten Fourier Finite Elemente-Methode mit Ersatzschaltbildern des Modells optimiert. Eine beste Approximationsfrequenz des dispersiven Volumenleitermodells für die frequenzabhängigen elektrischen Eigenschaften des Gewebes konnte für die Verwendung eines typischen THS Signals bestimmt werden. Die Quantifizierung von Unsicherheiten im THS Modell wurde durch eine Reihenentwicklung der stochastischen Spannungsantwort und des VTA mittels des Polynomialen Chaos erreicht. Der benötigte Rechenaufwand wurde weiter durch die Verwendung von Dünngitterverfahren mit verschachtelten Stützpunkten erreicht. Die Untersuchung des Einflusses von Unsicherheiten in den elektrischen Eigenschaften von Hirngewebe und den Parametern des Elektrode-Gewebe-Übergangs zeigte einen geringen Einfluss dieser Parameter und der relativen Permittivität von Hirngewebe, was auf einen dominanten Einfluss von Unsicherheiten in der Leitfähigkeit von Hirngewebe auf die zeitabhängige Spannungsantwort und das VTA im entwickelten Modell des menschlichen Gehirns schließen lässt. Die daraus bestimmten Schranken für die Unsicherheit in der Leitfähigkeit von Hirngewebe erfordern eine präzisere experimentelle Messung dieser Parameter. Ein Vergleich der resultierenden Unsicherheiten in der zeitabhängigen Spannungsantwort mit dem prognostizierten Einfluss der anisotropen Leitfähigkeit in der Umgebung der DBS Elektrode lässt vermuten, dass ein isotropes Modell des menschlichen Gehirns eine angemessene Approximation eines anisotropen Modells gewährleistet.